**Final Report**

**FDOT Contract No. BED30 977-11**

# Performance Testing of GRS Test Piers Constructed with Florida Aggregates – Axial Load Deformation Relationships

Submitted To:

Rodrigo Herrera, P.E.
Project Manager
Florida Department of Transportation

Scott Wasman, Ph.D.
Principal Investigator

Christian Matemu
Graduate Assistant

**July 31, 2024**

Florida State University

FAMU-FSU College of Engineering

Department of Civil and Environmental Engineering

## DISCLAIMER

The opinions, findings, and conclusions expressed in this publication are those of the authors and not necessarily those of the Florida Department of Transportation or the U.S. Department of Transportation

## APPROXIMATE CONVERSIONS TO SI UNITS

| SYMBOL | WHEN YOU KNOW | MULTIPLY BY | TO FIND | SYMBOL |
|---|---|---|---|---|
| LENGTH | | | | |
| in | inches | 25.4 | millimeters | mm |
| ft | feet | 0.305 | meters | m |
| yd | yards | 0.914 | meters | m |
| mi | miles | 1.61 | kilometers | km |
| **SYMBOL** | **WHEN YOU KNOW** | **MULTIPLY BY** | **TO FIND** | **SYMBOL** |
| AREA | | | | |
| $in^2$ | square inches | 645.2 | square millimeters | $mm^2$ |
| $ft^2$ | square feet | 0.093 | square meters | $m^2$ |
| $yd^2$ | square yard | 0.836 | square meters | $m^2$ |
| ac | acres | 0.405 | hectares | ha |
| $mi^2$ | square miles | 2.59 | square kilometers | $km^2$ |
| **SYMBOL** | **WHEN YOU KNOW** | **MULTIPLY BY** | **TO FIND** | **SYMBOL** |
| VOLUME | | | | |
| fl oz | fluid ounces | 29.57 | milliliters | mL |
| gal | gallons | 3.785 | liters | L |
| $ft^3$ | cubic feet | 0.028 | cubic meters | $m^3$ |
| $yd^3$ | cubic yards | 0.765 | cubic meters | $m^3$ |
| NOTE: volumes greater than 1000 L shall be shown in $m^3$ | | | | |
| **SYMBOL** | **WHEN YOU KNOW** | **MULTIPLY BY** | **TO FIND** | **SYMBOL** |
| MASS | | | | |
| oz | ounces | 28.35 | grams | g |
| lb | pounds | 0.454 | kilograms | kg |
| T | short tons (2000 lb) | 0.907 | megagrams (or "metric ton") | Mg (or "t") |
| **SYMBOL** | **WHEN YOU KNOW** | **MULTIPLY BY** | **TO FIND** | **SYMBOL** |
| TEMPERATURE (exact degrees) | | | | |
| °F | Fahrenheit | 5 (F-32)/9<br>or (F-32)/1.8 | Celsius | °C |
| **SYMBOL** | **WHEN YOU KNOW** | **MULTIPLY BY** | **TO FIND** | **SYMBOL** |
| ILLUMINATION | | | | |
| fc | foot-candles | 10.76 | lux | lx |
| fl | foot-Lamberts | 3.426 | candela/$m^2$ | $cd/m^2$ |
| **SYMBOL** | **WHEN YOU KNOW** | **MULTIPLY BY** | **TO FIND** | **SYMBOL** |
| FORCE and PRESSURE or STRESS | | | | |
| lbf | pound force | 4.45 | newtons | N |
| $lbf/in^2$ | pound force per square inch | 6.89 | kilopascals | kPa |

## APPROXIMATE CONVERSIONS TO ENGLISH UNITS

| SYMBOL | WHEN YOU KNOW | MULTIPLY BY | TO FIND | SYMBOL |
|---|---|---|---|---|
| LENGTH | | | | |
| mm | millimeters | 0.039 | inches | in |
| m | meters | 3.28 | feet | ft |
| m | meters | 1.09 | yards | yd |
| km | kilometers | 0.621 | miles | mi |
| **SYMBOL** | **WHEN YOU KNOW** | **MULTIPLY BY** | **TO FIND** | **SYMBOL** |
| AREA | | | | |
| $mm^2$ | square millimeters | 0.0016 | square inches | $in^2$ |
| $m^2$ | square meters | 10.764 | square feet | $ft^2$ |
| $m^2$ | square meters | 1.195 | square yards | $yd^2$ |
| ha | hectares | 2.47 | acres | ac |
| $km^2$ | square kilometers | 0.386 | square miles | $mi^2$ |
| **SYMBOL** | **WHEN YOU KNOW** | **MULTIPLY BY** | **TO FIND** | **SYMBOL** |
| VOLUME | | | | |
| mL | milliliters | 0.034 | fluid ounces | fl oz |
| L | liters | 0.264 | gallons | gal |
| $m^3$ | cubic meters | 35.314 | cubic feet | $ft^3$ |
| $m^3$ | cubic meters | 1.307 | cubic yards | $yd^3$ |
| **SYMBOL** | **WHEN YOU KNOW** | **MULTIPLY BY** | **TO FIND** | **SYMBOL** |
| MASS | | | | |
| g | grams | 0.035 | ounces | oz |
| kg | kilograms | 2.202 | pounds | lb |
| Mg (or "t") | megagrams (or "metric ton") | 1.103 | short tons (2000 lb) | T |
| **SYMBOL** | **WHEN YOU KNOW** | **MULTIPLY BY** | **TO FIND** | **SYMBOL** |
| TEMPERATURE (exact degrees) | | | | |
| °C | Celsius | 1.8C+32 | Fahrenheit | °F |
| **SYMBOL** | **WHEN YOU KNOW** | **MULTIPLY BY** | **TO FIND** | **SYMBOL** |
| ILLUMINATION | | | | |
| lx | lux | 0.0929 | foot-candles | fc |
| $cd/m^2$ | $candela/m^2$ | 0.2919 | foot-Lamberts | fl |
| **SYMBOL** | **WHEN YOU KNOW** | **MULTIPLY BY** | **TO FIND** | **SYMBOL** |
| FORCE and PRESSURE or STRESS | | | | |
| N | newtons | 0.225 | pound force | lbf |
| kPa | kilopascals | 0.145 | pound force per square inch | $lbf/in^2$ |

# TECHNICAL REPORT DOCUMENTATION PAGE

| 1. Report No. | 2. Government Accession No. | 3. Recipient's Catalog No. |
|---|---|---|
| 4. Title and Subtitle<br>Performance Testing of GRS Test Piers Constructed with Florida Aggregates – Axial Load Deformation Relationships | | 5. Report Date<br>July 2024<br>6. Performing Organization Code: |
| 7. Author(s)<br>Scott Wasman and Christian Matemu | | 8. Performing Organization Report No. |
| 9. Performing Organization Name and Address<br>Florida State University<br>FAMU-FSU College of Engineering<br>Department of Civil and Environmental Engineering<br>2525 Pottsdamer Street<br>Tallahassee, FL 32310 | | 10. Work Unit No.<br>11. Contract or Grant No.<br>BED30 977-11 |
| 12. Sponsoring Agency Name and Address<br>Florida Department of Transportation<br>605 Suwannee Street, MS 30<br>Tallahassee, FL 32399 | | 13. Type of Report and Period<br>Final Report<br>03/30/2020-07/31/2024<br>14. Sponsoring Agency Code |
| 15. Supplementary Notes | | |


16. Abstract:

A series of full-scale axial load-deformation tests on instrumented GRS piers were conducted using materials approved for use in Florida. The piers were designed and constructed following the FHWA and FDOT guidelines for dimensional ratio of height/width = 2, compacted backfill of poorly graded No. 57, well graded RCA-GAB, and a LWA (as a trial experiment), reinforced with biaxial and uniaxial woven polypropylene geosynthetics with a minimum of 4,800 lbs/ft strength spaced 8 inches apart, and confined with 86 lbs segmental facing blocks. The primary objectives were to investigate the behavior of GRS composites specific to Florida design practice, provide accurate stress-strain data for design purposes and evaluate the GRS composite structure axial and horizontal strains under service pressure. Large diameter triaxial tests were performed are appropriate for testing well graded materials. The analysis of triaxial results showed the influence of triaxial specimen on shear strength properties of well-graded RCA-GAB. Conducting triaxial tests on 6-inch diameter specimens led to an increase in the friction angle by 11.4° and 8.5° for peak and residual states, respectively, compared to 4-inch specimens. All GRS piers tested met the FHWA service limit criteria for GRS-IBS satisfactorily. At applied vertical g pressure of 4 ksf (FHWA recommended dead plus live load, with load factors =1), the vertical strain for all GRS piers was below 1%, with lateral strain below 0.51%. The applied vertical pressure needed to achieve 1% vertical strain ranged from 4.1 ksf to 19 ksf for all piers, while the pressure required to reach 2% lateral strain varied from 11 ksf to 32 ksf. Comparison of experimental data with FHWA design methods for GRS-IBS showed that the FHWA ultimate capacity equation consistently underestimated the measured vertical capacity of piers constructed with open graded-No 57 and well graded RCA-GAB backfills when the residual friction angle from large diameter triaxial tests are used. The FHWA equation for lateral displacement accurately predicted the lateral displacement of the facing walls during loading. The assumption of zero volume change was found to hold only below the applied vertical pressure of 4 ksf.

The results of the load-deformation tests provide 7 additional values to the dataset of FHWA bearing capacity bias with which new resistance factors were calculated following the AASHTO strength I load combination and using the First Order Second Moment (FOSM) method. For deal to dead + live load ratio of 0.37, resistance factors were calculated to be 0.57, 0.53, 0.44, and 0.37 for reliability indices of 2.33, 2.5, 3.0, ad 3.5, respectively.


| 17. Key Words | 18. Distribution Statement |
|---|---|
| Geosynthetics, Geosynthetic Reinforced Soil, GRS-IBS, GRS Abutment, Reinforcement Strain, Polypropylene Woven geotextile, Large Diameter Triaxial Test | No restrictions. |

| 19. Security Classif. (of this report) | 20. Security Classif. (of this page) | 21. No. of Pages | 22. Price |
|---|---|---|---|
| Unclassified | Unclassified | 206 | |

## ACKNOWLEDGMENTS

The researchers would like to thank the Florida Department of Transportation (FDOT) for the financial support that made this research possible. Special thanks to the staff at the FDOT Marcus Ansley Structure Research Center for providing access and assistance in construction, instrumentation, and testing. Additionally, researchers would like to thank the staff at the State Material Office for their assistance in testing the materials. Researchers are also grateful to Dr. Rawlinson at UF Structures lab and Steven Squillaqote at the FAMU-FSU Civil and Environmental Structures lab for their assistance during the preparation of the materials and casting of the footing.

## EXECUTIVE SUMMARY

Geosynthetic Reinforced Soil-Integrated Bridge Systems (GRS-IBS) have gained recognition as an innovative and cost-effective solution for bridge construction. The empirical approach, based on performance testing, is currently recommended by the Federal Highway Administration (FHWA) as one of the design methods for GRS-IBS. This approach relies on stress-strain curves derived from performance tests, utilizing a database of test results provided by FHWA. However, the current database has limitations concerning the tested materials, particularly in Florida where approved materials for GRS-IBS have not undergone performance tests, necessitating the need for additional testing.

To expand the database of performance test results, a series of full-scale load tests on instrumented GRS piers was conducted using materials approved for use in Florida (poorly graded No. 57 and well graded RCA-GAB, biaxial and uniaxial woven geotextiles with minimum strength of 4,800 lbs/ft, and segmental facing blocks). These tests aimed to investigate the behavior of GRS composites and provide accurate stress-strain data for design purposes. The research also aimed to compare the experimental data with existing design methods, assess their suitability for use by the FDOT, and incorporate the experimental results into the FHWA's performance test database. The experiments also included the investigation of a new lightweight aggregate for potential use in GRS-IBS. A new approach utilizing fiber optic strain sensors was proposed for measuring reinforcement strain in geotextiles.

The experimental results showed that all the piers tested performed well in terms of their vertical and horizontal strains at the FHWA recommended service pressure of 4 ksf (dead plus live load with load factors = 1). The results also demonstrate that the choice of backfill, and geotextile strength has a significant impact on the behavior of GRS piers. Piers constructed with high strength geotextiles exhibited higher loading capacities compared to those with low strength geotextiles. The same effect was observed for backfill materials, with higher strength backfills resulting in stiffer and stronger GRS composites compared to low strength backfills. The common construction practice of incorporating concrete in the top three to five courses of blocks affected the lateral deformation and stiffness of the piers under small applied vertical stress conditions, typically below 7.25 ksf in this study. The use of concrete fill reduces the lateral displacement while

increasing the stiffness. Lateral displacement was also influenced by the type of backfill used, with piers constructed with high strength backfill exhibiting less lateral displacement. The measurement of reinforcement strain further revealed that the backfill type influenced the strain magnitudes, with low strain values observed in piers constructed with high strength backfill.

Comparisons with design methods reveal that the FHWA capacity equation underpredicts measured vertical capacities while the FHWA equation for lateral displacement accurately predicted the lateral displacement of the facing walls during loading. The assumption of zero volume change was found to hold well below the FHWA service limit pressure of 4 ksf. Compaction-induced lateral stress was found to be significant during construction of the GRS pier. Among the methods for estimating earth pressure, the Westergaard method was found to perform better in the prediction of lateral earth pressure, vertical earth pressure and reinforcement loads during loading of GRS composite.

TABLE OF CONTENTS

## LIST OF TABLES

## LIST OF FIGURES

# 1 INTRODUCTION

## 1.1 Motivation

Florida Department of Transportation (FDOT) Structure's Design Guideline requires that a Geosynthetic Reinforced Soil-Integrated Bridge System (GRS-IBS) be designed according to the FHWA Geosynthetic Reinforced Soil Integrated Bridge System Interim Implementation Guide (Adams and Nicks, 2018), unless stated otherwise. It requires checking for both the external and internal stability of the structure. Adams and Nicks (2018) recommends checking for external stability which includes direct sliding, bearing resistance of the foundation soil, and global stability. For internal stability design, Adams and Nicks (2018) recommends checks for internal bearing resistance, tolerable deformation, and the required reinforcement strength. Depending on availability of stress-strain curves from performance tests, these structures can be designed using the empirical or analytical approach for internal stability.

The empirical approach involves using stress-strain curves, which are obtained from full-scale loading tests on Geosynthetic Reinforced Soil (GRS) piers, to predict the behavior of reinforced bridge abutments. Existing stress-strain curves were developed for GRS structures that use poorly graded and well graded aggregates, woven geotextiles (with spacing equals to block height) and facing blocks. Because aggregates are sourced from different geological formations or processes (e.g., recycled concrete aggregate), their mechanical properties will vary and new stress-strain curves should be developed for regularly used aggregates. Woven geotextiles are made of polypropylene strands weaved in two directions to achieve minimum tensile stiffness and strength. There are numerous manufacturers of geotextiles and, between them, their properties may vary because of the manufacturing process. Facing blocks are cement cast to meet minimum compressive strengths and vary in size and mass.

Materials approved by the FDOT for use in GRS-IBS have not been tested in performance tests and the properties of these materials are different from those that have been tested in the previous performance tests. For example, the poorly graded aggregate is predominantly sourced from a Florida limestone formation that is younger and not as consolidated, or softer, than the aggregate from Virginia that was used in previous performance tests. Also, segmental retaining blocks (SRB) are approved for use in GRS-IBS built in Florida, while concrete masonry unit (CMU) blocks have been used in most of the previous performance tests. Several studies have

shown that the facing blocks improve the performance of the GRS composite. Nicks et al. (2013), Pham (2009), and Wu et al. (2013) reported higher stiffness and load-carrying capacity in the GRS composite with facing blocks due to the confinement compared to GRS composite without. Facing block characteristics that factor into the confinement are it's geometry and mass. CMU blocks are smaller and have less volume making them lighter than the SRBs, thereby providing less resistance to the earth pressure in the backfill layer. On the other hand, CMU blocks rectangular shape result in end-to-end placement on each course and a square perimeter on which the backfill aggregate to act against. The SRB blocks are non-uniformly shaped on their perimeter, resulting in a discontinuous block perimeter on the pier interior and complex aggregate-block interactions in the SRB facing. Lastly, of the two types of woven geotextiles approved for use in GRS-IBS in Florida, the 7,200 x 5,760 lbs/ft geotextile has not been used in a performance test, to the best of the researchers knowledge. Given this information, it is apparent there is a need for performance tests testing and research to be conducted with materials approved for use in Florida.

## 1.2 Objectives and Supporting Tasks

The objectives of this project are to:

i. Perform a background review of the literature and reports (research journals, FHWA reports, NCHRP 24-41, DOT reports from other states, and AASHTO Bridge Design Specifications) on GRS structures and pier tests. This included test results and conclusions, designs of previous tests (H/B, types and properties of geosynthetics, facing elements), design guidelines in practice (axial capacity, internal capacity, aggregates, etc.), typical aggregates used in Florida, and their geotechnical properties.

ii. Design 8 full-scale axial load-deformation tests of GRS piers built with the selected and FDOT approved geosynthetic reinforcements, facing elements and aggregate.

iii. Construct and test each GRS pier where the axial load applied at the top of the pier is developed using hydraulic jacks and measured using load cells, in conjunction with the vertical and horizontal pier displacement measured using linear displacement transducers. A load reaction frame will be designed for minimal deflection under two times the predicted maximum axial load.

iv. Include internal instrumentation to measure the profiles of tensile strain distributions in the reinforcements and the vertical and horizontal earth pressures in the aggregate and on the facing blocks.

v. Compare the performance (deflection, maximum axial load at specific vertical strain, ultimate axial load, tensile load in reinforcement, horizontal earth pressures, etc.) with current design methods (FHWA) and proposed methods in the research literature (i.e., Zornberg, et al. 2018).

vi. For all the tests of pier performance with different aggregate, and reinforcement, identify the axial loads at limiting service vertical and horizontal strains (vertical = 1% and horizontal = 2%, respectively), as recommended by FHWA.

vii. Based on the findings of the research, make recommendations to the FDOT for predicting axial load capacity and vertical and horizontal deformation based on existing or modified methods or equations that account for aggregate properties, and reinforcement strength. Also, make recommendations for any future research that may be necessary.

### 1.2.1 Task 1-Review previous studies on GRS piers, design methods, and construction practices

A comprehensive review of all available literature (academic papers and federal and state transportation reports) on GRS structures and pier tests was performed. It encompasses the background of GRS technology, previous experimental works conducted on these structures, designs (H/B, types and properties of reinforcements and aggregates, facing elements), existing design guidelines (axial capacity, internal capacity, aggregates, construction methods, etc.), and performance of the limited GRS-IBS in service. A review of the types of aggregates typically used in Florida, including their gradations and mechanical properties was performed through close consultation with the FDOT State Materials Office.

### 1.2.2 Task 2-Design experimental plan for GRS performance tests

The design of the experiment was conducted. The design process encompasses the selection of test materials, various laboratory tests conducted, test setup, construction procedures,

instrumentation techniques, loading procedures, and data collection methods. Selection of aggregates and reinforcements through consultation with FDOT. Acquisition of the aggregates was made with the assistance of the FDOT State Material Office (SMO). The layout of the GRS pier was determined based on several factors including the standard method developed by FHWA for performance testing, the conditions of the triaxial test, the particle size of the backfill, the vertical reinforcement spacing, the approved block sizes by FDOT and the size of the available reaction frame and jack. A 36 in x 36 in x 11.125 in reinforced concrete footing with a 1.5 in steel plate at the top was designed to be used as a loading platform. Footing's design, formwork and steel preparation, and casting of concrete footing were done at the University of Florida Structural Laboratory. The piers were constructed with approved segmental blocks as the facing elements. Three different woven polypropylene geotextiles were selected for reinforcement. Three different types of aggregates were selected for structural backfill. To investigate the performance of the GRS pier during the test, the pier was externally and internally instrumented with several sensors to monitor vertical and lateral deformations, axial loads applied, reinforcement strains in the geotextiles, vertical earth pressure at the bottom, and the lateral earth pressures along the facing block located at the mid-height of the pier. For loading, the reaction frame consists of four columns (W14X90) with a jacking beam (Double W36X150) was used. Data were recorded continuously at a sampling frequency of 2 Hz. Instruments were read with a multi-channel data acquisition system (NI cDAQ-9188 having 8 slots). The construction and testing of the GRS pier took place at FDOT Marcus H. Ansley Structures Research Center.

### 1.2.3 Task 3-GRS performance tests (axial load-deformation tests)

Based on Task 2, a series of eight GRS pier performance tests were conducted. Table 1-1 shows the dimensions and test conditions of each GRS pier tested in this study. Experimental results obtained from the load tests conducted on eight GRS piers were presented and discussed. The focus was on the load-deformation behavior, lateral displacement measurements, reinforcement strains and earth pressure observations. The influence of each component of the GRS mass on its behavior was thoroughly investigated and discussed.

Table 1-1. Test conditions.

| Test No | Backfill Type | Reinforcement Type | $T_f$ (lb/ft) | $S_v$ (inch) | B (ft) | H/B |
|---|---|---|---|---|---|---|
| PT-1 | #57 stone | Biaxial woven geotextile [A] | 4,800 x 4,800 | 8 | 3 | 2 |
| PT-2 | #57 stone | Woven geotextile [B] | 7,200 x 5,760 | 8 | 3 | 2 |
| PT-3 | #57 stone | Biaxial woven geotextile [C] | 4,800 x 4,800 | 8 | 3 | 2 |
| PT-4 | RCA-GAB | Biaxial woven geotextile [A] | 4,800 x 4,800 | 8 | 3 | 2 |
| PT-5 | RCA-GAB | Woven geotextile [B] | 7,200 x 5,760 | 8 | 3 | 2 |
| PT-6 | RCA-GAB | Biaxial woven geotextile [C] | 4,800 x 4,800 | 8 | 3 | 2 |
| PT-7 | FGA | Woven geotextile [B] | 4,800 x 4,800 | 8 | 3 | 2 |
| PT-8[**] | #57 stone | Biaxial woven geotextile [A] | 4,800 x 4,800 | 8 | 3 | 2 |

Notes: [A] Tencate Mirafi HP570, [B] Tencate Mirafi HP770, [C] Hanes Geo TerraTex HPG 57, [**] Block cells in the upper three courses of blocks contain concrete and rebar.

### 1.2.4 Task 4-Comparison of GRS performance test results with published results and available methods

The results of the performance tests in Task 3 were compared to the published results of other tests on GRS piers and to predictions using design methods in the literature and reports. This included a comparison of the measured vertical capacity with the FHWA capacity equation, a comparison of lateral and volumetric behavior with the FHWA design approach, a comparison of measured earth pressure and reinforcement loads. For all the tests of pier performance with different aggregate and reinforcement, the axial loads at limiting service vertical and horizontal strains were identified. Also, recommendations for implementing the findings and any future research were proposed.

# 2 LITERATURE REVIEW

## 2.1 Background on GRS

Geosynthetics are products made of synthetic materials that have been utilized for decades to enhance the stability and performance of soil. These materials are made from various polymers such as polyethylene, polypropylene, and polyester and can be used in various forms such as geotextiles, geogrids, geomembranes, and geonets. They have been employed for various functions such as controlling drainage, separating dissimilar materials, acting as a filter, and reinforcing soil. The use of soil reinforcement is not a recent concept, as it has been in practice for thousands of years with ancient civilizations using materials like straw, branches, and woven mats to reinforce soil (Wu, 2019a). However, with advancements in technology, geosynthetics have proven to be an efficient and cost-effective solution for soil reinforcement.

One specific application of geosynthetics is in Geosynthetic Reinforced Soil (GRS), which is a type of soil reinforcement consisting of closely spaced (≤ 12 inches) layers of geosynthetic reinforcement and compacted fill materials (Adams and Nicks, 2018). The reinforcement layers in GRS typically consist of high strength geosynthetics, which are used to provide tensile strength to the soil mass. The use of geosynthetics in GRS leads to a more composite behavior and improved internal stability compared to other methods of soil reinforcement, resulting in low failure rates.

GRS structures share similarities with mechanically stabilized earth (MSE) in terms of their materials and appearance. Both GRS and MSE use structural backfill, geosynthetics reinforcement, and facing elements. However, the GRS structures are built with reinforcement spacing 12 inches or less which results in more composite behavior than the MSE, which has a spacing of 18-24 inches. The major difference is in the stability, GRS is internally stabilized while the MSE is externally stabilized using the anchorage to the wall face to resist the lateral soil and surcharge pressure. A GRS structure derives stability through internal friction resistance between the soil and tensile reinforcement layers by forming a geosynthetics-soil-geosynthetic composite. The reinforcements resist the tensile forces and restrain lateral deformation of the soil (Adams and Nicks, 2018). Other factors that contribute to the GRS behavior are the aggregate size, gradation, friction angle, unit weight, and the facing elements. GRS structures have an extremely low failure rate (service and strength limits), less than MSE walls and earth retaining walls (Wu, 2019a). This

is due to the close spacing of the reinforcement layers which results in more composite behavior and better internal stabilization.

Over the years, GRS structures have performed better than their conventional counterparts. Their applications in geotechnical engineering have been increasing and in recent years, the Federal Highway Administration (FHWA) has promoted its use in Geosynthetic Reinforced Soil Integrated Bridge System (GRS-IBS) abutments for single-span bridges through the Everyday Counts Initiative. Beyond their performance, the use of GRS-IBS has been driven primarily by its efficient construction and cost savings. Other benefits of GRS-IBS include the use of common materials and equipment without the need for specialized labor, flexibility, easier maintenance, better quality control, increased durability, and resistance to effects of earthquakes. A unique characteristic of GRS-IBS is the jointless connection between the abutment and approach roadway which eliminates the "bump at the end of bridge" problem caused by differential settlement (Adams and Nicks, 2018). This improves the overall ride quality and reduces the likelihood of damage to vehicles. Several full-scale load tests have shown that if GRS-IBS is designed and constructed properly, it will perform well under both static and dynamic loading conditions (Adams and Nicks, 2018; Zheng, 2017; Zheng et al., 2019a; Zheng et al., 2019b). Field observations by Talebi (2016), Saghebfar et al. (2017), Gebremariam et al. (2019), Ooi et al. (2019) and Nicks et al. (2020) have shown the GRS-IBS performs well under short and long term service conditions.

GRS-IBS is a structure designed to bear the load of a bridge deck and surcharge while undergoing limited vertical and horizontal deformations. The FHWA developed a performance test method to investigate the behavior of frictionally connected GRS abutments under axial load. It entails constructing a mini-GRS pier and the loading axially while monitoring its vertical and horizontal response to a satisfactory level or until failure. The results from performance tests are then used to establish the service and strength limits for design purposes. For validity, the materials used in the structure should have the same or similar properties to the materials used in the performance tests. If the materials change or are different, then new performance tests should be conducted. For example, the limestone aggregate backfills used in Florida is from a different geologic formation than that used in the FHWA pier tests, and likely doesn't have the same properties. Similarly, segmental retaining blocks (SRB) weigh about two times more than the blocks the FHWA used, meaning different confining pressures are expected. Numerical modeling

and field observations are valuable when calibrated and comparable. For these reasons, a new series of tests that pertain to Florida practice are warranted.

## 2.2 Soil Reinforcement Mechanism

A GRS pier consists of three main components: the structural backfill, reinforcement and facing. Structural backfill provides resistance to shear and normal compression stresses while the reinforcement provides tensile strength. The facing provides confinement to the reinforced soil under surcharge pressures. As the backfill is loaded vertically, the compressive stresses cause vertical and lateral deformation. The horizontal deformation of soil causes shear stresses that are transferred to reinforcement through interface friction and horizontal pressure acting against the back of the facing blocks which is resisted by the reinforcement and facing blocks. The surface roughness of the geosynthetic will control the friction resistance and amount of shear stress transferred. Depending on the geosynthetic characteristics, the soil particles can interlock with geosynthetics and when sheared they create a mechanical bond between the two. From this, reinforcement tension is mobilized, reducing deformation and increasing shear strength. Different concepts have been developed to explain the mechanism of soil reinforcement. Two early mechanism concepts of apparent cohesion by Schlosser and Long (1974) and apparent confinement by Yang (1972) are presented in the following sections.

### 2.2.1 Mechanism of Apparent Cohesion

In this concept, reinforcement is assumed to introduce apparent cohesion to the reinforced soil mass. If triaxial tests were conducted on the unreinforced and reinforced soil sample, the result in Mohr-Circles would be like the one shown in Figure 2-1. The reinforcement would increase the major principal stress by $\Delta\sigma_{1R}$ from $\sigma_1$ to $\sigma_{1R}$. The angle of internal friction is assumed to be the same for unreinforced and reinforced soil if the soil and reinforcement at the interface remain in contact and no slippage occurs. This assumption is still questionable as it has been shown in many studies that slippage does occur, and no relative movement between the soil and reinforcement exists only at small stress. At higher stresses, there is a combination of slippage and reinforcement rupture, thus relative movement that is important to consider when estimating the ultimate capacity of GRS-IBS structures.

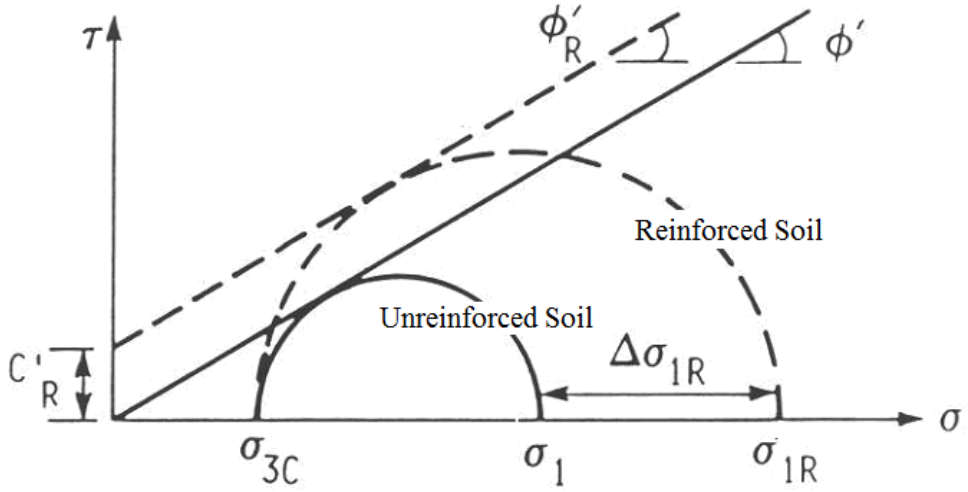


Figure 2-1. Introduction of apparent cohesion due to reinforcement.
(Pham, 2009).

### 2.2.2 Apparent Confining Pressure

In this concept, it is assumed that the addition of reinforcement increases the principal stress at failure along with an increase in the confining pressure, as illustrated in Figure 2-2 (Yang, 1972). The confining pressure increase is assumed to occur in a direction parallel to that of the reinforcement layers.

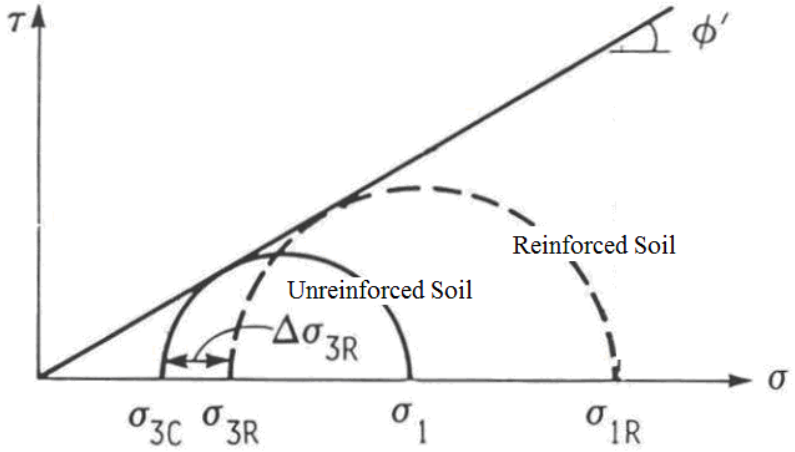


Figure 2-2. Increase in axial strength and confinement pressure.
(Pham, 2009).

## 2.3 Experimental History

Early studies to investigate the performance of GRS structures were based on the triaxial compression tests (ZEN et al. (1974), Broms (1977), Gray and Al-Refeai (1986), Ketchart and Wu (2001), MOGHADAS and Asakereh (2007) etc.) and plane strain compression tests (Whittle et al. (1992), Boyle (1995), Ketchart and Wu (2001), Ketchart and Wu (2002)). Although these tests have provided insight into the GRS mass's behavior, their results are questionable due to relatively small dimensions and can be misleading (Ketchart and Wu, 2001). Small scale laboratory tests by Gray and Al-Refeai (1986) and MOGHADAS and Asakereh (2007) have shown reinforced soil having smaller stiffness than unreinforced soil at smaller axial strains between 0 to 1-2%. This was attributed to compression of the geotextile, an exaggerated effect due to their smaller test specimen (Wu, 2019b). This makes full-scale load tests the best alternative for studying GRS behavior under various loading and soil conditions where the actual field conditions are simulated. Despite being more expensive and time-consuming, the full-scale test provides valuable information rather than scaled laboratory tests. This section summarizes previous experimental work research on large-scale GRS structures that are relevant to this work.

### 2.3.1 Full-Scale Load Testing

Adams (1997) carried out full-scale load test on a GRS pier that was 17.7 feet tall. The aim of the test was twofold: to evaluate its performance under different loading conditions and to demonstrate the feasibility of constructing a GRS pier using segmental block facing. The pier was reinforced with high-strength biaxial woven polypropylene geotextile, spaced vertically at 8 inches, while well-graded material (classified as GW-GM according to ASTM D2487) was used as structural backfill. The pier had a facing system made up of standard split face cinder blocks, and the walls were battered at a 20:1 (V:H) ratio. Pier was instrumented with load cells, displacement sensors and strain gauges to measure applied load, vertical and horizontal displacements, and reinforcement strains, respectively. The pier was constructed in two phases, with static load testing carried out at an intermediate depth of 9.8 feet and at its full height. The findings revealed that pre-straining the reinforced soil mass improved the pier's performance by decreasing vertical settlement by 50%. However, it had no impact on the pier's lateral displacement.

Gotteland et al. (1997) carried out a complete load test to investigate the failure behavior of a reinforced embankment functioning as a bridge abutment. The embankment was 4.35 m tall, with two symmetrical sections featuring distinct embankment profiles. One section was reinforced with non-woven geotextile (NW), while the other used woven geotextile (W), with both types of reinforcement spaced vertically 0.29 m. The W section had alternating short and long reinforcements to increase the bending resistance of the cellular facing. The backfill material was sand compacted to its maximum dry density. Both sections were loaded by beam on top of the embankment two months after construction, and their performances were monitored. The NW section exhibited a localized failure in the upper layers, while the W section had a deeper failure. The GRS walls failed at applied loads of 123 kN/m and 140 kN/m for woven and nonwoven geotextile-reinforced soil, respectively, with settlements of 33 mm and 36 mm, respectively. Despite having higher strength reinforcement, the woven GRS wall had a lower critical load due to its shorter reinforcement in the middle of long reinforcement layers.

Ketchart (1997) and Ketchart and Wu (1997) carried out full-scale load tests on two GRS piers and one GRS abutment in Denver, Colorado to examine the performance of the GRS bridge support system under less stringent conditions than in Adams (1997)'s test and to evaluate its long-term performance under a sustained design load. Each structure was reinforced with uniaxial woven polypropylene geotextile at a vertical spacing of 8 inches while 12 inches vertical spacing was used for the reinforced soil foundation. The backfill material used was a road base classified as A-1-A (0) and was compacted to a modified proctor relative compaction of 91% for the pier and 90% for the abutment. A levelling rod, elastic spring, strain gauges were used to measure vertical movement, lateral displacements, and reinforcement strains, respectively. Only the outer pier and abutment were load tested and both structures performed relatively well with a load capacity greater than the specified maximum pressure of 4 ksf and the creep deformation of the structure was observed to decrease with time.

Wu et al. (2001) conducted full-scale load tests on two GRS bridge abutments supporting a 118 ft span steel arched bridge in Black Hawk, Colorado. Each abutment consisted of GRS mass, footings, and two-tier rock-faced walls, and they were reinforced with a woven polypropylene geotextile (wide width tensile strength of 4,800 lb/ft) at a vertical spacing of 12 inches. The structural backfill material used was on-site soil classified as SM-SC. Both abutments were supported on stiff soil with bases at different depths. The GRS abutments were preloaded to a

vertical stress of 5.1 ksf and then reloaded to a design stress of 3.1 ksf using a hydraulic jack. Precision survey transition, dogmatic indicators, and strain gauges were used to measure vertical settlement, lateral displacements, and reinforcement strain, respectively. The results indicated that preloading reduced vertical settlement, differential settlement between the two abutments, lateral displacements of the GRS abutments, and the creep strains in the geotextile reinforcement.

Adams et al. (2002) conducted a comprehensive load test on a GRS pier to study its load-carrying capacity and deformation behavior. The pier was a square column measuring 3.7 ft x 3.7 ft x 8.0 ft, reinforced with a woven polypropylene geotextile at a vertical spacing of 6 inches, and had bearing bed reinforcements at the top two rows. Segmental retaining walls blocks with a split face was used for facing system. The backfill material was granular gravel (road base) classified as GP-GM. The study found that the vertical settlement increased linearly with the vertical stress up to 20.9 ksf, while the linear relationship between lateral deformation and vertical stress was limited to 12.5 ksf due to significant downward bowing of reinforcement sheets. The results showed that the reduction in volume due to vertical compression was nearly equal to the increase in volume due to lateral displacement. This led to the "postulate of zero volume change," which can be used calculate the maximum lateral displacement of the GRS structure. From this, Adams et al. (2002) developed an equation for estimating maximum lateral displacement as a function of vertical settlement, height, and width of the GRS structure.

Wu et al. (2006) carried out two full-scale experiments on segmental GRS bridge abutments to investigate their performance under varying load levels and to validate analytical models. The abutments had a height of 15.3 ft and were reinforced with two different types of woven geotextile having ultimate tensile strengths of 4,800 lb/ft and 1,440 lb/ft, respectively, at a vertical spacing of 8 inches. The facing system comprised of concrete cinder blocks. The backfill material used was non-plastic silty sand classified as SP-SM. Each abutment was instrumented to monitor the vertical movements, lateral displacement of the walls, and strains in geotextile reinforcements. The findings indicated that increasing the reinforcement strength increased the ultimate internal bearing capacity while reducing the lateral displacement and vertical settlement.

Adams et al. (2007) conducted five experiments called Mini Piers to investigate the effect of reinforcement spacing and strength on the performance of a GRS mass. Each pier had dimensions of 3.3 ft x 3.3 ft x 6.3 ft high. Reinforcement was provided by woven polypropylene

geotextiles with a tensile strength range from 1,440 lb/ft to 4,800 ft/lb and vertical spacing ranging from 8 inches to 23.6 inches. Crushed diabase rock classified as well-graded gravel (GW-GM) was used as backfill. Facing was provided by CMU blocks, which were removed before the load was applied to eliminate the effect of facing on the GRS mass performance and to observe soil deformation. While previous studies have indicated that facing blocks contribute to the strength of the GRS mass, they are not included in lateral force calculations during the design phase since the GRS mass is internally stable and does not require blocks to withstand lateral earth pressure. As a result, removing the blocks was deemed appropriate. The findings indicated that the spacing of vertical reinforcement had a greater impact on GRS mass performance than reinforcement strength. Additionally, the experiments demonstrated that GRS mass can be utilized as a freestanding structure that is internally stable.

Nicks et al. (2013) carried out a series of 19 full-scale load tests to assess the behavior of GRS piers under axial loading. The tests aimed to build a database of GRS materials, evaluate the relationship between reinforcement strength and spacing, quantify the contribution of facing elements, assess the new internal stability design method proposed by Adams et al. (2012b), and perform reliability analysis of the proposed soil-geosynthetic capacity equation for LRFD calibration. Throughout testing, the height to width ratio (H/B) of the piers was maintained constant at about 2, to mimic triaxial conditions. The tests employed frictionally connected concrete masonry blocks for facing. Six different backfill materials with friction angles ranging from 46° to 54°, apparent cohesion values of 0 psf and 115 psf, and maximum aggregate sizes ranging from 3/8 inch to 1 inch were employed. The piers were reinforced with a biaxial woven polypropylene geotextile with tensile strengths ranging from 1400 lb/ft to 4800 lb/ft at vertical spacing ranging from 4 to 16 inches. Two configurations were considered, one with facing elements and one without. The piers were instrumented to measure vertical and lateral deformation, reinforcement strain and applied load during loading. The results indicated that the load-deformation behavior of GRS composites is influenced by multiple factors, including preloading, aggregate angularity, compaction level, presence of bearing bed reinforcement, and facing confinement. The use of higher strength reinforcement resulted in a stiffer and stronger response compared to lower strength reinforcement, and the use of well-graded material increased the stiffness of the GRS composite. These experiments can be used to model the load-deformation behavior of different GRS parameters for pier construction.

Wu et al. (2013) carried out a series of experiments on large-scale generic soil geosynthetic composite (GSGC) to investigate the behavior of GRS mass under well-controlled conditions. The tests were conducted under plain strain conditions. The specimen dimensions were 3.9 ft x 4.6 ft x 6.6 ft. The structural backfill material used was a crushed diabase while woven polypropylene geotextile with an ultimate tensile strength of 4,800 lb/ft and 9,600 lb/ft was used for reinforcement. The GSGC were instrumented to monitor their behavior during loading. Wu et al. (2013) reported that the presence of geosynthetic reinforcement reduced the angle of dilation of the soil mass and prevented the dilation of surrounding soil. Also, the results demonstrated that reinforcement spacing has a higher influence on the performance of the GRS mass than the reinforcement strength. Additionally, Wu et al. (2013) developed an analytical model to describe the relationship between reinforcement strength and spacing and developed equations for calculating the apparent cohesion, ultimate load-carrying capacity, and required tensile strength of reinforcement.

Zheng et al. (2019a) conducted load tests on a GRS bridge abutment using clean angular sand backfill and polyethylene geogrid reinforcement. The study aimed to examine the behavior of the GRS abutment under applied surcharge stress, reinforcement spacing, and reinforcement tensile stiffness. The GRS abutments had dimensions of 6.9 feet in width, 7.7 feet in length, and 8.9 feet in height. A uniaxial polyethylene geogrid with an ultimate tensile strength of 2,605 lb/ft in the machine direction and 274 lb/ft in the cross-machine direction was used for reinforcement. Concrete modular blocks were used for facing and sidewalls. Three tests used a reinforcement spacing of 6 inches while the fourth test used a vertical spacing of 12 inches. Several instruments were used to monitor vertical and lateral total stresses, vertical settlements, lateral displacements, and reinforcement tensile strains. The results showed that facing displacements increased with an increase in vertical reinforcement spacing and a decrease in reinforcement tensile stiffness, while vertical settlement was more affected by reinforcement spacing than tensile stiffness. The maximum tensile strain was found to concentrate near the facing block connection for bottom layers and under bridge seat for upper layers.

A series of large-scale tests on GRS bridge abutments were conducted by Doger (2020), Doger and Hatami (2020) and Hatami and Doger (2021) to investigate the influence of facing type and reinforcement spacing on load-bearing performance. The tests were performed under plain strain conditions. The GRS abutments had dimensions of 8 feet in width, 15.6 feet in length, and

9 feet in height. Open-graded aggregate was used as structural backfill, and facing walls were constructed using either CMU or larger solid concrete blocks. The reinforcement used was woven polypropylene geotextile, placed at vertical spacings of 8 inches and 12 inches. The results indicated that the use of larger solid concrete blocks resulted in higher load-bearing performance compared to CMU, suggesting their potential use in GRS-IBS.

Key conclusions from a review of previous full-scale load tests are as follows:

- The use of higher strength geosynthetic reinforcement results in a stiffer GRS mass and increased load-carrying capacity.
- Decreasing the vertical spacing between reinforcements enhances the GRS mass's axial load capacity and reduces facing displacement.
- Facing blocks increases the stiffness and vertical capacity of the GRS mass.
- Well-graded backfill creates a stiffer GRS mass with greater axial capacity than open-graded backfill.
- The reinforcement vertical spacing has a greater influence on the GRS mass's performance than the reinforcement strength.
- Increasing the reinforcement strength reduces the dilation of the surrounding soil in the GRS mass.
- Preloading the GRS mass leads to strain hardening and a stiffer response to load, as well as reduced settlement, deformation, and creep strain.
- When uniformly loaded, the pier's volume is conserved such that the decrease in volume in a vertical direction is nearly the same as the increase in volume laterally.

## 2.4 FHWA Design Methodology for Internal Stability Design

GRS-IBS structures are internally stabilized due to their composite nature resulting from the interaction between the layers of backfill and reinforcement. These structures need to withstand applied loads at the service and strength limit states. The FHWA-HRT-17-080 guideline by Adams and Nicks (2018) provides recommendations for the design and construction of GRS-IBS. Adams

and Nicks (2018) recommends a maximum applied pressure of 4 ksf, vertical strain of 1 % and lateral strain of 2% for the service limit state. The guideline includes several checks for the external and internal stability of GRS-IBS structures. Adams and Nicks (2018) recommends checking for external stability which includes direct sliding, bearing resistance of the foundation soil, and global stability. The internal stability design involves checks for internal bearing resistance, tolerable deformation, and the required reinforcement strength.

### 2.4.1 Internal Bearing Resistance of GRS

The internal stability design of a GRS structure determines it's the ability to support external vertical loads. There are two main approaches commonly used to determine the ultimate capacity of the GRS mass: empirical and analytical methods. The empirical approach involves using stress-strain curves obtained from performance tests to determine the load-carrying capacity and deformations of the GRS mass. In contrast, the analytical approach (semi-empirical) uses equations to calculate the vertical capacity of the GRS mass.

The ultimate capacity ($q_{ult,an}$) is calculated as:

$$q_{ult,an} = \left[\sigma_c + 0.7^{\left(\frac{S_v}{6d_{max}}\right)} \frac{T_f}{S_v}\right] K_{pr} + 2c\sqrt{K_{pr}} \tag{2-1}$$

Coefficient of passive earth pressure ($K_{pr}$) is calculated as:

$$K_{pr} = tan^2(45 + \frac{\Phi_r}{2}) \tag{2-2}$$

The external confining pressure ($\sigma_c$) due to facing block is computed as:

$$\sigma_c = \gamma_b d \tan\delta \tag{2-3}$$

Where $S_v$ is the reinforcement spacing, $d_{max}$ is the maximum aggregate size, $T_f$ is the tensile strength of reinforcement, $\Phi_r$ is the internal friction angle of the reinforced backfill, $c$ is the cohesion of the backfill, $\gamma_b$ is the unit weight of facing block, $\delta$ is the interface friction angle between geosynthetic and the facing block, and $d$ is the depth of the facing block unit.

### 2.4.2 Deformation

Deformation is an important parameter in assessing the performance of the GRS structure in the service limit state. The vertical deformation of bridge abutment may be found empirically using the stress-strain curve generated from performance tests. The vertical deformation, at an applied stress of interest, is then obtained by multiplying the vertical strain with the height of the bridge abutment. The lateral deformation is estimated using analytical Equation (2-4) when the vertical deformation is known. Adams et al. (2002) developed an empirical equation for computing lateral displacement of the GRS pier when loaded vertically. The method assumes a zero-volume change in the GRS mass implying a reduction in volume due to vertical compression is equal to an increase in volume due to lateral expansion of the GRS. The computed lateral strain is limited to 2% in practice by FHWA (Adams and Nicks, 2018).

$$D_L = \frac{2b_{q,vol}D_v}{H} \tag{2-4}$$

$$\varepsilon_L = \frac{D_L}{b_{q,vol}} = \frac{2D_v}{H} = 2\varepsilon_v \tag{2-5}$$

Where $D_L$is the maximum lateral deformation, $D_v$ is the vertical settlement of GRS abutment, $b_{q,vol}$ is the width of the load along the top of the wall, $H$ is the height of the abutment, $\varepsilon_L$ is the lateral strain, and $\varepsilon_v$ is the vertical strain at the top of the abutment.

When the vertical settlement is not known, Zornberg et al. (2018a) recommends Equation (2-6) for estimating the maximum lateral displacement of free-standing walls and GRS abutments.

$$D_L = \left(\frac{\delta_R H}{50\frac{J}{S_v}.\frac{1}{p_O}}\right) x \left(1 + 1.25\frac{q}{p_O}\right) \tag{2-6}$$

$$\delta_R = 11.81\left(\frac{L}{H}\right)^4 - 42.25\left(\frac{L}{H}\right)^3 + 57.16\left(\frac{L}{H}\right)^2 - 35.45\left(\frac{L}{H}\right) + 9.471 \tag{2-7}$$

Where $\delta_R$ is an empirically derived relative displacement coefficient (dimensionless), $J$ is the reinforcement tensile stiffness defined by the secant modulus at 2% strain, $L$ is the reinforcement length, $q$ is the surcharge magnitude, and $p_O$ is the atmospheric pressure.

Wu (1994) proposed Equation (2-8) for estimating the maximum lateral displacement. It is commonly known as the Colorado Transportation Institute (CTI) method. It was developed based on the findings from instrumented full-scale GRS walls and finite element analyses. It is a service-load design method which is based on working stress and the ultimate strength of geosynthetics. It assumes a major part of wall deformation is contributed by the deformation of the geosynthetics reinforcement. The method applies only to walls that have a vertical or near-vertical (less than 80 degrees from horizontal) wall face, with height less than 20 ft, constructed with uniform and free-draining backfill containing less than 20 % fines, with horizontal crest, subjected to uniform vertical surcharge pressure less than $0.25\gamma H$, and constructed in non-seismic regions. It is accurate when used for walls with very low facing rigidity such as a wrapped-faced wall. It predicts smaller lateral wall displacement (less than 15 %) for GRS walls with higher facing rigidity.

$$D_L = \varepsilon_d \left(\frac{H}{1.25}\right) \tag{2-8}$$

Where $\varepsilon_d$ is the design limit strain for reinforcement (1% to 3 %).

Another method for estimating the maximum lateral strain is the one proposed by Giroud (1989), commonly referred to as the Geoservices method. The method relies on the limit equilibrium to compute the length of the required reinforcement. It assumes the triangular distribution of strain generated in the reinforcements. By using maximum reinforcement strain or established strain limit and reinforcement length, the maximum lateral deformation in this method is estimated by Equation (2-9).

$$D_L = \frac{\varepsilon_d L}{2} \tag{2-9}$$

Where $L$ is the reinforcement length as shown in Figure 2-3. and $\varepsilon_d$ is the strain limit (maximum strain).

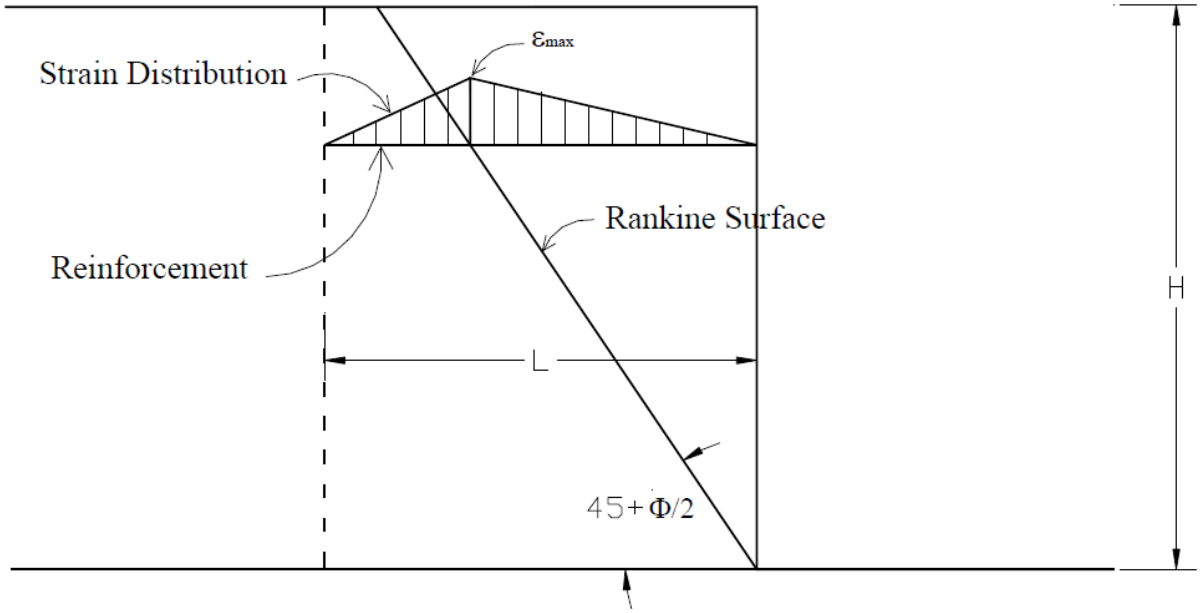


Figure 2-3. Assumed strain distribution in the Geoservices method. (Wu et al., 2013).

Jewell and Milligan (1989) presented design charts and procedures for computing lateral displacement of GRS walls at different depths within the wall using stress and deformation analysis. In their formulation, the rigidity of the facing was neglected and they established three zones based on limit equilibrium analyses, as depicted in Figure 2-4. In zone 1, large reinforcement force is required to maintain the equilibrium of critical planes and decreases into adjacent zones. With soil and reinforcement properties, a dimensionless parameter $\left(\frac{\delta_h K_{reinf}}{HP_{base}}\right)$ from the chart is identified and the deformation is computed. Wu and Pham (2010) concluded the method is best suited to compute the lateral displacement of the GRS wall with ideal reinforcement as defined by Jewell and Milligan (1989) when $L/H \geq 0.7$. The equation used to plot those charts was later rederived by Wu and Pham (2010) and the lateral displacement was estimated using Equation (2-10).

$$P_{base} = K_a S_v(\gamma H + q_s) \tag{2-10}$$

$$\Delta_i = \left(\frac{1}{2}\right)\left(\frac{P_{rm}}{K_{reinf}}\right)(H - z_i)\left[\tan\left(45° - \frac{\psi}{2}\right) + \tan(90° - \phi_{ds})\right] \tag{2-11}$$

Where $\delta_h$ or $\Delta_i$ is the lateral displacement of GRS wall at depth $z_i$, $P_{base}$ is the calculated reinforcement force at the base, $P_{rm}$ is the maximum reinforcement force at depth $z_i$, $K_{reinf}$ is the stiffness of geosynthetic reinforcement, $\psi$ is the angle of dilation of soil, and $\phi_{ds}$ is the effective direct shear friction angle of soil.

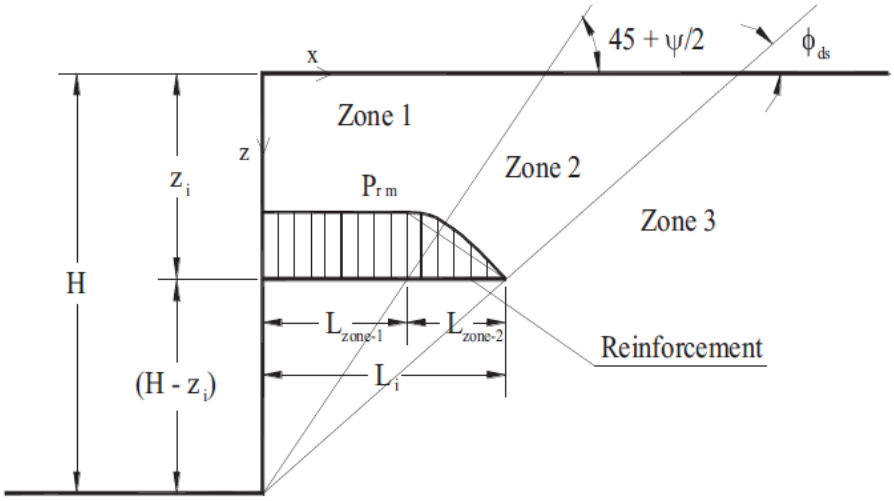


Figure 2-4. Zones of the reinforcement force in reinforced soil wall.
(Jewell and Milligan, 1989).

Wu and Pham (2010) developed an analytical model to predict the lateral displacement of the GRS wall with modular block facing subjected to surcharge loading. The equation is based on an earlier study conducted by Jewell and Milligan (1989), however unlike it in that it considers rigidity of the wall facing. They introduce an equation for finding the connection force at reinforcement and modify Equation (2-11) to Equation (2-12) in order to compute lateral displacement of a wall with modular facing. In the determination of connection force, the method assumes the wall is vertical or nearly vertical, adjacent facing blocks are rigid bodies and frictionally connected, and the uniform surcharge is applied over the horizontal crest.

$$\Delta_i = 0.5\left(\frac{K_h(\gamma_s z_i + q)S_v - \gamma_b b S_v tan\delta(1 + \tan\delta\tan\beta)}{K_{reinf}}\right)(H - z_i)\left[\tan\left(45° - \frac{\psi}{2}\right) + \tan(90° - \phi_{ds})\right] \quad (2\text{-}12)$$

If frictional resistance between wall facing and soil is ignored, Equation (2-12) is reduced to Equation (2-13). According to Wu and Pham (2010), the lateral displacement calculated by Equation (2-13) will be slightly larger than the one computed from Equation (2-12).

$$\Delta_i = 0.5\left(\frac{K_h(\gamma_s z_i + q)S_v - \gamma_b b S_v tan\delta}{K_{reinf}}\right)(H - z_i)\left[\tan\left(45° - \frac{\psi}{2}\right) + \tan(90° - \phi_{ds})\right] \quad (2\text{-}13)$$

Where $S_v$ is the vertical reinforcement spacing, $b$ is the width of facing block, $\gamma_b$ is the unit weight of facing block, $\delta$ is the friction angle between modular block facing elements or friction angle between modular block facing elements and geosynthetic, $\beta$ friction angle between back face of wall and soil, and $K_h$ lateral earth pressure coefficient.

Equations (2-15) and (2-16) are empirical and developed by Christopher et al. (1990) to compute the maximum lateral deformation of simple GRS walls/structures during construction. Its corresponding curve is shown in Figure 2-5. It is commonly known as the FHWA method, which correlates the reinforcement length/wall height with the lateral displacement of the reinforced soil, as expressed in Equation (2-14). The method assumes most of the lateral deformation occurs during construction. It was empirically developed based on actual structures and computer simulation models. The maximum lateral displacement is computed as a function of the two types of reinforcement, namely extensible and inextensible reinforcements. For critical structures, such as bridge abutments, Christopher et al. (1990) recommended the use of finite element analysis in this analysis for computing lateral displacement.

$$\delta_R = 11.81\left(\frac{L}{H}\right)^4 - 42.25\left(\frac{L}{H}\right)^3 + 57.16\left(\frac{L}{H}\right)^2 - 35.45\left(\frac{L}{H}\right) + 9.471 \quad (2\text{-}14)$$

$$D_L = \frac{\delta_R H}{250} \quad for\ inextensible\ reinforcement \quad (2\text{-}15)$$

$$D_L = \frac{\delta_R H}{75} \quad for\ extensible\ reinforcement \quad (2\text{-}16)$$

Where $\delta_R$ is the deformation coefficient of reinforced soil wall, $L$ is the reinforcement length, $D_L$ is the maximum lateral deformation, and $H$ is the height of the wall.

Khosrojerdi et al. (2017) evaluated these methods, with the exception of Zornberg et al. (2018a), and showed that Adams et al. (2002), known as the "Adams method," exhibited the highest accuracy in predicting lateral displacement.

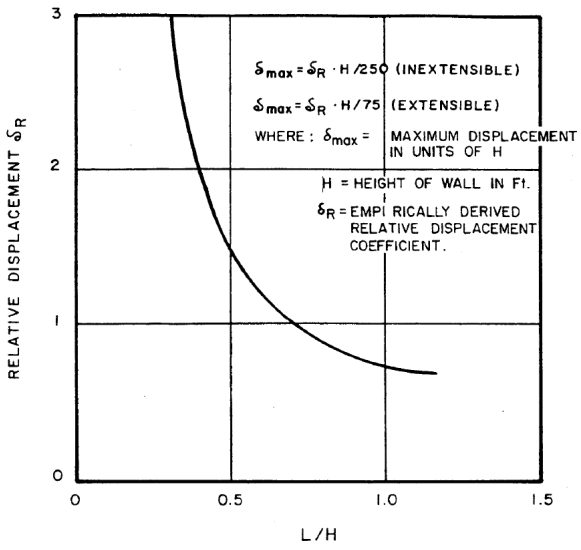


Figure 2-5. Empirical curve for estimating anticipated lateral displacement during construction for reinforced fill structures.
(Christopher et al., 1990).

### 2.4.3 Required Reinforcement Strength

GRS structures owe their stability under loading to the reinforcement strength and stiffness properties. Reinforcement with high strength and stiffness reduces the lateral deformation and increases the stiffness of the GRS composite. The required reinforcement strength can be defined as the minimum strength required to limit movement or prevent failure of the GRS composite at a given applied stress. To ensure adequate strength throughout the GRS mass, Adams et al. (2012b) recommends that the required strength should be computed at each layer of reinforcement.

$$T_{req,c} = \left( \frac{\sigma_h - \sigma_c - 2c\sqrt{K_{ar}}}{0.7^{\left(\frac{S_v}{6d_{max}}\right)}} \right) S_v \tag{2-17}$$

Where the confining stress due to facing element is given by:

$$\sigma_c = \gamma_b d tan\delta \quad (2\text{-}18)$$

Where $T_{req,c}$ is the required reinforcement strength in the direction perpendicular to the wall face, $\sigma_h$ is the total lateral stress withing the GRS composite at given depth and location, $K_{ar}$ is the coefficient of active earth pressure for the backfill, $\gamma_b$ is the bulk unit weight of the facing block, $d$ is the depth of the facing block unit perpendicular to the wall face, and $\delta$ is the interface friction angle between the geosynthetic and the facing element for a frictionally connected GRS composite.

A comprehensive review of GRS pier tests and an analysis of GRS-IBS using calibrated numerical models by Zornberg et al. (2018a) have resulted in suggested revisions that can be incorporated into the AASHTO Bridge Design Specifications. Zornberg et al. (2018a) proposed the use of equations Equation (2-19) through Equation (2-21) to determine the maximum tensile load for reinforcement, specifically for vertical spacing (Sv) up to 16 inches.

$$T_{max,i} = K_{ar}\gamma z_i S_v + \Delta\sigma_H S_v \quad \text{for } S_v \geq 16" \quad (2\text{-}19)$$

$$T_{max,i} = \frac{1}{2}K_{ar}\gamma H S_v + \Delta\sigma_H S_v \quad \text{for } S_v \leq 8" \quad (2\text{-}20)$$

$$T_{max,i} = K_{ar}\gamma S_v \left[z_i + \left(\frac{16"-S_v}{8"}\right)\left(\frac{H}{2} - z_i\right)\right] + \Delta\sigma_H S_v \quad \text{for } 8" \leq S_v \leq 16" \quad (2\text{-}21)$$

Where $\gamma$ is the backfill total unit weight, $z_i$ is the depth of backfill, and $\Delta\sigma_H$ is the change in the horizontal earth pressure of the backfill due to the applied surcharge. FDOT (2018) recommends a minimum ultimate tensile strength of 4800 lbs/ft in both machine and cross-machine directions.

## 2.5 Florida Practice

### 2.5.1 GRS Structures in Service

Just like other states in the United States of America, Florida has adopted the utilization of GRS-IBS technology for small-scale projects that have limited time and financial resources. Currently, over eight bridges in Florida have been successfully constructed using GRS-IBS technology. One of the most recent projects employing this technology was the Cow Camp Road bridge in Polk County, Florida. The objective of this project was to replace an aged timber bridge constructed back in 1964. The newly built bridge has a span length of 77 ft and was completed during the summer of 2018. It is supported by GRS abutments measuring 15.33 ft in height, with a facing system composed of CMU blocks. Additionally, GRS-IBS technology has been employed in the construction of pedestrian bridges such as the US 301 Trail Bridge located in Zephyrhills.

Notably, this bridge stands as the first multi-span structure in Florida that incorporates GRS abutments and GRS piers. Other bridges constructed in Florida using this technology can be found in locations such as Tallahassee's Orange Avenue bridge, Nassau County's CR 107 over Lanceford Creek, as well as various bridges in Escambia County, Nassau County, and Hillsborough County.

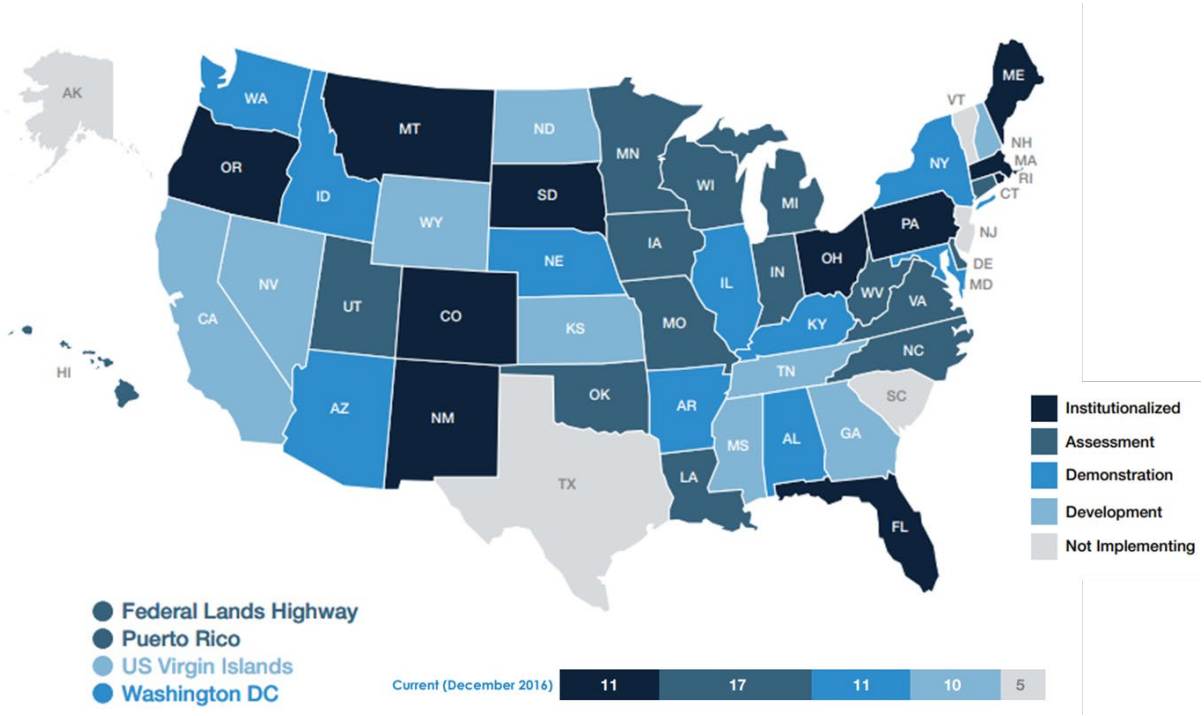


Figure 2-6. A map showing GRS-IBS implementation projects in the USA at the end of 2016 from EDC-3 Final report.
(FHWA, 2017).

Figure 2-7. Construction of U.S. 301 Trail Bridge with multi-span GRS-IBS in Zephyrhills, Florida.
(Daniyarov et al., 2017).

Figure 2-8. Orange Avenue Bridge in Tallahassee, Florida.
(https://ncma.org/updates/projects/florida-manages-orange-avenue-bridge-with-grs-ibs/).

Figure 2-9. Cow Camp Bridge in Polk County, Florida. (https://www.conteches.com/knowledge-center/case-studies/details/slug/cow-camp-road-grs-ibs-bridge).

### 2.5.2 Types of Aggregates

The primary structural component in the GRS-IBS system is the backfill material, which accounts for over 80% of the total volume. Therefore, the choice of backfill materials and their properties play an important role in the overall performance of GRS composite behavior. When examining failed GRS structures, investigations have revealed that structures constructed with backfill materials containing higher amounts of fines have exhibited more frequent failures and inadequate performance (Talebi, 2016). Several factors, including drainage, workability, strength requirements, and availability, must be considered when choosing backfill materials. State Departments of Transportation (DOTs) often recommend the use of locally sourced aggregates that meet the required specifications, depending on their availability. In cases where water presence is expected, the use of free-draining aggregates is recommended. The classification of aggregates is commonly based on particle size, distinguishing them as either coarse aggregates or fine aggregates. Coarse aggregates refer to those with particle sizes larger than the No. 4 sieve. Both FDOT and FHWA recommend the use of coarse aggregates for structural backfill in the GRS-IBS system.

#### 2.5.2.1 Gradation

Gradation plays an important role in the selection of structural backfill as it serves as an indicator of important engineering properties like shear strength, hydraulic conductivity, and compressibility. Gradations of interest are either well-graded or open-graded (poorly graded). In open-graded aggregates, the particles have a uniform size, while in well-graded aggregates, the particles are distributed fairly evenly across a range of sizes from fine to coarsest. When constructing GRS abutments, open-graded aggregates are preferred in wet environments such as flood zones due to their free-draining nature. This characteristic allows infiltrated water to drain easily, preventing the build-up of hydrostatic pressure. Moreover, open-graded aggregates can be utilized in all weather conditions. However, they are less stiff compared to well-graded aggregates. Figure 2-10 shows a comparison of the stress-strain response in performance tests of GRS piers using well-graded and open-graded backfill materials. The response curves demonstrate that GRS composites constructed with well-graded backfill materials exhibit higher stiffness than those with open-graded materials. Despite the advantages of higher stiffness and strength achieved by using well-graded aggregates in the GRS mass, most GRS-IBS projects in the US have employed open-graded aggregates. This choice is primarily due to ease of construction, availability, low fine content, minimal frost heave potential, and free-draining characteristics associated with open-graded aggregates.

According to FHWA, both well-graded and open-graded aggregates can be used as structural backfill in reinforced soil foundation (RSF) and GRS abutment. However, for an integrated approach, well-graded is recommended to be used. FDOT specifies the use of graded aggregate for RSF. The materials should be free from organic matter, shale, lumps, and clay balls. Its Limerock Bearing Ratio should be greater than 100. Table 2-1 below shows the FDOT's specification for well-graded aggregates. For GRS abutments, FDOT allows the use of well-graded or open-graded aggregates. Specification for well-graded aggregates is the same as that for their use in the RSF. For open-graded aggregates, the FDOT requires the materials to be coarse aggregates consisting of natural stones. The accepted gradation for coarse aggregates by FDOT is from Size No. 57 through Size No. 89, as shown in Table 2-2. The compaction of granular materials is significantly affected by the particle size. As the particle size increases, it becomes more challenging to achieve maximum compaction. To address this issue, both the FDOT and FHWA specify a maximum aggregate size of approximately 2 inches for both open-graded and

well-graded aggregates used in GRS-IBS construction. Table 2-3 and Table 2-4 present the FHWA's recommended properties for open-graded and well-graded backfill materials, respectively, in GRS-IBS projects.

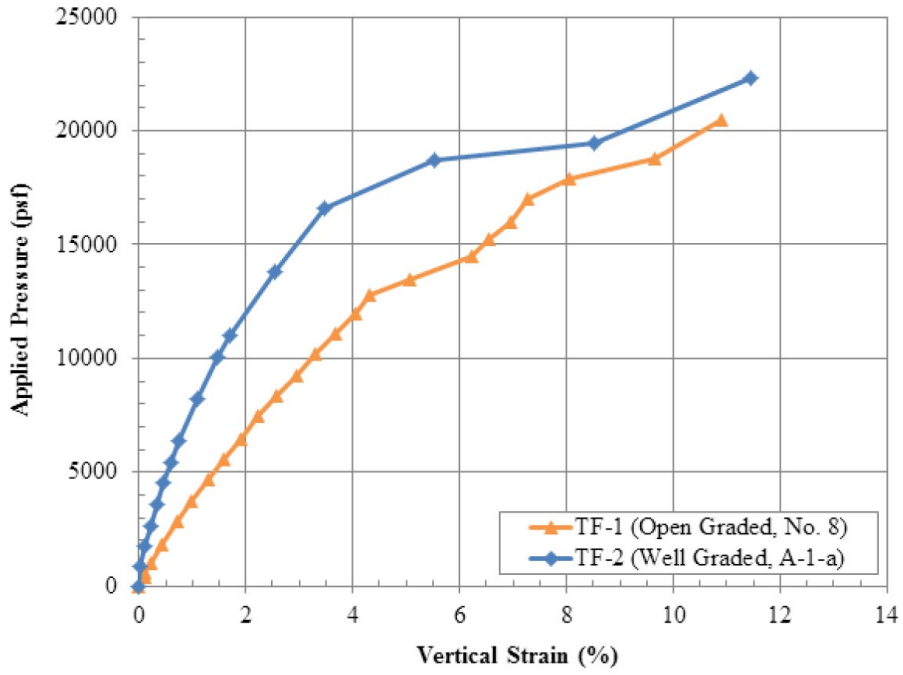


Figure 2-10. Applied pressure-strain curve showing a comparison of open-graded and well-graded backfills.
(Nicks et al., 2013).

Table 2-1. Well-graded aggregate gradation requirements.
(FDOT, 2020).

| Sieve Size | Percent by Weight Passing |
|---|---|
| 2 inch | 100 |
| 1 1/2 inch | 95 to 100 |
| 3/4 inch | 65 to 90 |
| 3/8 inch | 45 to 75 |
| No. 4 | 35 to 60 |
| No. 10 | 25 to 45 |
| No. 50 | 5 to 25 |
| No. 200 | 0 to 10 |

Table 2-2. Gradation requirements for coarse aggregates.
(FDOT, 2020).

| Standard Sizes of Coarse Aggregate | | | | | | | | | | | |
|---|---|---|---|---|---|---|---|---|---|---|---|
| Amounts Finer than Each Laboratory Sieve (Square Openings), weight percent | | | | | | | | | | | |
| Size No. | Nominal Size Square Openings | 2 inches | 1/2 inches | 1 inch | 3/4 inch | 1/2 inch | 3/8 inch | No. 4 | No. 8 | No. 16 | No. 50 |
| 57 | 1 inch to No. 4 | - | 100 | 95 to 100 | - | 25 to 60 | - | 0 to 10 | 0 to 5 | | |
| 67 | 3/4 inch to No. 4 | - | - | 100 | 90 to 100 | - | 20 to 55 | 0 to 10 | 0 to 5 | | |
| 68 | 3/4 inch to No. 8 | - | - | - | 90 to 100 | - | 30 to 65 | 5 to 25 | 0 to 10 | 0 to 5 | |
| 78 | 1/2 inch to No. 8 | - | - | - | 100 | 90 to 100 | 40 to 75 | 5 to 25 | 0 to 10 | 0 to 5 | |
| 89 | 3/8 inch to No. 16 | - | - | - | - | 100 | 90 to 100 | 20 to 55 | 0 to 30 | 0 to 10 | 0 to 5 |

Table 2-3. GRS open-graded backfill specifications by FHWA.
(Adams and Nicks, 2018).

| Parameter | Test Method | Criteria |
|---|---|---|
| Minimum maximum aggregate size | AASHTO T 27 | ≥ 0.5 inch |
| Maximum aggregate size | AASHTO T 27 | ≤ 2 inches |
| Percent passing No. 50 sieve | AASHTO T 11 | ≤ 5 percent |
| Friction angle | AASHTO T 236 | ≥ 38 degrees |
| Soundness | AASHTO T 104 | The backfill shall be substantially free of shale or other poor durability particles. The material shall have a sodium sulfate soundless loss of < 15 percent after five cycles |

Table 2-4. GRS well-graded backfill specifications by FHWA.
(Adams and Nicks, 2018).

| Parameter | Test Method | Criteria |
|---|---|---|
| Maximum aggregate size | AASHTO T 27 | Between 0.5 and 2 inches |
| Percent passing No. 200 sieve | AASHTO T 11 | ≤ 12 percent |
| Coefficient of uniformity | ASTM D6913 | ≥ 4 |
| Coefficient of curvature | ASTM D6913 | Between 1 and 3 |
| Plasticity index | AASHTO T 90 | ≤ 6 |
| Friction angle | AASHTO T 236 | ≥ 38 degrees |
| Soundness | AASHTO T 104 | The backfill shall be substantially free of shale or other poor durability particles. The material shall have a sodium sulfate soundless loss of less than 15 percent after five cycles. |

#### 2.5.2.2 Mechanical Properties

The mechanical properties of aggregates play a crucial role in the performance of the GRS mass. A numerical study conducted by Zornberg et al. (2018a) demonstrated a significant correlation between the internal friction angle of the backfill material and the performance of the GRS pier. As the friction angle increased, an increase in GRS pier stiffness modulus was observed, as shown in Figure 2-11. Additionally, an increase in the internal friction angle resulted in a decrease in lateral displacement of CMU blocks, maximum tensile force on reinforcement, and magnitude of lateral earth pressure. Regardless of whether well-graded or open-graded aggregates are utilized, the FHWA recommends that the internal friction angle be a minimum of 38°. On the other hand, the FDOT imposes a slightly higher requirement, specifying a minimum internal friction angle of 42°.

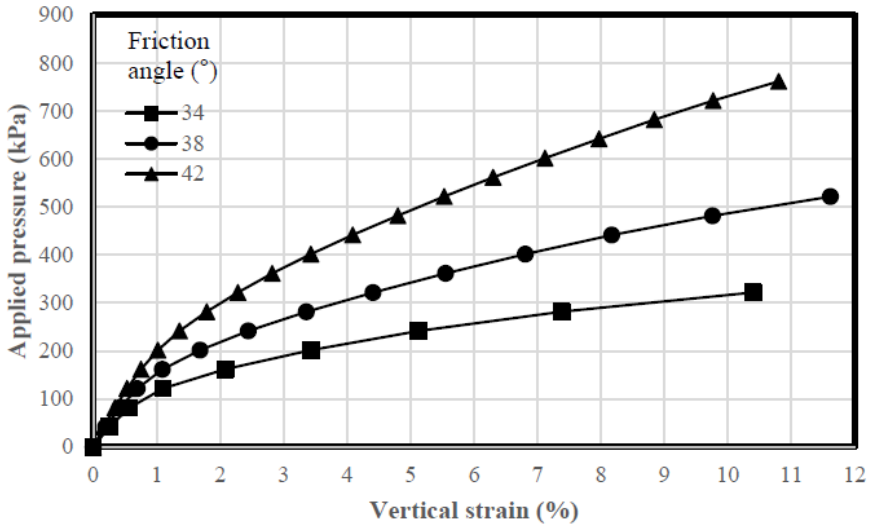


Figure 2-11. Effect of the friction angle of the backfill soil on the applied pressure – vertical strain curves.
(Zornberg et al., 2018a).

Table 2-5. Unit weight and internal angle of friction for backfill materials recommended by FDOT.
(FDOT, 2018).

| Aggregate type | Unit weight (pcf) | Friction Angle | Cohesion |
|---|---|---|---|
| Graded aggregate (GAB) | 140 | 42° | 0 |
| Coarse aggregate (#57 or # 67 stone) | 105 | 42° | 0 |

#### 2.5.2.3 Chemical Properties

The backfill aggregates should be free from non-deleterious substances that could have adverse effects. These substances include clay lumps, soft and easily crumbled particles, salt, alkali, organic matter, and any adherent coatings that may exhibit undesirable characteristics. The FDOT specifies that the pH of the aggregates should fall within the range of 4.5 to 10. However, when uncoated polyester geosynthetics are employed, the pH limit is set at 9. In the case of crushed limestone, the acid insoluble content is required to be a minimum of 12.

### 2.5.3 Types of Reinforcement

Geotextiles and geogrids are two commonly used geosynthetic reinforcements in the construction of GRS abutments. Most GRS-IBS structures currently in service have been built

using woven polypropylene geotextiles. Geosynthetics are classified as either uniaxial or biaxial reinforcements, depending on the magnitude of their tensile strength and orientation. Uniaxial reinforcement has a higher tensile strength in one direction compared to the other, while biaxial reinforcement exhibits equal tensile strength in both directions. In the case of GRS-IBS construction, the FDOT requires the use of biaxial geogrid or woven geotextiles that meet the minimum strength in the machine direction and cross-machine direction. This doesn't exclude the use of a uniaxial reinforcement if the minimum tensile strength is met in both directions.

#### 2.5.3.1 Mechanical Properties

The geosynthetic provides tensile strength and confinement in the GRS backfill, improving it's stiffness and load-bearing capacity. Nicks et al. (2013) showed that by doubling the reinforcement strength, there was a 1.14 increase in capacity and a 1.34 increase in the initial stress-strain ratio of GRS piers. When constructing the RSF, the FDOT recommends the use of woven geotextile with a minimum tensile strength of 4,800 lbs/ft in both the machine and cross directions. For GRS abutments, either a biaxial geogrid or a woven geotextile reinforcement can be employed, both with a minimum tensile strength of 4,800 lbs/ft in both the machine and cross directions. Machine direction (MD) refers to strength along the length of the roll while cross-machine direction (CD) refers to strength along the width of the roll (Adams et al., 2012a).

#### 2.5.3.2 Chemical Properties

The FDOT requires that the base plastic used in geosynthetic reinforcements contains stabilizers and/or inhibitors. These additives ensure that the polymetric filaments remain stable and resistant to deterioration caused by factors such as exposure to ultraviolet (UV) light, high temperatures, and potentially chemically damaging environments.

### 2.5.4 Facing Elements

Facing elements in GRS-IBS construction can be made from various materials, including modular concrete blocks, precast concrete panels, cast-in-place rigid facings, and timber. In the United States, modular concrete blocks are commonly used as facing elements, connected through friction with the geosynthetic reinforcement. No mortar is used to join the blocks, which can come in different shapes and sizes. The primary function of the facing system is to provide a form for compaction, act as a protective facade, and guard against the loss of granular fill due to weathering.

It is important to note that the facing system is not considered a structural element in the design of the GRS abutment, and while the GRS-IBS Interim Implementation Guide does not consider the effect of facing elements in determining the capacity of a GRS composite, a study conducted by Nicks et al. (2013) demonstrated facing elements do impact the performance of the GRS composite. The study found that the facing elements provide confinement, increasing the stiffness of the GRS mass and consequently enhancing the ultimate load-carrying capacity. A comparison of two performance tests, one with facing elements and another without, revealed that the GRS composite with the facing system exhibited a higher load-carrying capacity compared to the non-facing GRS mass, as shown in Figure 2-12.

FDOT permits the use of common concrete modular blocks as facing elements, with the options including normal weight concrete masonry units (CMU) or segmental retaining wall (SRW) units. Most of the completed projects have used CMU more than SRW. When employing 7-5/8-inch CMU, FDOT specifies that all CMU must be manufactured in accordance with ASTM C90, with a minimum 28-day compressive strength of 4,000 psi and a water absorption limit of 6.5%, per ASTM C140. In cases where an 8-inch-high facing block is required, FDOT recommends the use of dry-cast segmental retaining wall units manufactured according to ASTM C1372. These units should possess a minimum 28-day compressive strength of 4,000 psi and a water absorption of 6.5%, following the guidelines outlined in ASTM C140. Additionally, when scour protection is necessary, FDOT suggests the use of solid masonry blocks below the top elevation of the scour protection.

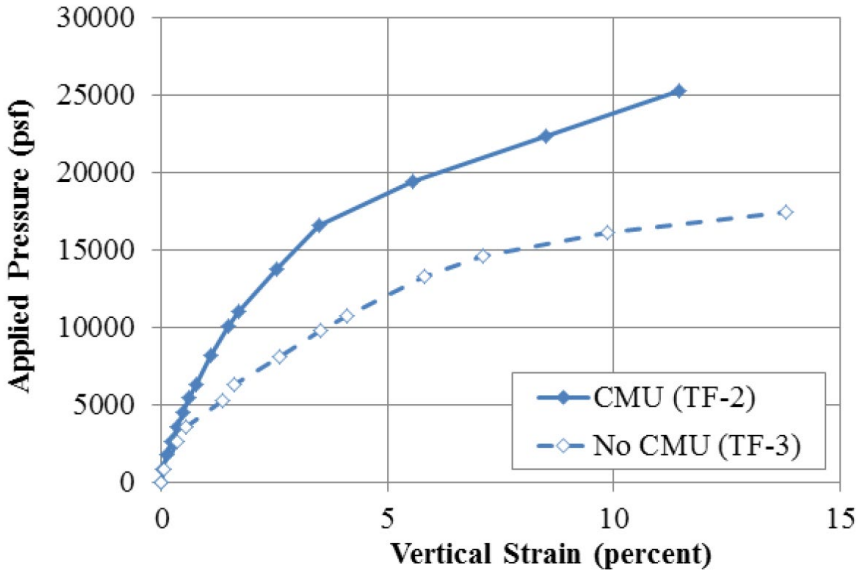

Figure 2-12. A plot of stress-strain response for TF-2 (CMU facing) and TF-3 (no CMU facing), Sv=7 5/8 inches, Tf=2400 lb/ft.
(Nicks et al., 2013).

### 2.5.5 Design Methods

Various guidelines for the deign of GRS-IBS have been developed, including the FHWA Geosynthetic Reinforced Soil Integrated Bridge System Interim Implementation Guide (Adams et al., 2012b) and the FHWA Design and Construction Guidelines for GRS-IBS (Adams and Nicks, 2018). The Florida Department of Transportation Structure's Design Guideline (FDOT SDG) requires that GRS-IBS be designed according to the FHWA Geosynthetic Reinforced Soil Integrated Bridge System Interim Implementation Guide, unless stated otherwise. The Interim Implementation Guide provides a comprehensive overview of the design process from project conception to final design. The outlined design method is limited to structures with spans less than 140 ft and subjected to combined bridge dead and live load of 4,000 $lb/ft^2$ or less (unfactored). It requires checking for both the external and internal stability of the structure. Internal stability design was presented in section 2.4. Detailed information about the external stability design can be found in Adams et al. (2012b) and Adams and Nicks (2018).

### 2.5.6 Construction Methods

Once the design of the GRS-IBS is completed, the next step is the installation of the structure, following the design information provided by the designer. FDOT has developed Developmental Specification 549 to assist contractors during the construction process of GRS-IBS. Additional useful information can be found in publications such as FHWA-HRT-11-026 (Adams et al., 2012b), FHWA-HRT-17-080 (Adams and Nicks, 2018), and FDOT Specifications for Road and Bridge (FDOT, 2020). The construction of GRS-IBS involves basic earthwork methods and practices. It is a relatively simple process that requires fewer personnel and equipment compared to conventional earthwork practices. The construction crew does not require specialized training, unlike traditional bridge construction crews. Furthermore, specialized equipment such as pile driving equipment is not necessary for the construction process. Simple hand tools, measuring devices, and a few pieces of equipment like a vibratory roller, trash pump, track hoe excavator, and backhoe are sufficient to complete the project. The construction of GRS-IBS follows a bottom-

up approach and involves several steps, including the laying of facing blocks, placement and compaction of granular backfill layers, and installation of geosynthetics. These steps are repeated until the final design height of the structure is achieved. Detail about each construction step can be found in Adams and Nicks (2018).

## 2.6 Performance of GRS Structures

FHWA has been promoting the use of GRS-IBS over the past 10 years because of its cost-effectiveness and time-saving benefits. This technology has been adopted by DOTs and many others (Ooi et al., 2019). The increasing number of GRS-IBS structures has caught the attention of the engineering community, leading to investigations into their performance. Various researchers have conducted full-scale testing and field monitoring to assess the performance of the GRS-IBS system. While full-scale load tests have demonstrated its good performance, field monitoring is crucial for understanding its long-term performance. Multiple bridges were instrumented for this purpose, and they have proven to excel in terms of load capacity, durability, and ability to withstand various weather conditions. This section provides a discussion on the performance of GRS-IBS structures.

### 2.6.1 Vertical Settlement

Vertical movement of the bridge is an important criterion used to assess the performance of the GRS-IBS structures during construction and in-service operation. The unique characteristic of the GRS-IBS is the jointless connection which eliminates the “bridge bump” problem at the bride. Several monitored bridges have proved this to be true. For example, Abu-Hejleh et al. (2002) observed no differential settlement between the two GRS abutments of GRS-IBS after two years in service. The GRS-IBS does not resist settlement to create the differences in the settlement, instead, it settles with it. The GRS abutment settles with an integral approach to create no differential settlement between the superstructure and the integral approach. Adams et al. (2011) reported performances of five bridges that were monitored for at least 2 years. Table 2-6 below shows the information on the observed movements of the five bridges. In all these bridges, the settlement was measured by either a standard survey level and rod system or an electronic distance

measurement (EDM) at abutment face wall and superstructure. The settlement in these structures primarily occurs during construction due to dead loads, and the settlement during service was reported to be minimal. Even for GRS-IBS structures with GRS abutments consisting of different geosynthetic characteristics, minimal differential settlement was observed. Adams et al. (2011) reported the results for the GRS-IBS structure built at FHWA's Turner-Fairbank Highway Research Center (TFHRC). The bridge superstructure was supported on embankment fill and GRS abutment reinforced with geotextile of different ultimate tensile strengths. The embankment was reinforced with 2,100 lb/ft, while the GRS abutment was reinforced with 4,800 lb/ft. After two years of service, the settlement difference between the two sides was only about 0.0024 ft (Adams et al., 2011). Figure 2-13 shows the measured vertical settlement for the TFHRC tunnel. Saghebfar et al. (2017) observed a maximum vertical settlement of 0.25 inches below the design value of 0.8 inches after 68 days in service. Ooi et al. (2019) presented three years of monitoring results, showing a maximum settlement of 1.2 inches. A study conducted by Talebi (2016) reported a maximum strain of 0.25%, which is well below the allowable value of 1% according to the GRS-IBS FHWA design guidelines. Most of the measured vertical settlements in these studies fell below the specified performance criteria.

Table 2-6. Movement information for five bridges

| Bridge | Average Abutment Height (ft) | Average Total Settlement (ft) | Average Total Vertical Strain (%) | Average GRS Settlement (ft) | Average GRS Vertical Strain (%) | Bridge Differential Settlement (ΔS) (ft) | Angular Distortion (ΔS/span length) |
|---|---|---|---|---|---|---|---|
| Vine Street | 11.36 | -0.035 | 0.31 | 0.023 | 0.2 | 0.009 | 0.00018 |
| Glenburg Road | 13.01 | -0.107 | 0.82 | 0.083 | 0.64 | 0.012 | 0.00039 |
| Huber Road | 16.73 | -0.004 | 0.024 | 0.015 | 0.09 | 0.01 | 0.00036 |
| Bowman Road | 16.69 | -0.07 | 0.42 | 0.047 | 0.28 | 0.019 | 0.00024 |
| Tiffin River | 19.26 | -0.175 | 0.91 | 0.106 | 0.55 | 0.033 | 0.00025 |

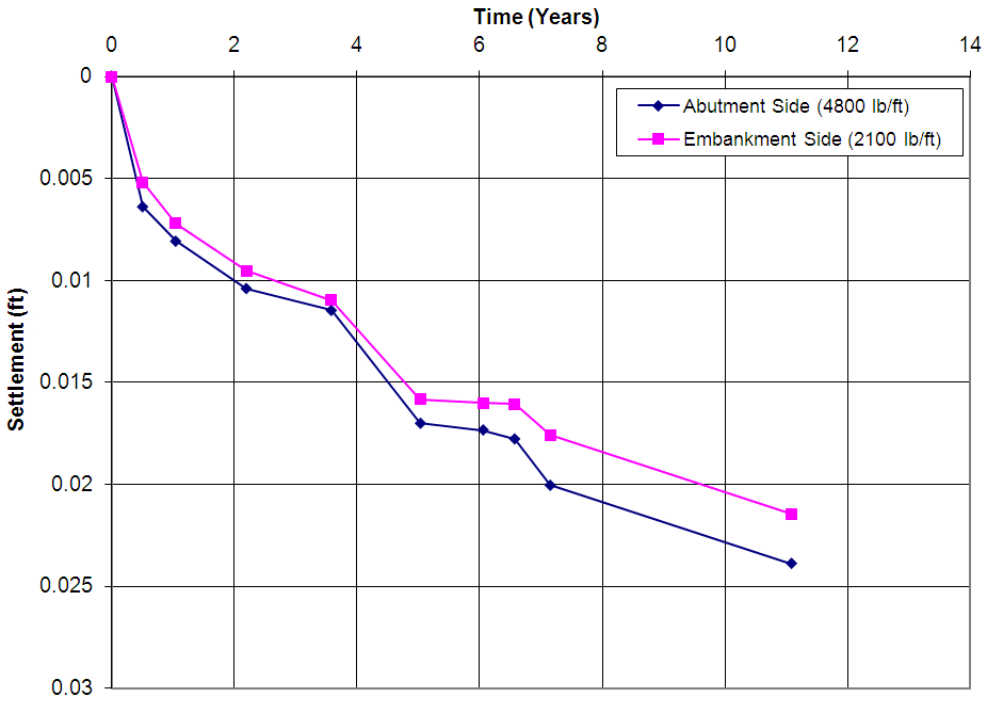


Figure 2-13. A plot of settlement versus time for TFHRC tunnel.
(Adams et al., 2011).

### 2.6.2 Lateral Deformation

This is another criterion used in evaluating the performance of the GRS-IBS structure. Lateral displacement is measured by monitoring the movement of the facing wall using the same techniques like the one for vertical settlement. For the GRS-IBS bridge in service, this is the difficult parameter to assess in the long term (Adams et al., 2011). Among the five bridges in Table 2-6, Adams et al. (2011) presented the lateral deformation for only the Tiffin River bridge (Figure 2-14). The graph shows a good correlation between the measured and predicted lateral deformation using the FHWA analytical equation for lateral displacement. Another study conducted by Talebi (2016) reported a good performance of GRS-IBS structure in which an average lateral strain of 0.4 % which is below the limit value of 2% was observed for GRS abutment. This indicates good performance of the GRS-IBS structure concerning lateral deformation.

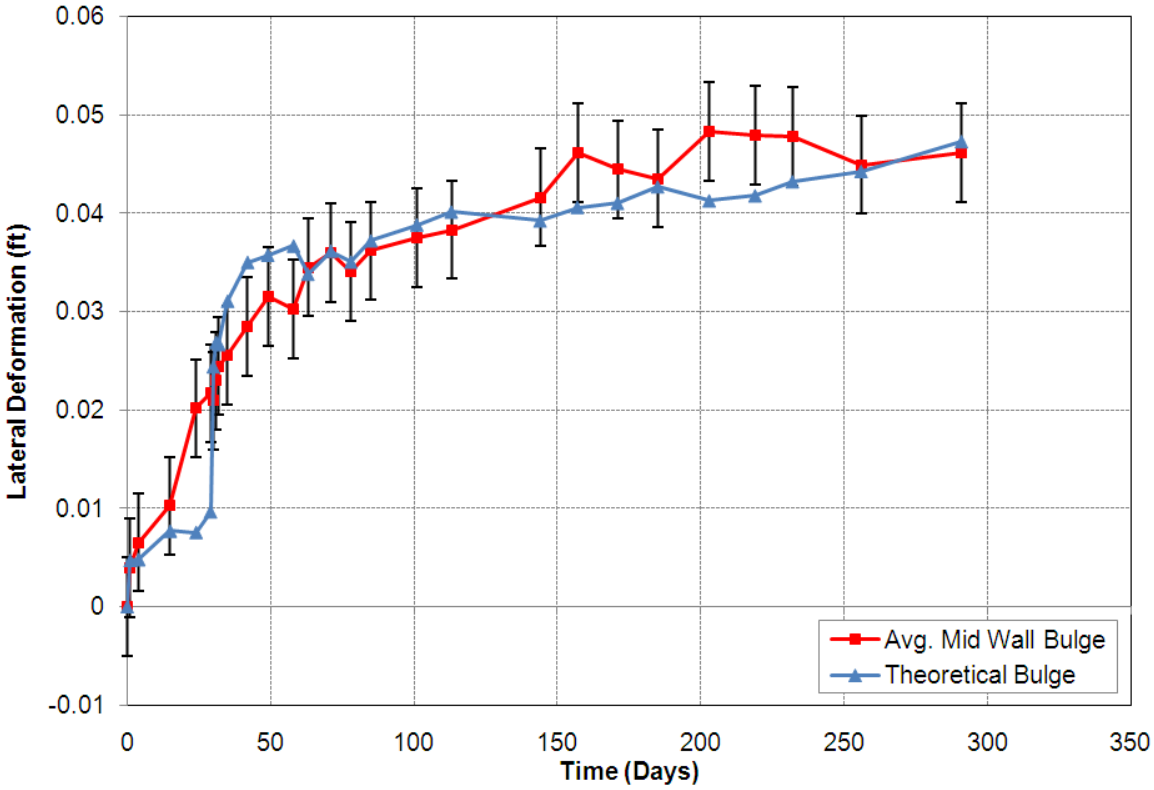


Figure 2-14. A comparison of the measured and calculated lateral deformation on the Tiffin River Bridge GRS abutment.
(Adams et al., 2011).

### 2.6.3 Daily and Seasonal Weather Variation

The performance of GRS backfill can be influenced by weather conditions such as precipitation and temperature. For instance, rainfall infiltration can impact the response of GRS, depending on its permeability. The presence of water in the soil can reduce its strength, potentially affecting the stability of the backfill and foundation. Koerner and Koerner (2013) conducted a study to investigate the failures of the 171 MSE walls with the geosynthetic reinforced wall, the results showed that 60% of the failures were caused by internal or external water.

Temperature change is another parameter that can affect the performance of GRS structures. Several researchers have studied the influence of temperature and water content on the stress and deformation behavior of GRS-IBS under various weather conditions. Long-term assessments have generally shown that GRS-IBS structures perform well in most of these conditions. For example, Talebi (2016) reported good performance of the GRS abutment over

several cycles, with water content not significantly influencing its deformation behavior. Similarly, Gebremariam et al. (2019) and Ooi et al. (2019) found that daily and seasonal variations had little impact on the performance of GRS-IBS structures. Adams et al. (2011) concluded, based on their study of structures in service, that the performance of GRS-IBS is not significantly affected by thermal cycles. Overall, the literature review suggests that GRS-IBS structure performance is not significantly affected by daily and seasonal variations. Figure 2-15 below shows the influence of weather conditions on the response of GRS mass after the study done by Ooi et al. (2019).

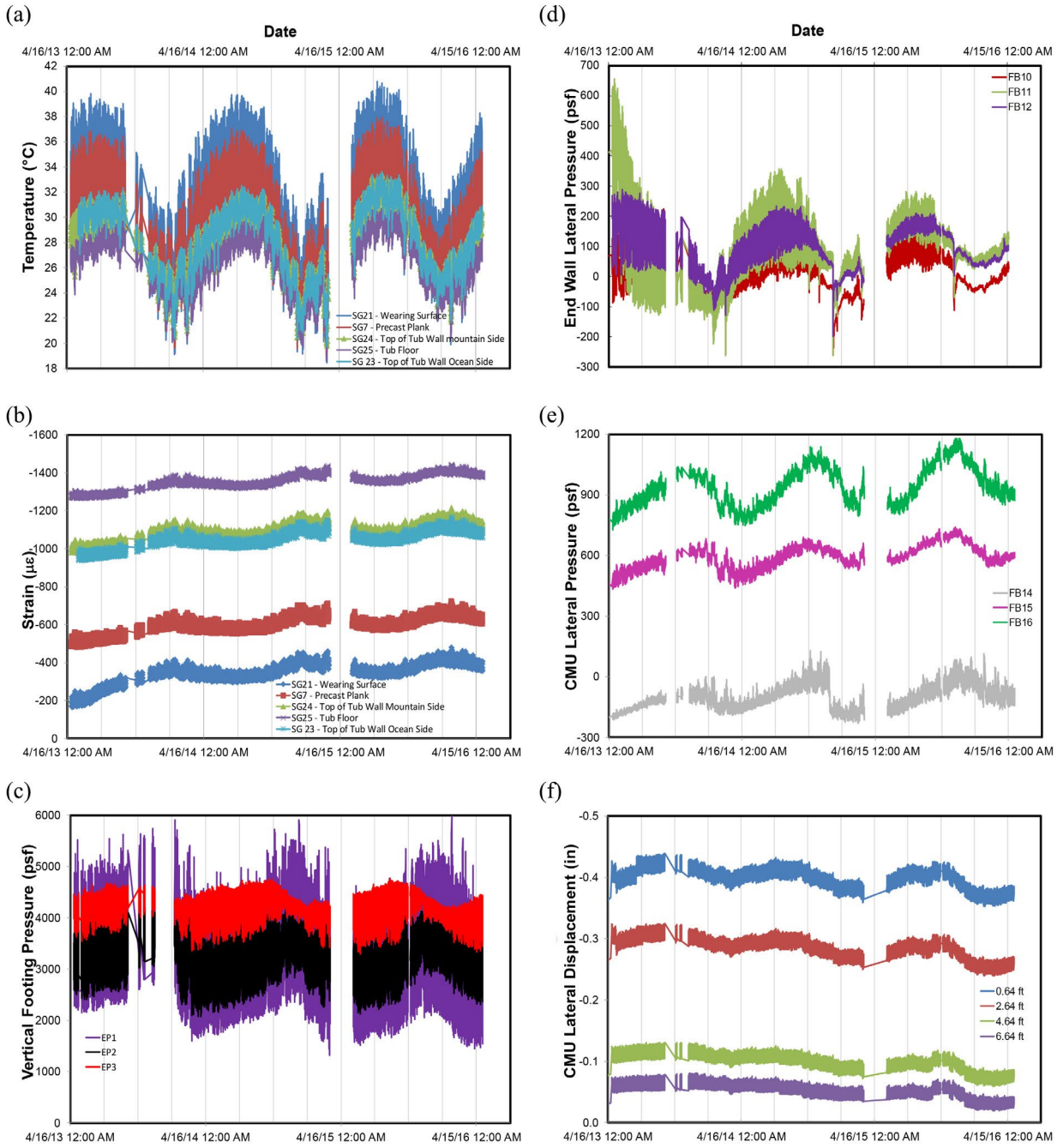


Figure 2-15. Influence of seasonal variation.
(a) Temperature; (b) Strain; (c) Footing vertical pressure; (d) End wall lateral pressure; (e) CMU lateral pressure; (f) CMU lateral displacement vs time (Ooi et al., 2019).

# 3 EXPERIMENTAL DESIGN

This chapter presents the experimental design of the GRS piers. It covers test materials used, different laboratory tests, tests setup, construction procedures, instrumentation, loading schedule and data collection.

## 3.1 Test Materials

The following sections provide information on the structural backfill, reinforcement, blocks, and footing utilized in the GRS Pier tests.

### 3.1.1 Backfill

The performance tests utilized three types of aggregate as structural backfill - crushed limestone rock (No. 57 Florida limestone), graded aggregate base-recycled concrete aggregate (RCA- GAB), and lightweight aggregate (foamed glass aggregate (FGA)). The No. 57 and RCA-GAB were chosen from the FDOT Materials Acceptance and Certification (MAC) System and the FGA was provided by AeroAggregates. Each pier needed approximately 83.8 $ft^3$ (3.1 $yd^3$) of compacted aggregate. No. 57 Florida limestone and RCA-GAB meet both FDOT and FHWA specifications for use in GRS-IBS, while FGA does not meet the specification for use in GRS-IBS. The FGA has high strength properties which could potentially improve the load-carrying capacity of GRS-IBS while reducing the weight of the pier. To the author's knowledge, this material has not been used in performance tests of GRS piers yet. The testing of this material will aid in understanding its behavior when used in GRS-IBS. Before performing the actual GRS pier test, gradation, specific gravity, density, and triaxial tests were conducted to determine the index and engineering properties of the aggregates. Most of the tests were conducted at the FDOT State Material Office, and some were conducted at the University of Florida (UF) and Florida State University (FSU) Soil Laboratories.

#### 3.1.1.1 Gradation

The aggregate gradation tests were conducted in accordance with the ASTM C136 standard. Figure 3-2 illustrates the particle size distribution curves for the aggregates and shows a photo of the No. 57 aggregate. The maximum particle size of all the aggregates ranges from 1 inch to 3 inches. The No. 57 and FGA are classified as poorly graded gravel (GP) while the RCA-GAB is classified as well-graded gravel (Figure 3-2 and Figure 3-1), according to the Unified Soil

Classification System (USCS). Table 3-1 presents the gradation properties of backfill material and the USCS classifications.

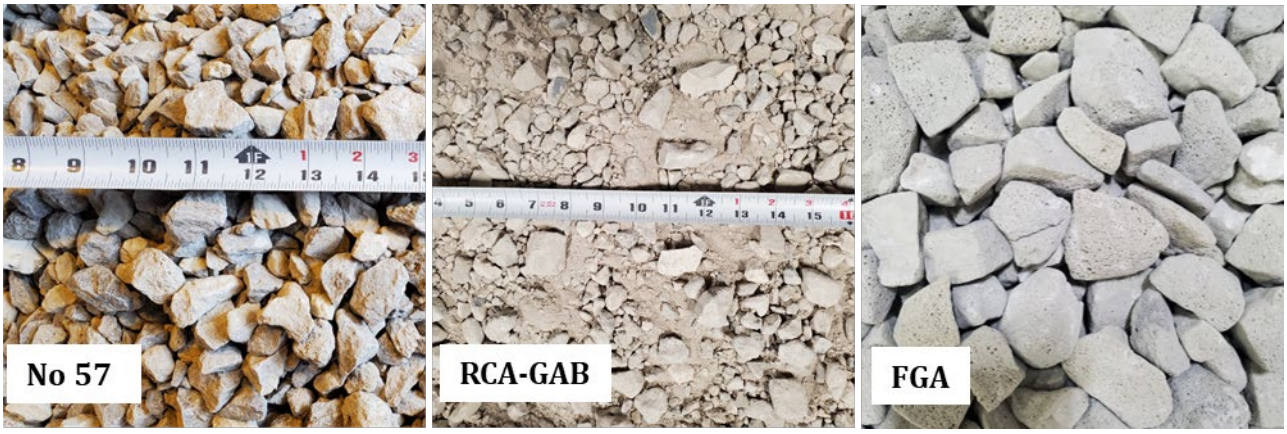


Figure 3-1. Photo of the aggregates.

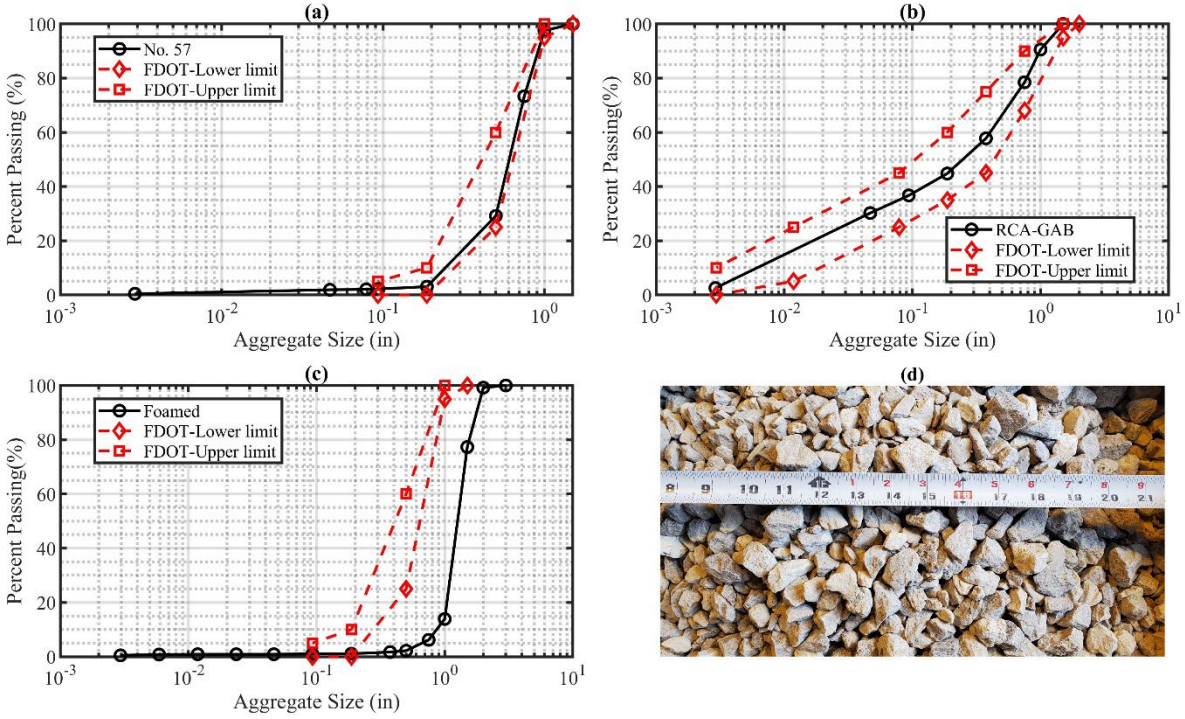


Figure 3-2. Sieve analysis results.
(a) No. 57 (b) RCA-GAB (c) Foamed aggregate (d) A photo of No. 57 aggregate.

Table 3-1. Gradation properties of backfill.

| Aggregate Type | $d_{max}$ (in) | $D_{10}$ (in) | $D_{30}$ (in) | $D_{60}$ (in) | $C_u$ | $C_c$ | USCS Classification |
|---|---|---|---|---|---|---|---|
| No. 57 | 1.3 | 0.357 | 0.500 | 0.663 | 1.856 | 1.057 | GP |
| RCA-GAB | 1.25 | 0.005 | 0.040 | 0.29 | 66.667 | 0.917 | GW |
| Foamed | 2 | 0.900 | 1.200 | 1.450 | 1.611 | 1.103 | GP |

Where $d_{max}$: maximum particle size of aggregate, $D_{10}$: the aggregate size in which 10 percent of the sample is finer, $D_{30}$: the aggregate size in which 30 percent of the sample is finer, $D_{60}$: the aggregate size in which 60 percent of the sample is finer, $C_u$ is the coefficient of uniformity ( $C_u = \frac{D_{60}}{D_{10}}$), and $C_c$ is the coefficient of curvature ($C_c = \frac{{D_{30}}^2}{D_{10}\, x\, D_{60}}$).

### 3.1.1.2 Unit Weight

The compaction requirements for the backfill used in GRS are outlined in FDOT Specifications for Road and Bridge Construction (FDOT, 2020) and FDOT Development Specification 549. The maximum and minimum dry unit weights of the open-graded backfills were tested according to ASTM D4253 (2006) and ASTM D4254 (2006) standards, respectively at the FDOT State material office (SMO). Modified standard proctor test was conducted for RCA-GAB backfill following AASHTO T 180 (2009) standard (Figure 3-3). Specific gravity of aggregates was determined according to FM 1-T085. Table 3-2 are the unit weight and specific gravity for each aggregate type.

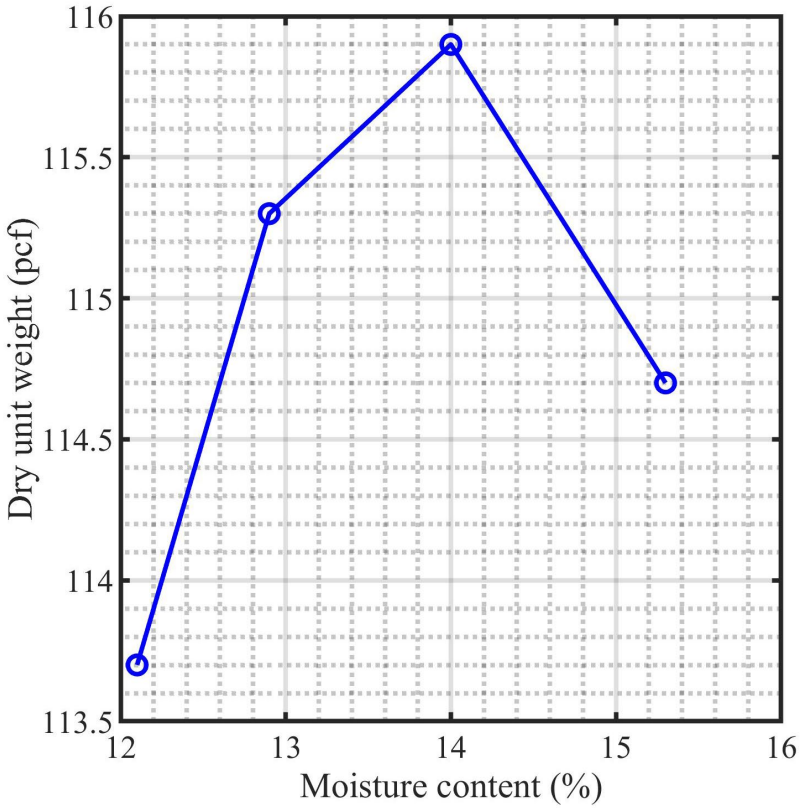


Figure 3-3. Proctor test's results for RCA-GAB.

Table 3-2. Maximum and minimum density index and specific gravity for aggregates.

| Aggregate Type | Maximum Dry Unit Weight (pcf) | Optimum Moisture Content (%) | Minimum Dry Unit Weight (pcf) | Specific Gravity |
|---|---|---|---|---|
| No 57 | 96.1 | N/A | 82.7 | 2.64 |
| RCA-GAB | 115.9 | 13.8 | | 2.55 |
| FGA[b] | 16.7 | N/A | 10.1 | 0.52 |

Notes; [b] based on the results reported by FHWA through internal communication.

### 3.1.1.3 Shear Strength Tests

Understanding the overall behavior of a geosynthetic reinforced soil (GRS) composite relies heavily on the strength properties (friction and apparent cohesion) of the backfill and reinforcement conditions (spacing, strength, and stiffness). These properties are used in determining the ultimate load-carrying capacity, required reinforcement strength, and lateral earth pressures of the GRS composite. The triaxial test, direct shear test, or plain-strain test, can be

performed to determine the strength properties of the backfill materials. For this study, triaxial and direct shear tests were performed.

#### 3.1.1.3.1 Triaxial Tests

Consolidated drained triaxial tests were conducted on the No. 57 and RCA-GAB aggregates according to ASTM D7181-11 to determine their shear strength properties. ASTM D 7181 (2020) recommends a specimen height to diameter ratio of 2 and a diameter at least $6d_{max}$. Specimen diameters of 4 inches and 6 inches were tested, while maintaining a height-diameter ratio equal to 2. For the 4-inch specimen, triaxial tests of the No. 57 aggregate were conducted on both scalped (particles greater than 0.67 inches removed) and non-scalped samples. Triaxial tests on the 4-inch specimen of the RCA-GAB were the whole sample (non-scalped). Triaxial tests on the 6-inch specimens of both aggregates were the whole samples (non-scalped). A 10-lbs hand

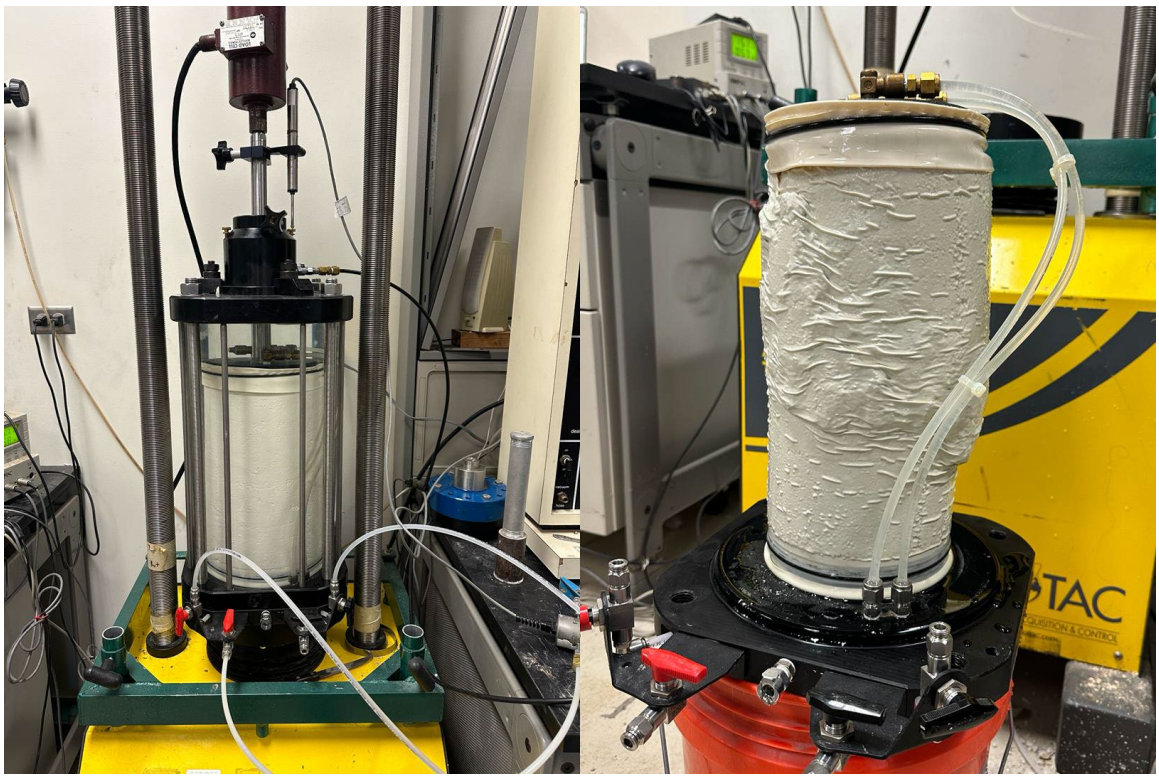

(a) (b)

Figure 3-4. Triaxial test on a 6-inch specimen before and after the test for RCA-GAB. (a) Before; (b) After.

hammer dropped 18 inches was used to compact the specimens. The No. 57 aggregates were compacted to their maximum density, while RCA-GAB aggregates were compacted to at least 98% of their optimum dry density. The 4-inch specimens were sheared at confining pressures of 5 psi, 10 psi, 20 psi, and 30 psi, while 6-inch specimens were sheared at confining pressures of 10 psi, 20 psi, and 30 psi. Figure 3-4 shows a 6-inch RCA-GAB specimen before and after shearing.

#### 3.1.1.3.2 Triaxial Test Results and Analysis

Figure 3-5 and Figure 3-6 present the triaxial test results conducted for No. 57 and RCA-GAB aggregates with specimen diameters of 4 inches and 6 inches, respectively. The comparison of the test results from the 4-inch and 6-inch triaxial tests is shown in Figure 3-7. Triaxial tests for No. 57 aggregates were conducted up to at least 13% axial strain. For RCA-GAB, 4-inch triaxial tests were conducted up to 5% axial strain, while for the 6-inch triaxial tests, they were carried out up to 10% vertical strain for confining pressures of 10 psi and 20 psi.

No. 57 and RCA-GAB aggregates exhibit different stress-strain relationships and volumetric behaviors under triaxial compression. In both 4-inch and 6-inch triaxial tests, RCA-GAB aggregates exhibit strain hardening until reaching peak strength at approximately 1 to 2.5% axial strain, followed by softening until the end of the test. The volumetric behavior of RCA-GAB aggregates involves initial contraction followed by dilation until the end of the test, observed across both specimen sizes and all confining pressures. In contrast, No. 57 aggregates undergo strain hardening until the end of test across all specimens and confining pressures, lacking a distinct intermediate peak strength. Initially, No. 57 aggregates experience contraction followed by dilation until the end of the test under all confining pressures, with minimal dilation under 30 psi confinement.

The test results were also analyzed for the shear strength properties, internal friction angle and apparent cohesion. The internal friction angle was assessed in three ways: the secant friction angle ($\phi'_s$), tangent friction angle ($\phi'$) based on the Mohr-Coulomb failure (MC) envelope, and the constant volume friction angle ($\phi'_{CV}$) derived from the zero dilation angle (ZDA) approach. The maximum secant friction angle was calculated at each confining pressure using Equation (3-7). This method assumes zero cohesion in the material and is particularly suitable for cohesionless materials such as No. 57 aggregate. The tangent friction angle from the Mohr-Coulomb failure envelope can be determined either by Equation (5-8), based on a tangent line

drawn to Mohr circles, or by Equations (3-5) and (3-6), utilizing a straight line (Kf-line) connecting the peak shear ($q'$) and mean stress path ($p'$) from the stress-strain curves. In Equation (5-8), Mohr circles are utilized to represent the stress states using peak or residual points or stress-strain curves. The tangent line is drawn through the tangents of the Mohr circles, and the failure envelope is represented through Equation (5-8) by assuming a linear failure relationship. In the ZDA approach, the constant volume friction angle is computed as the friction angle when the dilation angle is zero.

Figure 3-8 shows q-p plots of selected peak points extracted from the stress-strain curves for RCA-GAB and No. 57 aggregates. The parameters for kf-line are shown in Table 3-3.The strength properties, determined using the linear Mohr-Coulomb failure envelope, are presented in Table 3-4. The results show that RCA-GAB exhibits a higher peak friction angle than No. 57 in both 4-inch and 6-inch specimens. At the peak state, the friction angle of RCA-GAB surpasses that of No. 57 by 13.2 degrees. One contributing factor to the higher friction angle in RCA-GAB is its well-graded nature, leading to a larger number of interparticle contacts and interlock compared to No. 57. Also, there are fewer particle breakages in RCA-GAB compared to No. 57. When particles break, the number of particle interlocks decreases, resulting in a lower friction angle. No. 57 test specimens have higher initial void ratios than RCA-GAB which results in a lower friction angle. Nicks et al. (2015) conducted a series of direct shear and triaxial tests to evaluate the strength characteristics of open-graded aggregates. Utilizing a 6-inch specimen diameter for triaxial tests, Nicks et al. (2015) reported a friction angle of 40.5 degrees for AASHTO No. 57 based on the Mohr-Coulomb approach, which is 4.7 degrees less than the findings of this study. Knierim (2014) reported peak friction angles of No. 57 limestone varying from 52.9 degrees to 41.6 degrees, while residual friction angles varied from 49.1 to 40.8 degrees for the lowest confining pressure (3 psi) to the highest confining pressure (54.4 psi), respectively. Duncan (2007) carried out a series of triaxial tests on No 57 limestone and reported peak friction angles of 53.5 degrees and 42.8 degrees at confining pressures of 4 psi and 30.3 psi, respectively, for low density (117 pcf). For high density (150 pcf), friction angles of 53.1 and 44.1 degrees were reported at confining pressures of 3.7 psi and 30.0 psi, respectively. Wu et al. (2013) conducted a series of triaxial tests on a well-graded gravel backfill classified as GW-GM according to ASTM D 2487. The backfill in the triaxial tests was compacted at a dry unit weight of 150 pcf and 5.2 % moisture content. Based on the Mohr-Coulomb failure envelope, Wu et al. (2013) reported friction angles and cohesion of 50 degrees and 10.3 psi, respectively, for confining stress between 0 and 30 psi.

For confining stress between 30 and 110 psi, Wu et al. (2013) reported friction angles and cohesion of 38 degrees and 35.1 psi, respectively. Another study by Khosrojerdi et al. (2020) reported a friction angle of well-graded material AASHTO A-1-a based on 6-inch triaxial tests to be 48 degrees with a cohesion of 0.8 psi.

Triaxial tests in this study also show the influence of specimen size, with 4-inch specimen diameter tests yielding lower friction angles than those with a 6-inch diameter for RCA-GAB aggregates, with a difference of 11.4 degrees between the two peak friction angles. However, for No. 57 aggregates, no significant influence of specimen size is observed, with only a 1.1-degree difference between the two peak friction angles.

Constant volume friction angles based on the ZDA approach are presented in Table 3-5. Figure 3-9 shows the relationship between the peak secant friction angle and the maximum dilation angle used to determine the constant volume friction angle. Unlike in the Mohr-Coulomb failure approach, the RCA-GAB aggregate exhibits a lower constant volume friction angle than the No. 57 aggregate in the 4-inch triaxial specimen when the ZDA approach is applied. However, for the 6-inch specimen, the constant volume friction of RCA-GAB is greater than that of No. 57. Figure 3-11 provides a comparison of the friction angles determined using the Mohr-Coulomb and ZDA approaches. The Mohr-Coulomb failure envelope yields a higher friction angle than the ZDA approach. Nicks et al. (2015), utilizing a 6-inch specimen diameter for triaxial tests, reported a friction angle of 38.4 degrees for AASHTO No. 57 based on the ZDA approach, which is 2.8 degrees less than the findings of this study. The influence of specimen size is also evident when the ZDA approach is employed, with the 4-inch specimen resulting in a lower constant volume friction angle than the 6-inch diameter specimen. Regardless of whether well-graded or open-graded aggregates are utilized, the FHWA recommends that the internal friction angle be equal to or greater than 38 degrees. FDOT imposes a slightly higher requirement, specifying a minimum internal friction angle of 42 degrees. Depending on the approach used for interpreting the shear strength properties of aggregates, the peak friction angles of both aggregates based on the Mohr-Coulomb approach satisfy both FDOT and FHWA recommendations. However, if the ZDA approach is used, then the constant volume friction angles of No. 57 based on the 6-inch and RCA-GAB based on both 4-inch and 6-inch diameter specimens satisfy only the FHWA criterion. Only the constant volume friction angle of RCA-GAB based on the 6-inch diameter specimen satisfies the FDOT criterion.

Figure 3-10 presents a plot of peak secant friction angle versus confining pressure for each aggregate and different specimen diameters. At the same confining pressures, RCA-GAB shows higher peak secant friction angles compared to the No. 57 aggregate. Similar to Mohr-Coulomb friction angles, the increased inter-particle contacts in RCA-GAB may contribute to the higher observed shear strength and, consequently, higher secant friction angles. Moreover, the peak secant friction angle decreases as the confining pressure increases in both aggregates. Notably, the rate of change of the friction angle from one confining pressure to another is more pronounced when the confining pressure is low. Knierim (2014) conducted a series of consolidated drained triaxial tests on No 57-limestone aggregate. The limestone used had a maximum particle size of 0.88 inch and was classified as poorly graded gravel (GP). Knierim (2014) reported peak secant friction angle to vary from 52.9 degrees to 41.6 degrees while residual friction angle varies from 49.1 to 40.8 degrees for the lowest (3 psi) to highest confining pressure (54.4 psi), respectively. Duncan (2007) reported peak friction angles of 53.5 degrees and 42.8 degrees at confining pressures of 4 psi and 30.3 psi respectively, for low density. For high density, friction angles of 53.1 and 44.1 degrees were reported at confining pressures of 3.7 psi and 30.0 psi, respectively.

The dilation behavior of the aggregates is shown in Figure 3-10. Notably, at equivalent confining pressures, RCA-GAB exhibits a higher dilation angle than No. 57 aggregates. Both aggregates demonstrate a decrease in maximum dilation angle with an increase in confining pressure. However, the influence of specimen size on the dilation angle is not clearly evident, as there are instances where the maximum dilation angle is higher in the 4-inch specimen compared to the 6-inch specimen, and vice versa, for different confining stresses. For instance, the dilation angle of No. 57 at a confining pressure of 10 psi is 29.29 degrees for the 4-inch specimen diameter and 28.76 degrees for the 6-inch specimen diameter, while it is 21.09 degrees and 24.77 degrees, respectively, at a confining pressure of 30 psi.

This study also aimed to investigate the influence of removing larger particle sizes when using a small triaxial specimen. To explore this, a series of triaxial tests were conducted with and without the removal of larger particles (particles greater than 0.67 inches) using a 4-inch triaxial cell. Only No. 57 aggregate was tested for this scenario. Figure 3-5 illustrates the triaxial test results for No. 57 conducted using a 4-inch diameter triaxial specimen. The strength properties determined using the linear Mohr-Coulomb failure envelope show no noticeable influence of removing larger particles. The peak friction angle without removing larger particles is recorded as

45.21 degrees. However, when the larger particles were removed, the friction angle reduced to 44.73 degrees. The difference of 0.48 degrees is deemed insignificant, leading to the conclusion that, for this No. 57 aggregate, the presence or absence of larger particles has minimal impact on the shear strength properties.

Morh-coulomb failure (MC) envelope is represented as:

$$\tau_f = \sigma'_n \tan\phi' + c' \tag{3-1}$$

Where $\tau_f$ is the shear stress at failure, $\sigma'_n$ is the effective normal stress, $\phi'$ is the effective angle of internal friction, and $c'$ is the effective apparent cohesion.

In the triaxial tests, these parameters can be computed from shear ($q'$) and mean stress path ($p'$) computed as:

$$p' = \frac{1}{2}(\sigma'_1 + \sigma'_3) \tag{3-2}$$

$$q' = \frac{1}{2}(\sigma'_1 - \sigma'_3) \tag{3-3}$$

Where $\sigma'_1$ and $\sigma_3$ are is the major and minor principal stress at failure, respectively.

The failure envelope is determined from the plot of $q'$ versus $p'$ and their relationship is presented as:

$$q' = p' \tan\alpha + b \tag{3-4}$$

$$\phi' = \sin^{-1}(\tan\alpha) \tag{3-5}$$

$$c' = \frac{b}{\cos\phi'} \tag{3-6}$$

The secant friction angle ($\phi'_s$) at each confining pressure and load step is computed as:

$$\phi'_s = \left(\frac{\sigma'_1 - \sigma'_3}{\sigma'_1 + \sigma'_3}\right) \tag{3-7}$$

Maximum dilation angle ($\psi_{max}$) is computed as a function of axial and lateral strains:

$$\psi_{max} = \sin^{-1}\left[\frac{(d\varepsilon_1 + 2d\varepsilon_3)}{(d\varepsilon_1 - 2d\varepsilon_3)}\right] \tag{3-8}$$

Where $d\varepsilon_1$ is the incremental axial strain and $d\varepsilon_3$ is the incremental lateral strain.

Lateral strain ($\varepsilon_3$) is computed as:

$$\varepsilon_3 = \frac{(\varepsilon_v - \varepsilon_1)}{2} \tag{3-9}$$

Where $\varepsilon_v$ is the volumetric strain and $\varepsilon_1$ is the axial strain.

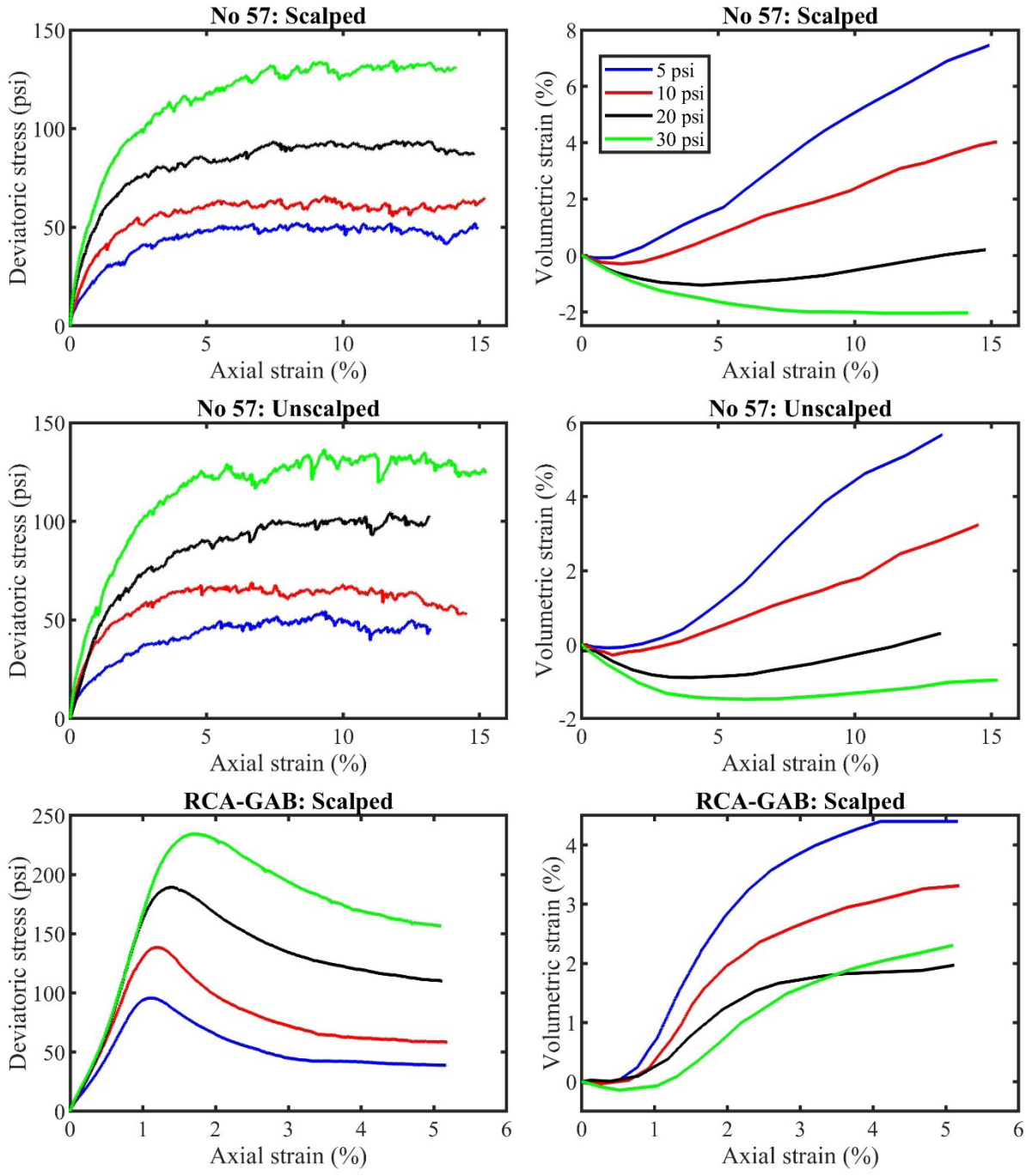


Figure 3-5. Results of triaxial tests from 4-inch triaxial testing.

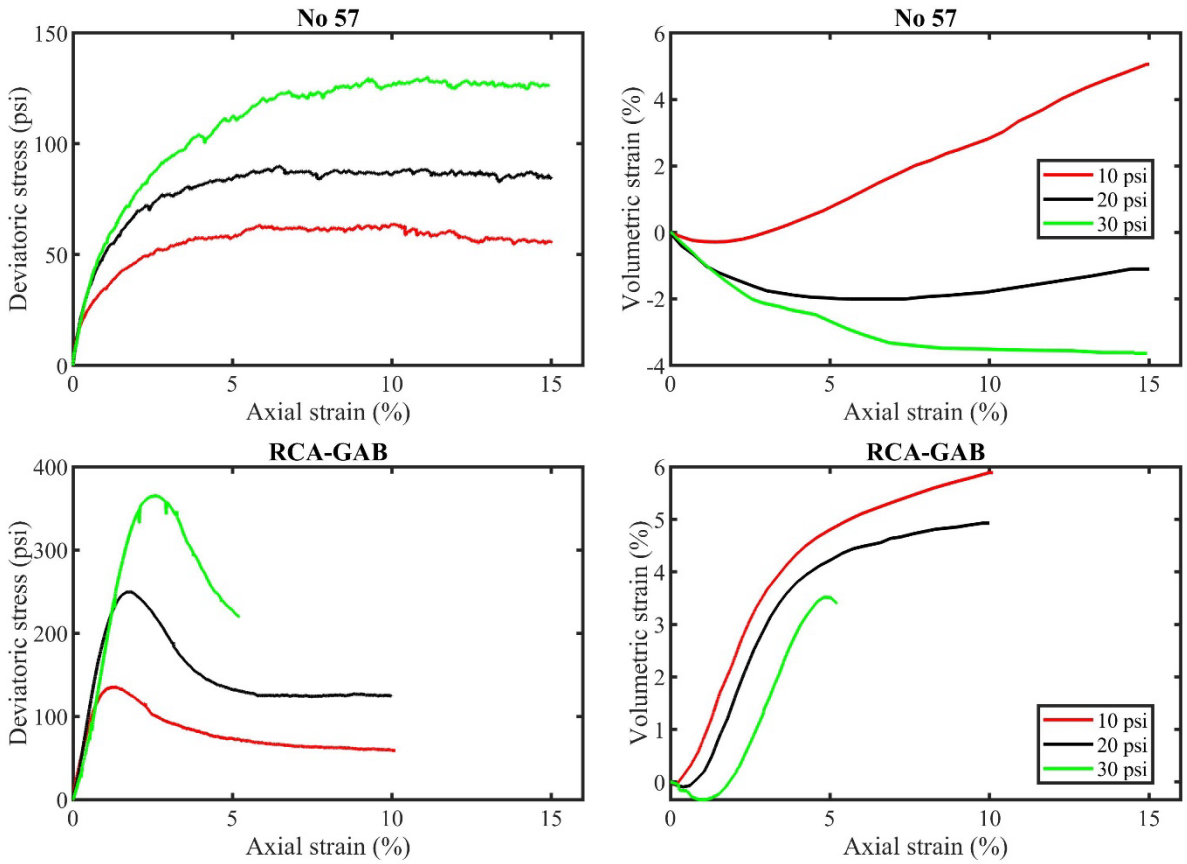


Figure 3-6. Results of triaxial tests from 6-inch triaxial testing.

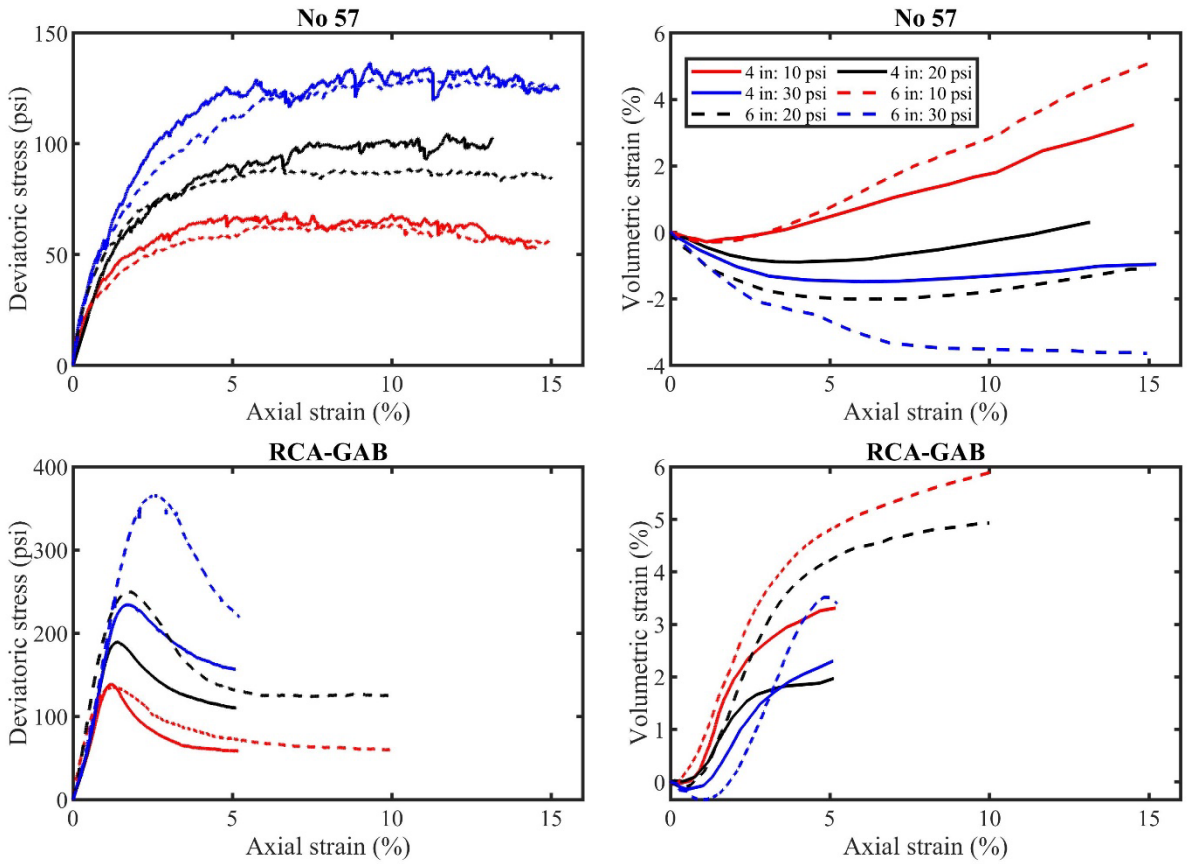


Figure 3-7. Comparison of results of triaxial tests from 4-inch and 6-inch triaxial testing.

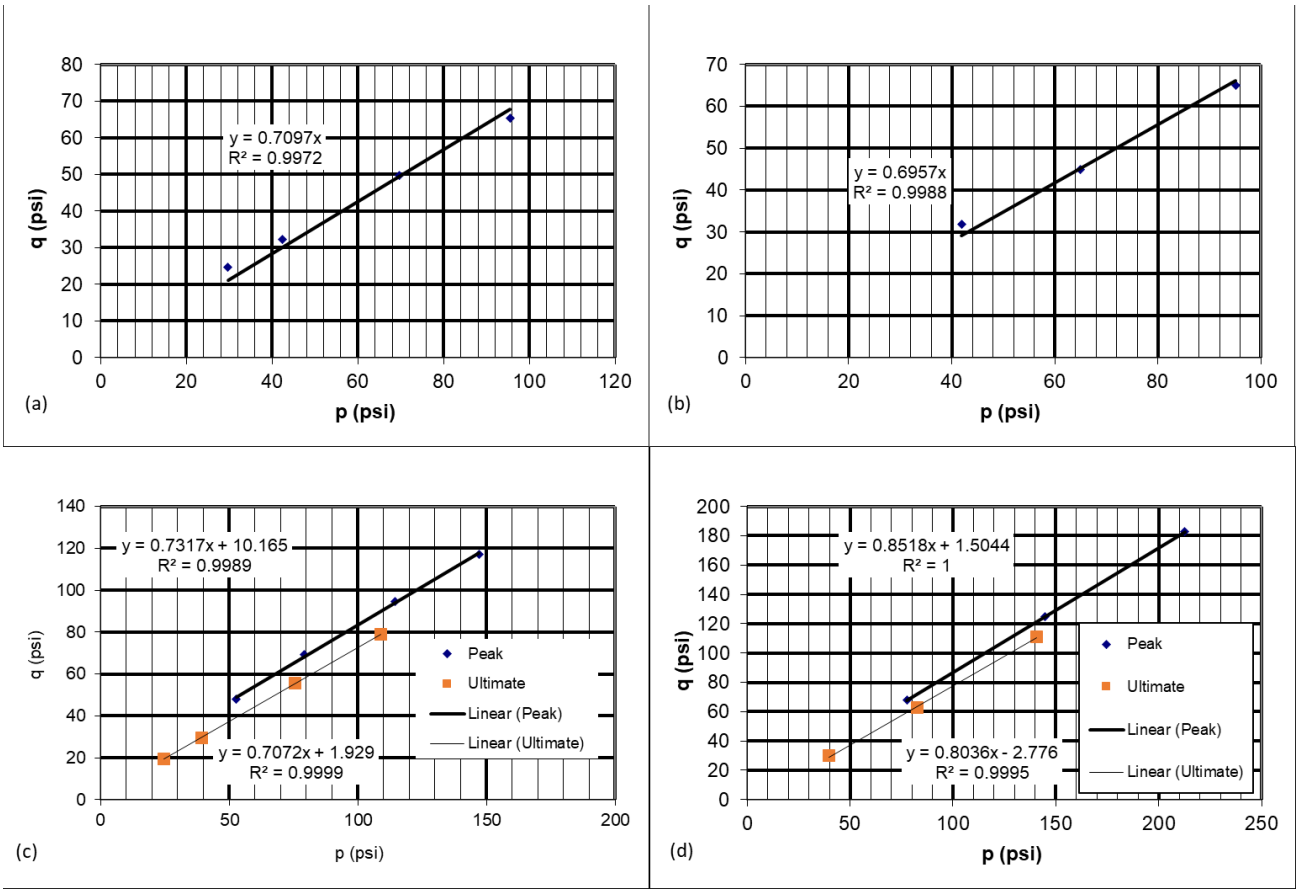


Figure 3-8. Plots of $q'$ versus $p'$ from triaxial tests.

Table 3-3. Parameters from kf-line.

| | Residual | | Peak | |
|---|---|---|---|---|
| Aggregate type | α | β (psi) | α | β (psi) |
| No 57[a] | 0.7097 | 0 | 0.7097 | 0 |
| RCA-GAB[a] | 0.7072 | 1.929 | 0.7317 | 10.165 |
| No 57[b] | 0.6957 | 0 | 0.6957 | 0 |
| RCA-GAB[b] | 0.8609 | -2.6612 | 0.8518 | 1.5044 |

Table 3-4. Strength Properties using Mohr-Coulomb Approach.

| | Residual | | Peak | | | |
|---|---|---|---|---|---|---|
| | With intercept | | With intercept | | With zero intercept | |
| Aggregate type | Friction angle (°) | Apparent Cohesion (psi) | Friction angle (°) | Apparent Cohesion (psi) | Friction angle (°) | Apparent Cohesion (psi) |
| No 57[a] | 38.46 | 7.86 | 38.46 | 7.86 | 45.21 | 0 |
| RCA-GAB[a] | 45.01 | 2.73 | 47.03 | 14.91 | 55.39 | 0 |

| | | | | | | |
|---|---|---|---|---|---|---|
| No 57[b] | 38.78 | 6.60 | 38.78 | 6.60 | 44.08 | 0 |
| RCA-GAB[b] | 53.48 | 2.52 | 58.41 | 2.87 | 59.42 | 0 |

Notes:

a-based on a 4-inch diameter triaxial test.
b- based on a 6-inch diameter triaxial test.

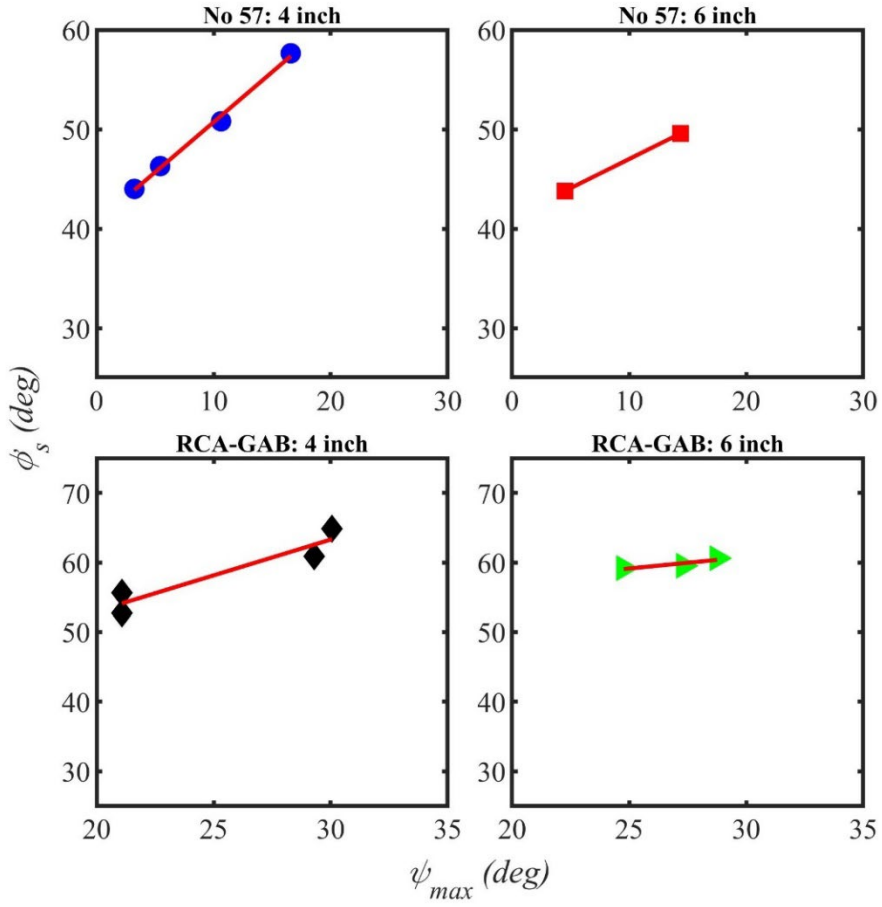


Figure 3-9. Plots of $\phi'_s$ versus $\psi_{max}$ from triaxial tests.

Table 3-5. Strength Properties using ZDA Approach.

| Aggregate | Peak Friction Angle (°) | |
|---|---|---|
| | 4 in | 6 in |
| No 57 | 40.65 | 41.17 |
| RCA-GAB | 32.50 | 50.90 |

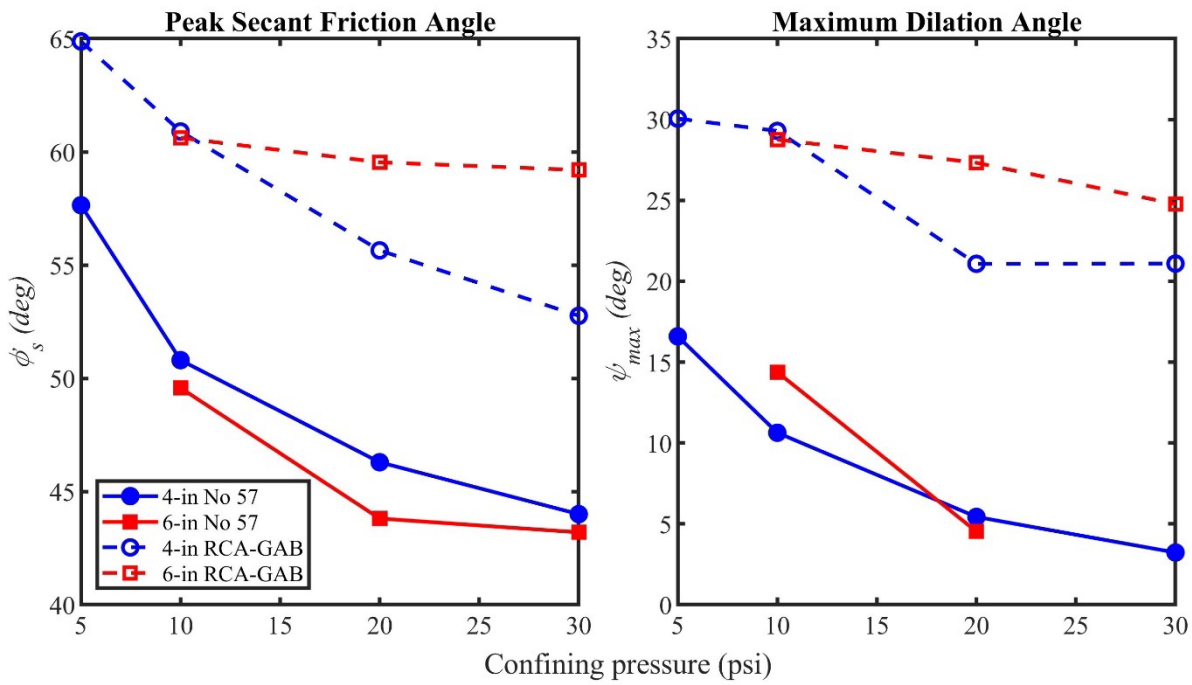


Figure 3-10. Peak secant friction angle and maximum dilation angle for different confining pressure.

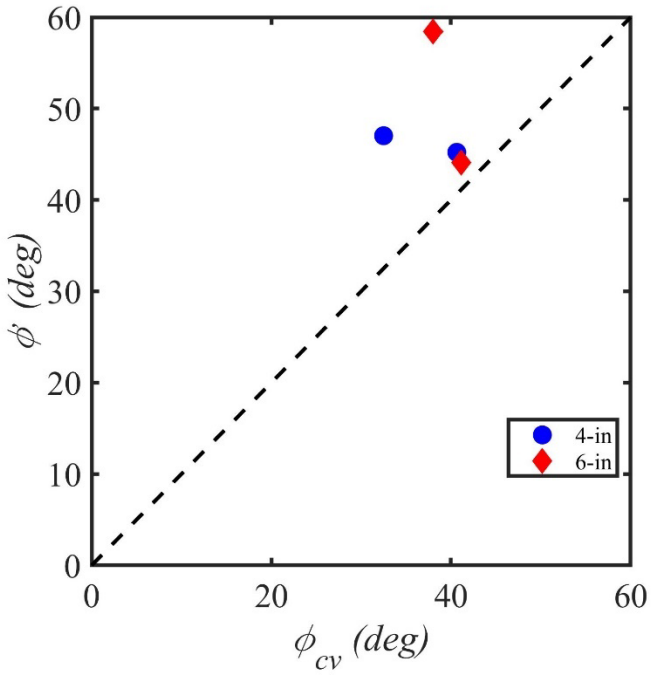


Figure 3-11. MC tangent Friction angle versus constant volume friction angle.

#### 3.1.1.3.3 Direct Shear Test

Both aggregates were tested in the direct shear test according to ASTM D3080 (2012) standard. ASTM D3080 (2012) specifies that the specimen diameter must be greater than 10 times the maximum particle size diameter. Therefore, for No 57, RCA-GAB, and FGA aggregates, the required device diameter would be at least 12.5 inches, 13 inches, and 30 inches, respectively. Unfortunately, testing devices with these dimensions were not available at FDOT, FSU, or UF laboratories. Typically, to meet the ASTM D3080 (2012) standard, larger materials are removed to accommodate the smaller testing device. However, during the construction of the piers, the larger particles were not removed, so testing the materials without removing the larger particles will provide a more accurate representation of the actual GRS pier conditions. No 57 and RCA-GAB were tested using a 4-inch diameter shear box at the FSU soil laboratory. No materials were removed, and as a result, the ASTM D3080 requirements were not met. Consequently, the results obtained from the 4-inch shear box may be influenced by the boundary conditions. During the small direct shear test, the rotation of the loading pad was observed, especially when approaching failure. This rotation was caused by the reorientation of larger particles that had limited space to move around. As a result, the test was stopped at a smaller horizontal strain than what the piers experienced during performance testing. The small direct shear tests (SDS) were conducted at normal stresses of 10 psi, 20 psi, and 30 psi. To ensure test repeatability, duplicate tests were conducted using No 57 aggregate and a 4-inch direct shear box. Figure 3-13 shows the results, demonstrating the repeatability of the test. No. 57 aggregate was tested under dry conditions and compacted to 95 percent of the maximum unit weight achieved through hand compaction. This compaction level is lower than the densities at which the piers were tested. Achieving 100% compaction using hand compaction proved to be difficult. RCA-GAB was tested at 96 %of its maximum unit weight. The tests were carried out under unsaturated conditions. Nicks et al. (2013) reported that the peak friction angle for well-graded material (AASHTO A-1-a) remains the same under both saturated and unsaturated conditions. To investigate the influence of the shear box size, No 57 aggregate was also tested using a 12x12-inch direct shear box at the FHWA laboratory. The setup of the 4-inch diameter direct shear testing device is shown in Figure 3-12, while Figure 3-14 and Figure 3-16 present the results of the small and large direct shear test, respectively. The friction angle and cohesion were determined through linear regression by fitting the best line through the

points at failure as shown in Figure 3-15and Figure 3-16 (c). Table 3-6 presents the strength properties of the tested materials.

This study also aimed to investigate the common practice of using both larger and smaller direct shear devices. Testing was conducted using a 4-inch diameter shear box and a 12-inch shear box. No materials were removed in either case to ensure accurate comparisons. Unfortunately, only No 57 was tested in this scenario. The results showed that using the Small-Direct Shear (SDS) method yielded a slightly higher friction angle compared to the Large-Direct Shear (LDS) method for No 57 in this study. However, the difference between the two methods was less than 1 degree. Nicks et al. (2015) examined the scale effect by conducting direct shear tests on different types of open-graded aggregates using a 2.5-inch diameter shear box and a 12-inch square shear box. In their study, samples were scalped in a 2.5-inch box. The results indicated that some materials exhibited a higher friction angle when tested in a 2.5-inch box, while others showed a higher friction angle when tested in a 12-inch box. In the case of No 57, which has similar properties to the material tested in this study except for its geological origin, a 12-inch box resulted in a higher friction angle compared to a 2.5-inch diameter box, contrary to the findings of this study.

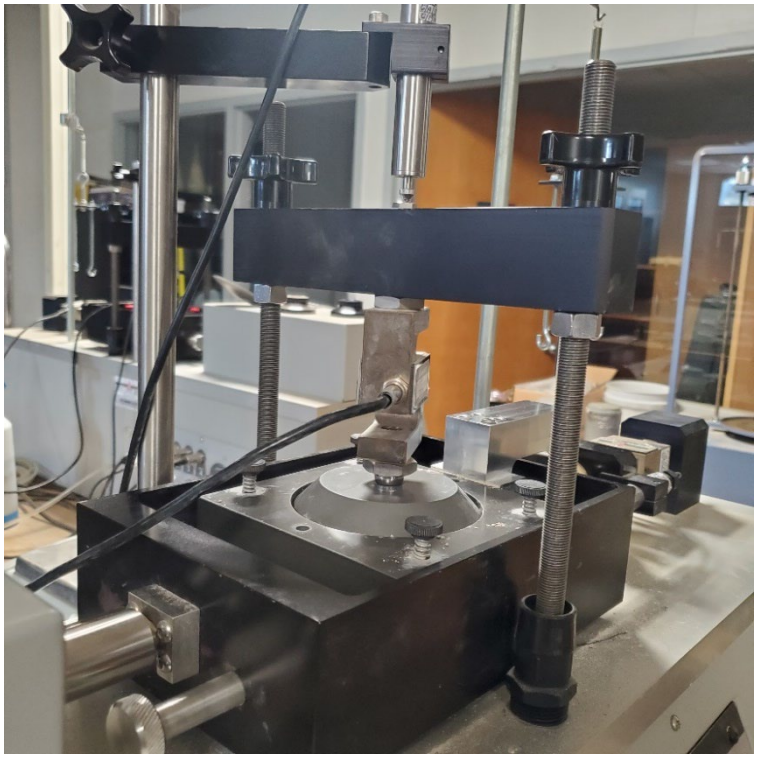

Figure 3-12. Direct shear device.

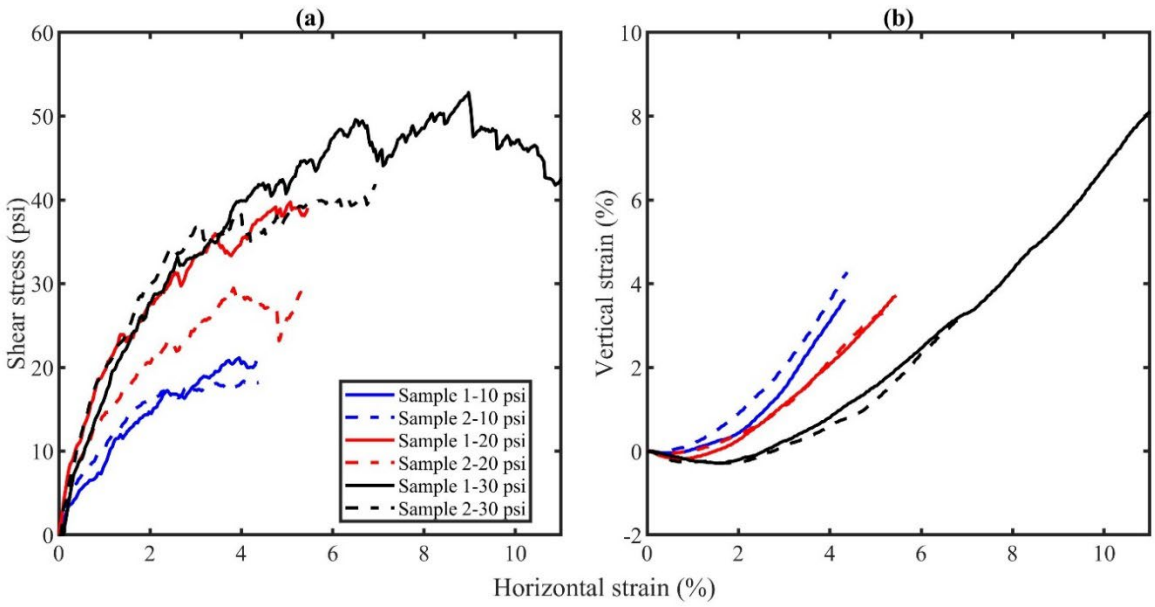


Figure 3-13. Direct shear test results for checking repeatability for No 57.

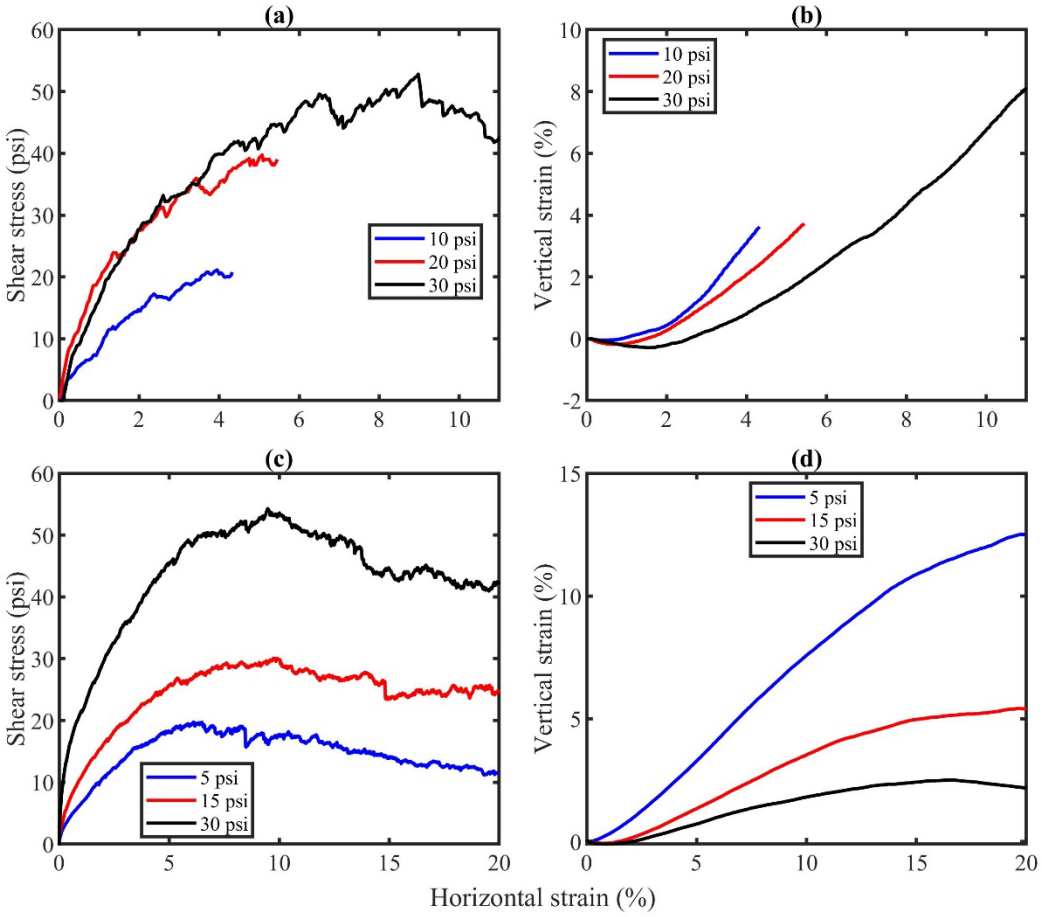


Figure 3-14. Direct shear results for No 57.
(a &b) From small direct shear box; (c &d) From large direct shear box.

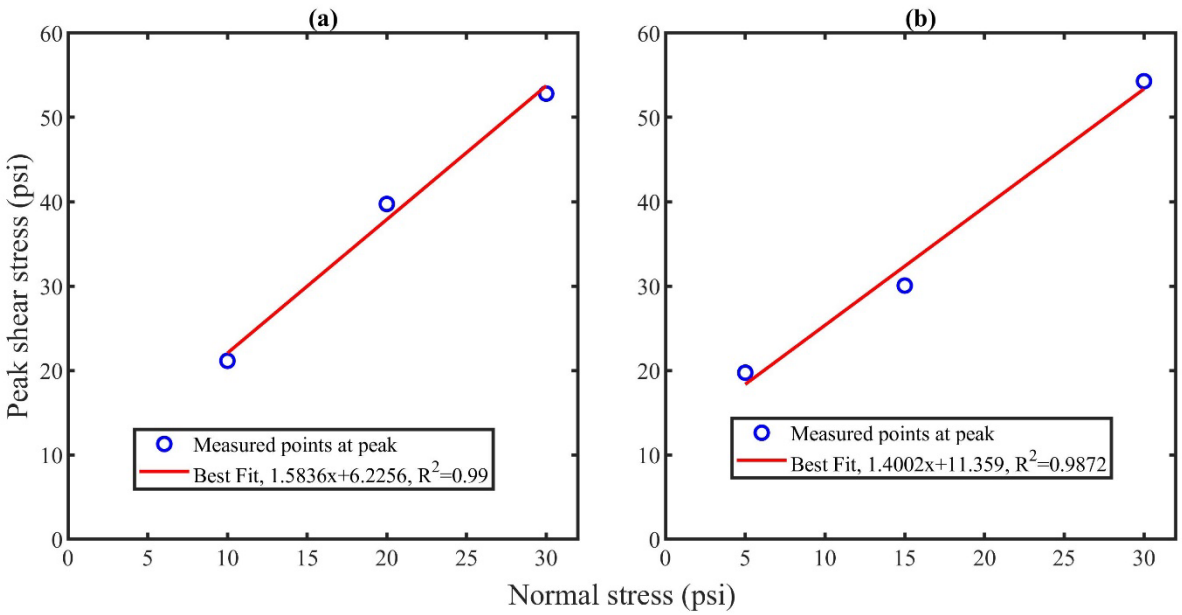


Figure 3-15. Direct shear results for No 57.
(a) From small direct shear box; (b) From large direct shear box.

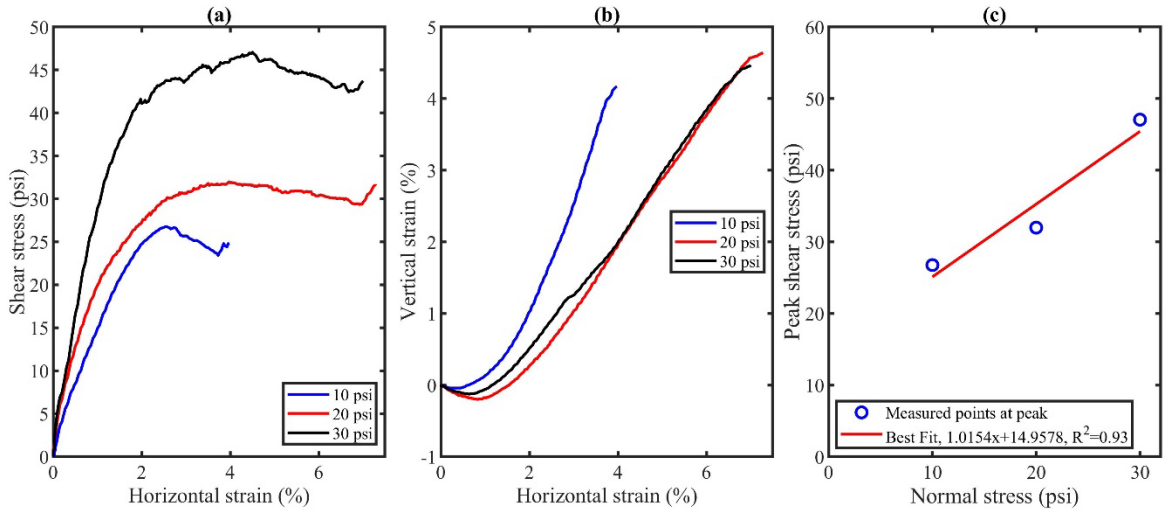


Figure 3-16. Direct shear results for RCA-GAB.
(a) Shear stress versus horizontal strain; (b) Vertical strain versus horizontal strain; (c) Peak shear stress versus normal stress.

Table 3-6. Strength Properties

| Aggregate type | SDS | | |
|---|---|---|---|
| | Friction angle (°) | Cohesion (psi) | |
| RCA-GAB | 45.44 | 14.96 | FSU |
| No 57 | 55.13 | 4.84 | FSU |
| | LDS | | |
| No 57 | 54.4 | 11.4 | FHWA |
| FGA | 54.0 | 1.28 | SGI Testing Services LLC |

#### 3.1.1.4 Interface Shear Strength

The behavior between dissimilar bodies is influenced by the properties of the interface. In geosynthetic reinforced soil (GRS) composites, the interface between the geosynthetic and soil is particularly important for stress transfer. Interface properties play an important role in describing the behavior between dissimilar bodies, particularly in geosynthetic reinforced soil (GRS) composites. The interface between the geosynthetic and soil is especially significant for stress transfer and soil-geosynthetic interaction. To ensure proper stress transfer between the soil and geosynthetic, a high interface friction is desired at the geosynthetic-soil interface. A low friction angle indicates a smoother surface, resulting in less soil stress being transferred through the interface.

To determine the interface properties between soil and geotextile, as well as between blocks and geotextile, a series of tests were conducted following the ASTM D 5321 standard. However, due to the unavailability of larger testing devices at FSU, a 4-inch diameter shear box was used. For the interface between the soil and geotextile, the soil was placed in both the top and bottom half of the shear boxes, with the geotextile positioned in between. Only No. 57 aggregate and RCA-GAB were tested in this study. No. 57 was tested at 95 percent of the maximum dry density, while RCA-GAB was tested at 96 percent of the maximum dry density and at optimal moisture content. For the interface between the blocks and geotextile, circular blocks with a diameter of 4 inches were placed in the bottom and top half of the shear boxes. These blocks were obtained by cutting them from larger blocks using a core cutter, as depicted in Figure 3-17. The results of the interface shear strength tests are shown in Figure 3-18, Figure 3-19, Table 3-7, and Table 3-6.

The results indicate that the highest friction angle is observed between HP 570 and the backfill. HP 570 and HPG 57 have the same tensile strength and stiffness according to the manufacturers. Both are made of polypropylene material, similar to HP 770. However, they are manufactured by different companies. The difference in the interface friction angle between the two materials and the backfill can be attributed to the fabric rigidity and the arrangement of yarns/filaments. Upon visual inspection, it was observed that HPG 57 is more rigid than HP 570. The lower rigidity of HP 570 allows some adjacent backfill particles to penetrate into the filaments, increasing interlocking between the particles and providing more resistance to shearing, similar to the passive resistance developed in geogrid-backfill interface. Additionally, the filaments in HPG 57 are closely and tightly integrated, making it difficult for adjacent backfill particles to penetrate compared to the filament arrangement in HP 570. Similar behavior was observed in a study by Zornberg et al. (2018b), where two woven geotextiles made of polypropylene but with different rigidity exhibited different interface friction angles. Zornberg et al. (2018b) conducted a comparison between two woven polypropylene geotextiles, namely HP 570 and RS5880i. Although both geotextiles shared the same wide-width ultimate tensile strength of 4,800 lb/ft, they differed in terms of tensile stiffness and fabric rigidity. At 5% tensile strain, HP 570 exhibited a stiffness of 60,069 lb/ft, while RS5880i had a higher stiffness of 96,000 lb/ft. RS5880i geotextile was more rigid than HP 570 geotextile. When subjected to testing for interface shear strength with AASHTO No aggregates, the results showed a higher interface shear strength for HP 570 than RS5880i. Zornberg et al. (2018b) attributed the higher interface shear strength observed in HP 570 to its lower fabric rigidity.

On the other hand, the interface friction angle between geotextiles and blocks is almost identical for all three geotextiles tested. This result was expected because the interaction between the geotextile and blocks occurs mainly through friction, which is primarily influenced by surface properties. In this case, all the geotextile materials are made of polypropylene. Block-geogrid interaction is different from the interaction between backfill and geotextile, where friction and interlocking of the particles adjacent to the geotextile's surface play a significant role.

Figure 3-17. Drilling of the block cores.

Table 3-7. Interface properties between Geotextile and Blocks.

| Testing Agency | Geotextile | Friction angle (deg) |
|---|---|---|
| FSU | HP570 | 21.86 |
| | HPG57 | 22.75 |
| | HP770 | 21.84 |

Table 3-8. Interface properties between Geotextile and Backfill.

| Testing Agency | Geotextile | Friction angle (deg) | |
|---|---|---|---|
| | | With No 57 | With RCA-GAB |
| FSU | HP570 | 42.23 | 40.39 |
| | HPG57 | 37.95 | 38.35 |
| | HP770 | 37.66 | 37.33 |

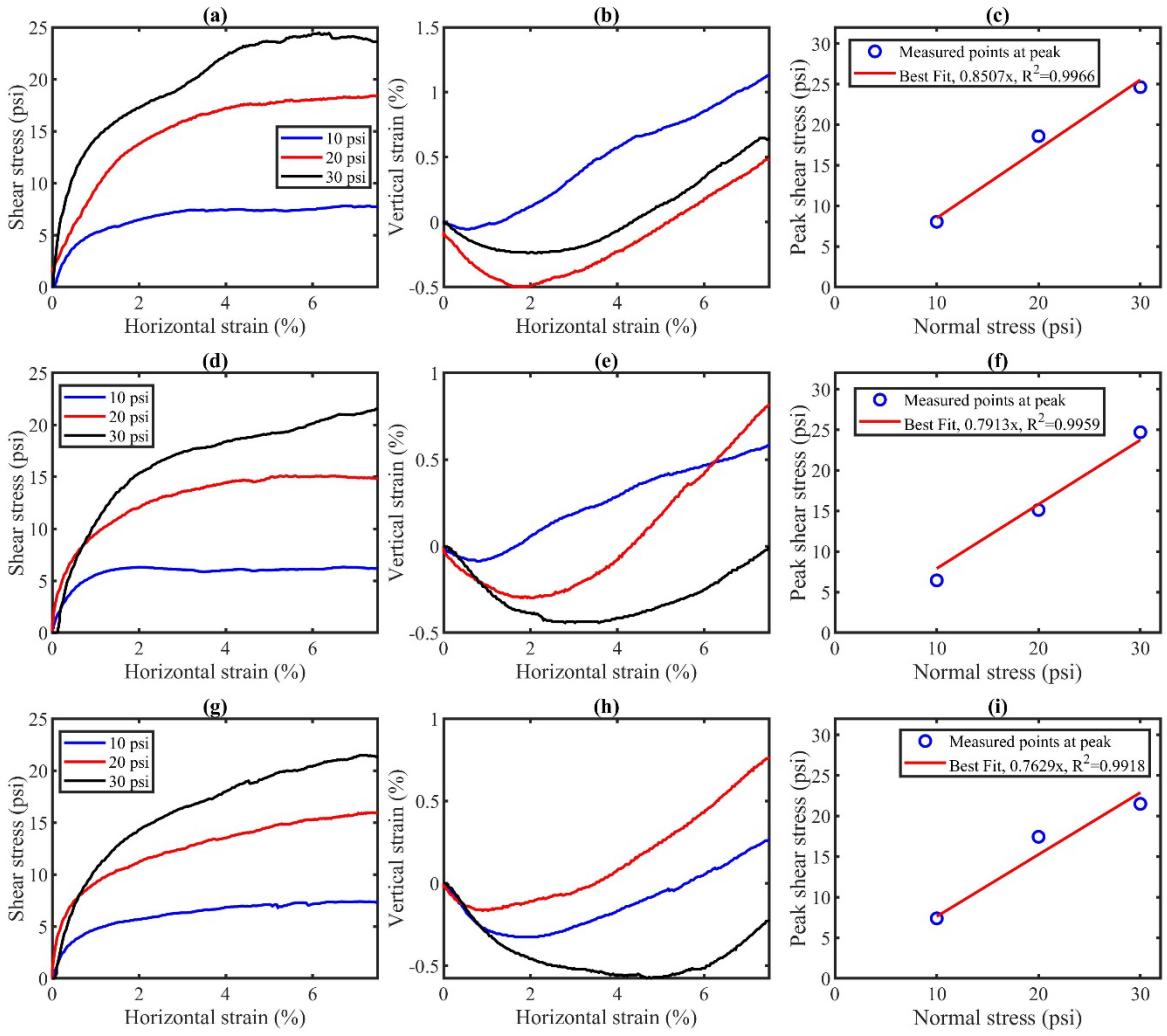


Figure 3-18. Interface shear strength results for RCA-GAB-aggregate with different geotextiles tested at FSU.

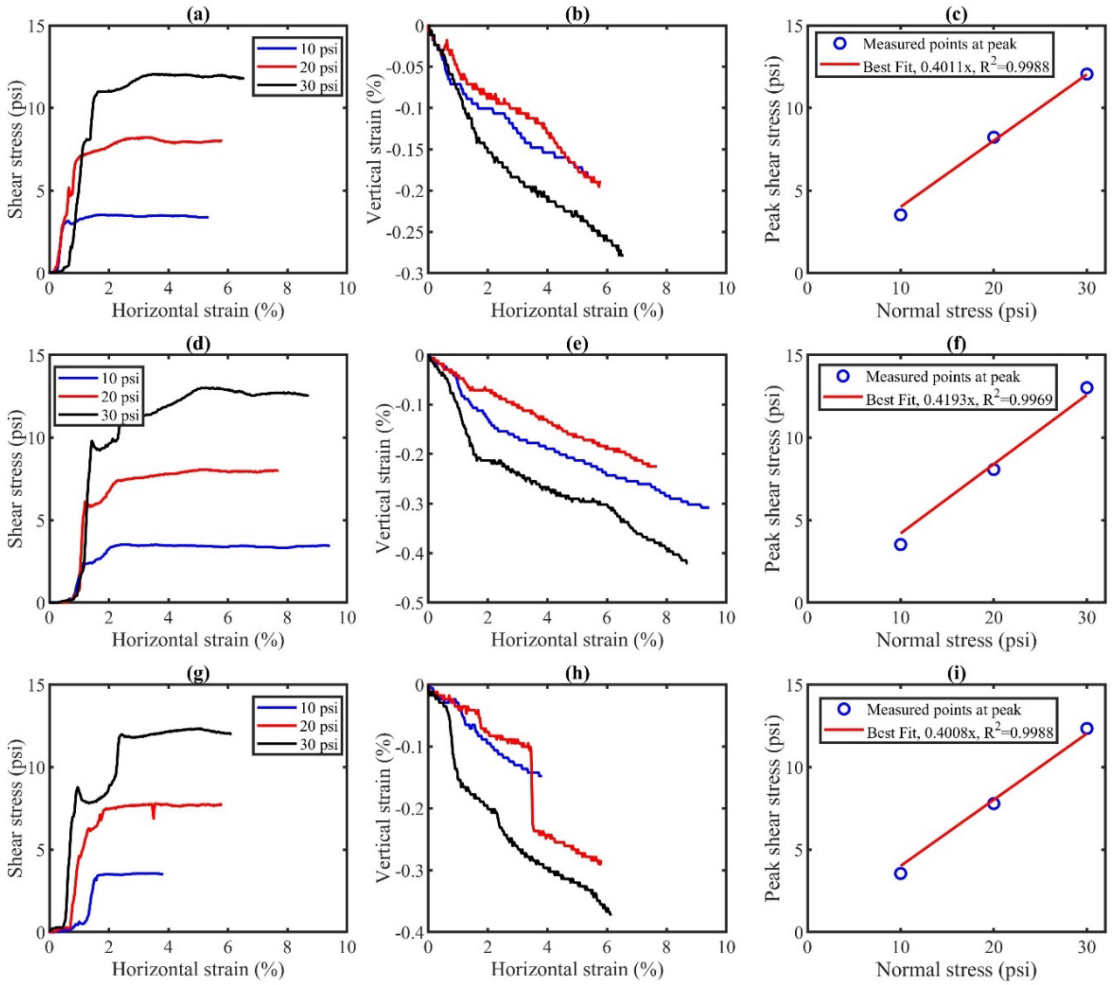


Figure 3-19. Interface shear strength results for block with different geotextiles tested at FSU.

### 3.1.2 Geosynthetics

In the construction of GRS abutments, geotextiles and geogrids are the most commonly used geosynthetic reinforcements. The majority of GRS-IBS structures that are currently in service have been constructed using woven polypropylene geotextile. Geosynthetics can be classified as uniaxial or biaxial based on the magnitude and orientation of their tensile strength. Uniaxial geosynthetics have a higher tensile strength in one direction than the other, while biaxial geosynthetics have equal tensile strength in both directions. FDOT Development Specification 549 requires the use of woven reinforcement (R-1 type) in GRS-IBS, with a minimum tensile strength of 4,800 lb/ft in both the machine direction (length of the roll) and cross-machine direction (width of the roll). Machine direction (MD) refers to strength along the length of the roll while cross-machine direction (CD) refers to strength along the width of the roll (Adams et al., 2012a). The

tensile strength of the geosynthetics is crucial for the load response of the GRS composites, as it increases the load-carrying capacity of the GRS mass. Studies have shown that by doubling the reinforcement strength, the ultimate capacity of the GRS pier can increase by a factor of 1.14, while the initial stress-strain ratio can increase by a factor of 1.34 (Nicks et al., 2013).

In this study, three types of woven polypropylene geotextiles were used as soil reinforcements in performance tests. These geotextiles met the requirements of both FDOT and FHWA for GRS-IBS. Two of the geotextiles (HP 570 and HPG 57) have similar strength properties in the MD and CD but are from different manufacturers. The third geotextile (HP 770) has a higher strength in the MD than in CD.

Table 3-9 shows the manufacturer's reported strength properties of the geotextiles. For confirmation, uniaxial tension tests were conducted according to the ASTM D4595 standard. A total of twelve specimens (8 inches wide and 4 inches long), six in each direction (MD and CD), were tested for each geotextile type. The test results for are presented in Figure 3-22. Mirafi HP 570 and TerraTex HPG 57 geotextile are stiffer in the CD than in the MD at all strain levels. On the other hand, the HP 770 has similar stiffness in the MD and CD at 5% strain. Testing results show TerraTex HPG 57 has less stiffness than Mirafi HP 570, contrary to what was reported by the manufacturer.

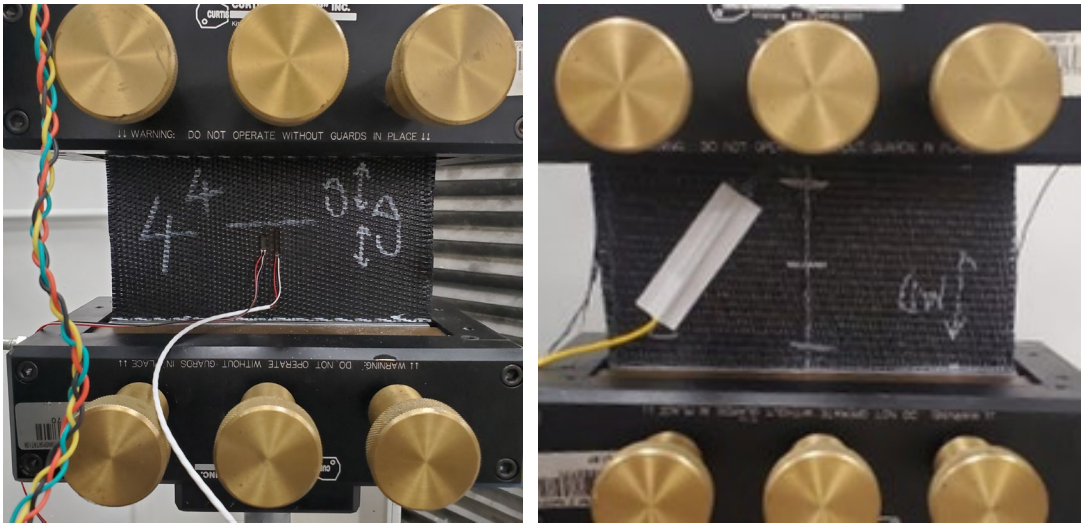


(a) (b)

Figure 3-20. Uniaxial tensile tests of geotextile.
(a)Test specimen with strain gauges installed; (b) Test specimen with fiber strain sensor installed.

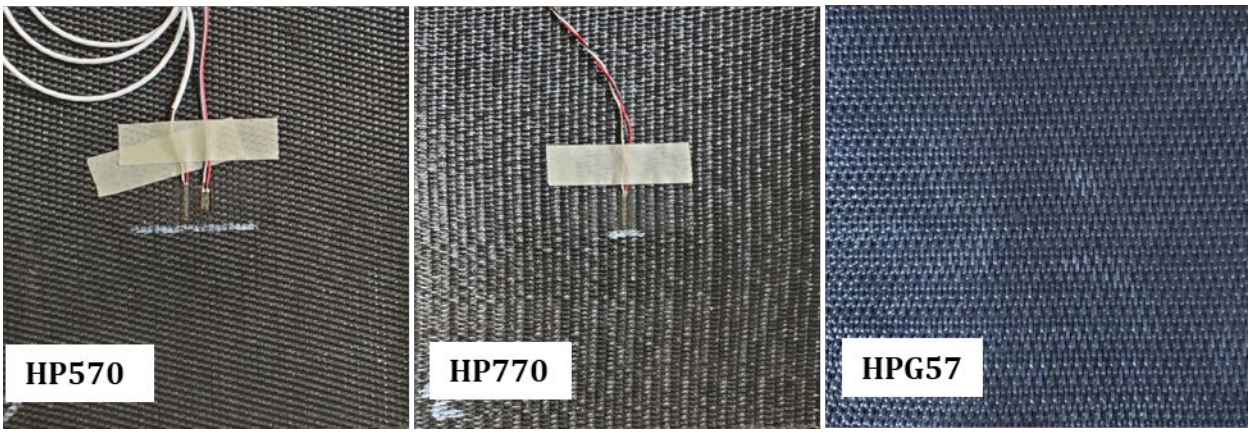


Figure 3-21. Picture of the geotextiles.

Table 3-9. Properties of geotextiles.

| Mechanical Properties | Test Method | Minimum Average Roll Value | |
|---|---|---|---|
| | | Machine Direction (MD) | Cross-Machine Direction (CD) |
| Mirafi HP 570 & TerraTex HPG 57 | | | |
| Tensile Strength (at ultimate) | ASTM D4595 | 4,800 lbs/ft | 4,800 lbs/ft |
| Tensile Strength (at 2% strain) | ASTM D4595 | 960 lbs/ft | 1,500 lbs/ft |
| Tensile Strength (at 5% strain) | ASTM D4595 | 2,400 lbs/ft | 3,000 lbs/ft |
| Mirafi HP 770 | | | |
| Tensile Strength (at ultimate) | ASTM D 4595 | 7,200 lbs/ft | 5,760 lbs/ft |
| Tensile Strength (at 2% strain) | ASTM D 4595 | 1,370 lbs/ft | 1,560 lbs/ft |
| Tensile Strength (at 5% strain) | ASTM D 4595 | 3,600 lbs/ft | 3,600 lbs/ft |

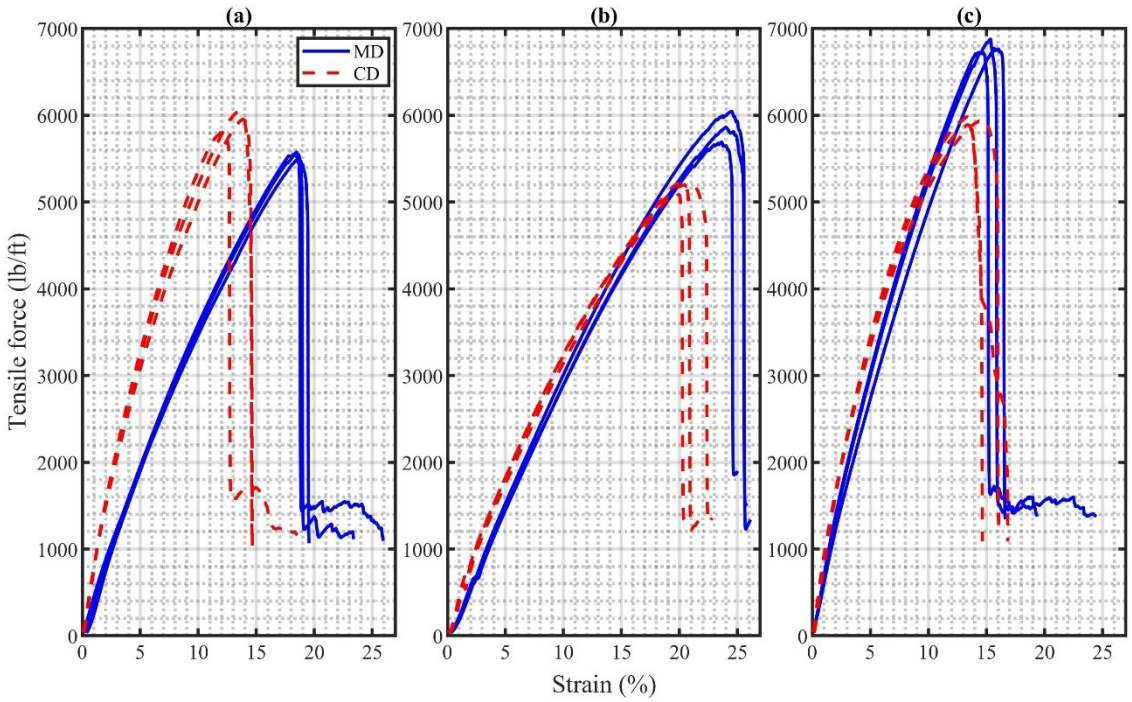


Figure 3-22. Results of uniaxial tensile tests of geotextile.
(a) HP570; (b) HPG5; (c) HP770.

### 3.1.3 Facing Blocks

Segmental retaining blocks (Figure 3-23) were used for the facing of the GRS piers. The blocks are manufactured by Oldcastle for Anchor Wall Systems and have approximate outside dimensions of 8 in x 18 in x 12 in and weight of 86 lbs. Some of the blocks were cut in order to achieve the pier layout. The blocks were cut with a wet concrete saw which resulted in smooth straight cuts as shown in Figure 3-24. Additionally, the “lug” or the raised portion on the tops of the blocks was removed from each block with a concrete grinder to make a flush surface as shown in Figure 3-25. As of September 2020, all GRS-IBS abutments in Florida have been constructed with these facing blocks.


Figure 3-23. Details of the segmental block.

Figure 3-24. Vertica straight face blocks after being wet cut.


Figure 3-25. Grinding the lug off the tops of the Vertica Straight Face blocks.

### 3.1.4 Footing

A reinforced concrete footing with a steel plate at the top was designed to be used as a loading platform. The footing without a steel plate is 36 in wide, 36 in long, and 11.125 in thick. The metal plate on top of the footing has the same plan area with a thickness of 1.5 in. The total thickness of the composite footing is 12.628 inches and has a total weight of 1485 lb. The concrete used was ready-mixed concrete and was supplied by Argos Ready Mix Supplier. It has a design compressive strength of 7 ksi in 27 days as per the supplier's specification. Footing's design, formwork and steel preparation, and casting of concrete footing were done at the University of Florida Structural Laboratory. The footing was designed for two-way and one-way shear, and flexural strength. Figure 3-26 shows the casting of footing. During casting, concrete was tested for slump following ASTM C 143 standard. The average slump height was 5.5 inches. Also, samples of concrete cylinders (Figure 3-27) were cast to be tested at different testing ages as per ASTM

C39 standard. The results of compressive strength at different testing ages are presented in Figure 3-28. Four threaded concrete anchors each with pull-out strength of 3.2 kips were installed after 28 days. The anchors provided attachment points for installing forged steel hoist rings used for lifting the footing.


Figure 3-26. Casting of a concrete footing.
(a) Pouring of concrete (b & c) Curing of concrete (d) Installation of anchor bolts (e) Testing the installed anchor by lifting (f) Finished footing with steel plate.


(a) (b)

Figure 3-27. Testing of concrete cylinders.
(a) Grinding of concrete cylinder; (b) Compressive test.

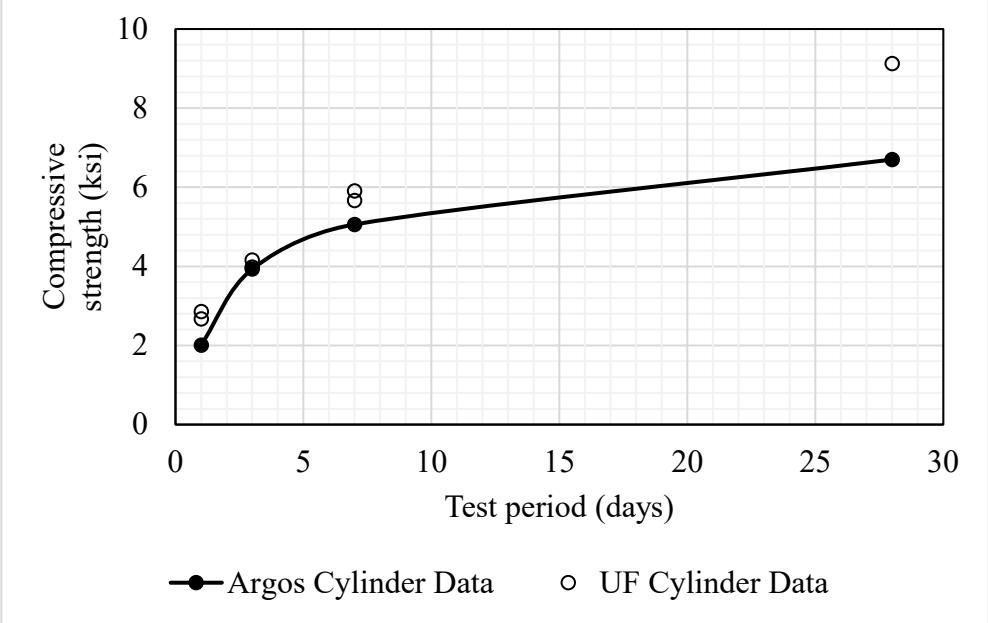


Figure 3-28. Concrete cylinder compressive strength versus time.

## 3.2 Test Conditions and Instrumentation

### 3.2.1 Test Layout

The layout of the GRS pier was determined based on a number of factors including the standard method developed by FHWA for performance testing, the conditions of the triaxial test, the particle size of the backfill, the vertical reinforcement spacing, the approved block sizes by FDOT and the size of the available reaction frame and jack. The dimensions of the pier were made greater than 6 times the maximum particle size and greater than 15 times the average particle size to alleviate the effects of particle size on the test specimen as recommended by the U.S. Army Corps of Engineers. Since FDOT does not allow the use of 4-inch blocks, the height of the pier was determined based on the approved block size of 8-inches, vertical reinforcement spacing, and the headroom between top of footing and the bottom of the reaction frame jack. Additionally, to mimic the triaxial condition, the height-to-width ratio was maintained to 2 throughout the tests. After several trials, the final layout of the GRS pier for 8-inch spacing is shown in Figure 3-29. The piers had a height-to-width (H/B) ratio of 2. The inside dimensions of the GRS pier were 36 inches wide (B) and 72 inches tall (H). With facing blocks, the width of the pier was 60 inches. By using an 8-inch-tall block, the pier had a total of 9 courses of segmental facing blocks (a total of 99 blocks required for one test). In each test, the pier had a bearing bed reinforcement at the upper two courses, where the reinforcement spacing was 4 inches. Table 3-10 shows the dimensions and test conditions of each GRS pier tested in this study.

Typically, in GRS-IBS structures, the upper three to five courses of blocks in the facing walls are filled with concrete to increase the confining pressure at the upper courses, as they are closer to the loading area. However, all the performance tests available in the literature have been conducted without concrete at the upper courses. Therefore, it was suggested to investigate how the GRS behavior would change in performance tests when the concrete fill is included. One test was conducted with aggregate fill at the upper three courses of blocks.

Table 3-10. Test conditions.

| Test No | Backfill Type | Reinforcement Type | $T_f$ (lb/ft) | $S_v$ (inch) | B (ft) | H/B |
|---|---|---|---|---|---|---|
| PT-1 | #57 stone | Biaxial woven geotextile [A] | 4,800 x 4,800 | 8 | 3 | 2 |
| PT-2 | #57 stone | Woven geotextile [B] | 7,200 x 5,760 | 8 | 3 | 2 |
| PT-3 | #57 stone | Biaxial woven geotextile [C] | 4,800 x 4,800 | 8 | 3 | 2 |
| PT-4 | RCA-GAB | Biaxial woven geotextile [A] | 4,800 x 4,800 | 8 | 3 | 2 |
| PT-5 | RCA-GAB | Woven geotextile [B] | 7,200 x 5,760 | 8 | 3 | 2 |
| PT-6 | RCA-GAB | Biaxial woven geotextile [C] | 4,800 x 4,800 | 8 | 3 | 2 |
| PT-7 | FGA | Woven geotextile [B] | 4,800 x 4,800 | 8 | 3 | 2 |
| PT-8** | #57 stone | Biaxial woven geotextile [A] | 4,800 x 4,800 | 8 | 3 | 2 |

Notes: [A] Mirafi HP570, [B] Mirafi HP 770, [C]TerraTex HPG 57.

** Block cells in the upper three courses of blocks contain concrete and rebar.

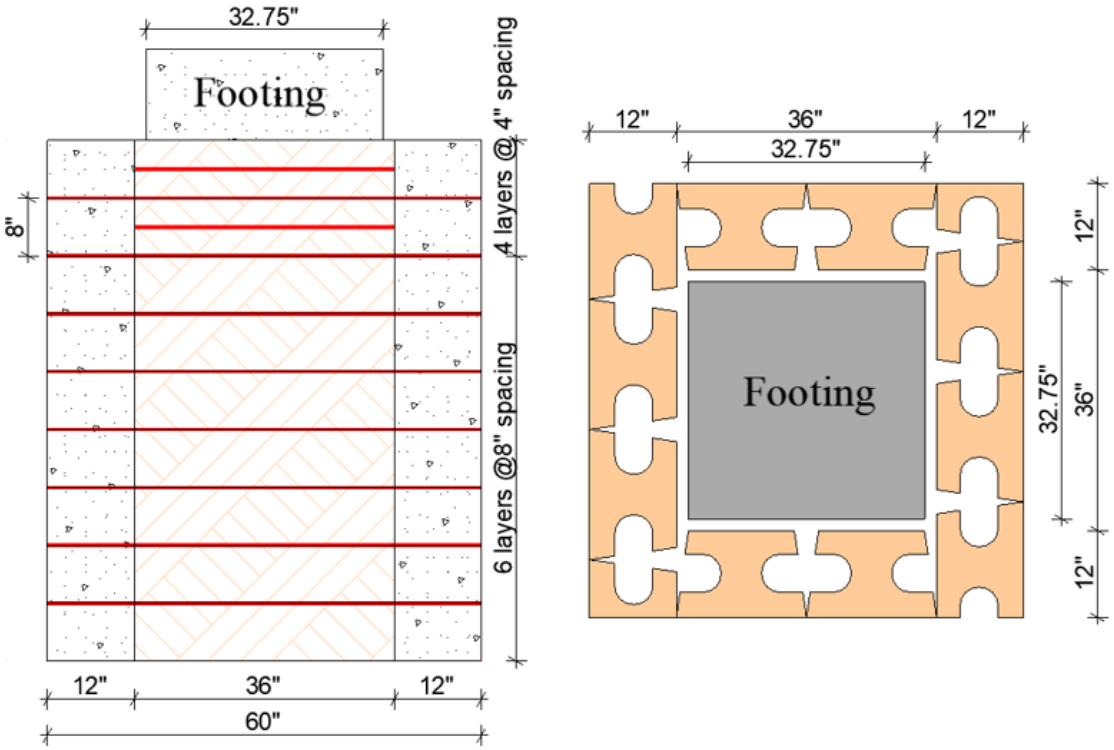


(a) (b)

Figure 3-29. Pier layout.
(a) Profile of the pier; (b) Plan view.

### 3.2.2 Construction

The construction and testing of the GRS pier took place at FDOT Marcus H. Ansley Structures Research Center. It is a bottom-up construction where the construction starts at the bottom and progresses upwards. To limit variations during the construction, procedures and steps were kept uniform and consistent including the number of passes with compactor, geometry check, and placement of aggregate. The step for constructing a pier is summarized as follows:

i. Since the strong floor was not level, a concrete grout leveling pad, 1.5 in thick was cast to level and protect the floor so the pier can be constructed on the leveled surface.

ii. The leveling pad was then cleaned. The inside and outside dimensions of the pier plan were marked following the drawings to make sure the pier is within the center of the reaction assembly.

iii. One sheet of geotextile was placed at the bottom to protect the leveling pad.

iv. After marking the pier's layout, the first layer of the blocks was placed as shown in Figure 3-30 and Figure 3-31. Due to the non-uniformity of the outside surface of blocks, lasers attached at the top of the reaction frame were used to check the alignment and squareness of the inside perimeter along the edge of the blocks.


Figure 3-30. Construction procedures for PTs 01-07.


Figure 3-31. Construction procedures in PT-08.

v. Straps were put around the blocks to hold them in place during compaction. The straps were removed later before starting the test.

vi. Because of the smaller compaction power of the compactor used, the aggregates were placed in two lifts of 4 inches. In the first five courses of blocks, the aggregates were placed using supersack. In the upper courses, due to the low headroom between top of pier and beam of the reaction frame, a concrete dumper was used to place aggregates. The aggregates were compacted until the required density was achieved with a minimum of

four passes in each direction. In all courses, the weight of the aggregates was measured before placement and compacted volume was determined after compaction. Also, for piers with RCA-GAB backfill, nuclear gauge density was used to check the density. For each lift, the compacted density of the aggregate was calculated as the measured weight of aggregates placed divided by the internal volume occupied by the aggregates. Figure 3-32 shows the measured densities. In the first test (PT-01), aggregates in the first two lifts were compacted using a standard 18-inch-wide, gas-powered vibratory plate compactor. However, it was observed difficult to control the compactor due to small area of compaction relative to compactor's size, therefore a new compactor, a 10.2-inch-wide gas-powered vibratory compactor was used in the remaining lifts and tests afterward. It is manufactured by YardMax with model number 152F-1. The compactor was adequate to achieve the target density at a 4-inch lift.

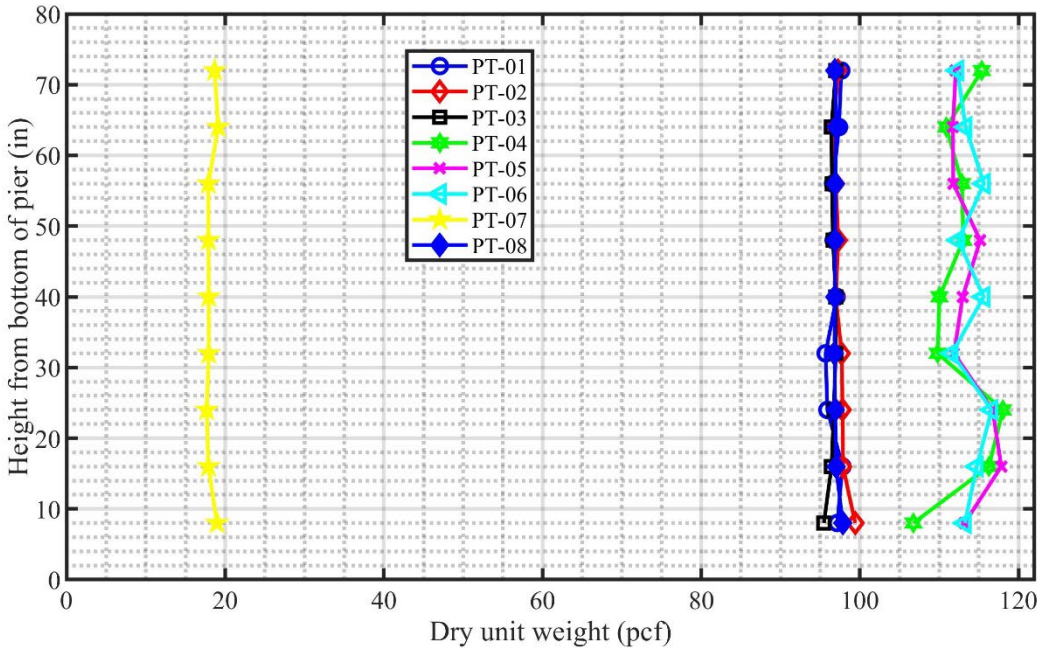


Figure 3-32. Measured densities during construction of each lift.

vii. After ensuring the fill met the specification, the remaining 4-inch lift was placed and compacted until it flushed with the top of the block. It was then leveled, and excess particles were removed.

viii. A layer of geotextile was laid down to cover the entire area of aggregate and 100% of the width of facing blocks. For those with strain gauges and fibers, connection wires were aligned along the center of geotextile to the outside of the blocks so that they can later be connected to the data logger. Connecting wires were protected by using a flexible plastic tube and a thin layer of fine sand. Grooves were drilled across the blocks for wire outlets. The wires were protected against scratches from block movement by using a flexible plastic tube. Also, for wires inside the aggregate, a layer of fine sand was placed on top to protect them from coarse particles.

ix. Then the second course of blocks was placed, and the layout was rotated at 90 degrees clockwise at each layer as you move up to create a staggered pattern. At each course, the verticality and center of the pier were checked.

x. Steps were repeated until the final height of the pier was reached.

xi. Due to differences in stiffness of some of the geotextiles in MD and CD, the geotextiles were placed in an alternating pattern as you move up with each layer rotated 90 degrees to prevent failure of the GRS pier in the direction of the geotextile with lower stiffness.

xii. The straps were then removed prior to placement of lateral displacement transducers.

xiii. Then, the lateral displacement transducers were installed.

xiv. The data were then collected from pressure cells, strain gauges, and displacement transducers before footing placement.

xv. For PT-08, during each concrete pouring, a sample was taken for compressive strength testing. It was tested for different testing ages (3 days, 15 days and on the day of pier testing which was 22 days). Figure 3-33 shows the compressive strength of the concrete fill.

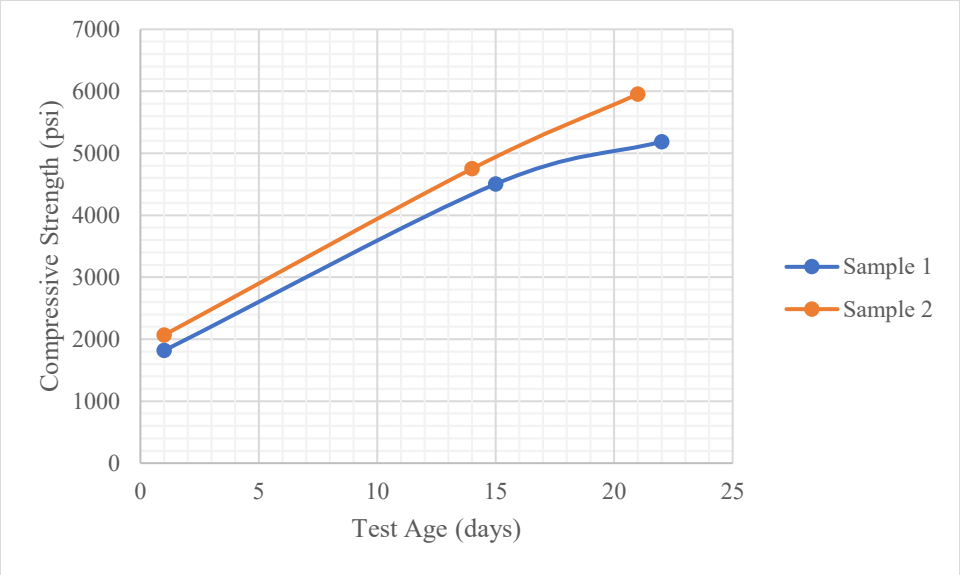


Figure 3-33. Compressive strength of the concrete fill.

xvi. A concrete footing with a steel plate was then placed on top of GRS pier. It was centered to avoid introducing eccentric loading. Then the hydraulic jack, load cells, and vertical displacement transducers were assembled for testing.

xvii. The construction and instrumentation of the pier took an average of 4 days for two people.

### 3.2.3 Instrumentation

To investigate the performance of the GRS pier during the test, the pier was externally and internally instrumented with several sensors to monitor vertical and lateral deformations, axial loads applied, reinforcement strains in the geotextiles, vertical earth pressure at the bottom, and the lateral earth pressures along the facing block located at the mid-height of the pier.

#### 3.2.3.1 Vertical Movement

The vertical settlement of the top of the footing was measured using four vertical optoelectronic sensors (Distance sensor BOD 66M-RA01-S92-C). The sensor's targets were placed along both sides of the footing as shown in Figure 3-34.

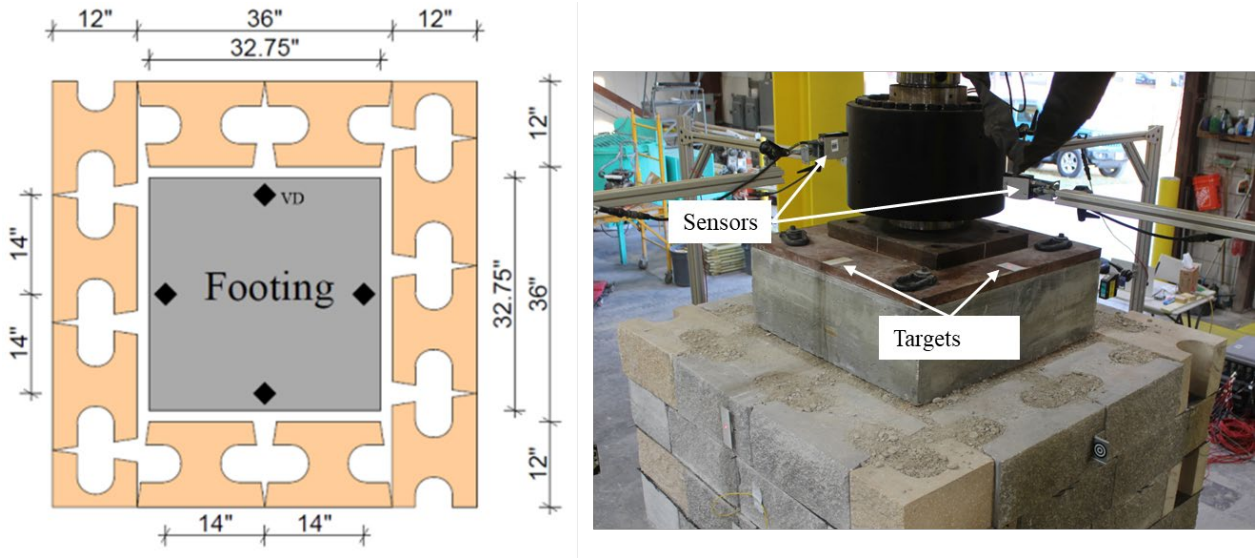


Figure 3-34. Layout of vertical displacement sensors.

### 3.2.3.2 Lateral Movement

Both walls were instrumented with displacement sensors to monitor their lateral deformations during the test. Lateral displacements were measured at five points along the facing walls using laser displacement sensors (MTI Microtrak 3 Series, model LTS 300-200) and a camera system (Imetrum Video Gauge Dynamic monitoring stations (DMS)). Laser displacement sensors were used in the north and south walls while the camera system was used for the east and west walls. Figure 3-28 shows the layout of lateral displacement sensors.

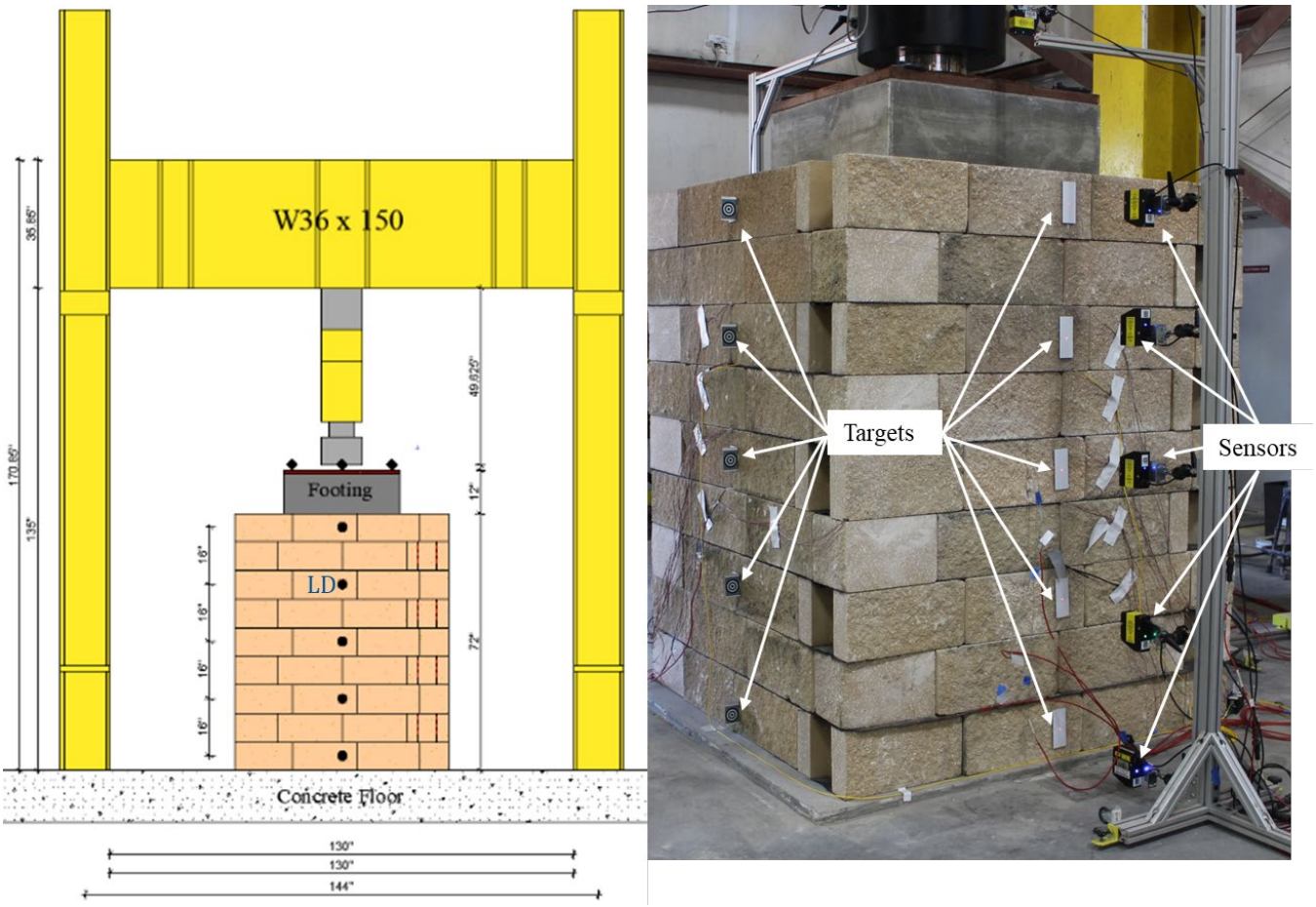


Figure 3-35. Lateral displacement measurement.

### 3.2.3.3 Reinforcement Strains

Geotextiles were instrumented with strain gauges (model: EP-08-250BG-120 and EP-08-500GB-120) and fiber optic cables to measure tensile strains developed during loading. Only geotextiles in the PT-1 were instrumented with strain gauges and the sixth geotextile layer was instrumented with additional fiber optic cables to measure the strains for comparison with strain gauge measurements. The instrumentation layout is shown in Figure 3-36. To develop the calibration factor (ratio of global strain to the measured local strain at the same tensile load), a geotextile specimen was tested in an extension test following ASTM D4595 standard for each geotextile type, both in the machine and cross-machine direction. The calibration factor calculated ranges from 1.3 to 2.1.

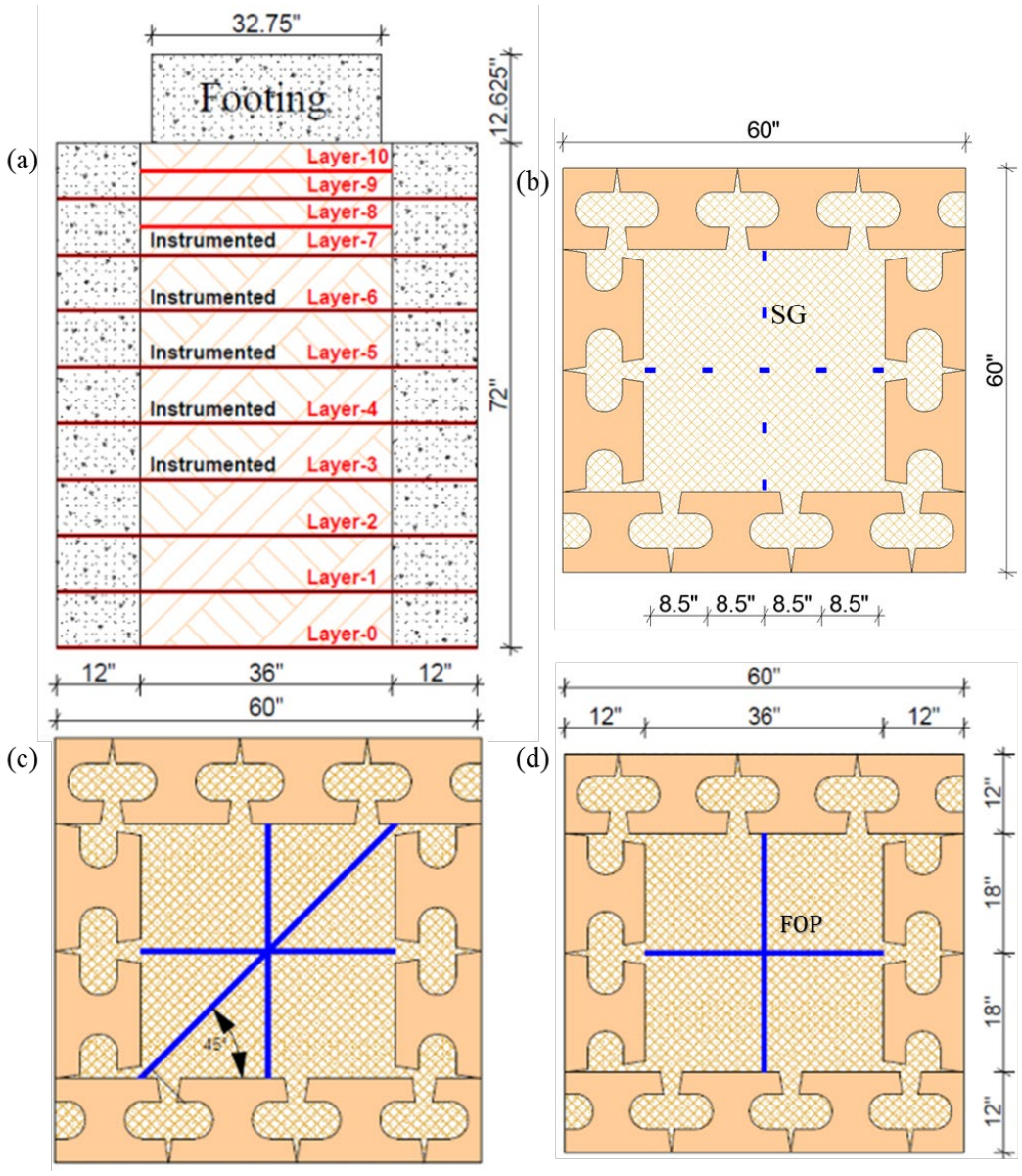


Figure 3-36. Installation of strain gauges and fiber optic cables.

### 3.2.3.4 Lateral Earth Pressure

In each test, a block at the mid-height of the pier was instrumented to monitor the lateral earth pressure distribution across the geosynthetic layers. Four miniature pressure transducers (TML PDB-PB) were inserted to be flush with the block facing and equally spaced along the block height. Since the backfill was aggregate, a cover of confined fine sand was installed over the line

of transducers for lateral stress transfer. The ratio of transducer's diameter (d) to median particle diameter (d50) was 38, which is greater than 10 recommended by Dave and Dasaka (2011). The goal was to measure the pressure distribution between subsequent geotextile layers. Figure 3-37 shows the instrumented block.


(a) (b) (c)

Figure 3-37. Lateral earth pressure transducer.
(a) Section view; (b) Transducers installed; (c) Block with transducers on the pier.

### 3.2.3.5 Vertical Earth Pressure

All piers except PT-1, PT-2, and PT-3 were instrumented with a vertical earth pressure cell to monitor earth pressure during construction and axial loading. A 9-inch diameter earth pressure cell (Geokon Model 4800) was used. Dave and Dasaka (2011) recommends the ratio of cell diameter (d) to median particle diameter (d50) to be greater than 10 to avoid eccentric, non-uniform and point load effects during measurement of earth pressure. Table 3-11 shows the values of d/d50. FGA has d/d50 less than 10. All of the piers had the earth pressure cell positioned 4 inches from the bottom (in the middle of the first course), except for PT-05 which was located at the bottom (under first course). Pressures were recorded at end of each lift placement and continuously during axial loading. Figure 3-38 shows the earth pressure cell at the bottom of the pier before placement of backfill.

Table 3-11. Ratio of cell diameter (d) to median particle diameter (d50).

| Aggregate Type | $d/d_{50}$ (in) |
|---|---|
| No. 57 | 15 |
| RCA-GAB | 45 |
| FGA | 6.9 |

Figure 3-38. Vertical earth pressure cell.

### 3.2.4 Loading and Data Collection

For loading, a reaction frame consisting of four columns (W14X90) with a jacking beam (Double W36X150) at the FDOT Structures Research Center in Tallahassee, Florida was used. The load was applied using a 1,000-kip hydraulic jack (Enerpac RR-40018) with a maximum stroke of 18 inches and a retracted height of 49.6 inches. It was measured using a 1,200 kips load cell mounted on the jack. The load was applied at an increment of 5 kips up to the service limit (4000 psf-equivalent to 30 kips) and after the service limit, a load increment of 20 kips was applied until failure was achieved, then unloaded in about three equal increments. In each load increment, the load was held for approximately five minutes. Data were recorded continuously at a sampling frequency of 2 Hz. Instruments were read with a multi-channel data acquisition system (NI cDAQ-9188 having 8 slots). Figure 3-39 shows the instrumented pier before the test.

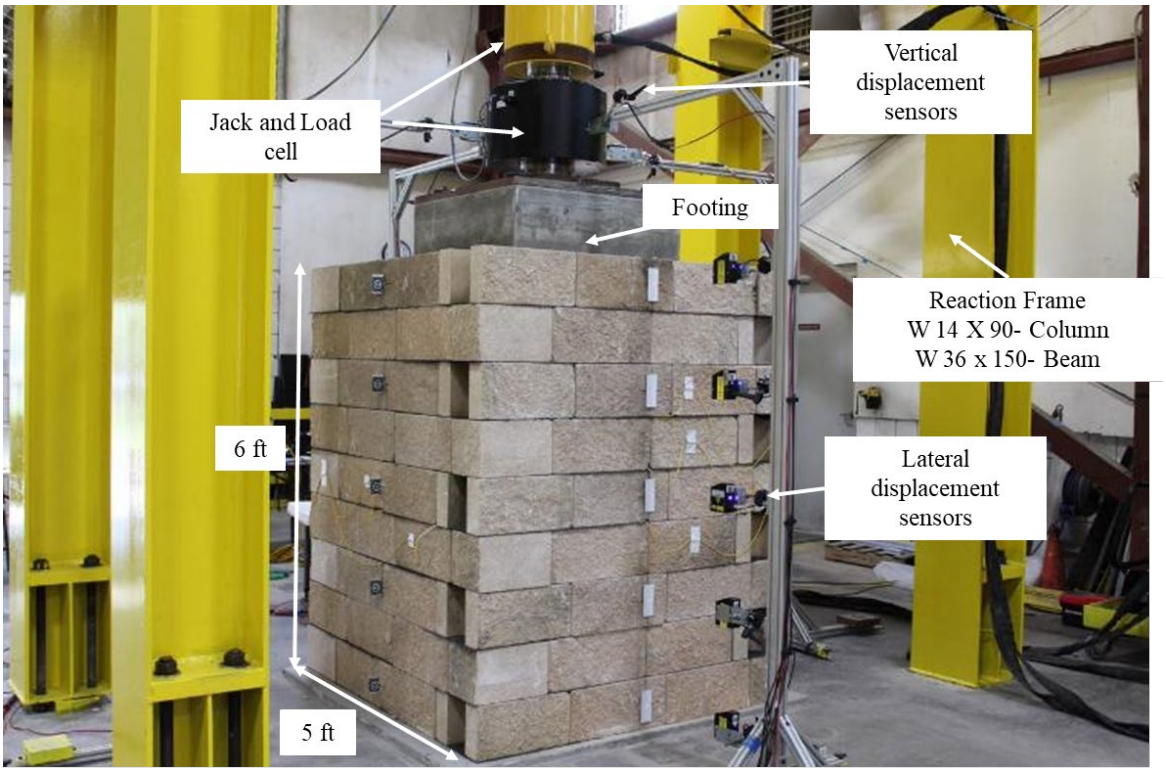


Figure 3-39. Completed and instrumented pier before testing.

# 4 EXPERIMENT RESULTS AND DISCUSSION OF RESULTS

## 4.1 Introduction of Chapter 4

The empirical approach, based on performance testing, is currently one of the design methods recommended by the FHWA for the design of GRS-IBS. It involves the use of stress-strain curves developed from performance tests. FHWA has developed a database of performance test results that can be used in the design. However, the database developed by FHWA only has direct applicability to materials used in the mid-Atlantic and northeast regions of the United States. To broaden its applicability, materials typically used in the southeast region of the United States should be tested. This chapter presents the experimental results of eight performance tests on GRS piers built with FDOT approved backfill, geosynthetics, and facing blocks. Load-deformation behavior, lateral displacement and earth pressure measurements are presented and discussed.

## 4.2 Capacity and Vertical Settlement of the Footing

The performance of each pier was evaluated by measuring the vertical strain response, which was calculated as the average of the vertical settlement from four linear displacement sensors at the top of the footing divided by the height of the GRS pier. The applied vertical stress was determined by dividing the load applied by the plan area of the footing. The results of the performance tests on all the GRS piers (Table 3-10) are presented in Figure 4-1, and the maximum capacities and corresponding vertical strains are presented in Figure 4-2 and Table 4-1. Figure 4-7 and Figure 4-8 show the PT-02 pier after completing the test. In this study, the maximum measured capacity refers to the maximum applied pressure at which GRS pier no longer sustain the applied load.

Comparing performance between piers with the same reinforcement shows the influence of backfill and their properties (unit weight, friction angle, etc.). The results in Figure 4-3 show GRS piers built with RCA-GAB exhibit higher stiffness and capacity than those with No 57 and FGA for all the reinforcement types. The RCA-GAB is a well graded aggregates and higher unit weights can be achieved through compaction, leading to higher stiffness, friction angle, and shear strength than the open graded aggregates. As a result, at the same vertical applied stress, the tests with RCA-GAB experience lower vertical settlement than those with No 57 and FGA. From Figure 4-

3, at FHWA service limit applied pressure of 4 ksf, PT-05 has a vertical strain of 0.25% while PT-02 and PT-07 have 0.51% and 0.97%, respectively, less than the 1% service limit for vertical strain (18.9 ksf for PT-05, 8.2 ksf for PT-02, and 4.1 ksf for PT-07). This indicates that the use of RCA-GAB backfill in GRS composite piers can be an effective way to improve the performance of these structures.

The effect of reinforcement tensile strength is more pronounced in the ultimate capacity for when GRS piers with the same backfill type, but different reinforcement strengths are compared as shown in Figure 4-4. GRS pier constructed with 7,200 lbs/ft reinforcement strength geotextile has higher capacity than the ones constructed with a 4,800 lbs/ft reinforcement, given the same backfill type is used. Higher reinforcement strength provides more resistance to the lateral stresses that develop during axial loading. This increased resistance leads to an increase in the shear strength of the backfill, which in turn leads to a higher load-carrying capacity for the pier. For example, PT-02 showed higher capacity than PT-01 and PT-03. Similarly, PT-05 showed higher capacity than PT-04 and PT-06. Similar observation was reported in several studies such as Wu et al. (2006), Pham (2009), Nicks et al. (2013), and Wu et al. (2013). This result confirms that increasing the strength of the reinforcement can significantly improve the load-carrying capacity of GRS piers, highlighting the importance of proper design and selection of reinforcement material for optimal performance and safety of GRS structures.

The reinforcement stiffness and surface texture of the geotextile reinforcement play a role in the performance of GRS piers, as evidenced by the differences in the stress-strain behavior from Figure 4-5 between piers constructed with HP570 and HPG 57, given the same backfill is used. For instance, PT-01 had higher capacity than PT-03. During PT-03, a small footing rotation was observed and the maximum eccentricity was calculated to be 1.12 inches. This rotation could potentially contribute to the reduced stiffness and capacity observed in PT-03 when compared to PT-01. A comparison of PT-04 and PT-06 also showed the influence of geotextile stiffness and surface texture. PT-04 had higher capacity than PT-06. Both HP570 and HPG57 have the same tensile strength. The differences in the stress-strain behavior between piers constructed with HP570 and HPG 57 geotextiles is attributed to the difference in tensile stiffness modulus between the HPG 57 and HP570. Wide width tensile tests showed that HPG 57 and HP 570 has a stiffness of 23,814 lbs/ft and 39,501 lbs/ft, respectively in MD. Lower stiffness for HPG 57means HPG 57 undergoes large deformation leading to lower global stiffness observed in the GRS piers

constructed with HPG 57. Also, from interface shear strength test results, HP570 has rougher surface texture than HPG57, leading to a stronger bond between the soil and geotextile and earlier mobilization of reinforcements. This is supported by comparing the stress-strain behavior of PT-01 and PT-03 piers after 0.5 percent vertical strain. Interface shear strength tests with No 57-aggregate showed HPG 57 and HP 570 have interface friction angles of 37.95 degrees and 42.23 degrees, respectively. A lower interface friction angle in HPG 57 means that less soil stress is transferred to the geotextile through the interface, resulting in less additional strength to the soil and longer time for the reinforcements to be fully mobilized.

The stress-strain behavior comparison between PT-01 and PT-08 reveals the influence of concrete fill as shown in Figure 4-6. Both tests employed similar backfill, geosynthetics, and facing blocks. However, in PT-08, the top three courses included concrete fill and rebar. Initially, the stress-strain behavior of PT-08 exhibited a stiffer response compared to PT-01 until reaching a vertical stress of approximately 7.25 ksf. This effect is due to the additional confinement provided by the concrete fill and rebar, which creates a more robust structure for the upper courses. However, as the load increased further, the bond between the concrete and blocks weakened, leading to cracks, especially in the blocks. This occurrence can be attributed to the possibility that the blocks have lower compressive strength compared to the concrete fill. Post-test observations revealed that most of the cracks were found in the blocks rather than the concrete fill, supporting this notion. Additionally, the presence of rebars in the concrete fill contributes to lateral confinement. Once the blocks start to crack, the load-deformation behavior shifts to that of a GRS pier without concrete fill. This transition becomes apparent through a sudden decrease in stiffness for PT-08. The stiffness for PT-08 is surprisingly less than that of PT-01 after the 7.25 ksf applied vertical stress, and the ultimate capacity of PT-08 is also less than that of PT-01. This could be due to the rupture of more geotextiles in PT-08 than in PT-01 tests. The upper geotextile layers in PT-08 are subject to higher connection strength due to the use of concrete fill and rebar in upper block courses. When cracks start to develop in the blocks, these layers are subjected to more stress, leading to less capacity and stiffness observed at higher applied vertical stresses.

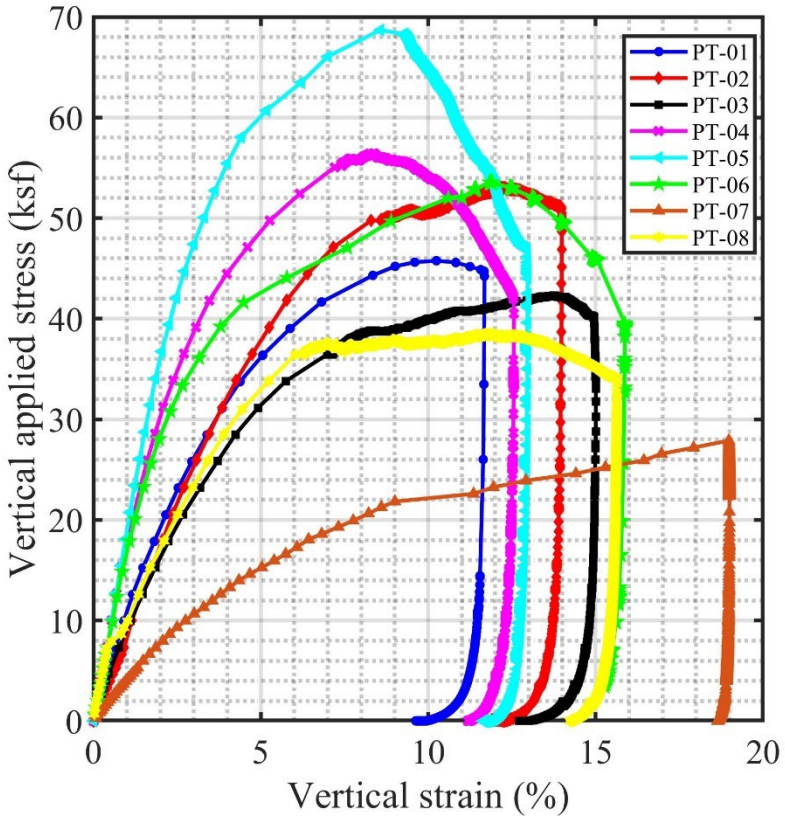


Figure 4-1. A plot of applied vertical stress versus average vertical strain for both tests.

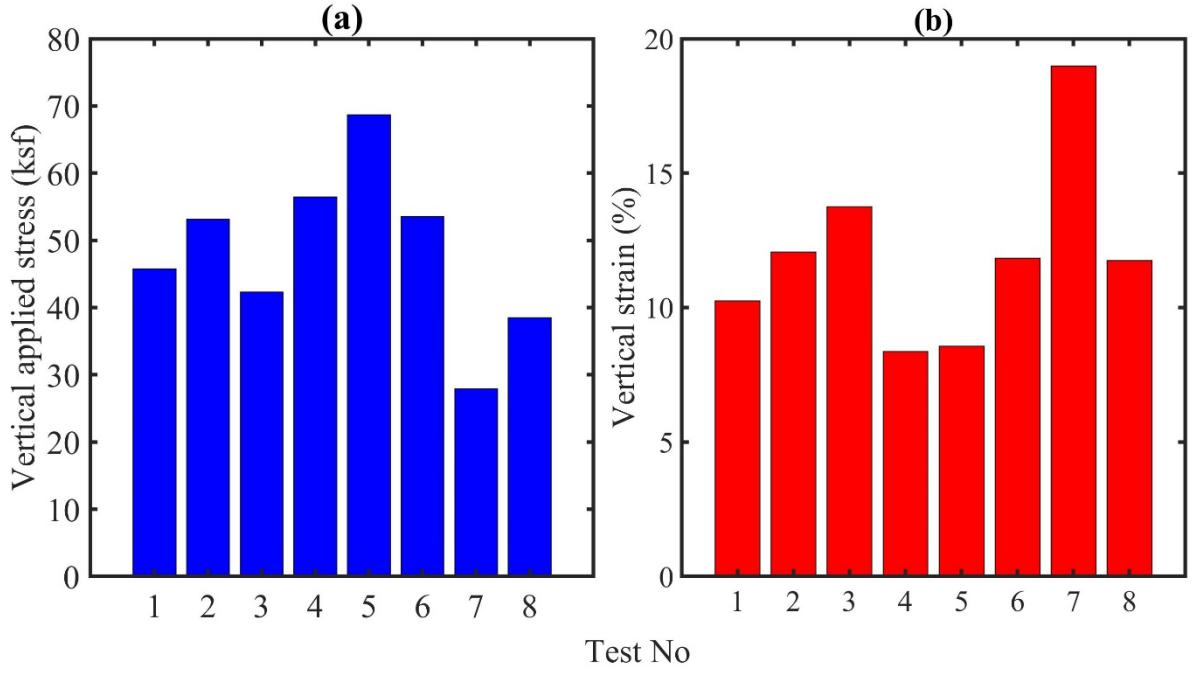


Figure 4-2. A plot of ultimate capacities and corresponding vertical strain versus test number.

Table 4-1. Measured ultimate capacities and corresponding vertical strain.

| Test No. | Strain (%) | Ultimate Vertical Capacity (ksf) |
|---|---|---|
| PT-01 | 10.24 | 45.77 |
| PT-02 | 12.06 | 53.13 |
| PT-03 | 13.75 | 42.29 |
| PT-04 | 8.37 | 56.42 |
| PT-05 | 8.57 | 68.70 |
| PT-06 | 11.84 | 53.55 |
| PT-07 | 18.98 | 27.89 |
| PT-08 | 11.75 | 38.45 |

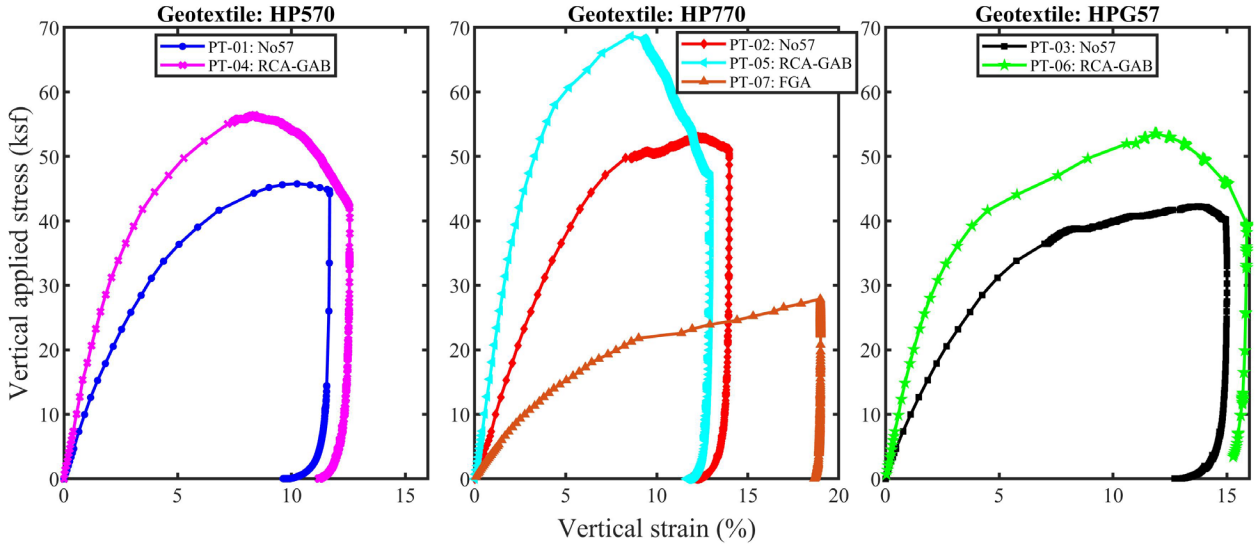


Figure 4-3. Influence of backfill strength properties.

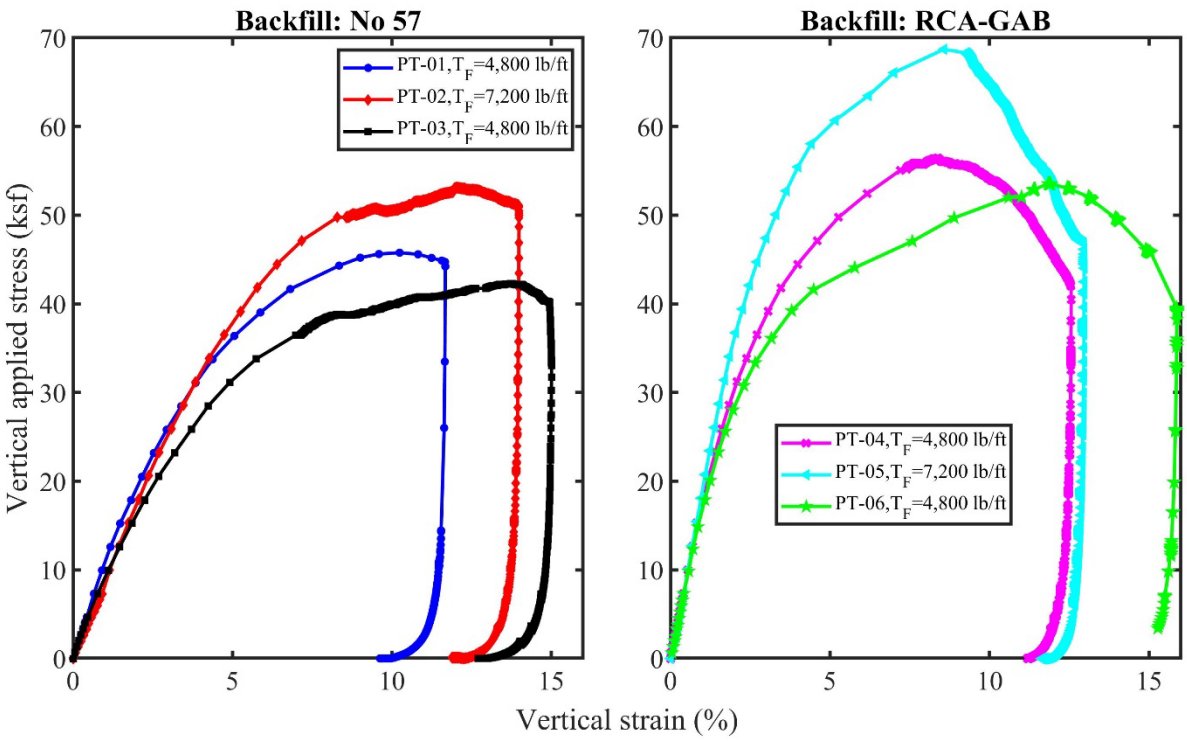


Figure 4-4. Influence of reinforcement strength.

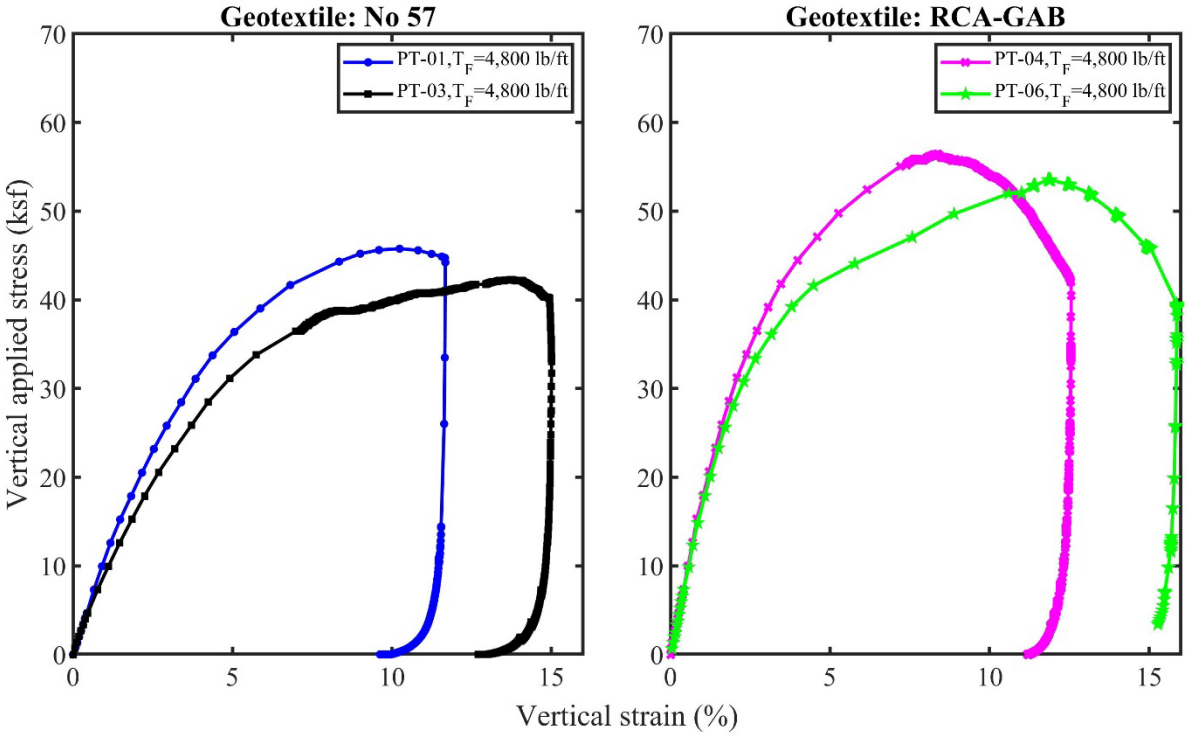


Figure 4-5. Influence of reinforcement stiffness.

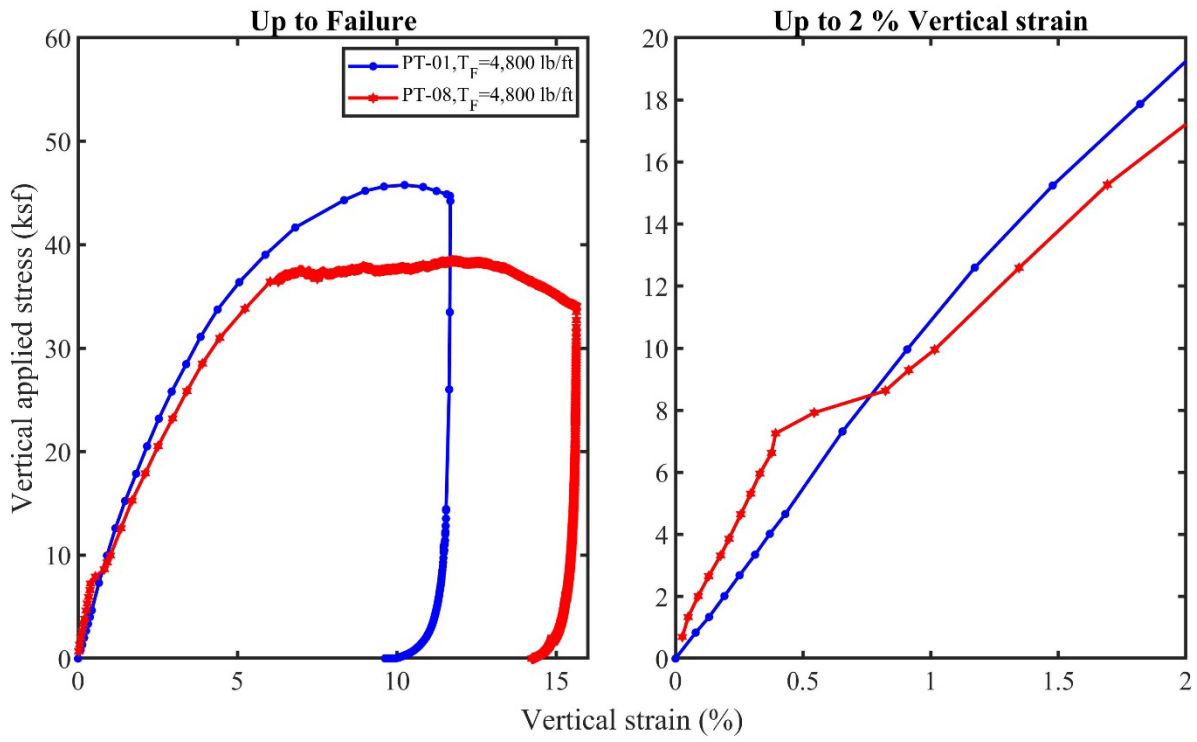


Figure 4-6. Influence of concrete fill.

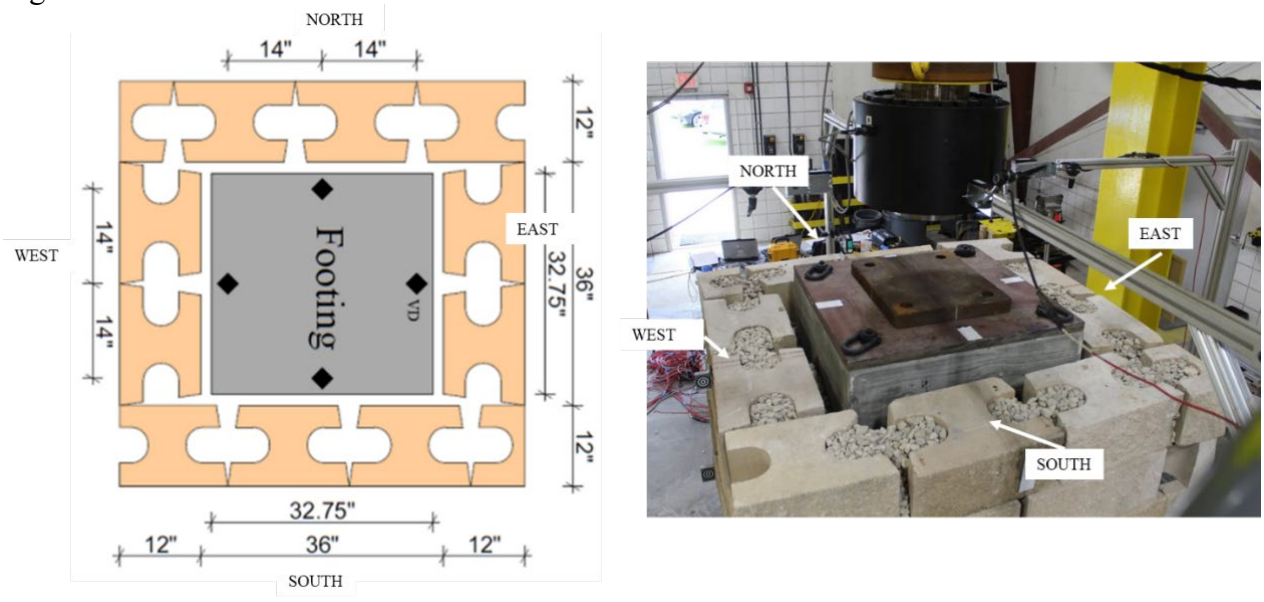


Figure 4-7. A top view of the failed pier after the PT-02 test.

Figure 4-8. A photo of the failed pier after the PT-02 test.

### 4.3 Lateral Displacement of the Facing Walls

The typical lateral displacement profile of each facing wall of the pier is shown in Figure 4-9 and Figure 4-10 for PT-02 and PT-05, respectively. The lateral displacement in all walls increases with an increase in the applied vertical stress. For each respective pier, the lateral displacements of each facing wall appear to be the same in magnitude and profile shape, especially at the initial loading. However, as the loading increases, the magnitude of the lateral displacement starts to increase more on the failure sides. For instance, for PT-02, at failure, the magnitude was greatest on the north and east sides. This is likely where the failure wedge moved to, as it was difficult to establish the orientation of the failure plane for piers tested in this study, especially for those constructed with No 57 stone. To compare the behavior of one pier with another, the average displacement of all four sides was taken and represented as a single profile for each pier.

The average lateral displacements of all the pier facing walls at different applied vertical stress are shown in Figure 4-11 and Figure 4-12. In all tests, the lateral displacement of each wall

increases with an increase in applied vertical load. At lower loads for all piers, except for PT-07 (FGA backfill), the displacement curve is almost linear with wall height and with maximum displacement at the top. As the load increases, the lateral displacement becomes more non-linear. With more load applied, the position of maximum displacement shifts from the top towards it's maximum near two-thirds of the wall height. At the maximum applied vertical stress, the maximum displacement for all the piers was around 52 inches from the bottom of the pier (H = 72 inches). It was also observed that the top portion of the walls moved inwards as the load approached failure. This is likely due to the maximum downward displacement of the geotextiles relative to the blocks at the upper layers, causing the sheets to pull the blocks inward because of friction between the geotextile and the block.

Like the vertical deformation behavior, the results also show that the lateral deformation behavior is influenced by the properties of the backfill material used, as shown in Figure 4-13. At the same applied vertical stresses, the wall facings in piers constructed with RCA -GAB showed the least lateral movement than the piers with No. 57 and FGA. This is due to the higher stiffness of the RCA-GAB (higher compacted unit weight), as shown in Figure 3-5 and Figure 3-6, which results in less deformation, or volumetric straining. Also, higher shear resistance through the compacted unit weight of the RCA-GAB backfill carries more of the internal lateral stress and thus reduces lateral deformation.

The comparison between PT-01 and PT-03, and between PT-04 and PT-06 shows differences that indicates the influence of the different geotextile surface textures on lateral deformation. Between the piers with the same backfill, the two reinforced with HP570 have smaller lateral displacements than those constructed with HPG57. Tests on HPG57 showed less interface friction with soil and between with the facing block. The smoother interface of the HPG57 provided less lateral restraint of soil, leading in part to larger lateral displacements.

Also, it is expected that reinforcement stiffness plays a role in lateral deformation, with an increase in stiffness leading to a decrease in lateral displacement. The comparison between PT-01 and PT-03, and between PT-04 and PT-06 showed that the stiffness has a significant influence on the lateral deformation as shown in Figure 4-14. Using the same backfill, piers reinforced with HP570 have lower lateral displacements than those constructed with HPG57. The higher stiffness of HP570 caused the geotextile to undergo less deformation which led to lower lateral

displacement of the facing walls. However, when piers constructed with HP570 and HP770 are compared, no clear conclusion can be drawn from the comparison of the tests only. For example, geotextile used in PT-01 has a rough surface texture and lower stiffness, while the one used PT-02 has a smooth surface texture and higher stiffness. At the service limit load, the average maximum lateral displacement was slightly higher in PT-02 than in PT-01, but as the load increased, the displacement between the two tests kept interchanging. The benefits of interface properties versus reinforcement stiffness becomes difficult to isolate.

The use of concrete fill in the top three courses was also found to influence the lateral deformation of the GRS pier, as shown in Figure 4-15. A comparison of the lateral displacements in PT-01 and PT-08 (No. 57 and HP570) reveals that the maximum lateral displacement of the facing walls was consistently lower in PT-08 than in PT-01 throughout the loading process. This outcome is expected because the presence of concrete fill and rebar increases the confinement pressure, providing greater restraint against lateral movement. Additionally, the concrete fill has an impact on the lateral displacement profile. Unlike in other tests, at smaller loads, the maximum lateral displacement in PT-08 does not occur at the top of the walls but rather outside the location where the concrete fill was placed. For a significant portion of the loading process, it was consistently observed that the position of maximum displacement was 52 inches from the bottom. The use of concrete fill increases the confining pressure at the top courses which allows the applied load to be transferred deeper into bottom layers unlike the ones with no concrete fill. This causes the deeper soil to experience more stress starting at lower loads which causes higher deformation than the top layers. When the applied vertical pressure was less than 7.3 ksf, maximum lateral displacement was at the bottom course of the block. Around applied vertical pressure of 7.3 ksf, the blocks at the top started cracking causing a loss of confining pressure at the top which leads to the shift in the lateral displacement with more displacement occurring at the top courses of the blocks. As the applied load keeps increasing, the profile changes and the maximum displacement moves at 36 inches from the bottom.

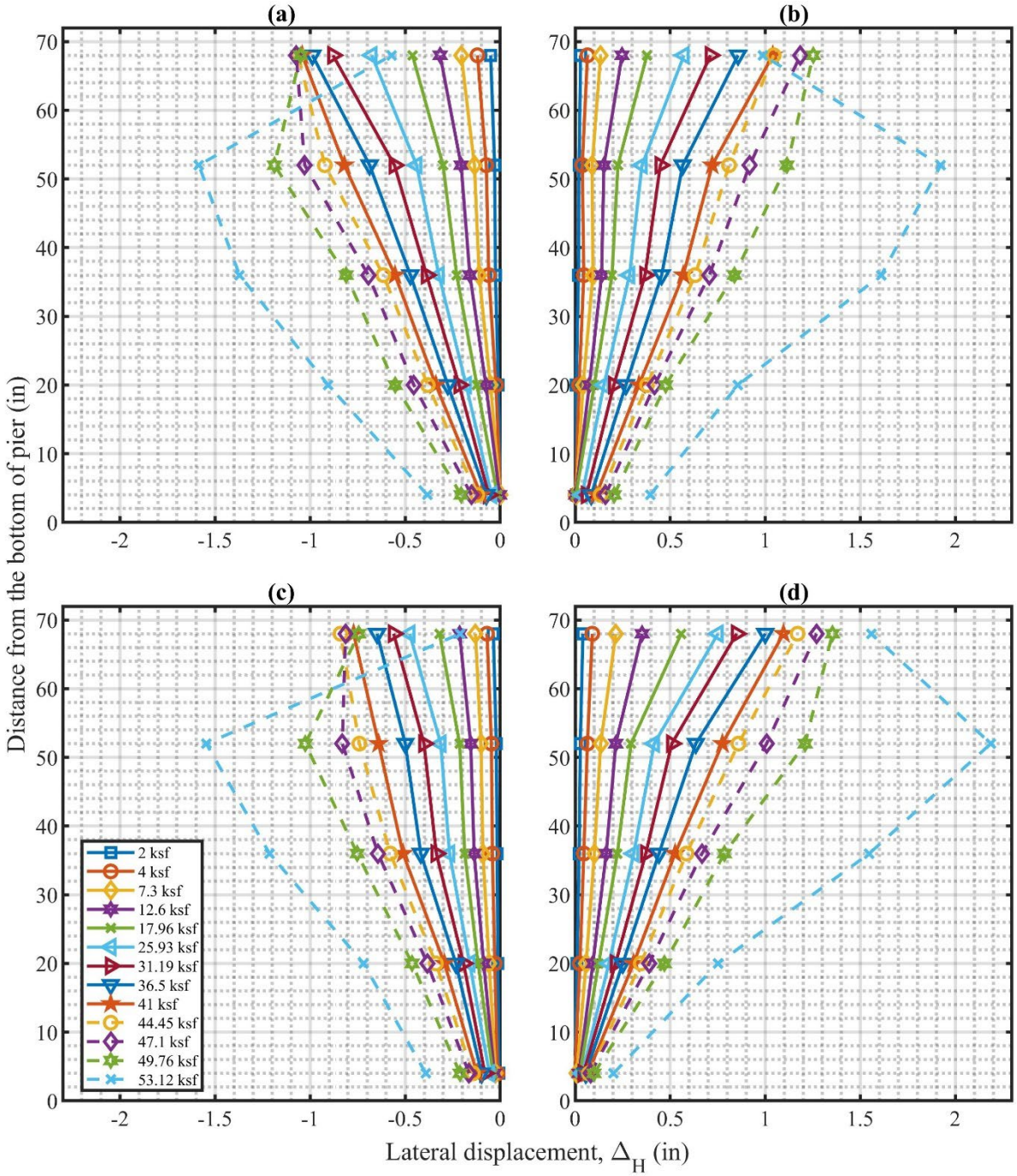


Figure 4-9. Measured lateral displacements along the facing walls for PT-02.
(a) South wall; (b) North wall; (c) West wall; (d) East wall.

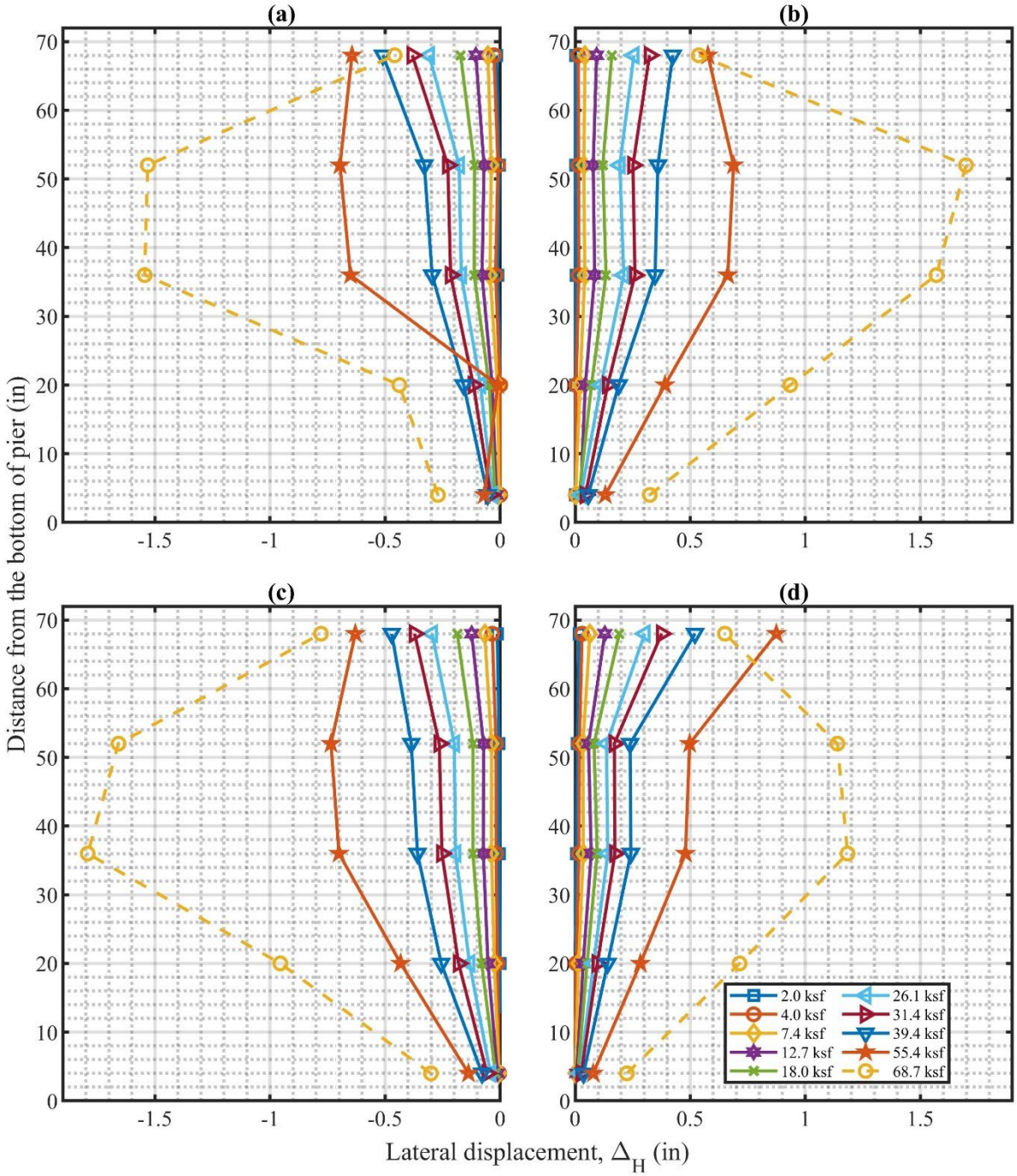


Figure 4-10. Measured lateral displacements along the facing walls for PT-05.
(a) South wall; (b) North wall; (c) West wall; (d) East wall.

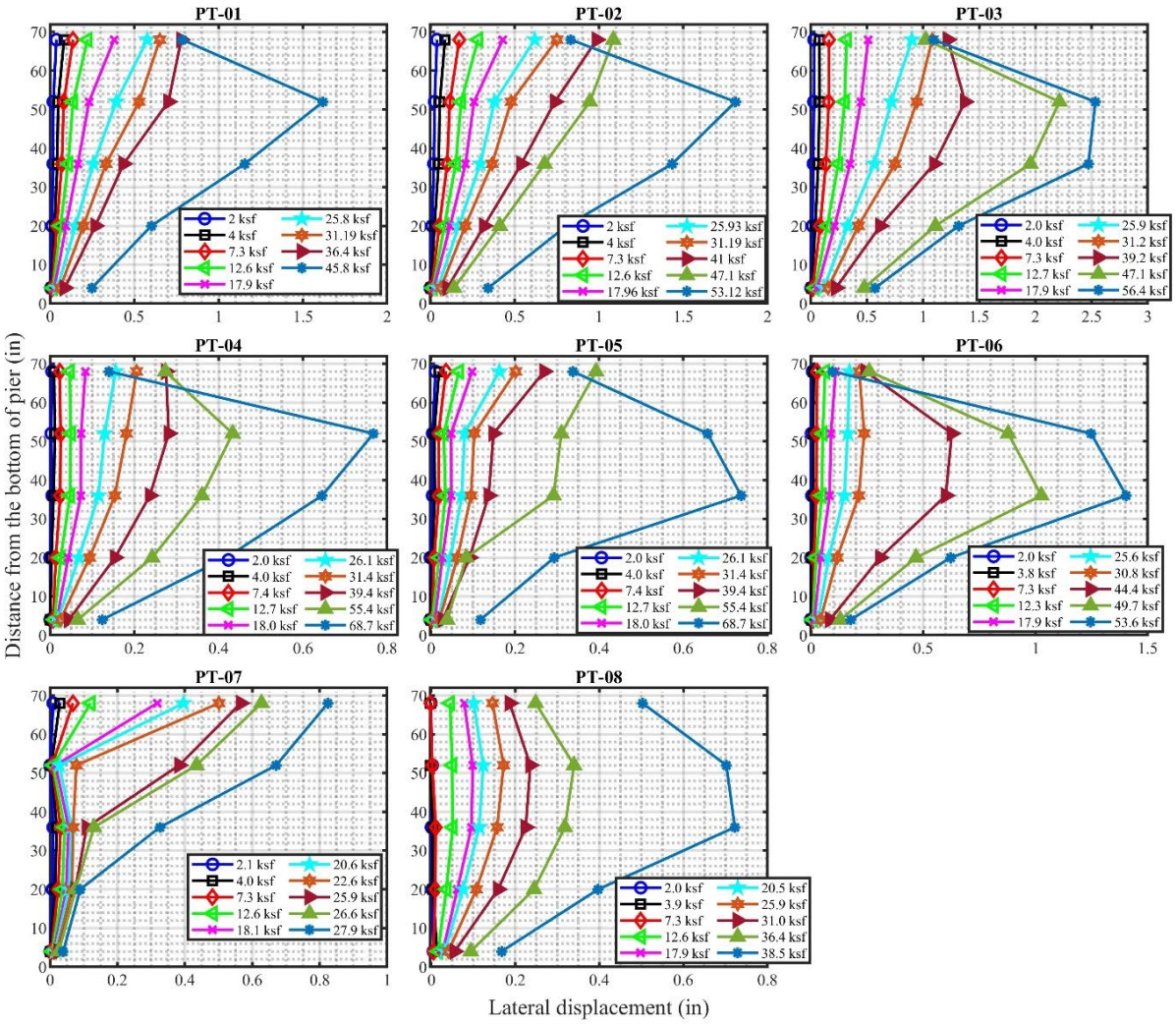


Figure 4-11. Measured lateral displacements along the facing walls for different applied vertical stresses.

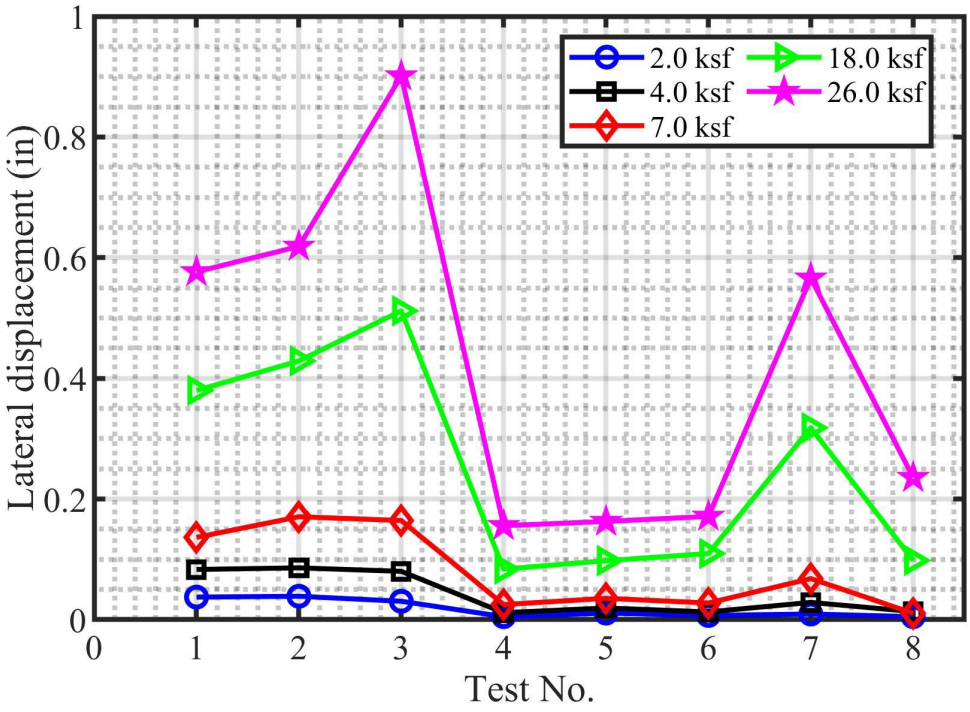


Figure 4-12. Maximum measured lateral displacements along the facing walls for different applied vertical stresses and pier tests.

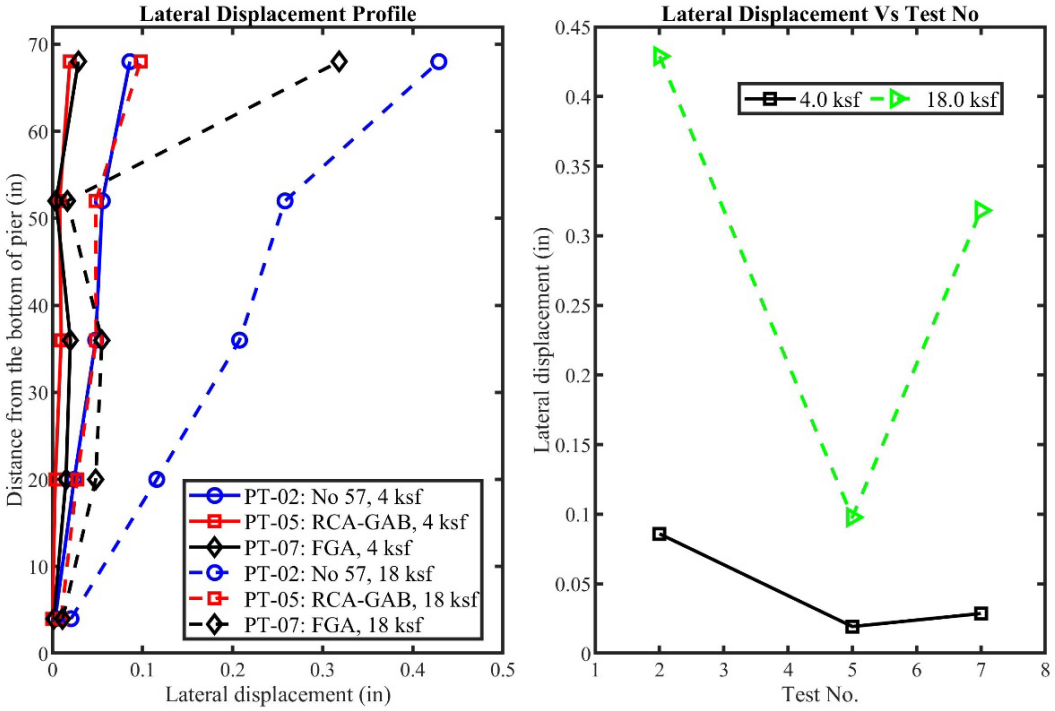


Figure 4-13. Influence of backfill stiffness.

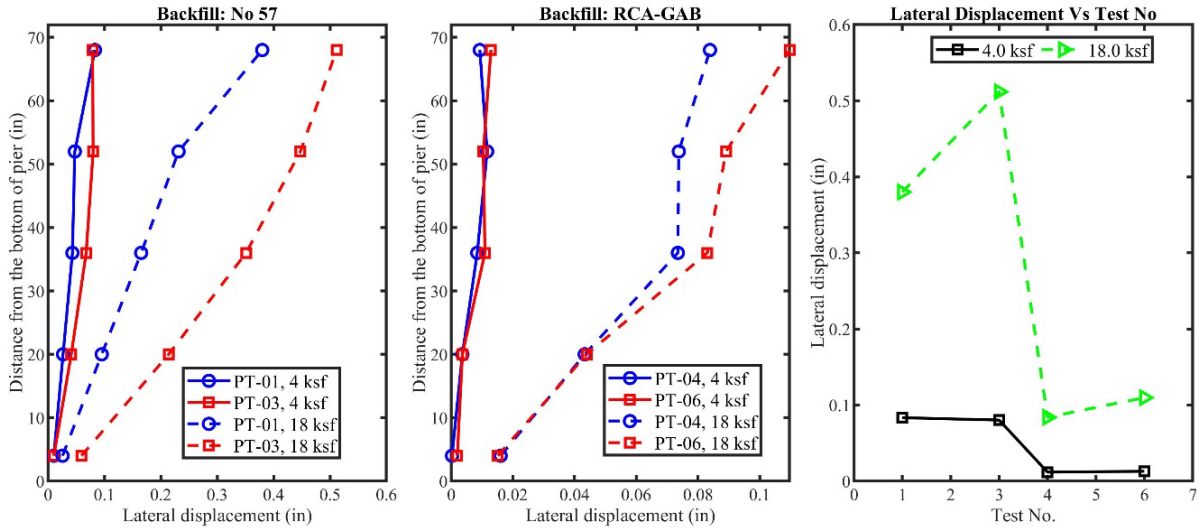


Figure 4-14. Influence of reinforcement stiffness.

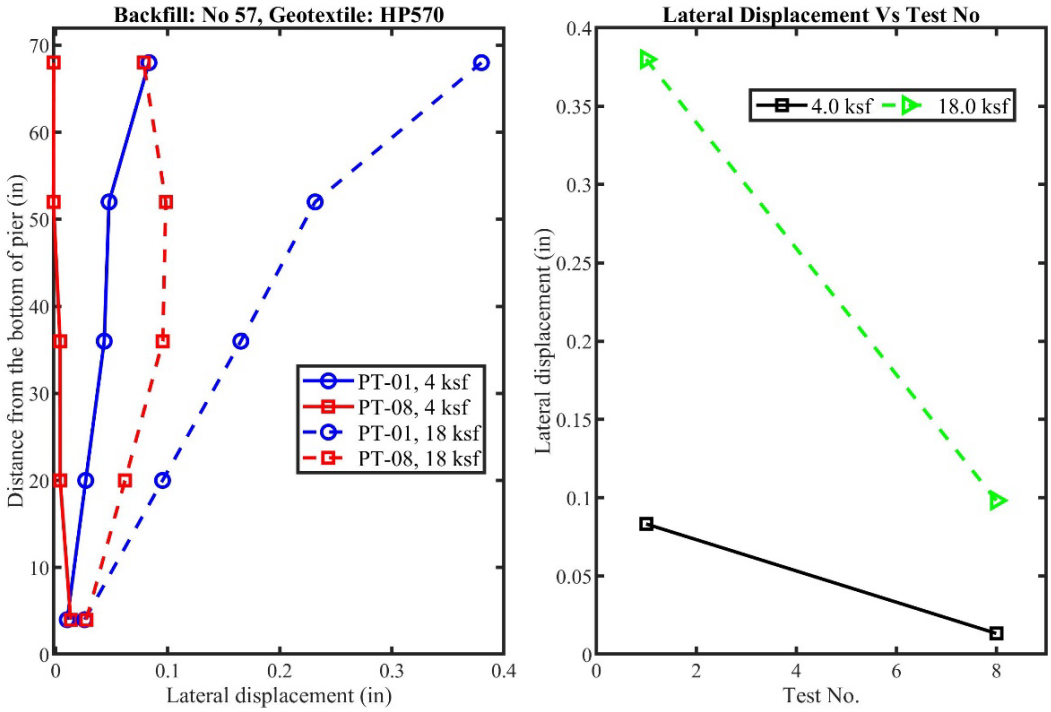


Figure 4-15. Influence of concrete fill.

## 4.4 Internal Lateral Earth Pressure

Four pressure transducers were installed in the fifth block course, on the interior facing of a block to measure the changes in the distribution of internal lateral earth pressure during axial loading of the pier. Lateral earth pressure distribution was recorded for both the construction and loading phases in several tests, except for PT-04, which was the only test without pressure transducers. Throughout the pier tests there were a few sensor failures for some tests and the measurements were limited to 3 sensors.

The lateral earth pressures measured during construction of PT-05, PT-07, and PT-08 are presented in Figure 4-16. PT-08 was monitored only until the placement of the seventh lift of backfill. PT-05, PT-07, and PT-08 tests indicated that the measured pressure was below 0.6 ksf. As the fill height increased, PT-05 and PT-08 exhibited an increase in lateral pressure. In contrast, PT-07 displayed a distinct behavior where the pressure initially increased, then decreased with increasing fill height, only to increase again when the final layer was added. This fluctuation in lateral earth pressure observed in PT-07 could be attributed to the characteristics of the FGA material. The FGA backfill contains larger particles, and during compaction, these particles tend to fracture. Consequently, when compacting the uppermost layer, some of the particles likely fractured leading to a denser state than the lower layers where much particle fracturing didn't occur. Additionally, some of the FGA particles were around 4 inches in size and in an 8-inch layer only two to three larger particles may contact the back of the facing block. If these particles were located close to the pressure sensing area (a strip less than 8 inches in length, Figure 3-37), their rearrangement during compaction could also result in the loss or gain of contact with the pressure transducers.

Figure 4-17 shows the lateral earth pressure versus applied vertical pressure measured at the back of a facing block in the fifth course for the PT-01 test. Lateral earth pressures change due to self-weight were not recorded for this test and the comparison is made only for an incremental change of pressure due to axial loading. It is observed that the lateral earth pressure increases as the applied vertical stress increases. Initially, when the applied vertical stress is below 17.9 ksf, the lateral pressure is higher at the top and bottom of the block. This phenomenon can be attributed to the interaction between the block and the geotextile. The downward movement of the geotextile adjacent to the block causes the aggregates to press against the block, particularly near the corner

formed by the block and geotextile. Assuming the geotextile is intact and the blocks are not cracked at this point, the pressed aggregates become confined within the smaller corner spaces at the top and bottom, resulting in an increase in lateral pressure at those locations. Also, the high earth pressure at the top of the layer is due to stress increase caused the applied load which is high at top and its effect decreases as moving away from the position of the load. As more load is applied, the position of the maximum lateral earth pressure gradually shifts towards the middle of the block, showing a pressure distribution in general agreement with the bin pressure diagram proposed by Wu (2001). When the applied load approaches the ultimate capacity, the pressure begins to decrease significantly. This decrease occurs because the facing walls have moved significantly and geotextile has carried more load, thereby reducing confinement and shifting the max pressure towards the center. This observation is further supported by the openings that form at the joints between blocks, allowing the aggregates to infiltrate into the gaps. At this stage, or right after, the geotextiles have begun to tear along the edges of the blocks, resulting in additional reduced lateral restraint that was provided by the geotextile to the backfill through friction. The complete lateral earth pressure measurements for the pier tests are in the Appendix.

Figure 4-18 shows the relationship between lateral earth pressure and the applied vertical stress for all tests based on the geotextile reinforcement. The results show that piers constructed with the same geotextiles exhibit nearly identical relationships between lateral earth pressure and vertical applied stress. For instance, PT-02 and PT-05 employ the same reinforcement type (HP770) but have different backfills, and their curves display similar trends except when the applied vertical stress falls between 10 and 17 ksf. A comparable behavior can be observed for PT-03 and PT-06, except for the applied vertical stress range of approximately 15 to 23 ksf. Throughout each test, lateral earth pressure increases as the applied vertical stress increases until it reaches a peak value while the peak lateral earth pressure is reached before the peak applied vertical stress. Initially, there is a slight increase of lateral earth pressure at smaller loads. This phenomenon occurs because most of the load is carried by the topsoil and geotextile layers, as evidenced by the maximum lateral displacement observed in the upper courses of the blocks. Additionally, there is greater confinement provided by the geotextile at this stage. As the loads increase, stress is transferred deeper into the soil layers, resulting in an increase in lateral pressure. When the block containing the pressure transducers begin to move, there is a slight decrease in lateral earth pressure, which is counterbalanced by the increase in pressure due to the restraint

offered by the geotextiles. As the geotextiles begin to rupture, particularly along the perimeter of the blocks, there is a decrease in lateral pressure due to the loss of confinement provided by the geotextile. This process repeats itself since most of the geotextiles do not rupture simultaneously but progressively, starting from the upper layers and moving downward. At a certain point, which cannot be precisely determined, the lateral pressure ceases to build up further due to significant block movement, extensive geotextile rupture, block cracks, and particle loss through gaps formed at the interfaces between blocks. This phenomenon of pressure increase followed by a decrease was also observed in the FHWA experimental study conducted by Lwamoto (2014).

Stability and deformation of the composite GRS system may be studied considering the successive axial stresses and the stress paths of the composite GRS system. The measured lateral earth pressure at a single facing block and the measured axial stress gives the values to develop stress paths for each type or geotextile reinforced composite GRS using the q-p stresses at a point (Equations 4-1 and 4-2). Wu (2001), Mitchell (2002) and Zornberg et al. (2018a) have demonstrated that lateral earth pressure is nearly uniformly distributed with depth when using a uniform small reinforcement spacing. However, these studies primarily focused on smaller vertical stresses. At higher stresses, the pressure distribution differs, as shown by Bhattarai (2018) and Yazdandoust and Taimouri (2023), and as indicated by the pier profiles of lateral displacement in this study (section 4.3). Lwamoto (2014) performed an equilibrium analysis of a GRS pier using measured experimental data and analysis indicated that the shear stress at the interface between the backfill and facing block is relatively small compared to the vertical and horizontal stresses. Therefore, the vertical and horizontal stresses may be assumed to be the major and minor principal stresses, respectively, and the measured lateral pressure is assumed to represent an average pressure to construct the stress paths (q-p plots) for all tests. Shown in Figure 4-19 are the stress paths for PT-01 through PT-03 and PT-05 through PT-08 tests. The piers generally follow a stress path about 45° ($\Delta\sigma_3 = 0$ and $\Delta\sigma_1 > 0$) for smaller applied vertical stresses (up to approximately q = 8 ksf). However, as the applied vertical stress increases, piers with the same geotextile exhibit similar stress paths. This similarity aligns with the observations made regarding lateral earth pressure. However, the pier with concrete fill in the top courses deviates from the others due to the additional restraint provided by the concrete fill and rebar, which contributes to additional lateral earth pressure. The influence of backfill materials is not explicitly shown in the analysis, and it can be concluded that the stress path and lateral earth pressure are more influenced by the

reinforcement conditions rather than the specific backfill materials used. It's important to note that only three types of backfill and geotextile, one type of blocks, and a specific test configuration were utilized in these experiments. Conducting additional tests with different types of materials, unit weights, and without facing blocks would provide more confining pressures ($\sigma_3$) and the determination of other stresses at failure (failure envelope) from which the strength properties of the composite GRS system could be calculated. Lwamoto (2014) performed this analysis on different types of GRS piers based on two confining pressures and showed that the composite strength properties (c and $\phi$) were less than the properties of the backfill aggregate (values used in the FHWA equation for predicting GRS bearing capacity.

$$p = \frac{1}{2}(\sigma_1 + \sigma_3) \tag{4-1}$$

$$q = \frac{1}{2}(\sigma_1 - \sigma_3) \tag{4-2}$$

Where $\sigma_1$ is the applied vertical stress and $\sigma_3$ is the lateral earth pressure.

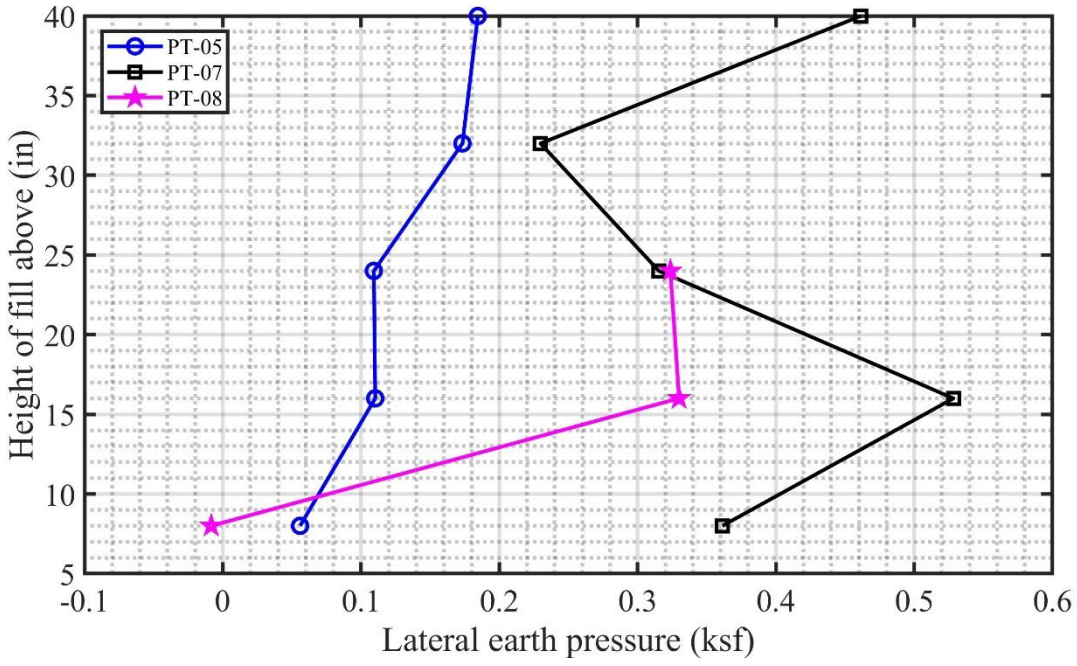


Figure 4-16. Change in lateral earth pressure distribution along the block height during construction.

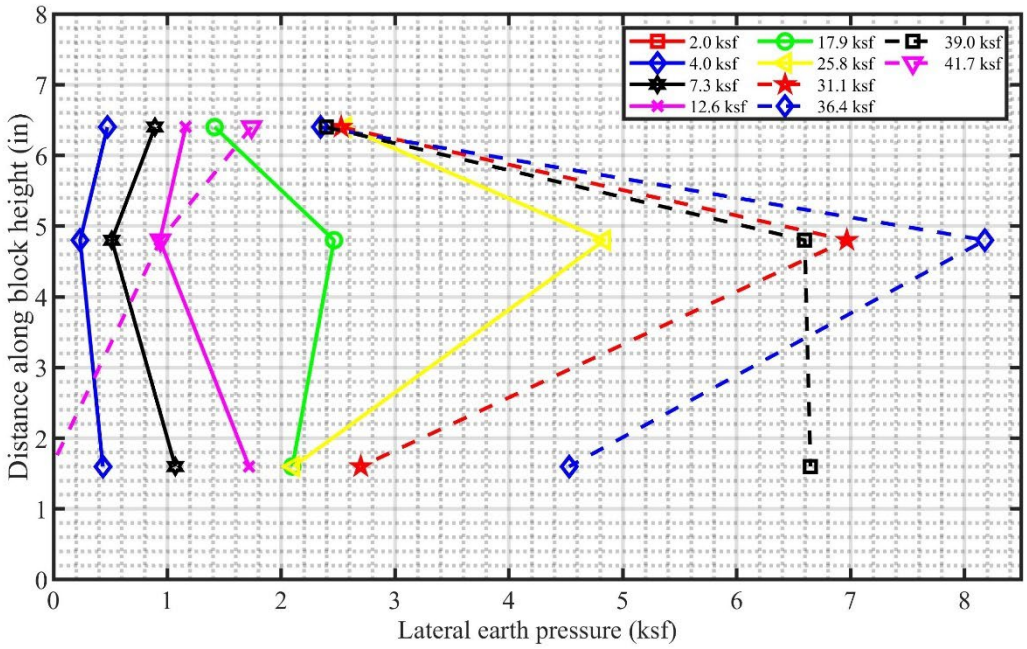


Figure 4-17. Change in lateral earth pressure distribution along the block height at different applied vertical stresses.

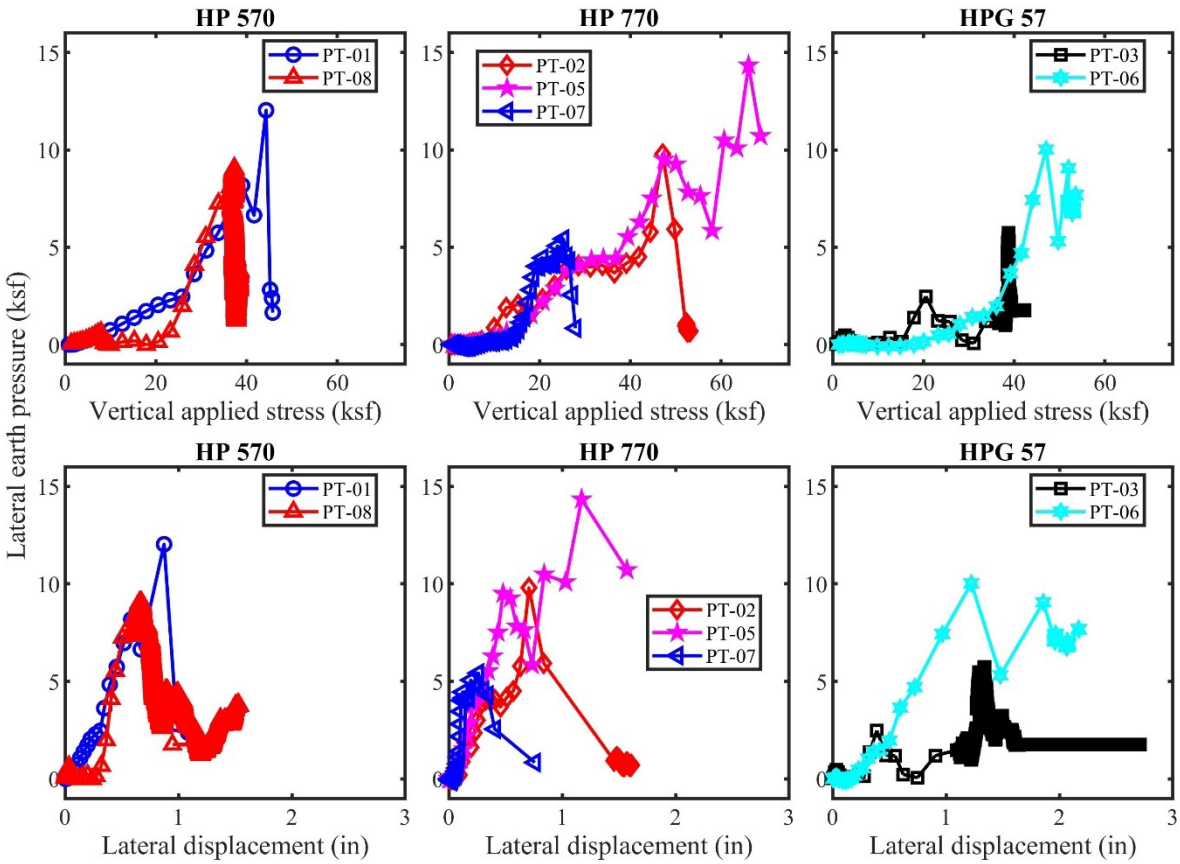


Figure 4-18. A plot of lateral earth pressure changes versus applied vertical stress and lateral displacement of the block with pressure transducer.

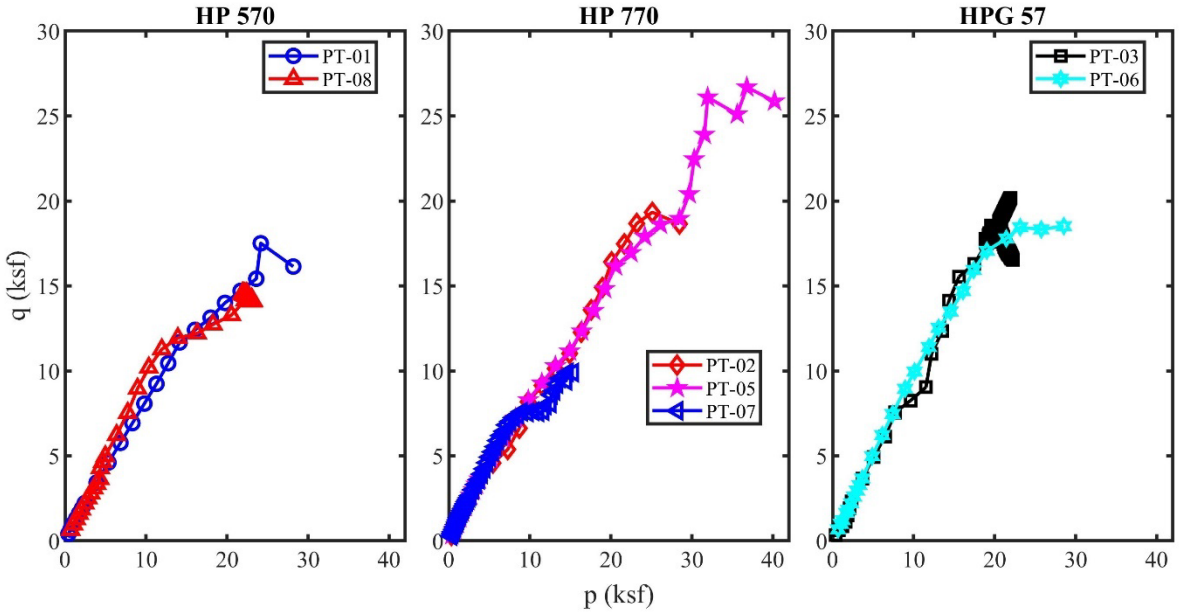


Figure 4-19. Stress path during axial loading.

## 4.5 Vertical Earth Pressure

The only piers that were equipped with vertical earth pressure cells were those built after PT-03 test. All of the piers had the earth pressure cell positioned 4 inches from the bottom (in the middle of the first course), except for PT-05 which was located at the bottom (under first course). Figure 4-20 shows the vertical earth pressure measured during construction and under axial loading. As anticipated, the vertical earth pressure increases as the fill height increases. The lowest pressure readings during construction were seen in PT-07, primarily due to its light mass and larger particles leading to less compact density. When the second layer was added to PT-07, the pressure readings decreased, likely due to the larger particle size of the FGA and the vertical stress increase being carried by the reinforcement. A similar decrease in pressure was observed in PT-5 when the sixth fill was added. During loading, the earth pressure readings increased with the applied vertical pressure. There was a linear correlation between the measured and applied vertical pressures until approaching the pier's axial capacity. Following that the additional applied pressure was transferred to the lower part of each pier, as evident in the earth pressures in Figure 4-20 (b). The pier built with FGA (PT-07) exhibited a similar trend, with some fluctuations in the measured pressure likely due to fracturing of the larger particles and rearrangement near the cell.

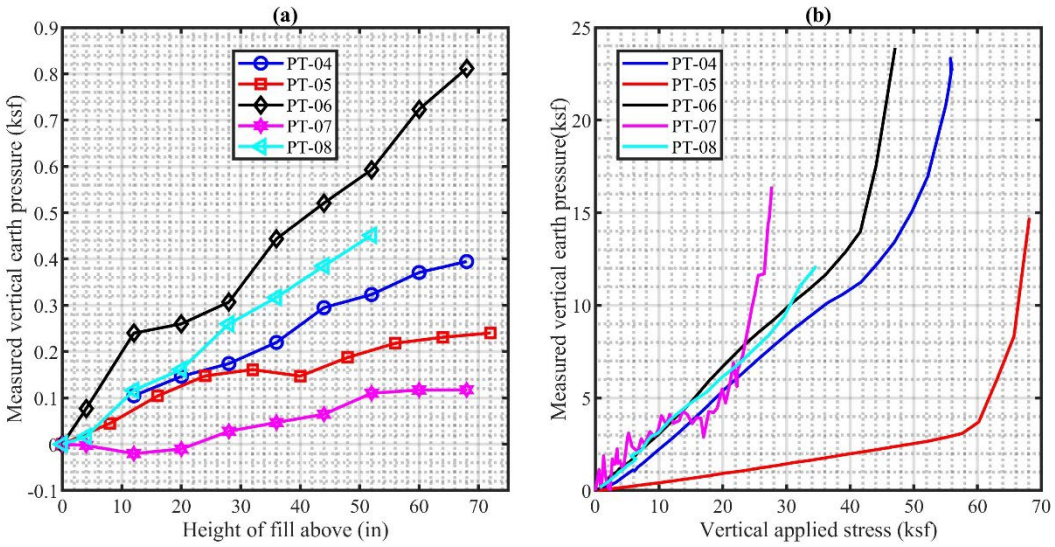


Figure 4-20. Earth pressure measured during construction and axial loading of the pier. (a) During construction; (b) During axial loading.

## 4.6 Reinforcement Strains

Accurate measurement of reinforcement strain in geosynthetic reinforced soil systems is crucial for evaluating their performance. In these systems, strain gauges have been the commonly used method for measuring strain in geosynthetics. However, these gauges only provide measurement at one point and would require multiple gauges and connecting wires to capture a continuous strain profile across the geosynthetic. This can introduce additional complexities that may interfere with the reinforcement mechanism of the geosynthetic system. To address these limitations, this section introduces a new approach that utilizes fiber optic strain sensors for measuring reinforcement strain in geosynthetic reinforced soil systems. The use of fiber optic strain sensors offers several advantages such as high accuracy, immunity to electromagnetic interference, simplicity in installation, and the ability to measure multiple points simultaneously. The procedures for installing and calibrating the fiber optic strain sensors were presented, and the results from the strain measurements were compared with those from strain gauges. The results were also compared to two widely used design methods.

### 4.6.1 Calibration of Strain Gauge and Fiber Optic

The installation of strain gauges and fiber optic strain sensors on geotextile using adhesive can cause the specimen to stiffen at the attachment points. Proper selection of the adhesive and protective materials may minimize this effect. However, the strain measured by the strain gauge is a local strain that may be different from the global strain along the test section. The local stiffening effect causes the under-registration of global strains (Bathurst et al., 2002). To ensure accurate and repeatable measurements, it is important to calibrate the strain gauges on geotextiles. Calibration of the strain sensors was conducted to establish a correlation between the local strain and global strain. To develop the calibration factor, instrumented geotextile specimens were tested in an extension test shown in Figure 4-21 for each geotextile type, orientation, and bonding technique both in the machine and cross-machine direction following the ASTM D4595 standard. Figure 4-22a shows the load-deformation of geotextile with and without the strain sensors. The results showed that the installation of fiber optic sensors and strain gauges has little to no effect on the overall behavior of the geotextile. However, when the local strains recorded by sensors were compared with global strain recorded by extension machine cross-heads, they were found to be different and a need was identified to develop a calibration factor. There wasn’t a clearly more

accurate method between the two sensing methods (CF in Figures 4-22a and 4-22b), however, a direct comparison is a little misleading as the strain gage measurement is local, over the length of the gage, while the fiber optic strain sensor has many measurements over the length of the fiber. Table 4-2 shows the calibration of factors. The local strain was converted to global strain by multiplying it with the calibration factor as shown in Equation (4-3). The strain sensors used can easily break when comes in direct contact with aggregate, especially during compaction of the backfill. To protect the gauges from mechanical damage during construction, a thin layer of RTV silicon rubber and fine sand were used. These materials were placed over gauges and wires to provide added protection.

$$\varepsilon_{r,global} = \varepsilon_{r,local} \times CF \qquad (4\text{-}3)$$

Where $strain_{local}$ is the local strain, $strain_{global}$ is the global strain, and $CF$ is the calibration factor.

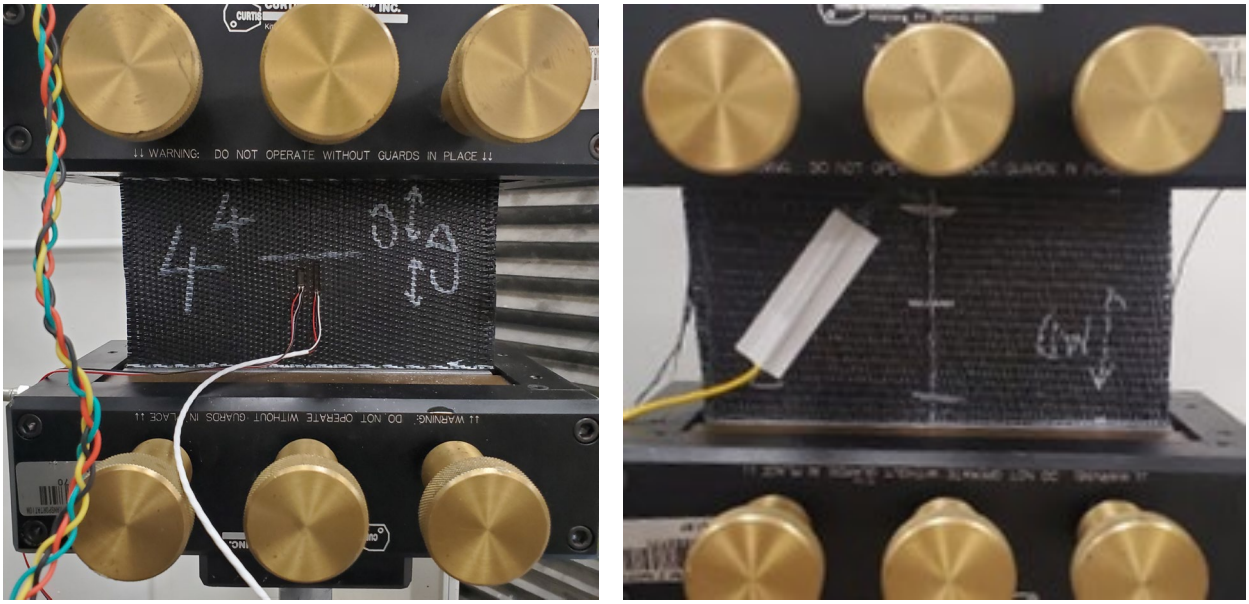


(a) (b)

Figure 4-21. Uniaxial tensile tests of geotextile.
(a)Test specimen with strain gauges installed; (b) Test specimen with fiber strain sensor installed. Photo courtesy of author.

Table 4-2. Calibration Factors

| Strain Measurement Sensor | HP570 | | HP770 | | HPG57 | |
|---|---|---|---|---|---|---|
| | MD | CD | MD | CD | MD | CD |

| | | | | | | |
|---|---|---|---|---|---|---|
| Fiber Optic Strain Gauges | 1.53 | 1.54 | 1.70 | 1.70 | 2.05 | 2.36 |
| A. Short gauge (EP-08-250BG-120) | 1.49 | 2.08 | NA | NA | NA | NA |
| B. Long gauge (EP-08-500GB-120) | 1.33 | 2.08 | 1.88 | 2.12 | NA | NA |

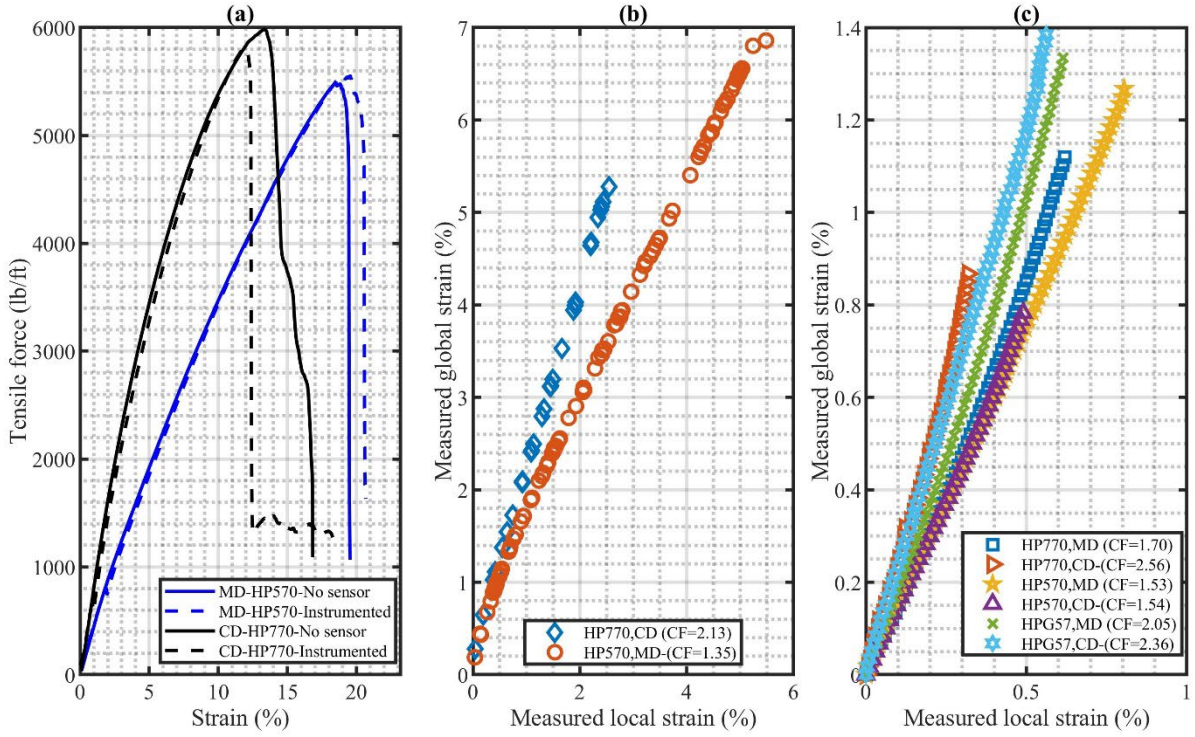


Figure 4-22. Results of uniaxial tensile tests of geotextile and calibration.
(a) Comparison of global tensile force-strain from geotextiles with and without strain sensors; (b) Calibration factors developed from a plot of global strain (from crossheads) versus local strain (from strain gauge) for the long gauge in the cross-machine direction; (c) Calibration factors developed from a plot of global strain (from crossheads) versus local strain (from fiber optic sensors) for the long gauge in the cross-machine direction.

### 4.6.2 Reinforcement Strain Distribution in Geotextile During Loading

In each pier test, each subsequent layer of geotextile was rotated and Figure 4-23 shows the perpendicular sections AA and BB that are presented for the strain measurements. Figure 4-24 and Figure 4-25 show the measured reinforcement strains across sections A-A and B-B in response to applied vertical stresses in the PT-05 and PT-02 tests, respectively. The fiber optic strain sensors did not survive until the end of any of the tests, so the measurements presented are for the cases

prior to the GRS piers reaching their ultimate failure capacities. The tensile strain increases across all reinforcements as the applied load increases indicating the backfill stress being increasingly carried by the geotextiles. In the upper geotextile layers (Layer six and Layer seven), the tensile strains were the greatest near the facing blocks, which was observed in all pier tests, regardless of the type of geotextile type. This was observed in cases where the fiber optic strain sensor ends very close to the facing blocks. As a result of being situated in close proximity to the footing, the upper geotextile layers within the soil mass are likely to undergo uniform vertical settlement. Around the facing perimeter of the pier, each geotextile layer (with the exception of the geotextile layers eight and ten) is bounded by facing blocks (Figure 3-29). With frictional resistance to pullout, high tensile strains, and stress concentration can develop at the aggregate-facing block boundary under uniform settlement response to applied load as illustrated in Figure 4-29. Assuming that the vertical settlement of the footing is comparable to the vertical movement at the level of the seventh layer during loading, it becomes evident from Figure 4-28 that the vertical movement at the seventh layer surpasses both the lateral displacement of facing blocks and the displacements computed from measured reinforcement strain. The observation that the geotextile experiences greater vertical than horizontal pushing reinforces the notion of stress concentration forming at the boundary between the geotextile and facing block. Post-analysis of the tests also showed that most of the vertical movement occurred at the upper layers and most of the geotextile sheets at the upper layers had torn around the inside perimeter of the blocks as shown in Figure 4-26.

In the fourth and fifth geotextile layers, the positions of the maximum strains were around the center of the geotextile within the soil mass. This is because most of the backfill layers in these locations are subjected to more lateral expansion rather than vertical expansion. During the loading process, the vertical movement of each layer was not monitored. However, the vertical movement of each layer was measured during the test deconstruction phase. Figure 4-27 presents a comparison of the vertical and lateral displacements of each layer at the end of PT-01. Assuming that the displacement patterns observed at the end of the tests accurately reflect the actual behavior during the loading of the piers, it becomes apparent that the backfill near layers four and five experienced greater lateral movement than vertical movement. This is further supported by post-analysis of the failed geotextiles, which showed these layers were more torn apart at the center than at the connections, indicating that they were stretched more at the center. Additionally, there

was no significant change in strain magnitude observed as one moves from the facing wall to the center of the geotextile in the middle layers.

The effect of the backfill type is more pronounced on the magnitude of the measured strain. Geotextiles in the piers constructed with RCA-GAB backfill showed less reinforcement strain than the ones constructed with No 57 backfill. This is because RCA-GAB backfill has higher stiffness than No 57 backfill as shown in Figure 3-5 through Figure 3-7. Therefore, less deformation occurred in piers constructed with RCA-GAB than in No 57. However, the backfill type did not influence the nature of the strain distribution across the center of the geotextile. This means that the distribution of the strains across the geotextile is not affected by the type of backfill used, but rather by the applied vertical stress and the location of the geotextile within the structure.

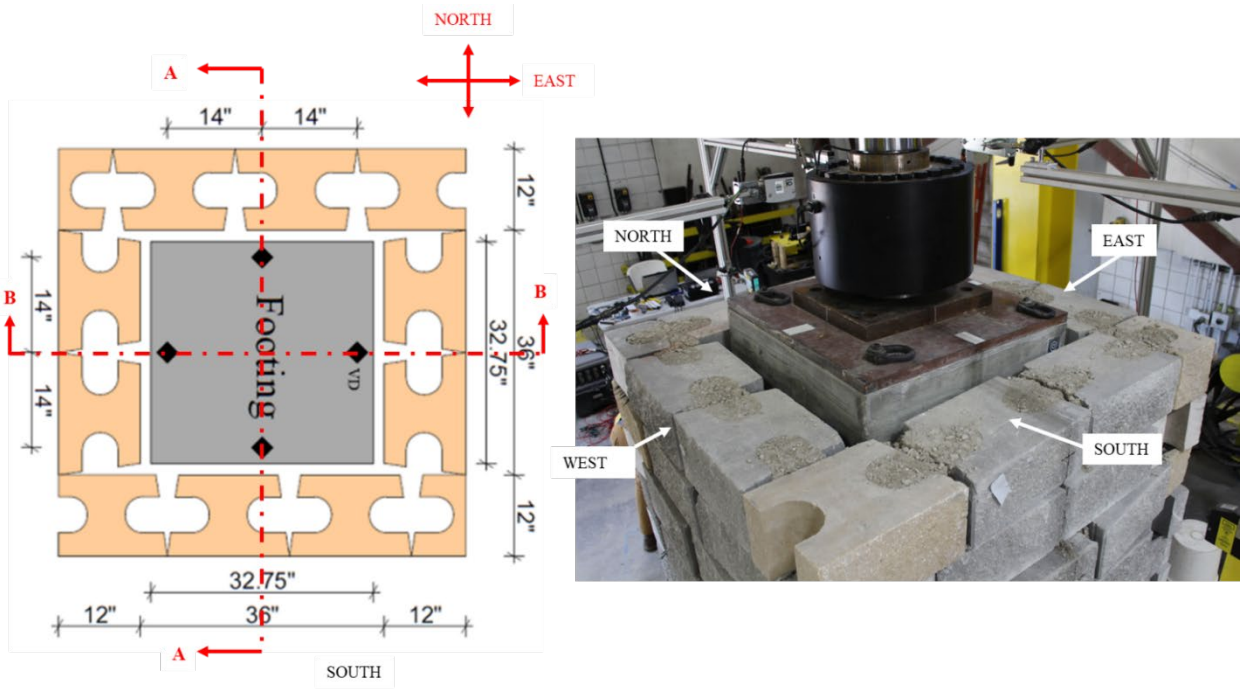


(a) (b)

Figure 4-23. Illustration of the pier orientation.
(Section A-A: South-North view, Section B-B: West-East View)
(a)Top view with sections considered (b) Top view of the pier after failure.

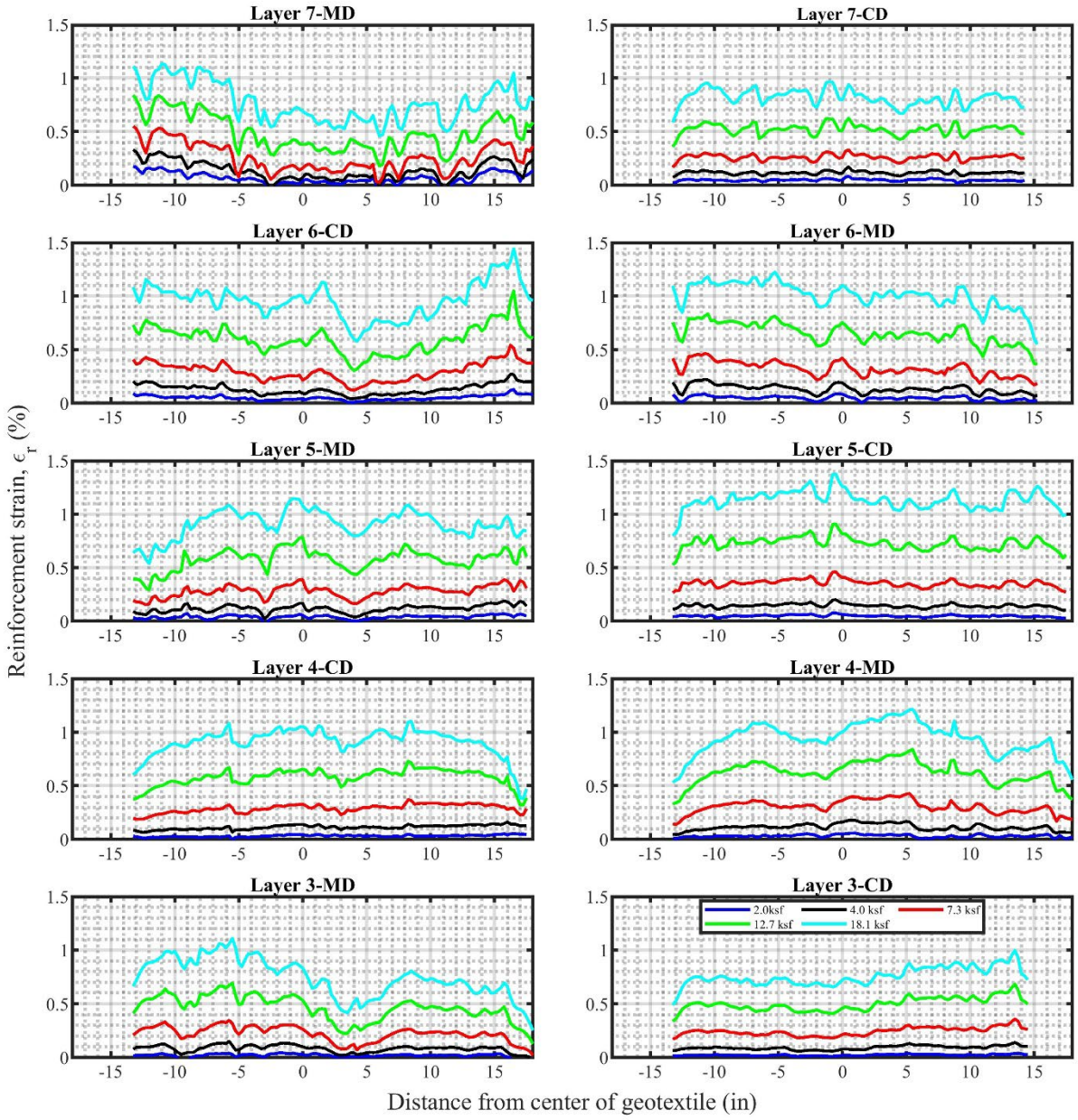


(a) (b)

Figure 4-24. Reinforcement strain distribution in geotextile at different applied vertical stress for PT-05.
(a) Section B-B: West -East (WE); (b) Section A-A: South-North (SN).

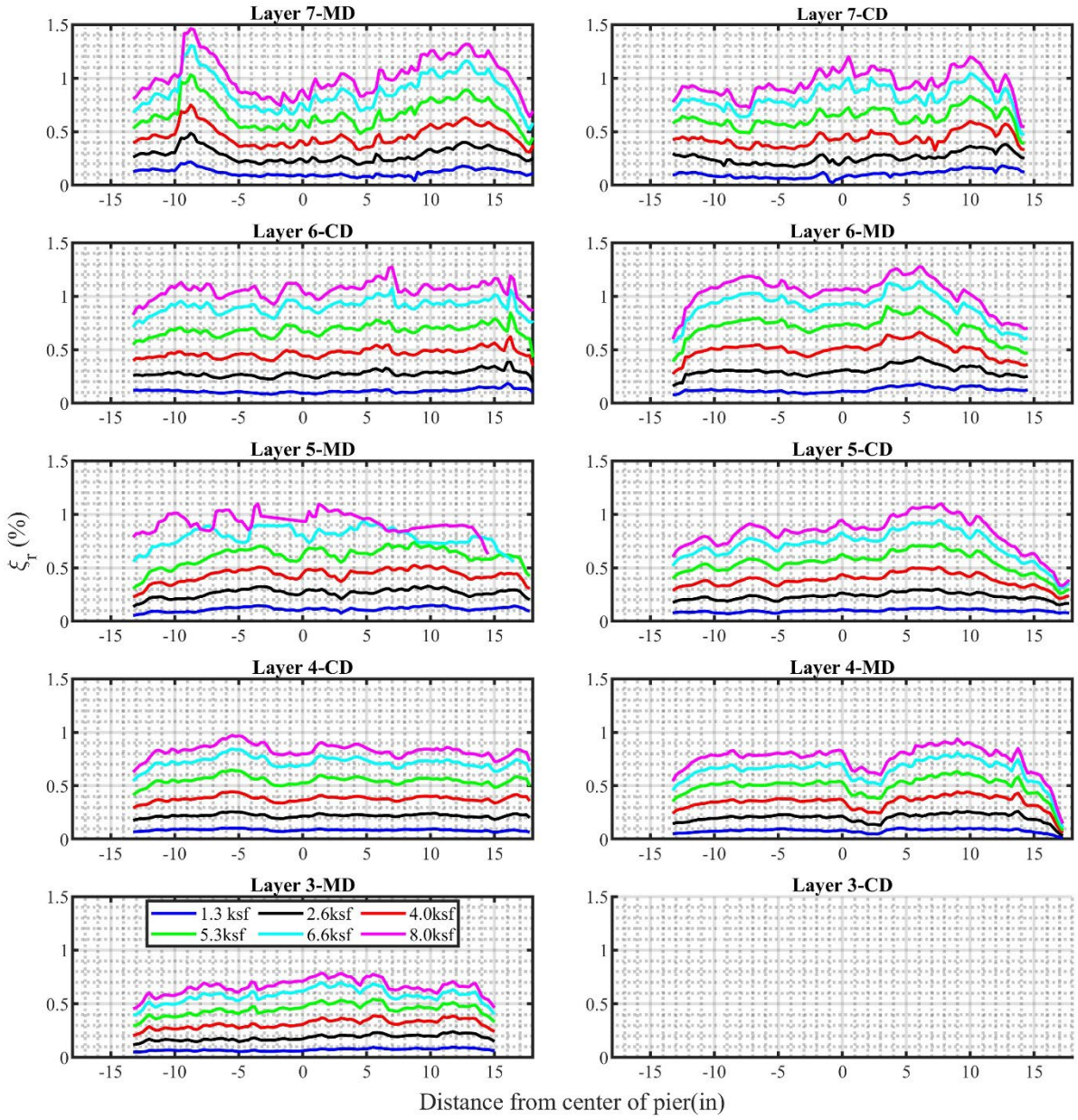


(a) (b)

Figure 4-25. Reinforcement strain distribution in geotextile at different applied vertical stress for PT-02.
(a) Section B-B: West -East (WE); (b) Section A-A: South-North (SN).

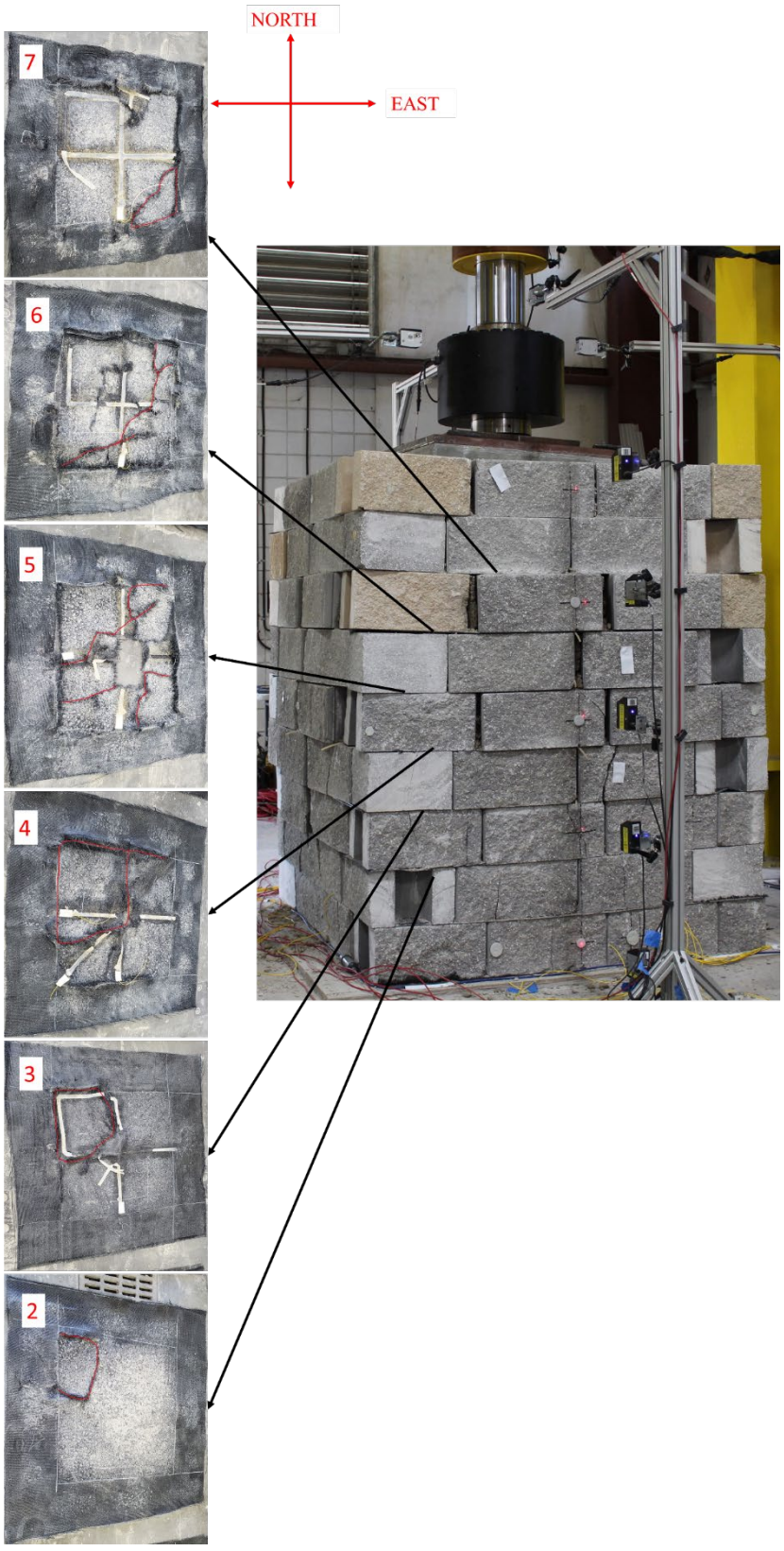


Figure 4-26. Progression of geotextile rupture from PT-05 test.

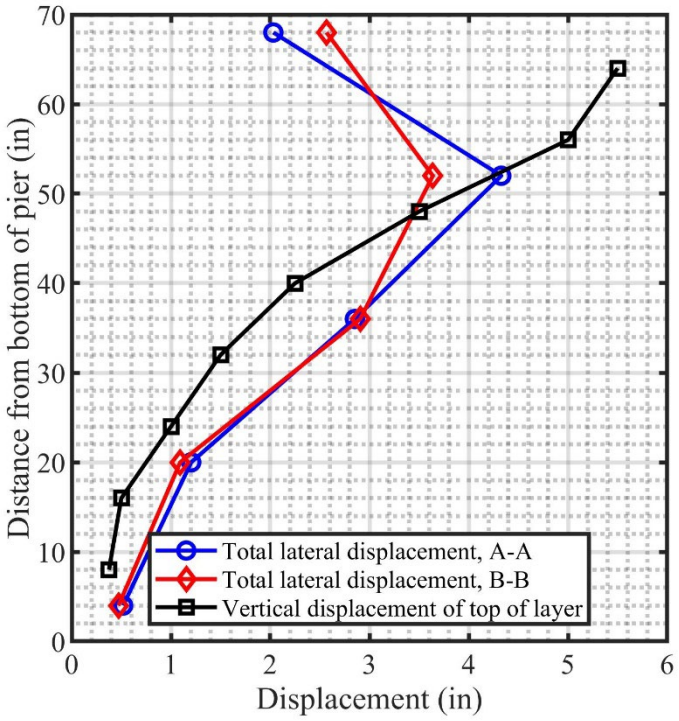


Figure 4-27. Comparison of the maximum lateral and total vertical displacement of each layer at the end of the PT-01.

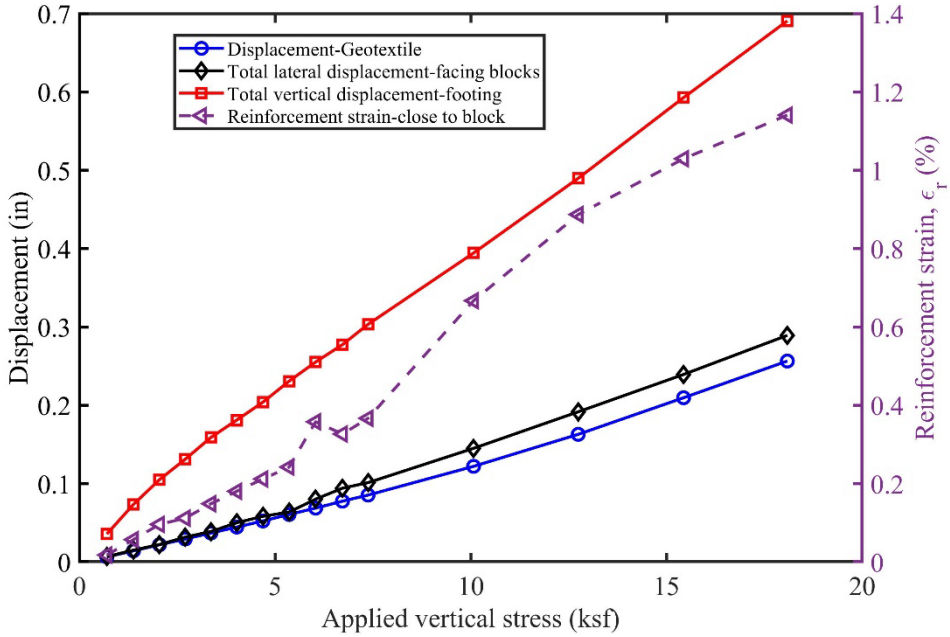


Figure 4-28. Comparison of the displacements and strain for seventh layer in PT-05.

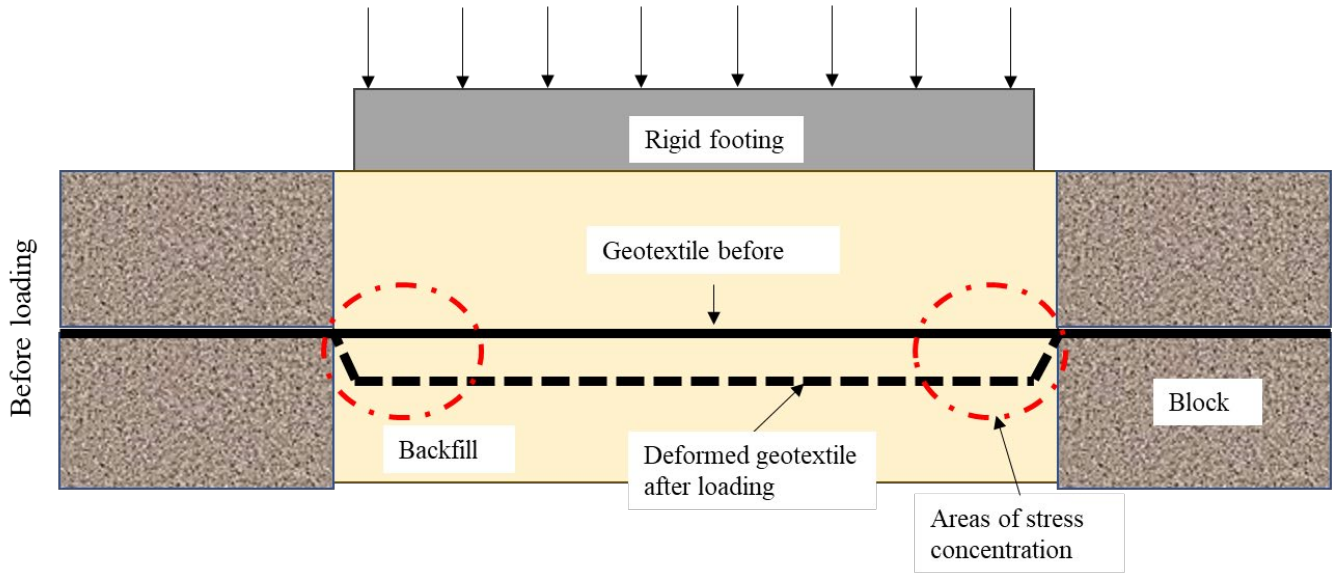


Figure 4-29. Illustration of geotextile displacement for the seventh layer.

### 4.6.3 Reinforcement Strain Distribution in the Fourth Layer During Loading

The fourth geotextile layer in each test was equipped with fiber optic strain sensors at an angle of 45 degrees to the horizontal. This setup is suitable for situations where two walls meet, such as when a facing wall connects with a wingwall. Additionally, it is relevant for walls that are oriented at angles greater or less than 90 degrees in relation to the geotextile. In these cases, the geosynthetic material needs to be able to withstand the forces acting on it from multiple directions. However, the current design guidelines do not provide specific instructions on how to account for the unique stresses and strains that occur at corners in internal stability evaluations. This means that engineers need to use their own judgement and experience to determine the appropriate geosynthetic strength to use in these situations. Examples of this type of configuration can be found in Figure 4-30, which illustrates the different ways that geosynthetic materials can be used in corner configurations and the challenges associated with them.

Examples of the reinforcement strains in the fourth layer for PT-05 are shown in Figure 4-31 through Figure 4-33. These figures provide visual representation of the distribution of strains in the geotextile material at different locations. From the figures, it can be seen that at a distance close to the center, the strains are distributed uniformly across all directions, equidistant from the center of the geotextile. This behavior is observed in all tests, regardless of the materials used, indicating that the center of the geotextile is experiencing similar strain levels in all directions. However, as

the distance from the center increases, the distribution of tensile strains becomes slightly different. The strains become greater towards the north and east sides, while the difference in strain magnitude is not significant. Despite this slight difference in strain distribution, overall, it can be concluded that for this type of structure, the reinforcement strain distribution is relatively uniform across all directions. This means that the geotextile material is able to evenly distribute the forces acting on it, providing an effective reinforcement solution.

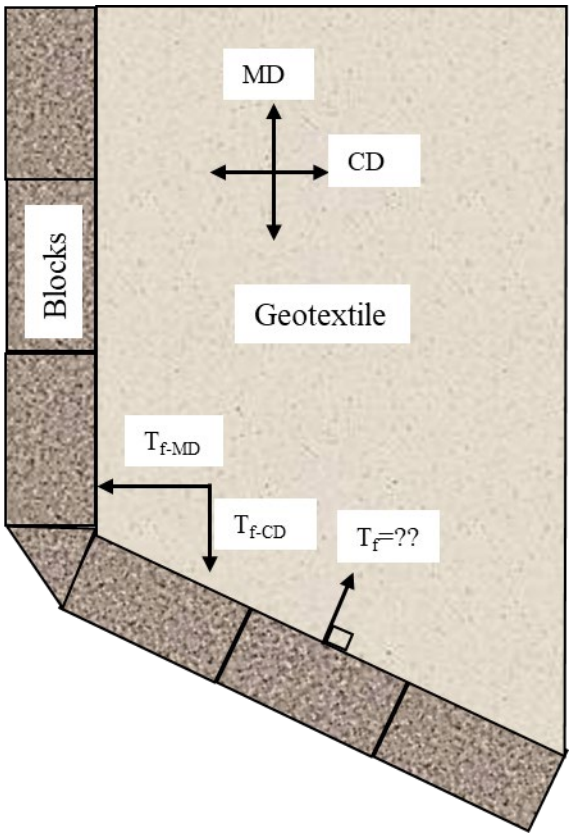


Figure 4-30. Illustration of the facing walls meeting at angle greater than 90 degrees.

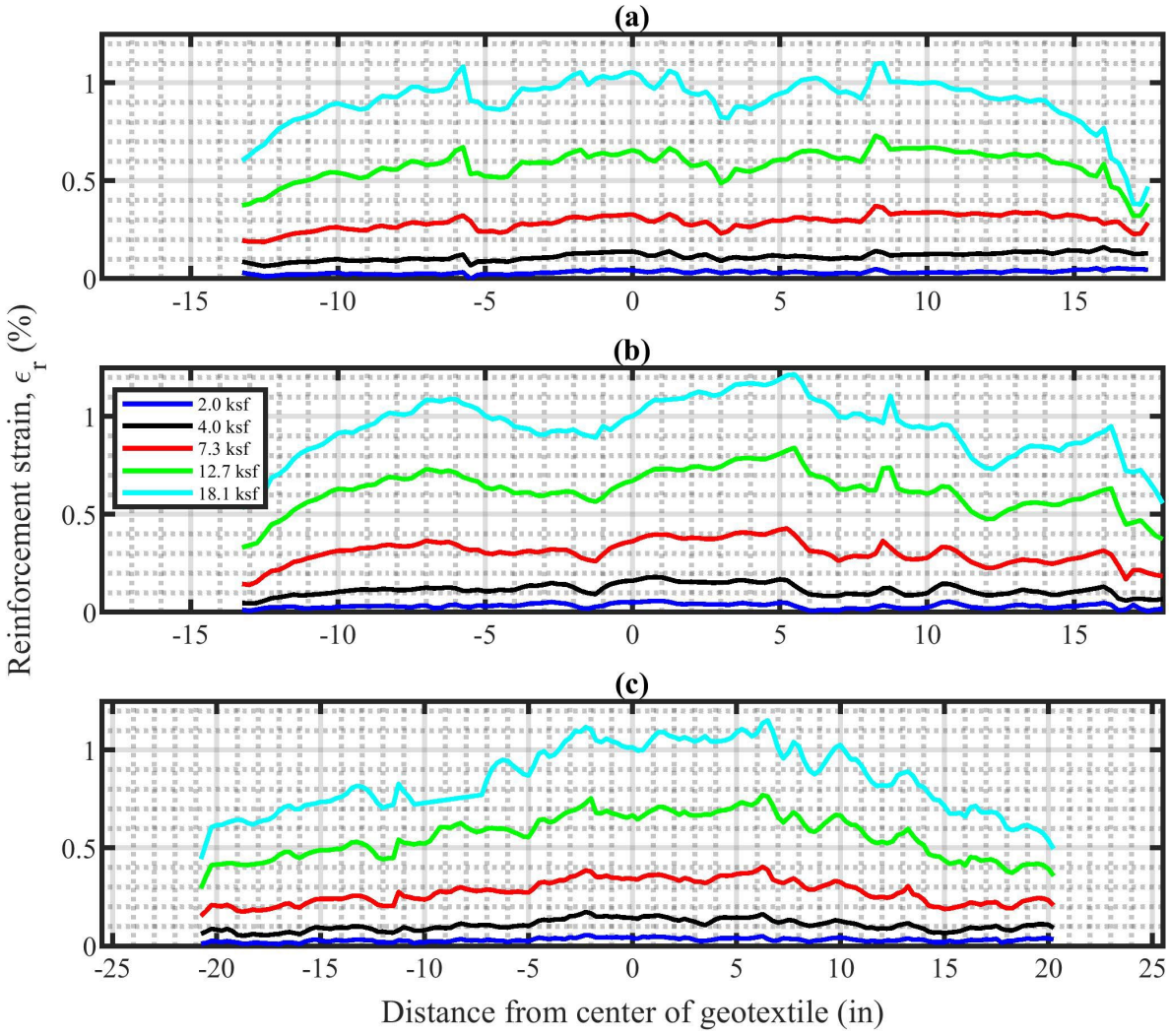


Figure 4-31. Reinforcement strain distribution in the fourth geotextile at different applied vertical stress and orientation in PT-05.
(a) cross-machine direction, (b) machine direction (c) at 45 degrees from the horizontal.

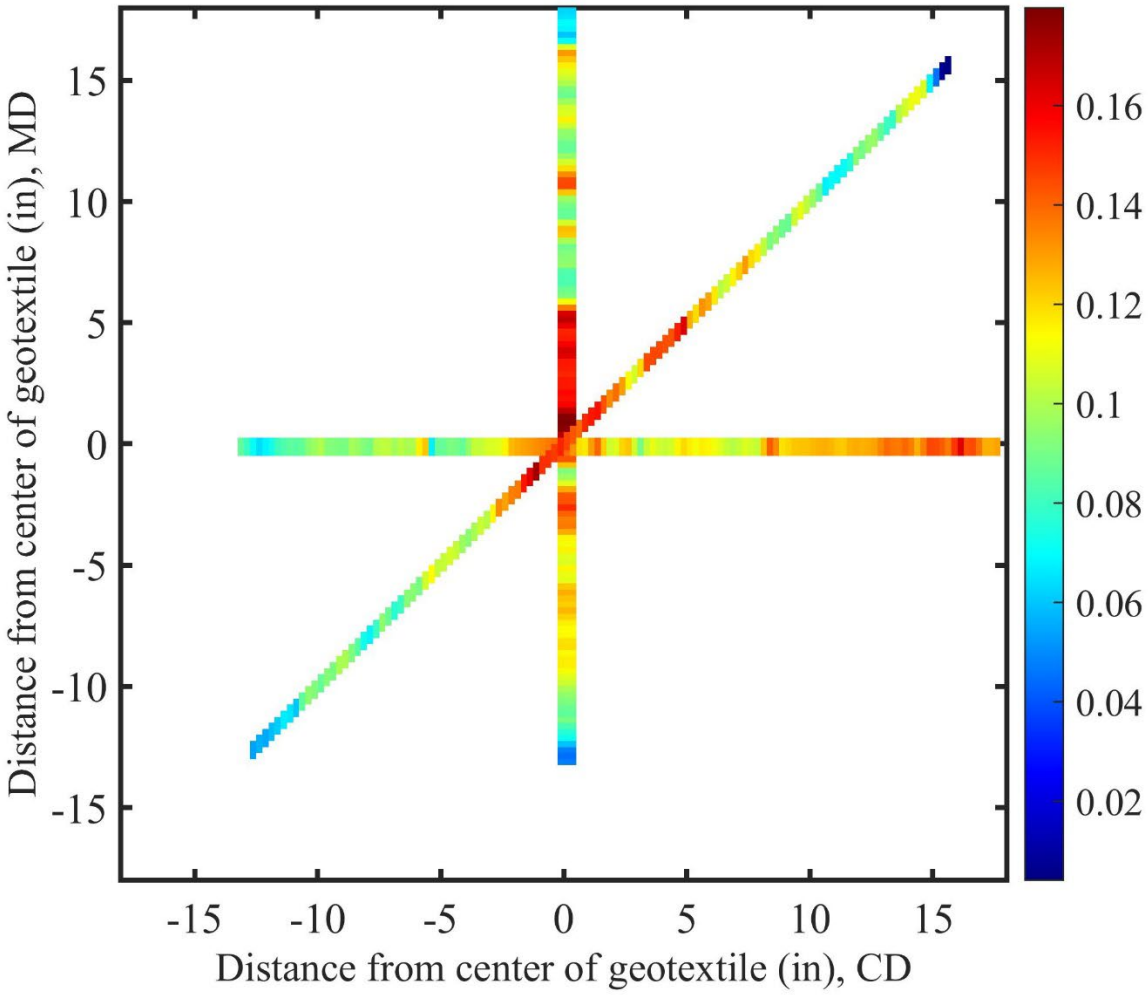


Figure 4-32. Distribution of reinforcement strain in the fourth geotextile when the vertical applied stress is 4 ksf for PT-05.

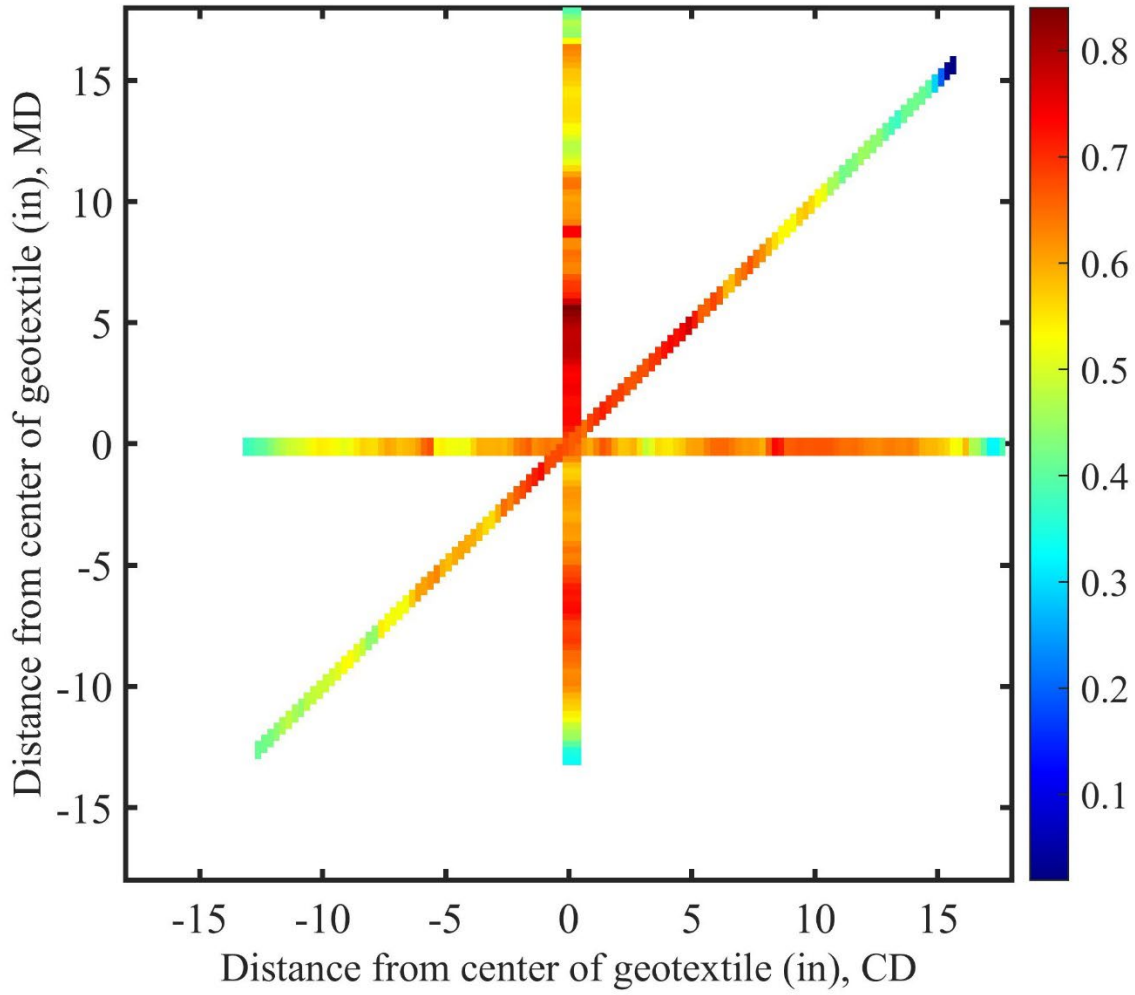


Figure 4-33. Distribution of reinforcement strain in the fourth geotextile when the vertical applied stress is 12.7 ksf for PT-05.

### 4.6.4 Reinforcement Strain Profile

Figure 4-34 shows profile distribution of maximum reinforcement strain for at different applied vertical stresses for all piers tested in this study. The maximum reinforcement strains along the wall height increases as the applied vertical stresses increase. In all tests except for PT-01, the results indicate that the highest reinforcement strain occurs within the top half of the pier height. This means that the maximum strain is concentrated in the top-mid section of the pier, which is where the load is most heavily concentrated and agrees with the position of the maximum lateral displacement observed during the tests. An interesting pattern is observed in PT-03, PT-04, PT-05

and PT-06 where the position of maximum strain initially appears at the seventh layer for lower vertical stresses but shifts to the sixth or fifth layer as more load is applied. This suggests that the reinforcement strain is redistributed from the top layers to the bottom as more load is applied. This redistribution of strain is likely because the top layers are more heavily loaded and are therefore more likely to fail first, allowing the load to be redistributed to the lower layers. This is further supported by the progressive failure of geotextiles observed during deconstruction of the piers, which starts at the top layers and moves downwards. As the top layers fail, the load is transferred to the lower layers, leading to a progressive failure of the geotextile. This is an important consideration when designing GRS structures, as it suggests that the top layers should be designed to withstand higher loads than the lower layers. These findings can be used to calculate the reinforcement loads in geotextile, given the appropriate stiffness values. By knowing the maximum strains at different applied vertical stresses, engineers can estimate the loads that the geotextile is experiencing and design accordingly.

The effect of the backfill type is more pronounced on the magnitude of the measured maximum reinforcement strain as shown in Figure 4-36(a). Geotextiles in the piers constructed with RCA-GAB backfill showed less reinforcement strain than the ones constructed with No 57 and FGA backfill. This is because RCA-GAB backfill has higher stiffness as shown in Figure 3-5 through Figure 3-7. Therefore, less deformation occurred in piers constructed with RCA-GAB than those with No 57 and FGA. The backfill type also influenced the nature of reinforcement strain profile especially when FGA backfill was used. The position of the maximum reinforcement strain remained at the seventh layer throughout the loading phase for PT-07. This is because of larger lateral displacement which was occurring at the higher layers which caused geotextile to stretch more. The larger displacement at upper layers is due to the high compressibility property of FGA backfill.

Also, it is expected that reinforcement stiffness plays a role in reinforcement strain, with an increase in stiffness leading to a decrease in reinforcement strain. Figure 4-35 shows the influence of reinforcement stiffness. The comparison between PT-01 and PT-03, and between PT-04 and PT-06 showed that the stiffness has a significant influence on the reinforcement strain. Using the same backfill, piers reinforced with HP570 have lower reinforcement strains than those constructed with HPG57. The higher stiffness of HP 570 caused the geotextile to undergo less deformation which led to lower reinforcement strain.

Similar to vertical and lateral deformation, the use of concrete fill was also found to influence the reinforcement strain profile. As shown in Figure 4-34 and Figure 4-36(b), a comparison of the reinforcement strain profile in PT-01 and PT-08 reveals that the maximum reinforcement strain was consistently lower in PT-08 than in PT-01 throughout the loading process. This outcome is expected because the presence of concrete fill and rebar increases the confinement pressure, providing greater restraint against lateral movement which leads to less stretching of geotextiles. Unlike in other tests, at smaller loads, the maximum reinforcement strain in PT-08 does not occur at the top of the walls but rather outside the location where the concrete fill was placed. For a significant portion of the loading process, it was consistently observed that the position of minimum reinforcement strain was at the sixth layer which was the boundary between blocks with and without concrete fill.

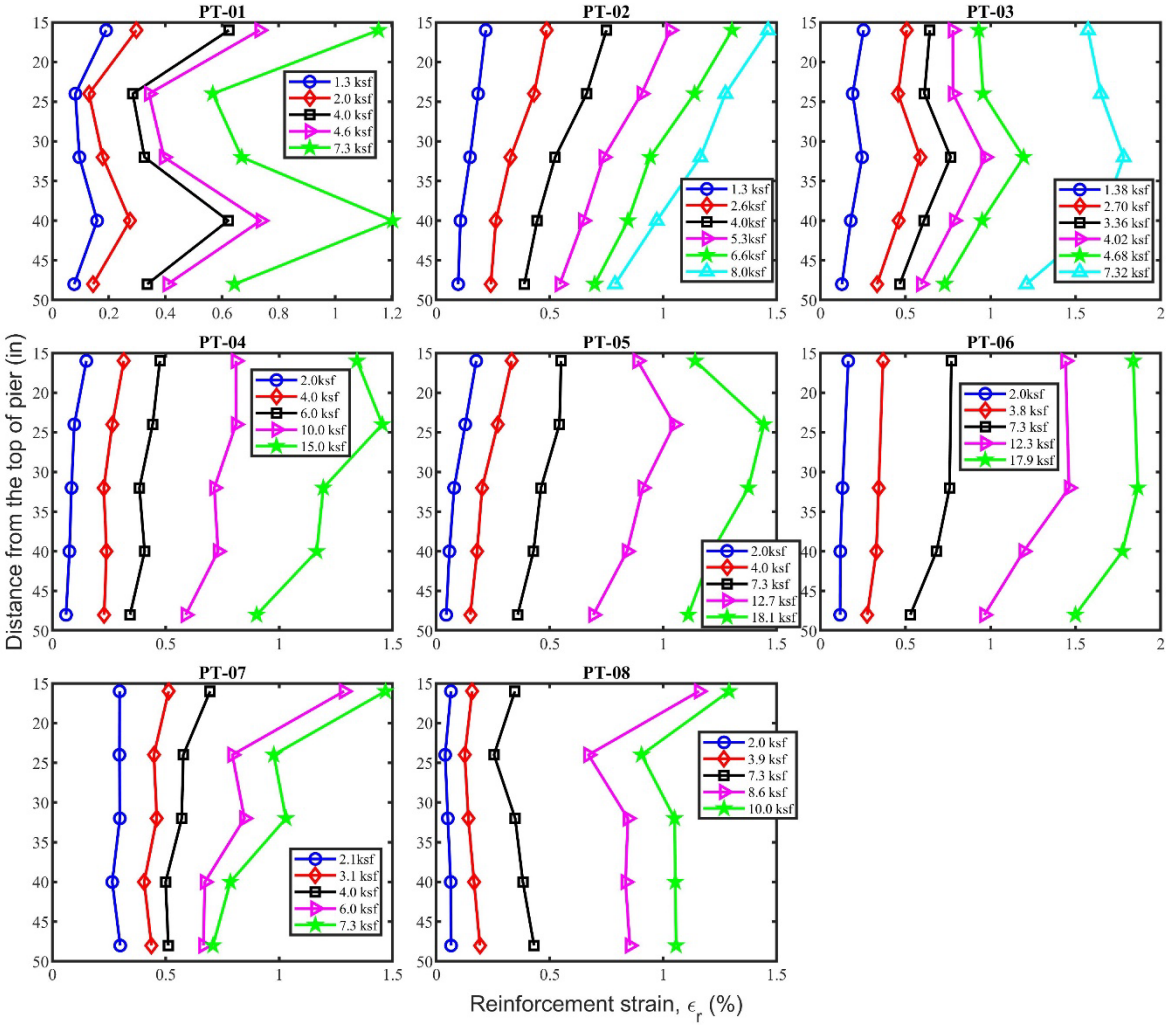

Figure 4-34. Profile of maximum reinforcement strain in geotextile at different applied vertical stresses.

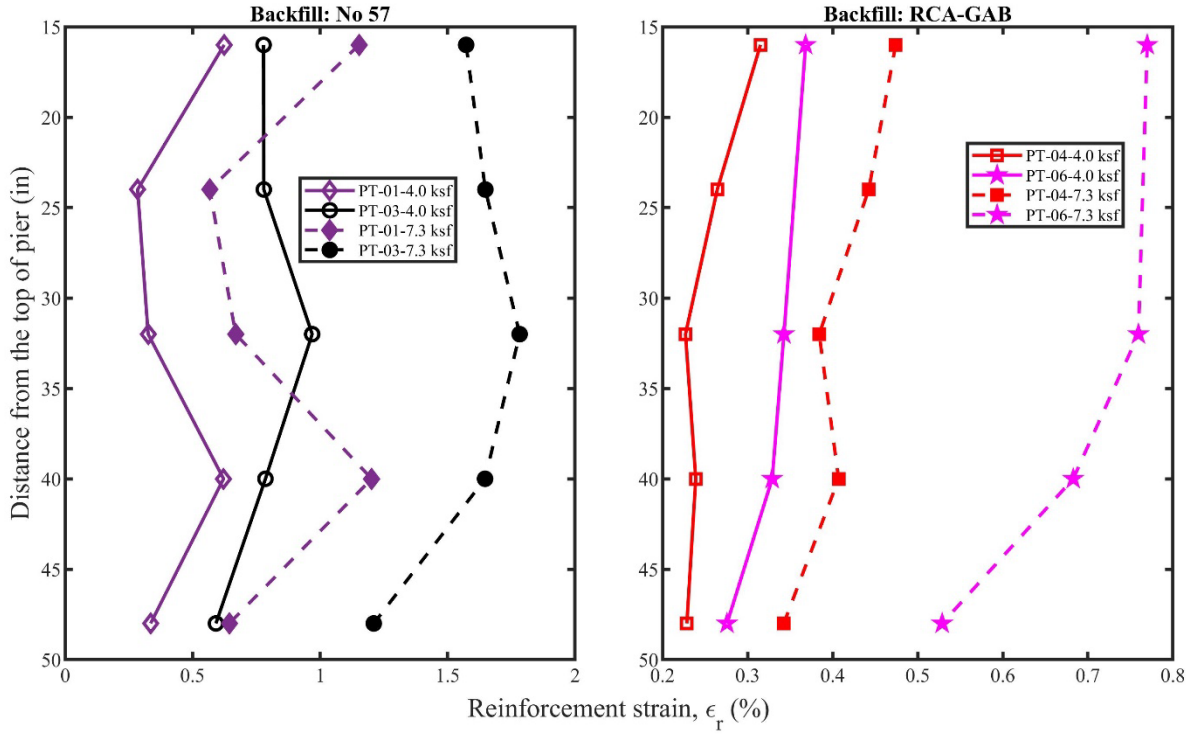


Figure 4-35. Influence of reinforcement stiffness

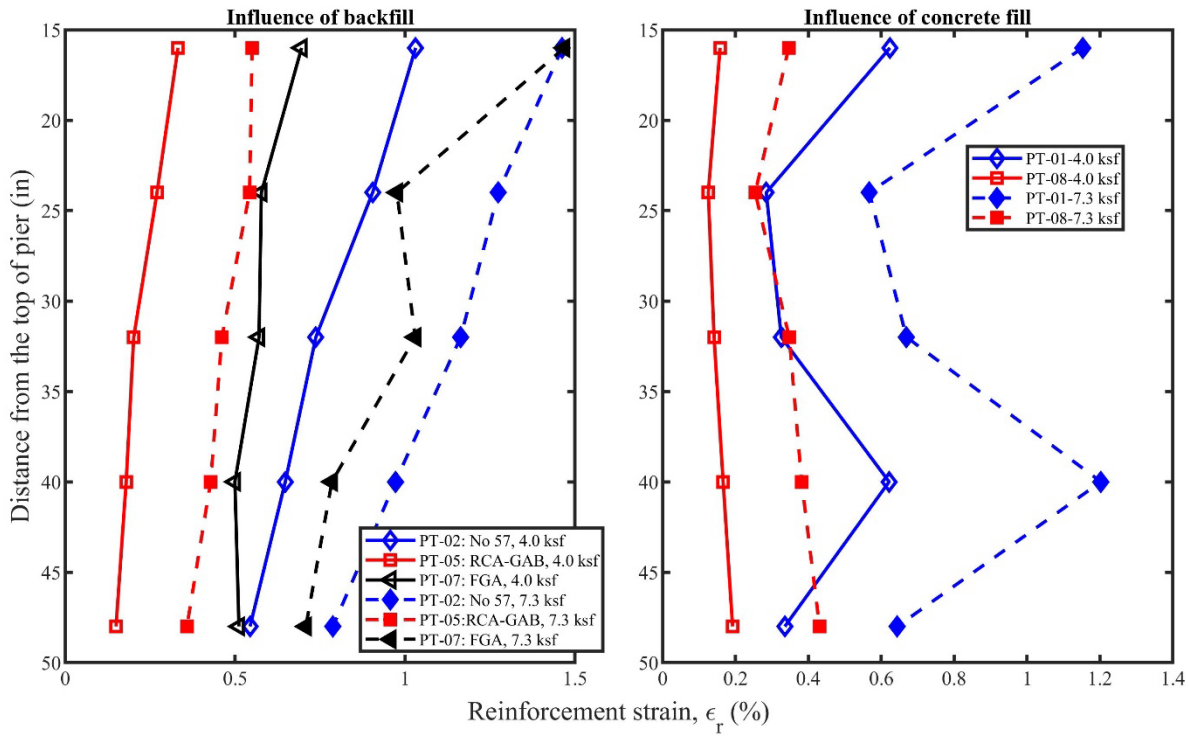


Figure 4-36. Influence of backfill and concrete fill.

## 4.7 Conclusion

A series of full-scale axial load tests of GRS piers constructed with different backfill and geotextiles materials were conducted. Their results were presented and discussed. The experimental results demonstrate that the choice of backfill, and geotextile strength has a significant impact on the behavior of GRS piers. Based on the findings in this chapter, the following conclusions are drawn:

i. For the FDOT approved aggregates, geotextile reinforcement, and facing block, the GRS piers showed axial and horizontal strains less than the recommended service limits for the design pressures of 4 ksf (unfactored dead and live loads).

ii. An experimental GRS pier with FGA showed about 0.96% vertical strain at the FHWA limit applied pressure of 4 ksf.

iii. GRS piers constructed with higher strength geotextile showed higher loading carrying capacity than the ones with lower strength geotextile.

iv. GRS piers constructed with higher strength backfill showed higher stiffness and load carrying capacity than those with lower strength backfill.

v. The use of concrete fill on the top courses of blocks has little effect on the ultimate capacity of the GRS pier.

vi. The use of concrete fill on the top courses of blocks affects the global stiffness of the GRS pier when the applied vertical stress is less than 7.25 ksf. Above that, the concrete fill has no impact on the load-deformation behavior.

vii. Maximum lateral displacement occurred within the top one-third of wall height. Below the FHWA recommended service limit bearing pressure, the lateral displacements are greatest at the top of the wall.

viii. Lateral earth pressure is influenced by the reinforcement conditions.

ix. Using fiber optic strain sensors bonded to the geotextile reinforcement is an effective method of measuring tensile strains in response to the axial loading as compared to traditional resistance foil strain gauges. Advantages of the fiber optic strain sensors include: it offers more measurement points, efficient installation, and more reliable results.

x. The type of backfill materials used does not affect the strain distribution in the geotextile reinforcement, but rather the magnitude of the strain is influenced by the properties of the backfill materials. In particular, systems constructed with backfill materials of lower strength properties will exhibit higher strains than those constructed with backfill materials of higher strength properties, for a given applied vertical stress.

xi. The highest strain magnitudes occur closest to the connection points of upper layers, while they are located near the middle for lower layers of geotextile reinforcement.

xii. The maximum reinforcement strain was found to occur within the upper half of the wall heights, which was found to be true for all tested GRS piers.

# 5 COMPARISON WITH DESIGN METHODS

This chapter focuses on the comparison between experimental data and design methods, specifically examining vertical capacities, lateral deformation, earth pressures, and reinforcement loads. Each of these aspects is presented and discussed in detail. The discussion of lateral deformation centers around volumetric change assumptions, which are based on an equation commonly utilized in FHWA.

## 5.1 Capacity and Vertical Settlement of the Footing

### 5.1.1 At Service Limit

No 57 and RCA- GAB backfill used in this study meet the material's specifications for GRS-IBS. Results were compared with FHWA service and strength limits criteria for bearing pressure and vertical strains. The results in Figure 5-1 and Figure 5-2 show when the applied vertical stress was equal to the service limit of 4 ksf recommended by FHWA (Adams and Nicks, 2018), vertical strain was less than 0.55% for all pier tests except for PT-07 (FGA backfill), which is slightly below the 1% vertical strain limit recommended by the FHWA. While the FGA currently doesn't meet the FHWA or FDOT specifications on acceptable GRS backfill, a few abutments in Pennsylvania and New York have recently been built using it and PT-07 had a vertical strain of 0.96 % at 4 ksf vertical stress.

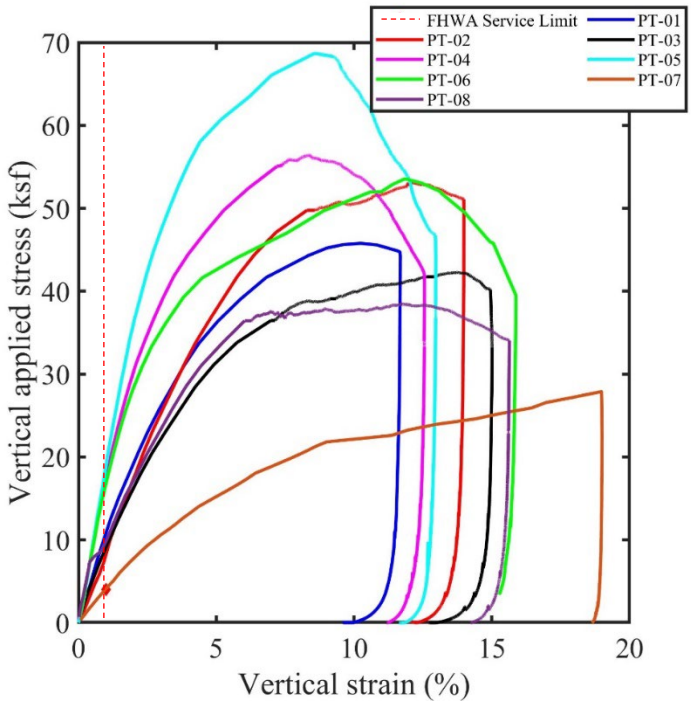


Figure 5-1. A plot of applied vertical stress versus vertical strain.

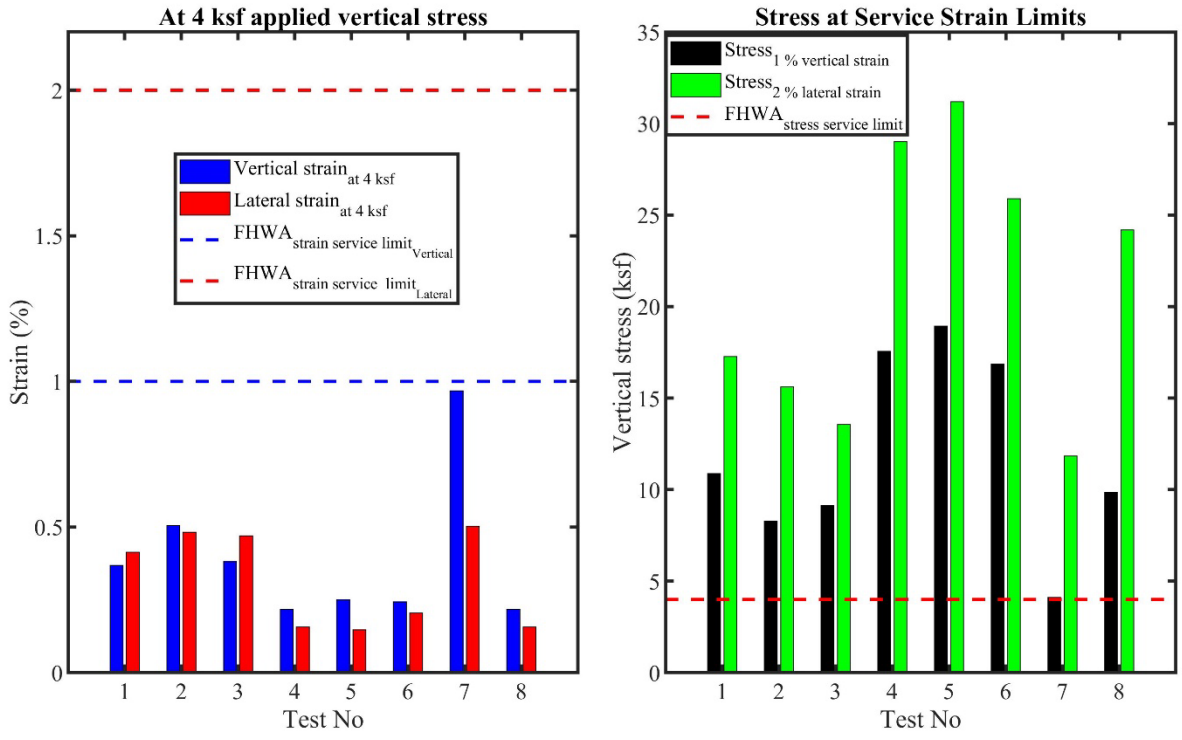


Figure 5-2. Stress and strain at FHWA service limits.

### 5.1.2 At Strength Limits

#### 5.1.2.1 FHWA Capacity Equation

FHWA recommends using the analytical equation proposed by Pham (2009), Wu and Pham (2013) and Wu et al. (2013) to calculate the ultimate capacity of GRS composites. The equation was developed based on the concept of apparent cohesion, confinement pressure, and average stresses. This equation is recommended for internal stability design of GRS-IBS by FHWA. To assess the performance of the piers at their strength limit, the measured capacities were compared with those computed using the FHWA ultimate capacity equation (Equation (5-1)). According to the results of triaxial tests, No. 57 and RCA-GAB aggregates behave differently under triaxial compression. RCA-GAB aggregates demonstrate strain hardening until reaching peak strength at approximately 1 to 2.5% axial strain, followed by softening until the end of the test. In contrast, No. 57 aggregates exhibit strain hardening until the end of the test across all specimens and confining pressures, without a distinct intermediate peak strength. All piers constructed with RCA-GAB reached their capacity at strains greater than 8%, which is beyond the range where peak strength was observed in triaxial tests. Therefore, based on the triaxial tests, aggregates in the piers with RCA-GAB can be assumed to be in the residual state when GRS piers fail. Three different friction angles of the aggregates from triaxial testing were used in the calculations of vertical capacity using the FHWA ultimate capacity equation: peak, ultimate, and secant friction angles. Secant friction angles were computed from the triaxial stress-strain curve using the axial strain at which each GRS pier failed.

Figure 5-3 shows comparisons of the measured and predicted vertical capacities for all piers. The comparison indicates that the equation consistently underpredicts the GRS vertical capacities of piers constructed with No. 57, regardless of which friction angle from the triaxial test is used. For piers with RCA-GAB, using the peak friction angle led to an overprediction of vertical capacity with a mean bias of 0.80. Conversely, when the secant friction angle was utilized, the vertical capacity was underpredicted with a mean bias of 1.44. A more accurate prediction of vertical capacity for piers with RCA-GAB is achieved when the residual friction angle is employed, resulting in a mean bias of 1.14. The residual friction angle is more representative of the backfill under similar axial strains in the piers and triaxial tests. In the case of No. 57, a slight improvement in prediction accuracy was reached when the secant friction angle was used, resulting in a mean

bias of 1.42. Combining predictions from all piers, the lowest mean bias was obtained when the peak friction angle was applied, however the COV (stdev/mean) was higher than is the residual friction angles are used (most representative for RCA-GAB piers).

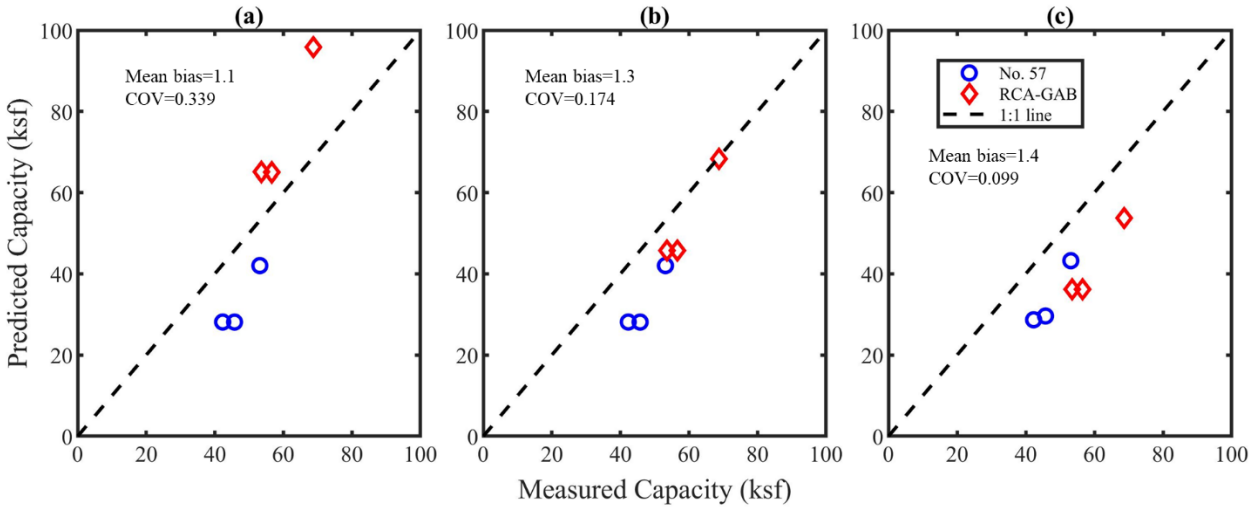


Figure 5-3. Comparison of the measured and predicted vertical capacities. (a) Based on peak friction angle; (b) Based on residual friction angle; (c) Based on secant friction angle at failure of GRS pier.

The ultimate capacity ($q_{ult,an}$) is calculated as:

$$q_{ult,an} = \left[\sigma_c + 0.7^{\left(\frac{S_v}{6d_{max}}\right)} \frac{T_f}{S_v}\right] K_{pr} + 2c\sqrt{K_{pr}} \tag{5-1}$$

The coefficient of passive earth pressure ($K_{pr}$) is calculated as:

$$K_{pr} = tan^2(45 + \frac{\Phi_r}{2}) \tag{5-2}$$

The external confining pressure due to facing blocks is computed as:

$$\sigma_c = \gamma_b d \tan\delta \tag{5-3}$$

Where $q_{ult,an}$ is the ultimate capacity, $\sigma_c$ is the external confining pressure caused by the facing, $S_v$ is the reinforcement spacing, $d_{max}$ is the maximum aggregate size, $T_f$ is the tensile strength of reinforcement, $\Phi_r$ is the internal friction angle of the reinforced backfill, $c$ is the cohesion of the backfill, $\gamma_b$ is the unit weight of facing block, $\delta$ is the interface friction angle between geosynthetic and the facing block, $d$ is the depth of the facing block unit, and $K_{pr}$ is the coefficient of passive earth pressure.

#### 5.1.2.2 Hoffman (2015) and Hoffman and Wu (2017)'s Method

Hoffman (2015) and Hoffman and Wu (2017) proposed two equations for calculating the ultimate capacities of GRS composites. In their research, they proposed a quad chart (Figure 5-4) that illustrates the transition behavior of GRS mass from composite behavior to decoupled behavior. Composite behavior is primarily influenced by reinforcement spacing, while decoupled behavior emerges once the transition load is surpassed, and there is robust facing. Initially, the GRS mass can stand on its own and support external loads independently, a concept known as coherence. During this phase, the GRS mass behaves as a composite material, with its behavior mainly governed by closely spaced vertical reinforcement. As the vertical load increases, each reinforcement and soil layer of the GRS mobilizes, resulting in lateral deformation due to the Poisson effect. When the transition load defined in Equation (5-6) is reached, the bond between the soil and reinforcement decouples, accompanied by the failure of soil layers. Once the soil layers fail, they become plastic and move against the facing, resulting in an increase in facing pressure if facing is present. The ultimate capacity of GRS with facing can be calculated using Equation (5-7). All GRS piers tested in this study had facing blocks; therefore, Equation (5-7) was used to determine their ultimate vertical capacities. Like FHWA capacity calculations, peak, ultimate, and secant friction angles were used in the calculations of ultimate vertical capacity.

Figure 5-5 shows comparisons of the measured and predicted vertical capacities for all piers. The comparison indicates that the method overpredicts the vertical capacities for piers with RCA-GAB when the peak or residual friction angle was used in the calculation. When the peak friction angle was used in the calculation, the mean bias for piers with RCA-GAB was 0.58, while for the residual friction angle, it was 0.79. A more accurate prediction of vertical capacity for piers with RCA-GAB was achieved when the secant friction angle was used, resulting in a mean bias of 0.99. In the case of piers constructed with No. 57 aggregates, the equation yields a better prediction for all friction angles used, with mean bias ranging from 0.99 to 1.03. Combining predictions from all piers, the most accurate results were obtained when the secant friction angle was applied, resulting in a mean bias of 0.99. The least accurate prediction was obtained when the peak friction angle was used, resulting in a mean bias of 0.80.

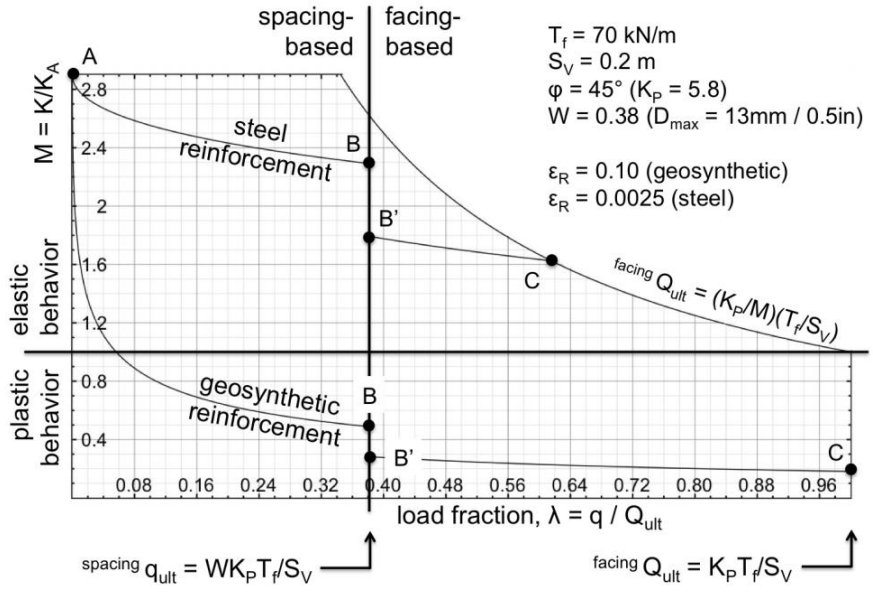


Figure 5-4. Quad chart for a soil reinforced with geosynthetic or with steel.

In the Hoffmans method, the ultimate capacity of unfaced GRS mass can be calculated as

$$q_{ult,an} = WK_{pr}\frac{T_f}{S_v} \tag{5-4}$$

Where $W$ is W-factor ($W = 0.7^{\left(\frac{S_v}{6d_{max}}\right)}$), $K_{pr}$ is the coefficient of passive lateral earth pressure.

The ultimate capacity of faced GRS mass is calculated as:

$$q_{ult,an} = K_{pr}\frac{T_f}{S_v} \tag{5-5}$$

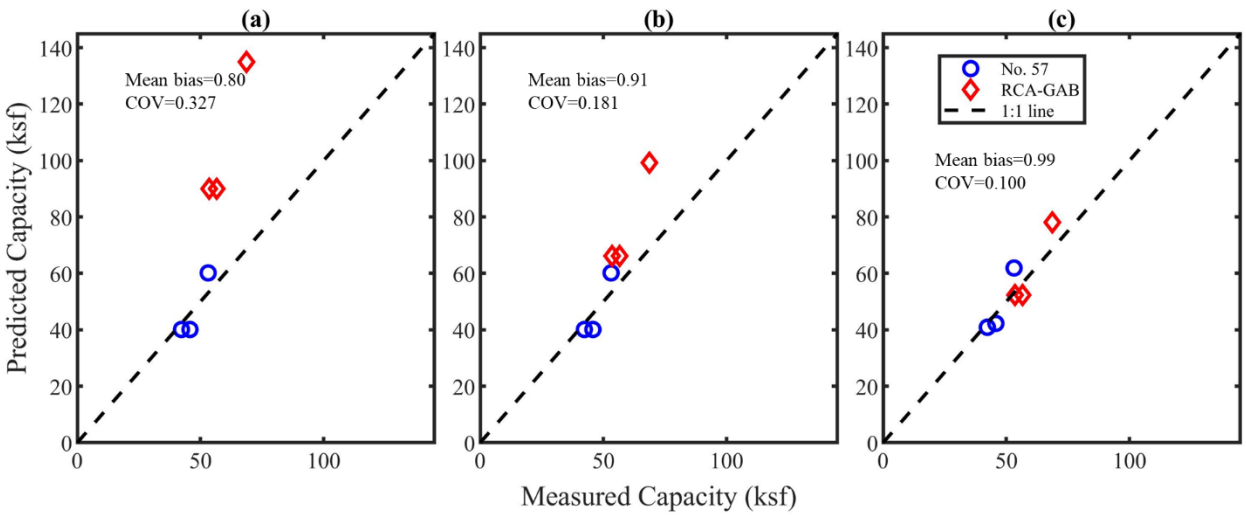


Figure 5-5. Comparison of the measured and predicted vertical capacities. . (a) Based on peak friction angle; (b) Based on residual friction angle; (c) Based on secant friction angle at failure of GRS pier.

## 5.2 Lateral Displacement of the Facing Walls

The comparison of lateral strain under the service limit bearing pressure is depicted in Figure 5-3 (a). The results from the tests indicate that the GRP piers exhibit excellent lateral deformation behavior when subjected to the service limit load. At the point where the applied vertical stress equaled the service limit applied pressure of 4 ksf, the maximum lateral strains computed from the average lateral displacements were all below the recommended limit of 2% by FHWA (Adams and Nicks, 2018), indicating that the GRP piers can handle the service limit loads without exceeding the recommended limit for lateral strain.

Lateral movement is one of the criteria utilized in the design of GRS-IBS, with FHWA recommending a maximum limit of 2 percent lateral strain for the service bearing pressure. Several methods are available for predicting lateral displacement in GRS structures, including those proposed by Jewell and Milligan (1989), Christopher et al. (1990), Wu (1994), Adams et al. (2002), Wu and Pham (2010), and Zornberg et al. (2018a). Khosrojerdi et al. (2017) evaluated these five methods, excluding the one by Zornberg et al. (2018a), and discovered that the method introduced by Adams et al. (2002), known as the "Adams method," exhibited the highest accuracy in predicting lateral displacement. In this study, the Adams method is also evaluated using experimental results from GRS piers. The method is based on the assumption of zero-volume

change in the GRS, meaning that the reduction in volume due to vertical compression is equal to the increase in volume resulting from lateral expansion of the GRS. It was developed from the load test results of the experiment commonly known as Vegas Mini Pier. Both soil and reinforcement assumed to strain laterally together. This method is also recommended by FHWA in the design of GRS-IBS. The computed lateral displacement is highly dependent on the vertical settlement of the GRS mass. When the vertical settlement is known, the maximum lateral deformation can be estimated using Equation (5-7). Both equations were developed based on assumptions of uniform vertical deformation and triangular lateral deformation (Adams and Nicks, 2018).

Figure 5-6 shows the comparison between the maximum measured and predicted lateral displacement for various GRS piers subjected to axial loading. The method demonstrates accurate predictions of maximum lateral displacements, particularly at lower levels of vertical applied stresses. However, with an increase in applied stress, there is a slight underprediction of the measured displacement, particularly noticeable in the case of PT-03. This deviation observed in PT-03 is attributed to the development of footing rotation during testing, leading to more lateral deformation towards one wall. To assess the Adams method's bias, Figure 5-7 and Figure 5-8 present a scatterplot of the measured and predicted maximum lateral displacement for all the tests. When outliers in PT-07 are removed, the analysis reveals that the Adams method slightly underpredicts the lateral displacement, with a bias ratio of 1.40. Notably, the comparison shows good agreement when the lateral displacement is less than 1.2 inches, with more data points close to the 1:1 line. In conclusion, the method demonstrates overall good performance in predicting the maximum lateral displacement.

Maximum lateral deformation for GRS wall where on side is allowed to deform is calculated as:

$$D_L = \frac{2b_{q,vol}D_v}{H} \tag{5-6}$$

In the GRS pier, four facing walls are allowed to deform, therefore the above equation is modified to:

$$D_L = \frac{2b_{q,vol}D_v}{H} x \frac{1}{4} \tag{5-7}$$

Where $D_L$is the maximum lateral deformation, $D_v$ is the vertical settlement of GRS abutment, $b_{q,vol}$ is the width of the load along the top of the wall, and $H$ is the height of the abutment.

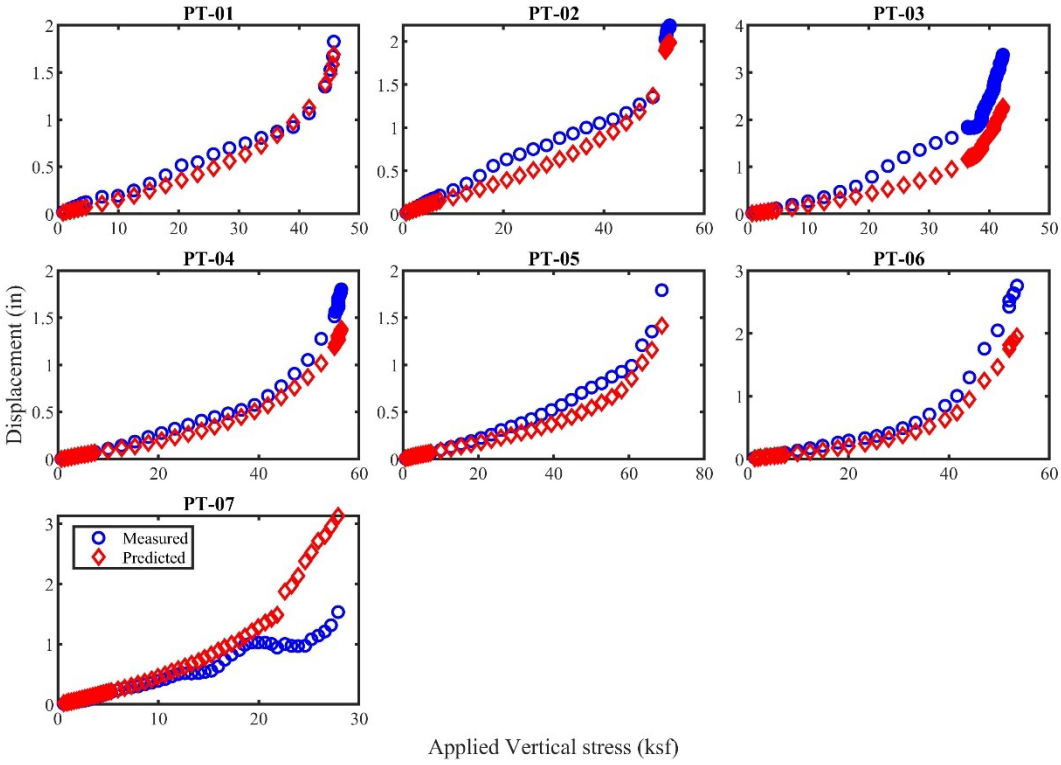


Figure 5-6. A comparison of measured and predicted maximum lateral displacement during loading.

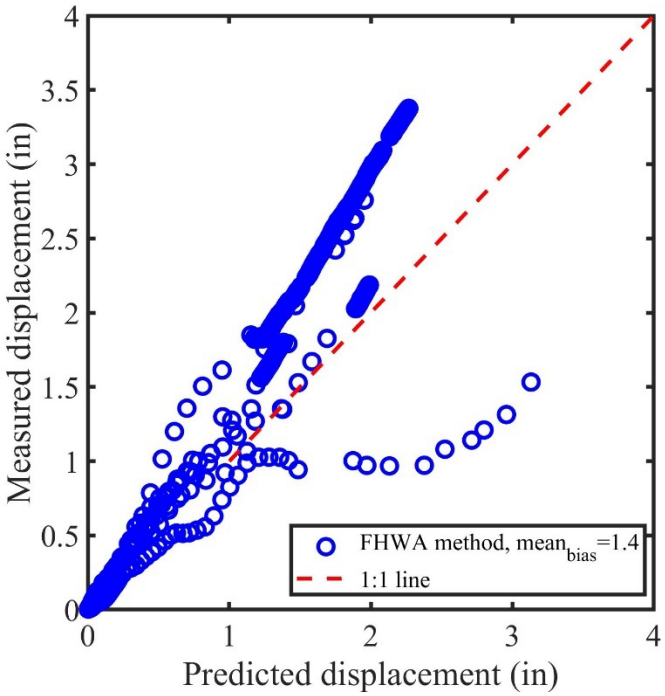


Figure 5-7. A comparison of measured and predicted maximum lateral displacement.

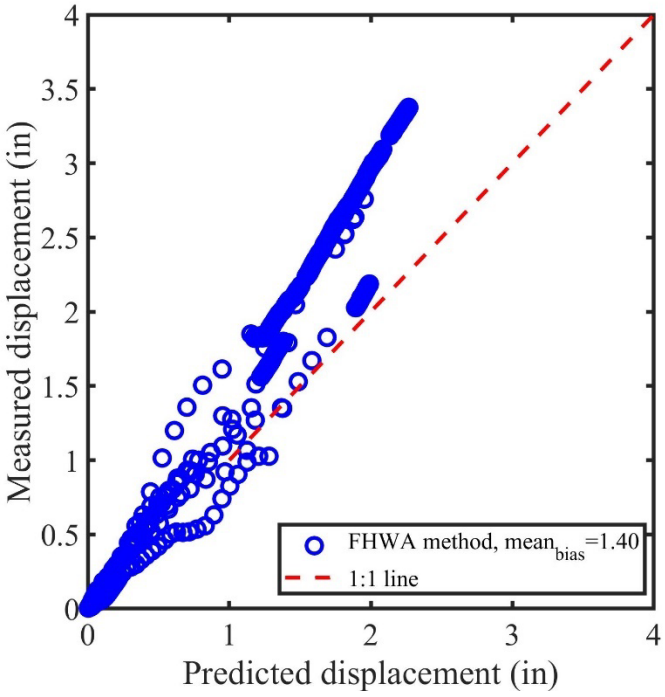


Figure 5-8. A comparison of measured and predicted maximum lateral displacement after removing the outliers in PT-07.

## 5.3 Volumetric Behavior of GRS

Adams et al. (2002) investigated volume changes during a load test on large-scale GRS mass. Based on their test result, Adams et al. (2002) proposed a "postulate of zero volume changes" for GRS structures. Using the postulate, maximum lateral displacement can be found as a function of the vertical settlement of the GRS structure. To evaluate this assumption, volume changes during the vertical loading of the pier were investigated in this study. Volume loss due to vertical settlement of footing was calculated using Equation (5-8), by taking the inside plan area of the pier times the vertical settlement. The volume gain due to lateral expansion of the GRS pier was computed by integrating the lateral displacements of facing walls multiplied by the plan area of the deformed shape of the wall assuming the corner block doesn't move as shown in Figure 5-9. Volumetric strain was computed using Equation (5-12). Comparison of volume change behavior to the applied vertical stresses is shown in Figure 5-10. Comparison of volume change behavior to the axial strain is shown in Figure 5-11 and Figure 5-12. The results show that the volume changes did not exactly follow the zero net volume change line. Initially, at applied vertical stress below 1 ksf, all piers had more vertical compression than lateral expansion. As the applied vertical stress increases, the behavior changed, with piers constructed using open-graded aggregate except PT-03, experiencing more vertical compression than lateral expansion. Piers constructed with RCA-GAB showed higher lateral expansion than vertical compression, while the pier with FGA backfill showed the highest volume change, with more vertical compression than lateral expansion, due to the brittle and soft nature of the FGA particles which fractured and crushedunder increasing compressive loading. This was evidenced from the very beginning of the test where there was more vertical compression at the top lift than lateral displacement. Post test analysis showed FGA particles in these locations were crushed significantly compared to the one at the bottom. This indicated the postulate doesn't hold for softer materials. At the failure point, the maximum changes in volumetric strain observed were 13.4% for FGA, -1.88% for No 57, and +1.85% for RCA-GAB. For loads below the service limit bearing pressure of 4 ksf, the changes in volumetric strains were below 0.14%, which is not significant, indicating that the postulate of zero volume change holds well within the service limit range.

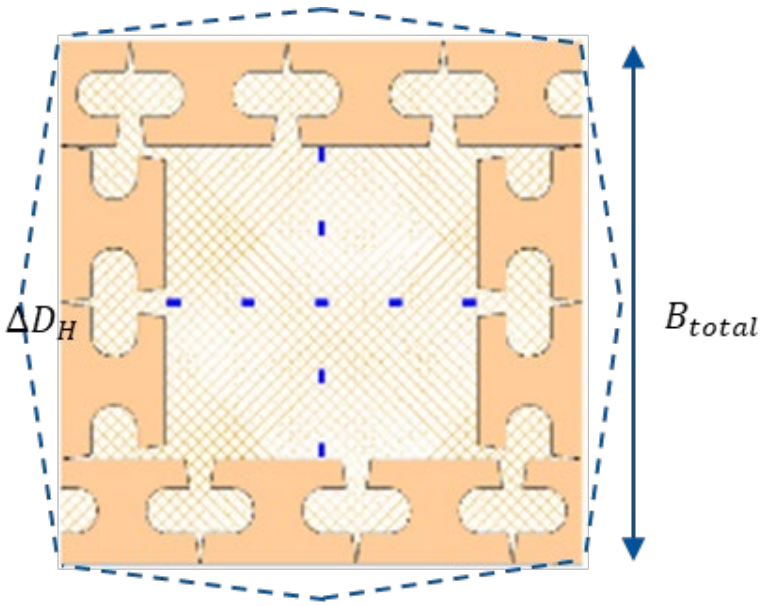


Figure 5-9. Plan view showing the assumptions of the lateral deformation.

$$\Delta V_V = A_S \, x \, \Delta D_v \tag{5-8}$$

$$A_S = B \, x \, B \tag{5-9}$$

$$\Delta V_H = \sum_{i=1}^{4} \Delta V_{L_i} \tag{5-10}$$

$$\Delta V_{L_i} = \int_0^H \left( \frac{1}{2} x \, B_{total} \, x \, \Delta D_H \right) \mathrm{d}h \tag{5-11}$$

$$\Delta \varepsilon_{L_V} = \frac{\Delta V_H - \Delta V_V}{V_o} \tag{5-12}$$

Where $\Delta V_V$ is the vertical volume change,$\Delta V_H$ is the lateral volume change, $A_S$ is the plan area of the backfill soil, $B$ is the inside width of the pier, $\Delta V_{L_i}$ is the lateral volume change on each wall, $\Delta D_H$ is the lateral displacement of the wall, $\Delta D_v$ is the vertical settlement of the footing, $\Delta \varepsilon_{L_V}$ is the volumetric strain change, $V_o$ is the original volume of the pier and $H$ is the height of the pier.

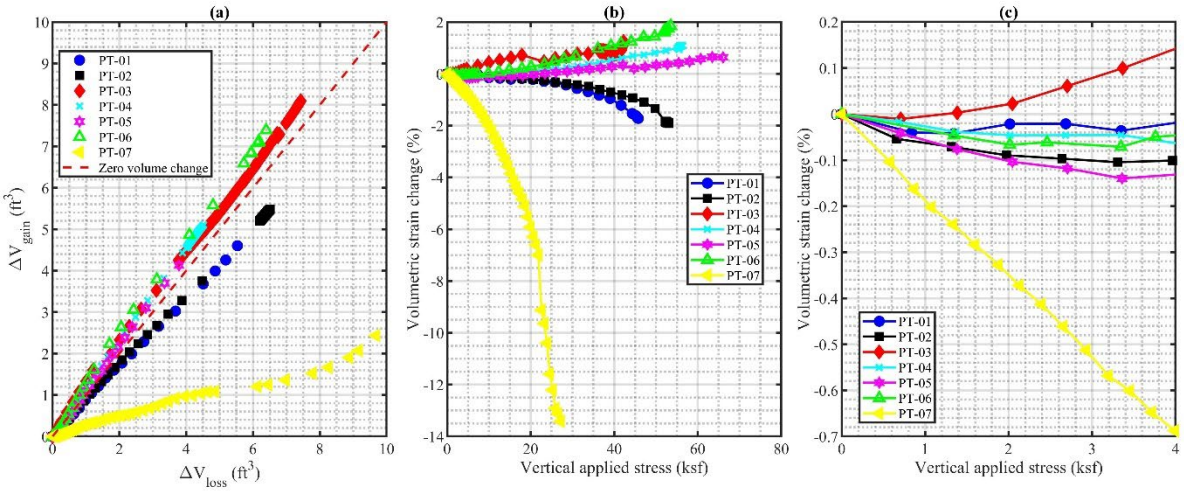


Figure 5-10. Volumetric behavior of GRS piers. (a) Comparison of volume gain versus volume loss for different piers (b) Volumetric strain change as a function of applied vertical stress up to failure (c) Volumetric strain change as a function of applied vertical stress up to 4 ksf.

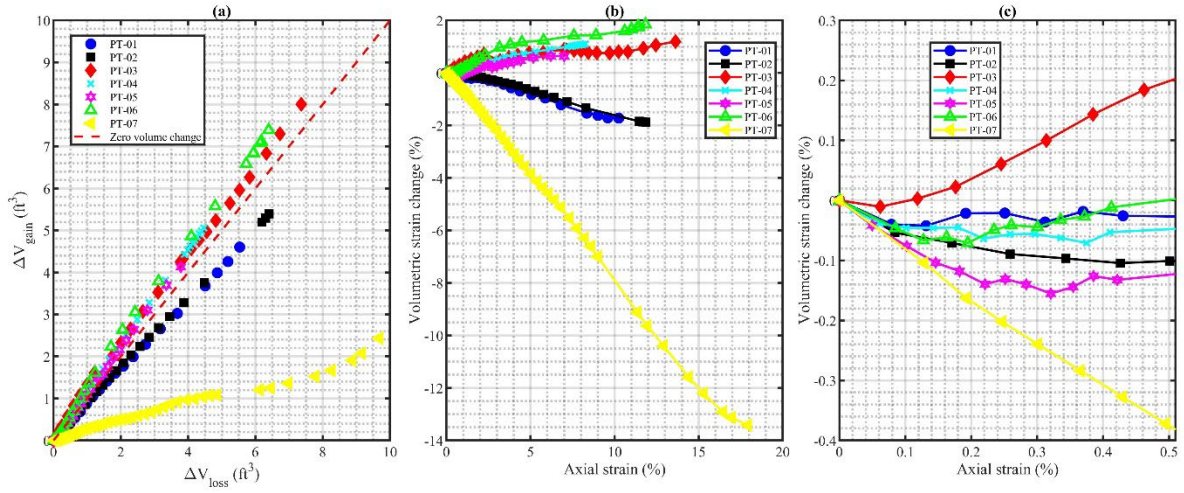


Figure 5-11. Volumetric behavior of GRS piers. (a) Comparison of volume gain versus volume loss for different piers (b) Volumetric strain change as a function of axial strain up to failure (c) Volumetric strain change as a function of axial strain up to 0.5 % axial strain.

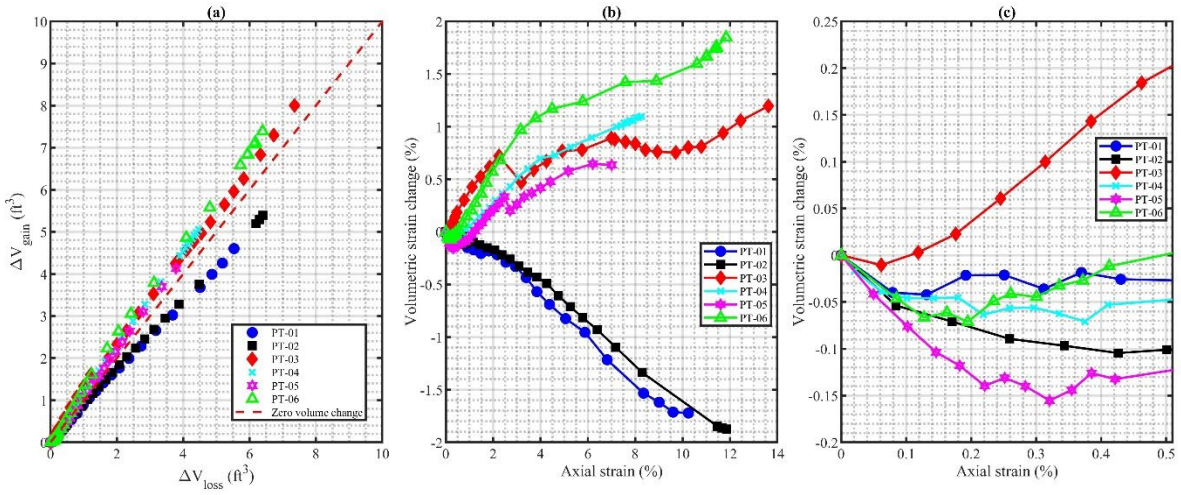


Figure 5-12. Volumetric behavior of GRS piers after removing PT-07. (a) Comparison of volume gain versus volume loss for different piers (b) Volumetric strain change as a function of axial strain up to failure (c) Volumetric strain change as a function of axial strain up to 0.5 % axial strain.

## 5.4 Reinforcement Strains

### 5.4.1 Reinforcement Strain and Lateral Displacement

Bathurst et al. (2002) investigated the short-term strain and behavior of geosynthetic walls under working stress conditions. To evaluate the accuracy of the interpretation of measured reinforcement strains from strain gauges, Bathurst et al. (2002) suggested comparing them to the lateral displacement of the facing wall. This was achieved by converting the measured reinforcement strains into lateral displacement by integrating them along the length of the reinforcement where measurements were taken. A similar approach was used in this study. However, this method has some limitations. It assumes that all reinforcement strains result in lateral movement of the walls, which is not always the case. Additionally, it does not take into account any reinforcement strains at the connection points between the blocks, which would affect the results. Due to the difficulty in measuring the strains at the connections, most fiber optic strain sensors were installed with an offset of at least 0.25 inches from the facing walls, meaning deformations in areas without fiber are neglected. Figure 5-13 illustrates the assumptions used in the strain integration method.

An example of estimated lateral displacement using the strain integration method (Equation (5-15)) is shown in Figure 5-14 for PT-5 test. It can be seen that the strain-derived displacements

match the pattern of the maximum reinforcement strain profile, and the location of maximum displacement coincides with the peak reinforcement strain. As the applied vertical stress increases, the estimated lateral displacements increase for both tests, regardless of the geotextile type. A comparison between the estimated and actual measured lateral displacements is shown in Figure 5-15 for different performance tests. When the applied vertical stress is equal to the recommended service limit applied pressure of 4 ksf, there is good agreement between the two measurements for piers constructed with RCA-GAB backfill, which had a higher stiffness than the No. 57 backfill and experienced smaller settlements than the piers tested with the No. 57 backfill. This suggests that the majority of the strains in these layers of reinforcement are primarily caused by horizontal movement rather than vertical movement of the backfill layers. However, when the applied vertical stress is equal to 7.3 ksf, there is a slight overestimation of the lateral displacement for both types of piers. Despite this, the difference is minimal, and it can be concluded from the comparison of the two measurements that the fiber optics effectively measured the reinforcement strains. The comparison also shows that integrating the reinforcement strains over the reinforcement length is a useful method for comparing the performance of geotextiles in GRS walls, although some of the above-mentioned limitations need to be taken into account.

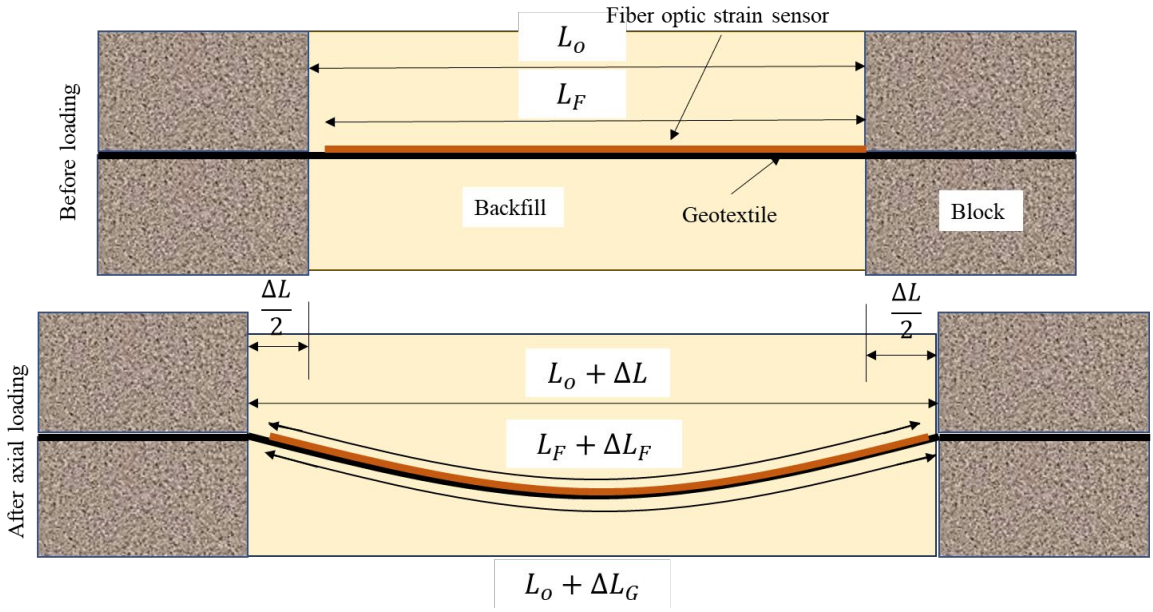

Figure 5-13. Illustration of the displacement computation from measured reinforcement strains.

The following assumptions were made during the calculation of the displacement from measured reinforcement strains.

i. The initial length of the fiber optic strain sensor ($L_F$) is approximately the same as the initial length of the geotextile ($L_G$). In the tests, the start of fiber optic strain sensors was offset by a small distance of about 6.35 mm from the facing blocks.

$$L_F \cong L_G \tag{5-13}$$

ii. The change in length of the fiber optic strain sensor ($\Delta L_F$) or geotextile ($\Delta L_G$) is approximately equal to the total lateral displacement of the facing blocks ($\Delta L$).

$$\Delta L_F \cong \Delta L_G \cong \Delta L \tag{5-14}$$

$$\Delta_{H\,integrated} = \Delta L_F = \int_0^{L_F} \varepsilon_r \, dx \tag{5-15}$$

Where $\varepsilon_r$ is the measured reinforcement strain, $L_F$ is the total length of section that fiber optic strain sensor is being considered, and $\Delta_{H\,integrated}$ is the computed lateral displacement from measured reinforcement strain.

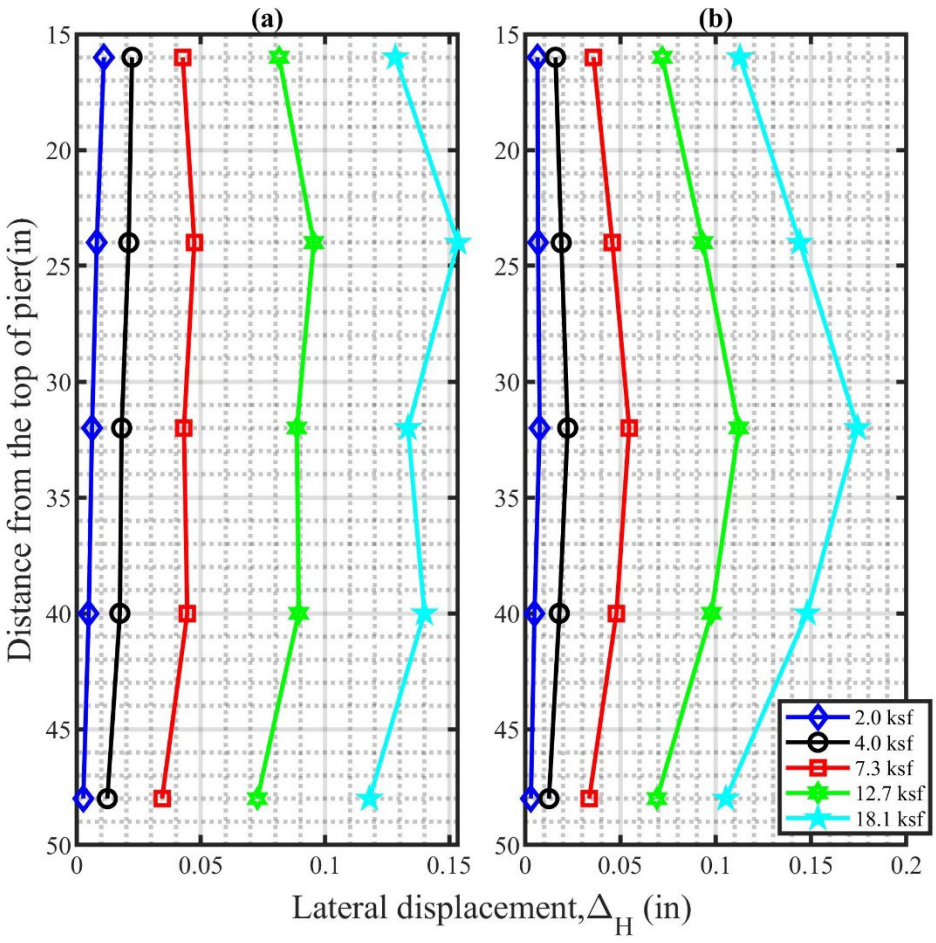


Figure 5-14. Lateral displacement estimated from integrated tensile strain at different applied vertical stresses for PT-05 test.
(a) West-East section; (b) South-North section.

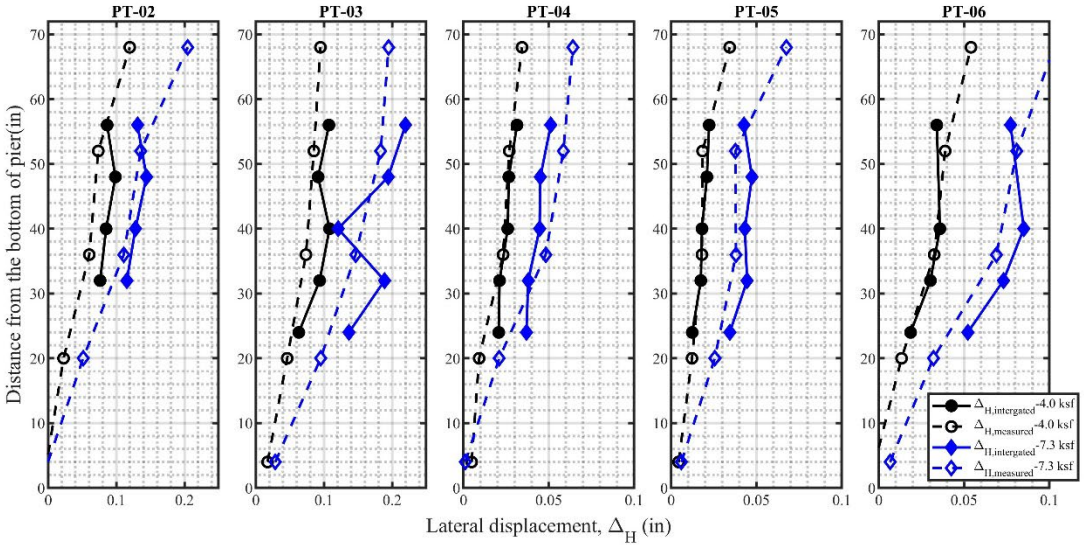


Figure 5-15. Comparison of lateral displacement estimated from the integration of reinforcement strain with measured lateral displacement at different applied vertical stresses.

### 5.4.2 Reinforcement Loads

One of the parameters considered in the design of GRS structures is the reinforcement strength of geosynthetics. The tensile forces developed in the geosynthetic due to the self-weight of the soil and applied loads should not exceed its strength. To investigate this, the relationship between strain and reinforcement load, as expressed in Equation (5-16), is used to calculate the reinforcement loads in the geotextile layers during pier loading. The stiffness modulus at 2% strain was used, which was determined according to the ASTM D4595 standard where unconfined geotextile is tested in tension. Figure 5-18 shows the profile of measured reinforcement loads at different applied vertical stresses. Measured reinforcement loads exhibit a pattern similar to the strain profile, with the reinforcement loads increasing as the load is applied. Geotextile layers in GRS piers built using RCA-GAB experience lower reinforcement loads than those constructed using No. 57.

After obtaining the measured reinforcement loads, the Simplified AASHTO, FHWA GRS-IBS, K-Stiffness, and Elton and Patawaran (2005)'s methods were used to predict the reinforcement loads using Equations (5-24), (5-26), (5-28), and (5-36), respectively. These methods require lateral earth pressure to compute the reinforcement load. Three different methods were used to estimate the vertical earth pressure: an approximate method (2:1), Boussinesq theory

and Westergaard solution for AASHTO and FHWA GRS-IBS methods. Then the computed vertical earth pressure was converted to lateral earth pressure by multiplying it with coefficient of lateral earth pressure. During each test, the fiber optic strain sensors were zeroed before the load application, and therefore, the measured reinforcement strains were only due to the applied load. The component due to the self-weight of soil was not considered in the calculations using any method, and load factors were not applied in the calculation of predicted loads. Peak, ultimate friction and secant friction angles based on triaxial tests were used in the calculation of the predicted loads, which is reasonable given the boundary conditions of the GRS piers.

Figure 5-19 through Figure 5-21 compares the maximum reinforcement load profile between the measured and predicted reinforcement loads. As expected, the predicted reinforcement loads increase with an increase in applied load. AASHTO and FHWA GRS-IBS methods show the maximum reinforcement load to occur in the upper layers while decreasing as getting down from the top of the pier. This behavior was observed in some of the piers but was not consistent throughout all piers. On the other hand, the K-Stiffness method demonstrates lower reinforcement loads at the upper part of the pier height compared to the middle section of the pier. When comparing the reinforcement load profile, the FHWA GRS-IBS method based on Westergaard solution generally predicts the reinforcement load profile well, especially when the applied vertical stress is below 4 ksf. Both K-Stiffness, and Elton and Patawaran's methods underpredict the reinforcement loads. In all methods, better reinforcement profile prediction is shown most in the third and seventh reinforcement layers.

Each method's bias is assessed and shown in Figure 5-22 through Figure 5-24, scatterplots of the measured and predicted reinforcement loads of all the tests with fiber optic strain sensor for vertical applied stresses of 2 ksf, 4 ksf and 7.3 ksf. Using the peak and ultimate friction angles, the FHWA GRS-IBS method based on the Westergaard solution predicts the reinforcement load better than other methods, with a mean bias ratio of 0.99 and 0.84, respectively. Regardless of the method used to estimate the reinforcement load, predicting earth pressure using an approximate method (2:1) results in underprediction of the reinforcement loads when peak and ultimate peak friction angles are used, with a mean bias ratio exceeding 1.6. AASHTO Methods with approximate 2:1 method did not perform well when the ultimate and peak friction angles were used in the prediction.

Based on the triaxial tests, RCA-GAB aggregates exhibit strain hardening until reaching peak strength at approximately 1 to 2.5% axial strain, followed by softening until the end of the test. In contrast, No. 57 aggregates exhibit strain hardening until the end of the test across all specimens and confining pressures, lacking a distinct intermediate peak strength. However, at applied vertical stresses below 7.3 ksf (which was the maximum applied vertical stress where most of the reinforcement strain measurements were available from fiber optic sensors), neither aggregate is in its peak or residual state based on the triaxial stress-strain results. Therefore, an assumption was made to calculate the secant friction angles of each aggregate material at which the reinforcement strain measurements were taken. It was assumed that the stress state of the aggregate backfill during the initial loading of the GRS pier is equivalent to that during the triaxial compression loading. This assumption was supported by the stress-strain behavior results of the GRS pier tests, which indicated that during the initial loading of the pier, most of the stresses are carried by aggregates rather than reinforcements. The reinforcement loads were then calculated by replacing the peak and ultimate friction angles with the secant friction angle. The comparison of predicted reinforcement loads using the secant friction angle is presented in Figure 5-24. With the exception of the FHWA GRS-IBS method based on the Westergaard solution, all methods yield mean bias ratios ranging from 0.7 to 1.35. The AASHTO method based on the Boussinesq method outperforms other methods when secant friction angles are used which results in a bias ratio of 1.03. The FHWA GRS-IBS method based on the Westergaard solution overpredicted the reinforcement load with a mean bias ratio of 0.49. Based on the comparison, it can be concluded that the FHWA GRS-IBS method based on the Westergaard solution is better at predicting the reinforcement load for the GRS piers when using ultimate and residual friction angles, while the AASHTO method based on the Boussinesq method is better when the secant friction angle is used. Lastly, comparison of reinforcement loads based on measurements from fiber optic sensors provides additional support for the usefulness of fiber optic sensors in reinforcement strain measurement in geotextiles.

Reinforcement load ($T_{F,i}$) in the geotextile was computed from measured strains as:

$$T_{F,i} = J_c \times \varepsilon_i \tag{5-16}$$

***2:1 Approximate method***

In this method, the increase in vertical stress ($\Delta\sigma_z$) due to surcharge load is estimated using Equation (5-18). The footing at the top of GRS pier was treated as isolated footing and not strip footing.

$$\Delta\sigma_z = \frac{Q_v}{D_1(L+z)} \tag{5-17}$$

$$D_1 = b_f + z\,, for\ z \leq z_1 \tag{5-18}$$

$$D_1 = \frac{b_f + z}{2} + d, for\ z > z_1 \tag{5-19}$$

Where $D_1$ is the effective width of applied load at any depth, $b_f$ is the width of the footing, $L$ is the length of the footing, $Q_v$ is a load on isolated footing, $z_1$ is the depth where effective width intersects back of wall face, and $z$ is the depth of a stress point below footing.

***Boussinesq theory***

FHWA recommends the use of this method to calculate stress increase due to surcharge load. The increase in vertical stress due to applied load from a strip footing is calculated using the following expression:

$$\Delta\sigma_z = \frac{q}{\pi}[\propto + \sin(\propto)\cos\propto + 2\beta] \tag{5-20}$$

where $q$ is surcharge pressure, and $\propto$ and $\beta$ are inclination angles for a point of interest.

However, the concrete footing was square in shape, therefore the solution of Boussinesq equations proposed by Newmark (1935) was used to compute the change in vertical stress ($\Delta\sigma_z$) due to the applied vertical stress as:

$$\Delta\sigma_z = \frac{q}{4\pi}\left[\left(\frac{2mn(m^2+n^2+1)^{0.5}}{(m^2+n^2+m^2n^2+1)}\right)\left(\frac{m^2+n^2+2}{m^2+n^2+1}\right) + \tan^{-1}\left(\frac{2mn(m^2+n^2+1)^{0.5}}{m^2+n^2-m^2n^2+1}\right)\right] \tag{5-21}$$

Where $n = \frac{L}{z}$ and $m = \frac{B}{z}$

***Westergaard solution***

As the GRS pier comprises reinforcement layers, the Westergaard method, which assumes that the soil consists of alternating layers of thin, rigid reinforcements, was also examined. This method calculates the vertical stress beneath the corner of a uniformly loaded rectangular area using Equation (5-22) (Das, 2019; Westergaard, 1938).

$$\Delta\sigma_z = \frac{q}{2\pi}\left\{\cot^{-1}\left[\eta^2\left(\frac{1}{m^2}+\frac{1}{n^2}\right)+\eta^4\left(\frac{1}{m^2n^2}\right)\right]^{0.5}\right\} \quad (5\text{-}22)$$

The parameter $\eta$ is computed as follows:

$$\eta = \sqrt{\frac{1-2v}{2-2v}} \quad (5\text{-}23)$$

where $L$ is the length of the footing, $B$ is the width of the footing, $z$ is the depth of point of interest, $n = \frac{L}{z}$, $m = \frac{B}{z}$, $v$ is poison ratio of backfill between reinforcement and $q$ is the applied pressure.

The reinforcement loads were computed using the following methods:

#### 5.4.2.1 Simplified AASHTO Method

In this method, maximum reinforcement load ($T_{max,i}$) is calculated as:

$$T_{max,i} = \sigma_H \times S_v \quad (5\text{-}24)$$

Horizontal soil stress is computed as:

$$\sigma_H = \sigma_v k_a + \Delta\sigma_H \quad (5\text{-}25)$$

Where $S_v$ is the vertical spacing of reinforcement, $\sigma_H$ is the horizontal soil stress at the reinforcement, $k_a$ is the earth pressure coefficient, $\sigma_v$ pressure due to resultant of gravity forces from soil self-weight within and immediately above the reinforced wall backfill, and any surcharge loads present, and $\Delta\sigma_H$ horizontal stress at reinforcement level resulting from any applicable concentrated horizontal surcharge load.

#### 5.4.2.2 FHWA GRS-IBS Method

In the FHWA GRS-IBS Method, the required reinforcement strength ($T_{req,i}$) which is equal to the maximum reinforcement load ($T_{max,i}$) in during pier loading is calculated as:

$$T_{req,i} = \left( \frac{\sigma_h - \sigma_c}{0.7^{\left(\frac{S_v}{6d_{max}}\right)}} \right) S_v \tag{5-26}$$

Where $T_{req,i}$ is the required reinforcement strength in the direction perpendicular to the wall face, $\sigma_h$ is the total lateral stress within the GRS composite at a given depth and location computed using Boussinesq theory, $\sigma_c$ is the external confining pressure caused by the facing, and $d_{max}$ is the maximum aggregate size.

Lateral earth pressure ($\sigma_h$) was computed as:

$$\sigma_h = \Delta\sigma_z k_a \tag{5-27}$$

#### 5.4.2.3 K-Stiffness Method

Allen and Bathurst (2003) and Allen and Bathurst (2003) proposed an empirical approach for predicting reinforcement loads in geosynthetics reinforced earth walls. The proposed equation was later modified by Bathurst et al. (2008). This method considers various factors, including soil strength, reinforcement stiffness, reinforcement spacing, facing stiffness, and facing batter. The method is useful under working stress conditions and is used for internal stability design.

In this method the maximum reinforcement load (${T^i}_{max}$) is calculated as:

$${T^i}_{max} = S_v^i \, \sigma_h D_{tmax} \, \Phi \tag{5-28}$$

Where $S_v^i$ is the tributary area (equivalent to the average vertical spacing of the reinforcement near each layer when analyses are carried out per unit length of wall), $\sigma_h$ is the lateral earth pressure acting over the tributary area, $D_{tmax}$ is the load distribution factor based on layer location that modifies the reinforcement load, and $\Phi$ is an influence factor that is the product of factors that account for the influence of local and global reinforcement stiffness, facing stiffness, and face batter.

The lateral earth pressure ($\sigma_h$) is calculated as:

$$\sigma_h = \frac{1}{2} K\gamma(H + S) \tag{5-29}$$

Lateral earth pressure coefficient ($K$) is calculated as :

$$K = 1 - \sin \phi_{ps} \tag{5-30}$$

Where $K$ is lateral earth pressure coefficient, $\gamma$ is unit weight of the soil, $H$ is height of the wall, $S$ is equivalent height of uniform surcharge pressure ($q$) calculated as $S = \frac{q}{\gamma}$, and $\phi_{ps}$ is peak plane strain friction angle.

The influence factor is calculated as:

$$\Phi = \Phi_g \, \Phi_{local} \, \Phi_{fs} \, \Phi_{fb} \tag{5-31}$$

Where $\Phi_g$ is the global stiffness factor, $\Phi_{local}$ is local stiffness factor, $\Phi_{fs}$ is the facing stiffness factor, and $\Phi_{fb}$ is the facing batter factor.

The global stiffness factor ($\Phi_g$) accounts for influence of stiffness and spacing of reinforcement layers and is computed as:

$$\Phi_g = \alpha \left( \frac{S_{global}}{p_a} \right)^{\beta} \tag{5-32}$$

Global reinforcement stiffness ($S_{global}$) is calculated as:

$$S_{global} = \frac{J_{ave}}{\left( H/n \right)} = \frac{\sum_{i=1}^{n} J_i}{H} \tag{5-33}$$

Where $p_a$ is atmospheric pressure, α and $\beta$ are constants, $J_{ave}$ is average tensile stiffness of all "$n$" reinforcement layers over the wall height, and $J_i$ is the tensile stiffness of an individual reinforcement layer.

Local stiffness factor ($\Phi_{local}$) accounts for relative stiffness of the reinforcement layer with respect to the average stiffness of all reinforcement layers and is calculated as:

$$\Phi_{local} = \left( \frac{S_{local}}{S_{global}} \right)^{a} \tag{5-34}$$

Coefficient $a$ is equal to 1 for geosynthetic reinforced soil walls.

Where $S_{local}$ is the local reinforcement stiffness for reinforcement layer i, calculated as:

$$S_{local} = \left( \frac{J}{S_v} \right)_i \tag{5-35}$$

The load distribution factor ($D_{tmax}$ ) is obtained from Figure 5-16 as a function of normalized depth below the top of wall.

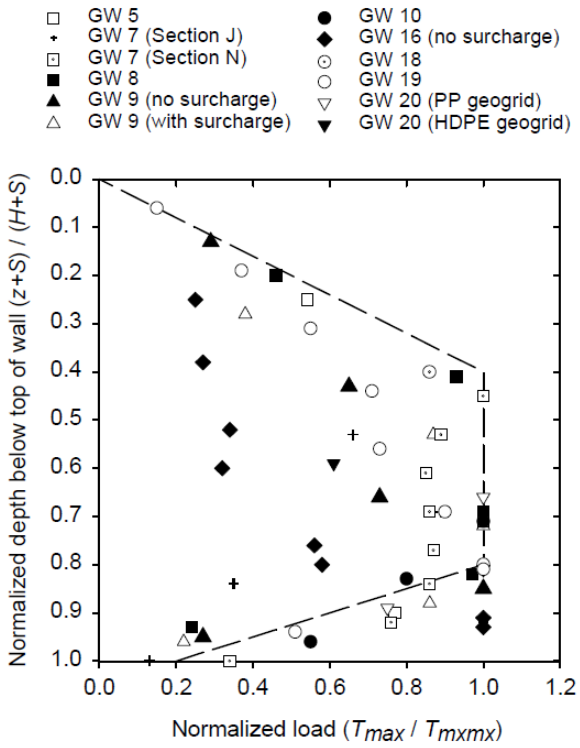


Figure 5-16. A plot of load distribution factor as a function of normalized depth.
(Allen and Bathurst, 2003)

#### 5.4.2.4 Elton and Patawaran (2005)'s Method

Elton and Patawaran (2005) developed an equation to predict maximum tensile force in the reinforcement layers. The equation was developed from the analysis of the reinforced samples tested in unconfined compression tests. The equation takes into accounts factors such as reinforcement spacing, soil strength, vertical stress and strain distribution.

The maximum tensile force ($T_{\max AU}$) in a reinforcement layer is calculated as:

$$T_{\max AU} = (K\sigma_v)\, S_v SDF \qquad (5\text{-}36)$$

Where $K$ is the lateral stress coefficient, $S_v$ is the reinforcements spacing, $SDF$ is the strain distribution factor, and $\sigma_v$ is the vertical stress.

The lateral earth pressure coefficient in this method is calculated as:

$$K = K_o - K_a \tag{5-37}$$

At rest pressure coefficient ($K_o$) is computed as:

$$K_o = \frac{1 - \sin\phi}{1 + \sin\phi}\left(1 + \frac{2}{3}\sin\phi\right) \tag{5-38}$$

Active earth pressure coefficient is calculated as:

$$K_a = tan^2\left(45 - \frac{\phi}{2}\right) \tag{5-39}$$

The strain distribution factor ($SDF$) is obtained from as a function of normalized depth as shown in Figure 5-17.

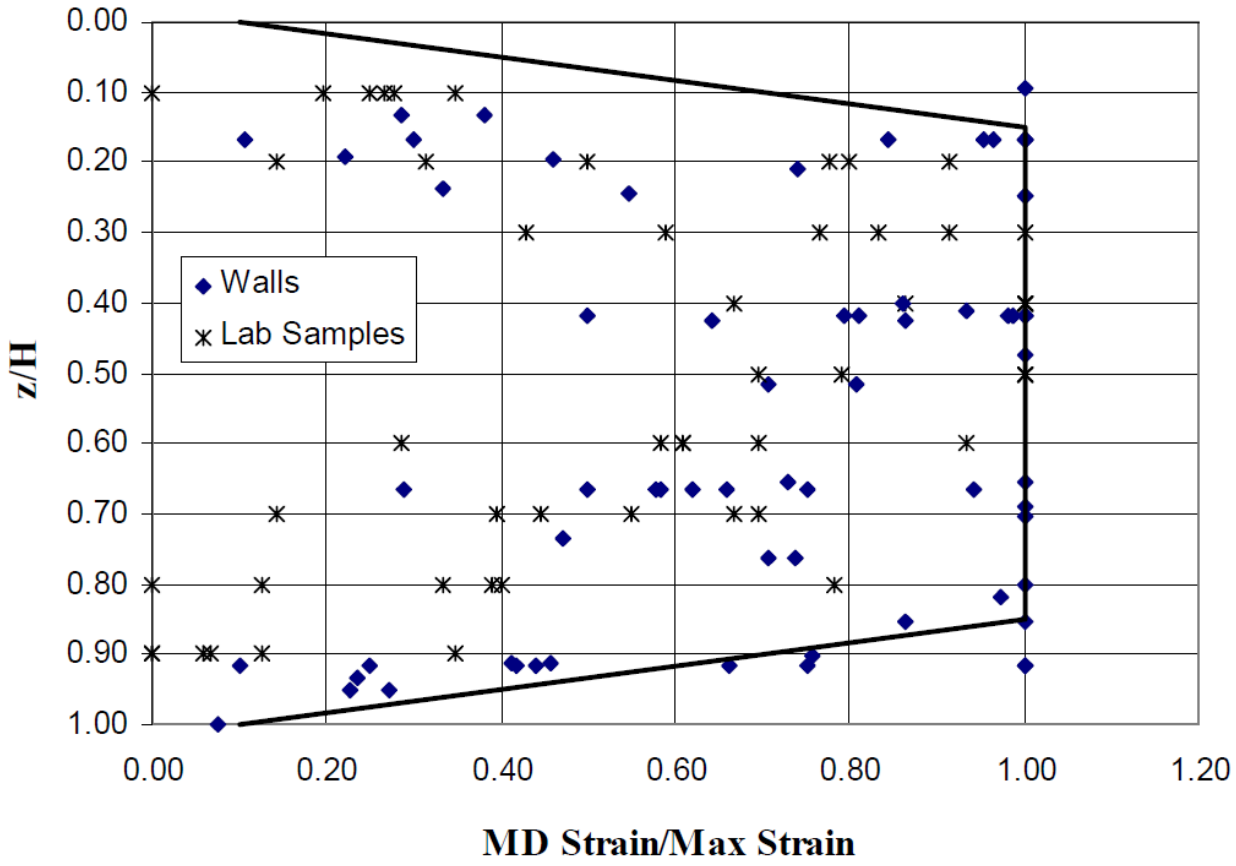


Figure 5-17. A plot of strain distribution curve as a function of normalized depth. (Elton and Patawaran, 2005).

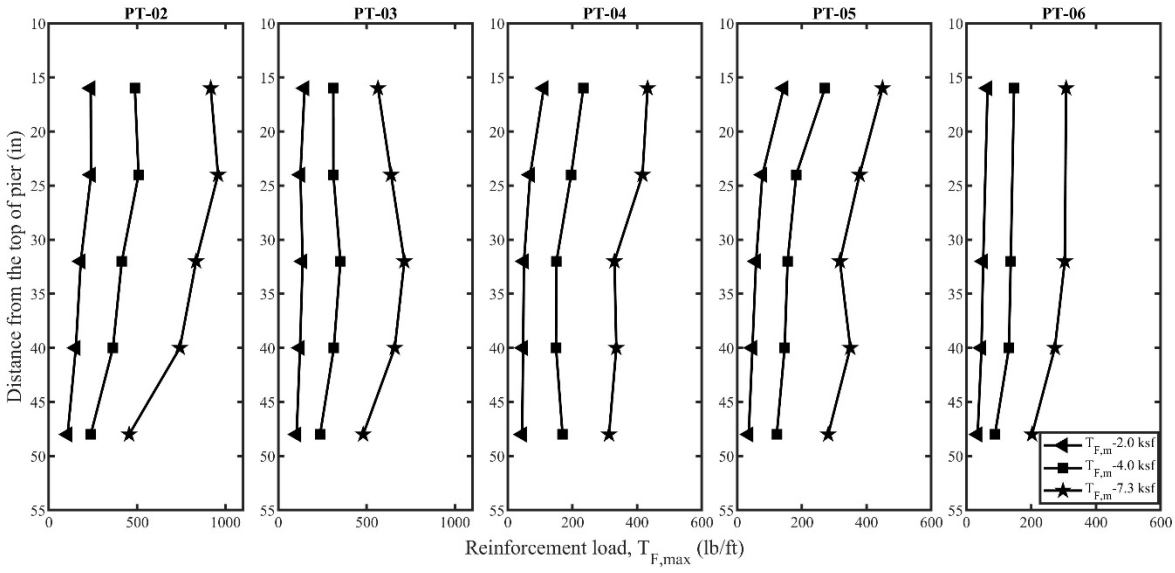


Figure 5-18. Measured reinforcement load profile from reinforcement strains.

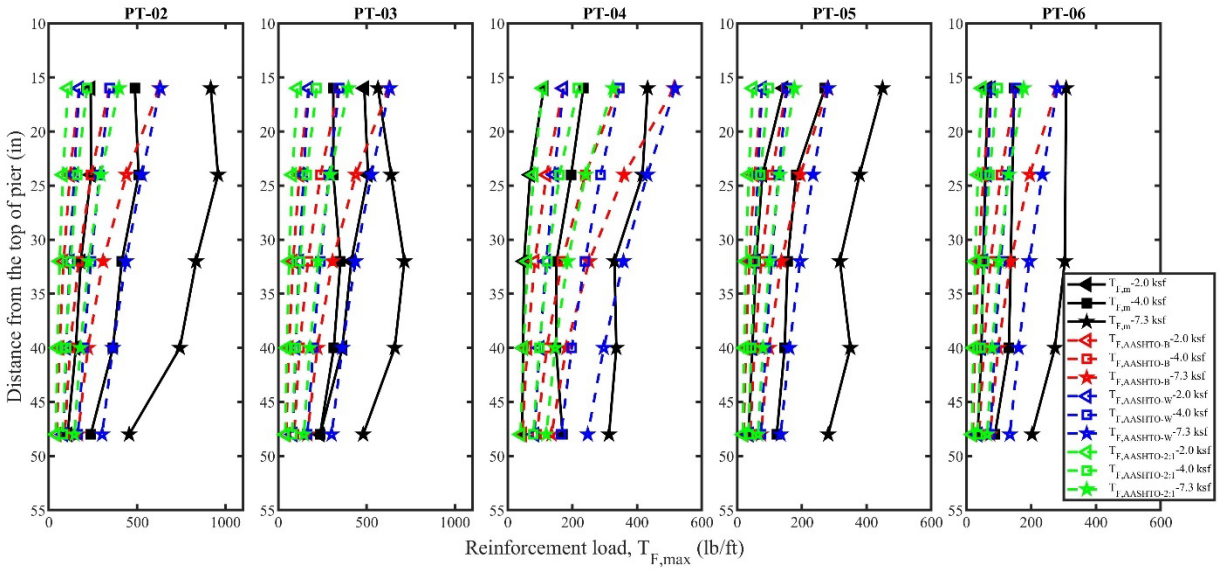


Figure 5-19. Comparison of the measured and predicted reinforcement load profile using AASHTO method.

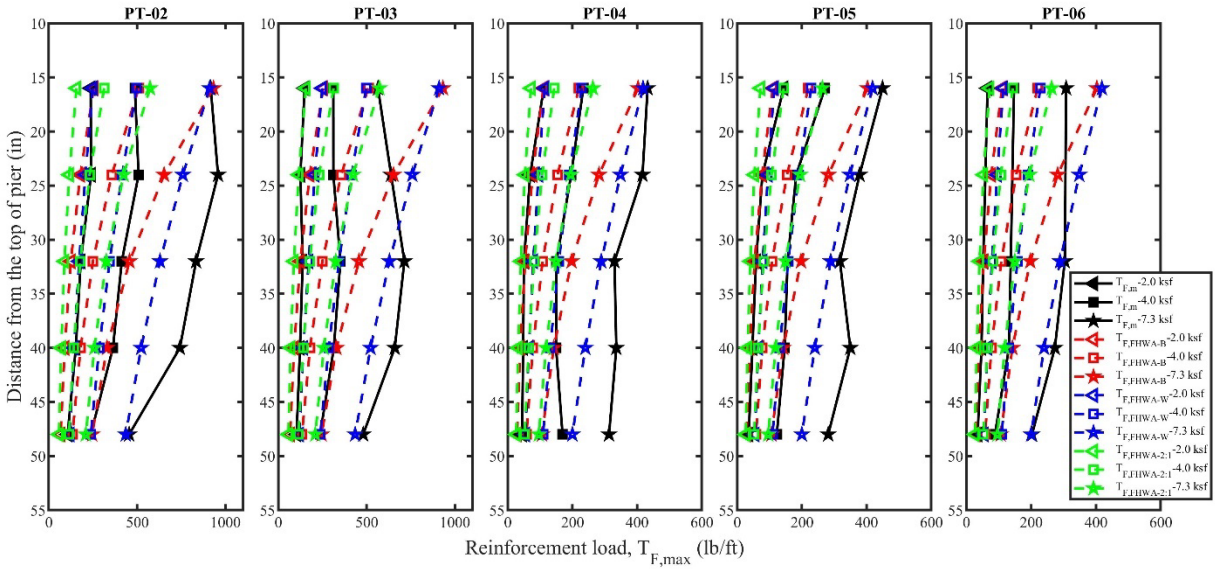


Figure 5-20. Comparison of the measured and predicted reinforcement load profile using FHWA-GRR-IBS method.

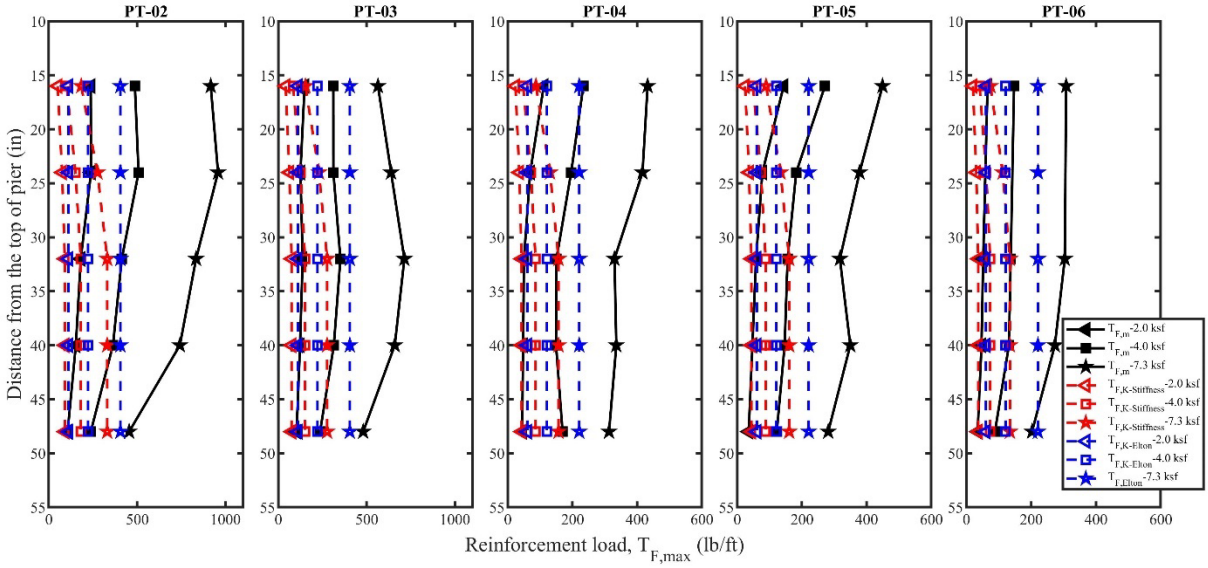


Figure 5-21. Comparison of the measured and predicted reinforcement load profile using K-Stiffness and Elton and Patawaran's method.

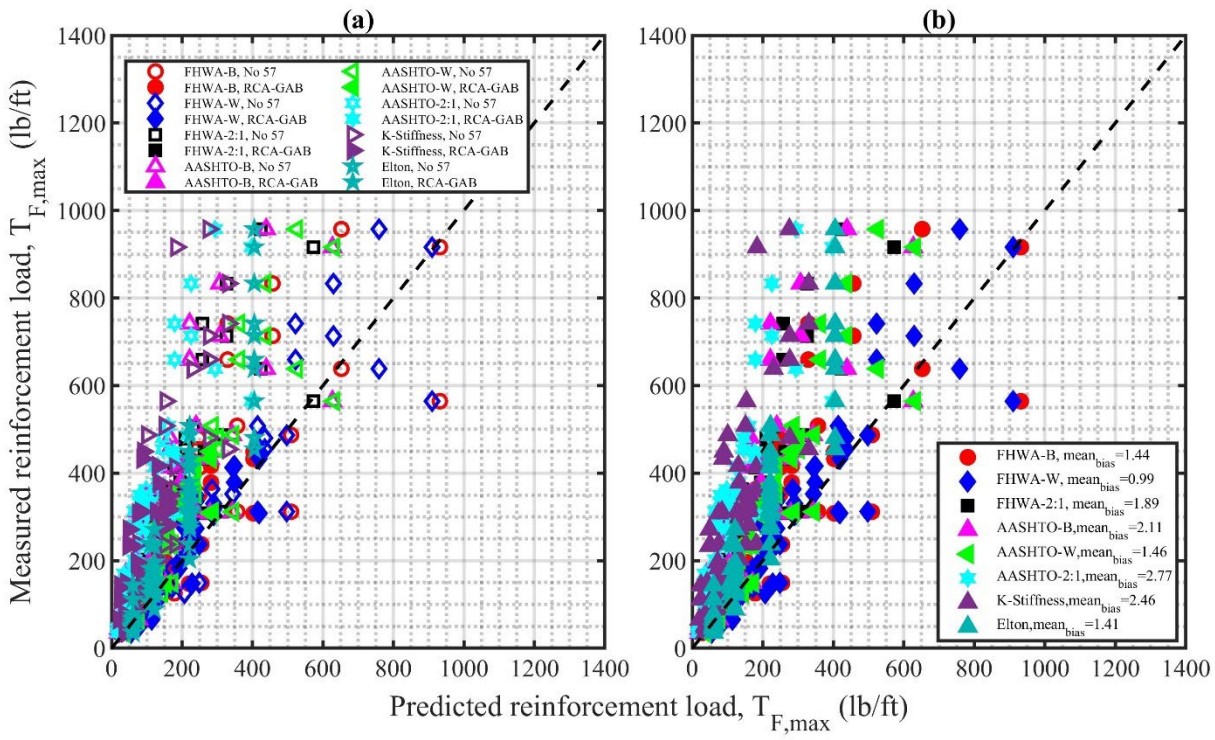


Figure 5-22. A plot of measured versus predicted reinforcement load at 2, ksf, 4 ksf and 7.3 ksf.

(Using peak friction angle (Φ), $For\ No\ 57, \Phi_{No.57} = 44.08°$; $For\ RCA-GAB, \Phi_{RCA-GAB} = 58.42°$ ): (a) Based on backfill type; (b) All combined.

( $FHWA-B$ is from reinforcement loads based on FHWA and Boussinesq method, $FHWA-W$ is from reinforcement loads based on FHWA and Westergaard solution, $FHWA-2{:}1$ is from reinforcement loads based on FHWA and approximate 2:1 method, $AASHTO-B$ is from reinforcement loads based on AASHTO and Boussinesq method, $AASHTO-W$ is from reinforcement loads based on AASHTO and Westergaard solution, and $AASHTO-2{:}1$ is from reinforcement loads based on AASHTO and approximate 2:1 method).

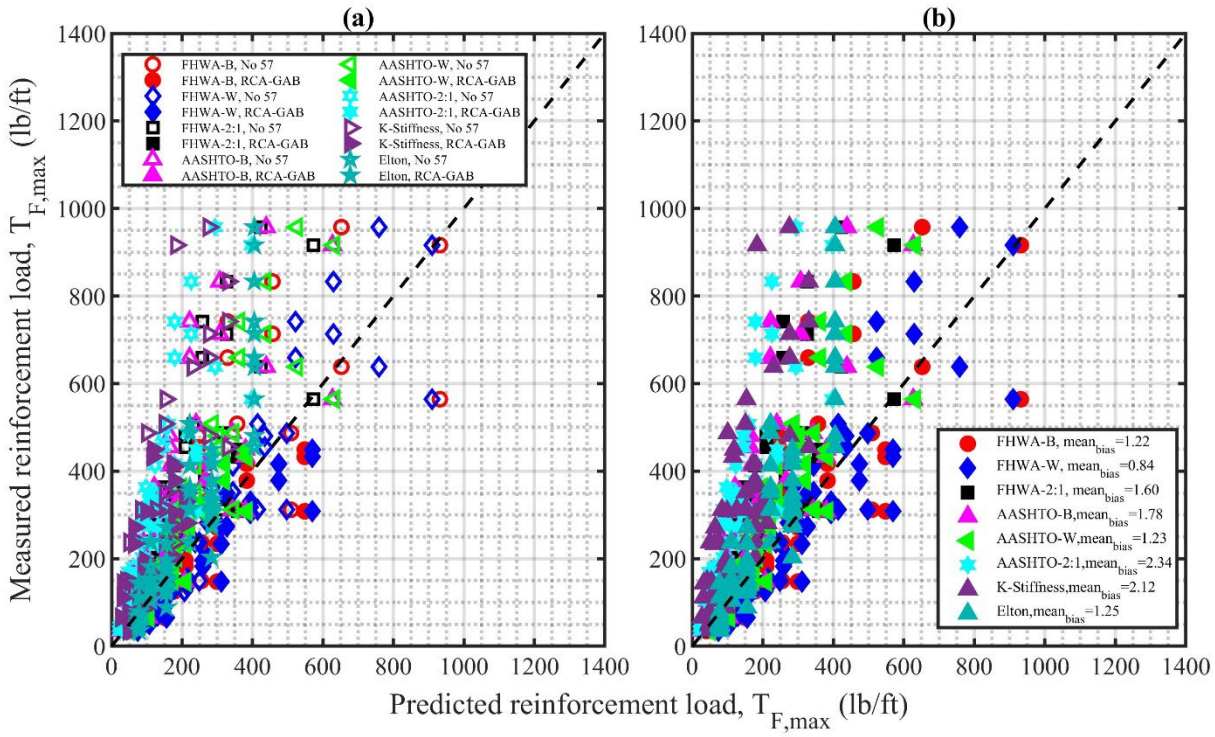


Figure 5-23. A plot of measured versus predicted reinforcement load.
(Using ultimate friction angle (Φ), $For\ No\ 57, \Phi_{No.57} = 44.08°;\ For\ RCA - GAB, \Phi_{RCA-GAB} = 53.48°$ ): (a) Based on backfill type; (b) All combined.

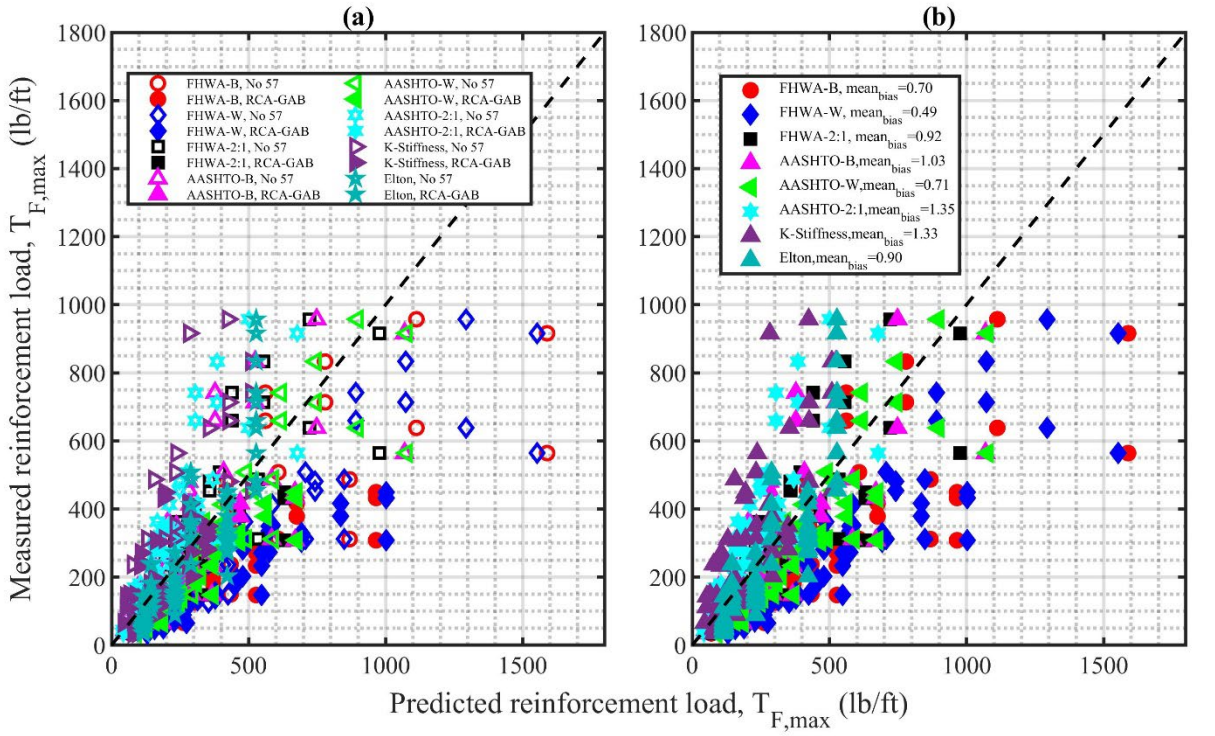


Figure 5-24. A plot of measured versus predicted reinforcement load.
(Using secant friction angle (Φ), $For\ No\ 57, \Phi_{No.57} = 32.09°;\ For\ RCA - GAB, \Phi_{RCA-GAB} = 42.7°$ ): (a) Based on backfill type; (b) All combined.

## 5.5 Lateral Earth Pressure

Figure 5-25 shows the comparison between the measured lateral earth pressure during construction and the estimated pressure based on the self-weight of the backfill. The estimated lateral earth pressure, calculated assuming an at-rest condition using Equation (5-40), is consistently lower than the measured earth pressure in both tests. This difference is attributed to the induced lateral stress during compaction. Additionally, it is important to note that the estimation method used in this analysis is applicable to unreinforced soil and does not account for the presence of reinforcement layers and induced stress from compaction.

Figure 5-26 presents a comparison of the measured and estimated lateral earth pressure distribution for PT-01 during axial loading. The vertical earth pressure was computed using the Boussinesq and Westergaard methods, which were then converted to lateral earth pressure assuming an active state condition. The active state condition was assumed because the backfill exerted sufficient pressure on the block during loading to induce an active state condition where the facing wall was moving away from soil. Equation (5-42) was used to calculate the lateral earth pressure induced by the applied load. The estimated lateral earth pressure distribution exhibits a different behavior compared to the measured distribution. The estimated pressure decreases with increasing depth from the top of the pier, while the measured pressure shows maximum values at the top and bottom of the layer, except for an applied vertical stress of 25.8 ksf, where the maximum pressure occurs in the middle of the layer. When comparing the magnitudes of the lateral earth pressure, the pressures estimated by the Westergaard method closely align with the measured values compared to those estimated by the Boussinesq method. This implies that the Westergaard method can be a more suitable approach for estimating earth pressure in reinforced soil structures.

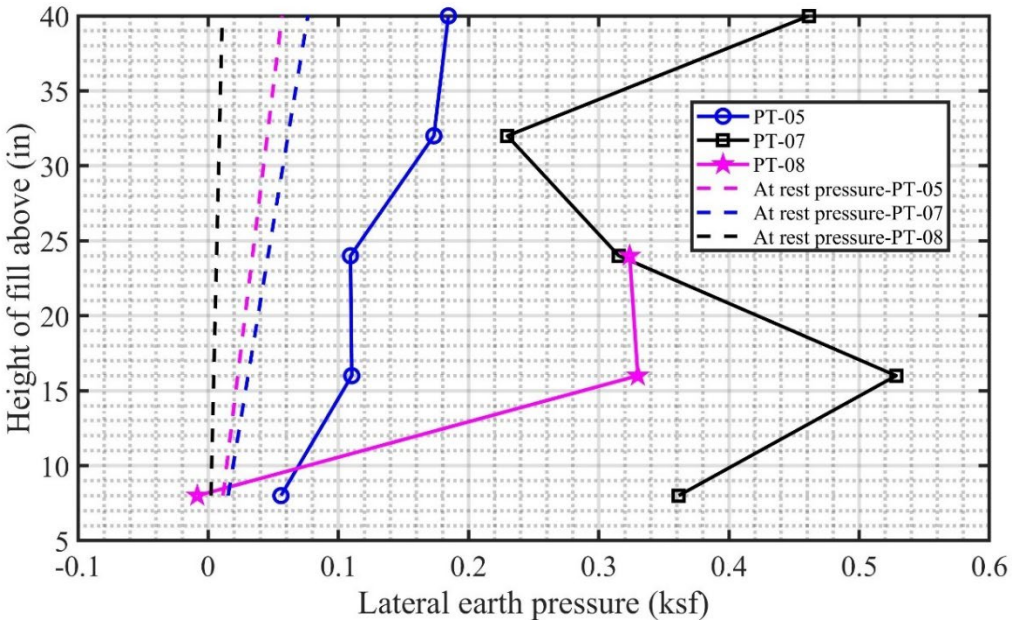


Figure 5-25. Comparison of lateral earth pressure during construction.

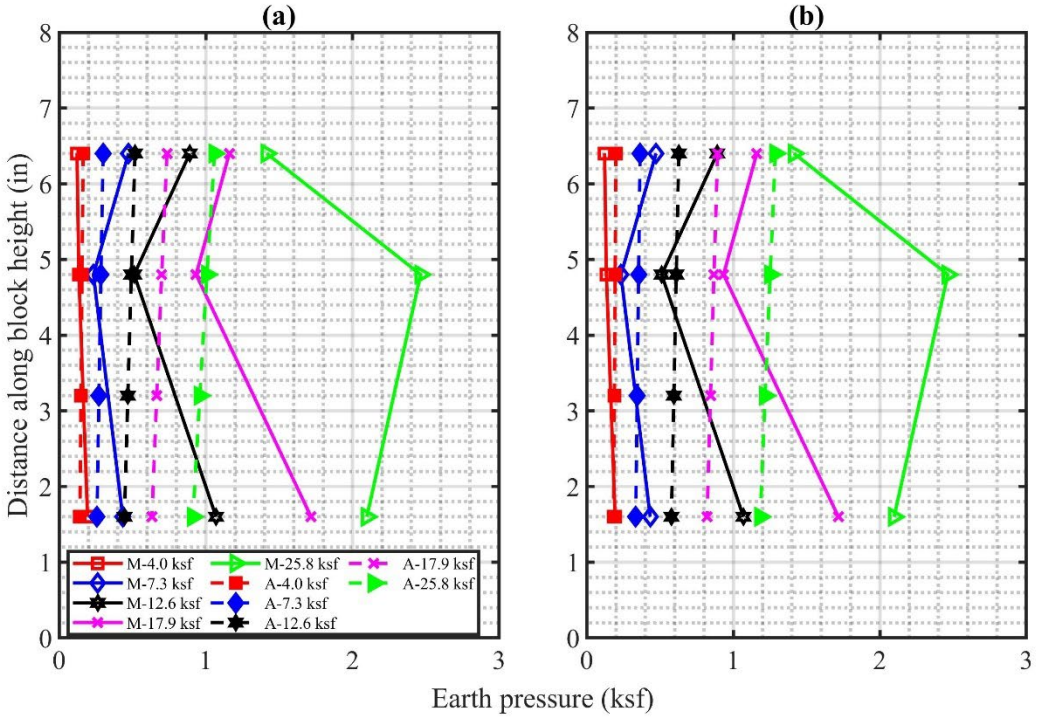


Figure 5-26. Comparison of lateral earth pressure during loading.
(a) Boussinesq; (b) Westergaard. (M is Measured earth pressure and A is calculated earth pressure)

The lateral earth pressure during construction ($\sigma_h$) was computed as:

$$\sigma_h = \gamma_{bf} z k_o \tag{5-40}$$

The coefficient of lateral earth pressure at rest ($k_o$) was calculated as:

$$k_o = 1 - \sin \Phi_r \tag{5-41}$$

The lateral earth pressure during loading ($\sigma_h$) was computed as:

$$\sigma_h = \sigma_v k_a \tag{5-42}$$

The coefficient of active earth pressure ($k_a$) is calculated as:

$$k_a = tan^2(45 - \frac{\Phi_r}{2}) \tag{5-43}$$

Where $\gamma_{bf}$ is the unit weight of backfill and $z$ is the depth of a stress point below footing.

## 5.6 Vertical Earth Pressure

Figure 5-27 shows the comparison between the measured and estimated vertical earth pressure during the construction of the pier. Similar to the lateral earth pressure, the estimated vertical earth pressure was based on the self-weight of the backfill above the pressure cell. It was calculated as unit weight of backfill times the fill height above the pressure cell. The results in Figure 5-27 indicates PT-07 and PT-08 exhibit nearly equal measured and estimated vertical pressures, while PT-06 shows that the measured earth pressure exceeds the estimated vertical pressure. For PT-04 and PT-05, the measured earth pressure is less than the predicted earth pressure. The larger difference seen in PT-05 can be attributed to the placement of the earth pressure cell at the base of the pier, in direct contact with the strong floor which could lead to the under-registration of pressure due to soil arching.

Figure 5-28 and Figure 5-29 show the comparison of the vertical earth pressure during loading. The Simplified 2:1 method, Boussinesq method, and Westergaard method were employed to calculate the vertical earth pressure induced by applied vertical stress. When the measured vertical earth pressures were compared with the predicted pressures, it was found that all methods consistently underestimated the measured vertical pressure throughout most of the loading process except for PT-05. Both methods demonstrate more accurate predictions at lower applied vertical stress, primarily because the soil remains within the elastic range and both methods assume soil elasticity. However, as the applied vertical stress increases, the GRS composite exhibits greater

non-linearity, which is not accounted for by these methods. Bias was calculated for each pier with vertical earth pressure measurement, focusing on the linear stress-strain range response of the pier to reflect the linear elastic assumption of the estimation methods. From Figure 5-29, it can be seen that the Westergaard solution outperforms the others in predicting the vertical earth pressure, with a bias ratio of 1.25, while the Boussinesq and AASHTO 2:1 methods yield lower predictions, with bias ratios of 2.76 and 2.65, respectively. Based on this comparison, it can be concluded that the Westergaard solution provides better predictions for the vertical earth pressure in the tested GRS piers in this study.

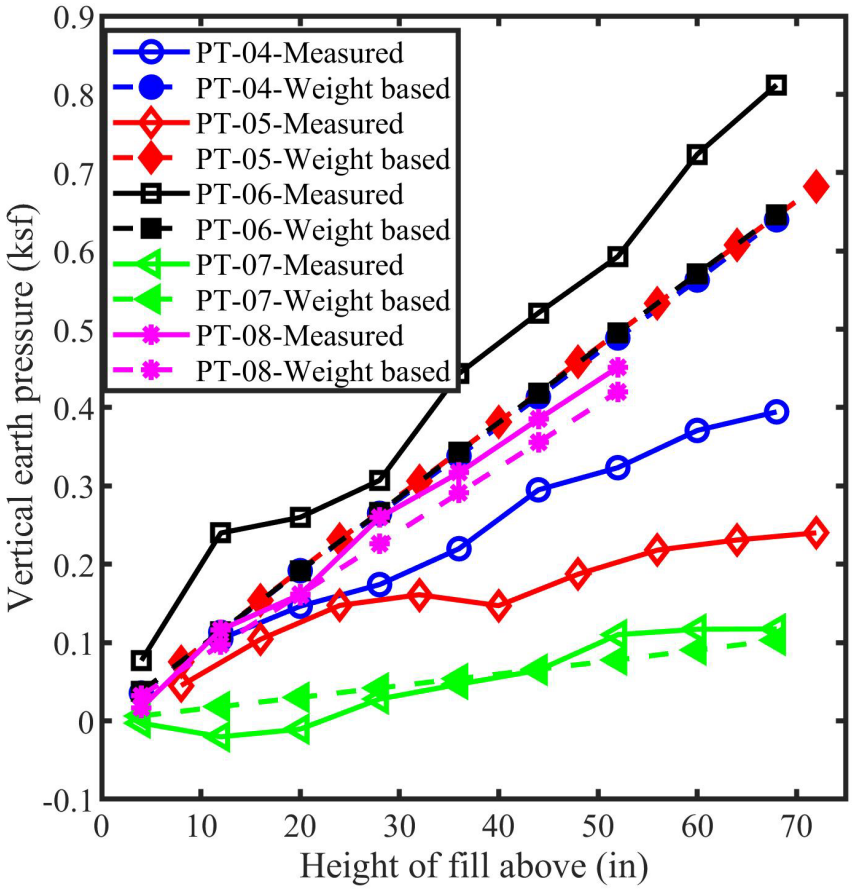


Figure 5-27. Comparison of vertical earth pressure during construction of GRS pier.

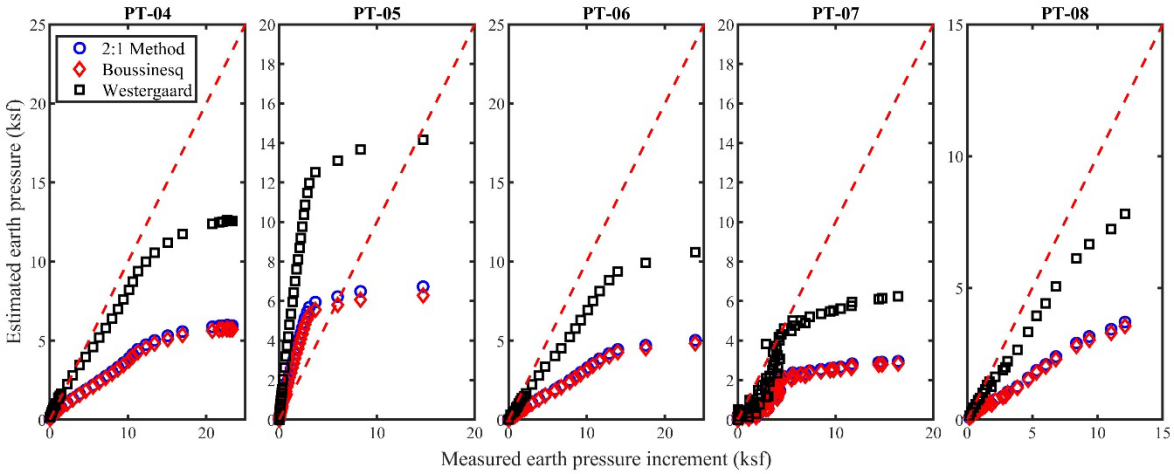


Figure 5-28. Comparison of vertical earth pressure during loading of GRS pier.

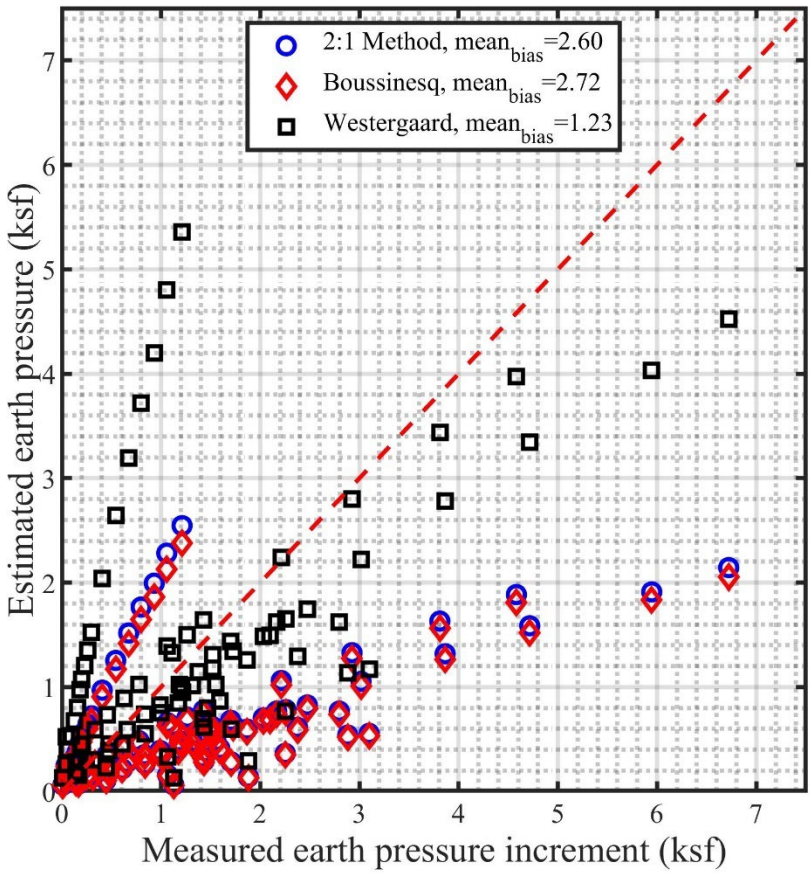


Figure 5-29. Comparison of vertical earth pressure during loading of GRS pier up to linear elastic range of the pier response.

## 5.7 Comparison with Previous Experiments

Several studies (Adams, 1997; Adams et al., 2002; Adams et al., 2007; Gotteland et al., 1997; Iwamoto et al., 2015; Ketchart and Wu, 1997, 2001; Nicks et al., 2013; Nicks et al., 2016; Wu et al., 2013) have investigated the performance of GRS mass through physical modeling. The experiments range from model tests to full scale loading tests. In this section, results from previous GRS tests (Nicks et al. (2013), Doger (2020), Doger and Hatami (2020) and Hatami and Doger (2021)) that employed materials having similar properties to the ones used in this study are compared to the experimental results from this study.

### 5.7.1 FHWA Performance Tests

Nicks et al. (2013) carried out a series of 19 full-scale load tests to assess the behavior of GRS piers under axial loading. The tests aimed to build a database of GRS materials, evaluate the relationship between reinforcement strength and spacing, quantify the contribution of facing elements, assess the new internal stability design method proposed by Adams et al. (2012b), and perform reliability analysis of the proposed soil-geosynthetic capacity equation for LRFD calibration. Throughout testing, the height to width ratio (H/B) of the pier was maintained constant at about 2, to mimic triaxial conditions. The tests employed frictionally connected concrete masonry blocks for facing walls. Six different backfill materials with friction angles ranging from 46° to 54°, cohesion values of 0 psf and 115 psf, and maximum aggregate sizes ranging from 3/8 inch to 1 inch were employed. The piers were reinforced with a biaxial woven polypropylene geotextile with tensile strengths ranging from 1,400 lb/ft to 4,800 lb/ft at vertical spacing ranging from 4 to 16 inches. Two configurations were considered, one with facing elements and one without. The piers were instrumented to measure vertical and lateral deformation during loading. The results indicated that the load-deformation behavior of GRS composites is influenced by multiple factors, including preloading, aggregate angularity, compaction level, presence of bearing bed reinforcement, and facing confinement. The use of higher strength reinforcement resulted in a stiffer and stronger response compared to lower strength reinforcement, and the use of well-graded material increased the stiffness of the GRS composite.

In the FHWA experiments, only two tests (DC-3 and TF-6) utilized materials with properties closely aligned to those employed in this study. DC-3 and TF-6 tests incorporated CMU

blocks for facing and biaxial woven polypropylene geotextile with an ultimate tensile strength of 4,800 lb/ft in both the MD and CD directions for reinforcement. DC-3 employed open graded aggregate (No 57 aggregate) for structural backfill, with a maximum particle size of 1-inch, a peak friction angle of 52 degrees, and zero cohesion. In contrast, TF-6 utilized well-graded Virginia Department of Transportation (VDOT) 21A aggregates, with a maximum particle size of 1-inch, a peak friction angle of 53 degrees based on direct shear test, and 48 degrees based on triaxial test. Refer to Table 5-1 for a comprehensive comparison of material properties. DC-3 is compared to PT-01 and PT-03, while TF-6 is compared to PT-04 and PT-06.

Figure 5-32 shows the comparison of the stress-strain relationship for GRS piers. The GRS piers tested in this research exhibited higher performance than those previously tested by FHWA. Both DC-3 and TF-6 exhibited lower stiffness compared to FDOT piers. Additionally, TF-6 shows lower capacity than PT-04 and PT-06. These differences can be attributed to variations in the materials utilized, particularly in the facing blocks and backfill. The FHWA experiment employed CMU blocks, whereas this study utilized heavier segmental retaining blocks, resulting in higher confining pressure which increases the vertical capacity. Also, the backfill used in the FDOT piers have higher friction angles than those used in FHWA which increases the shear strength of the GRS pier. However, the backfill used in the FHWA experiments were compacted to a higher density compared to those in the FDOT tests. If the same facing blocks were used in both FDOT and FHWA pier, the stiffness of DC-3 and TF-6 piers would have been greater than those used in the FDOT tests, but the results indicate the opposite, suggesting that the lower stiffness observed from stress-strain curves in DC-3 and TF-6 piers is due to the lightweight facing blocks which offer less confinement pressure.

Reinforcement strain distribution is shown in Figure 5-33 and Figure 5-34. The observed reinforcement strains in TF-06 exceeded those in PT-04 and PT-06. This difference arises from the use of heavier facing blocks in the PT tests, which provide greater resistance against lateral movement. Therefore, facing walls in TF-06 undergo more lateral displacement, resulting in greater stretching of the geotextile and therefore higher reinforcement strains.

Figure 5-30. Photo of TF-6 PT setup with reaction frame.
(Nicks et al., 2013).

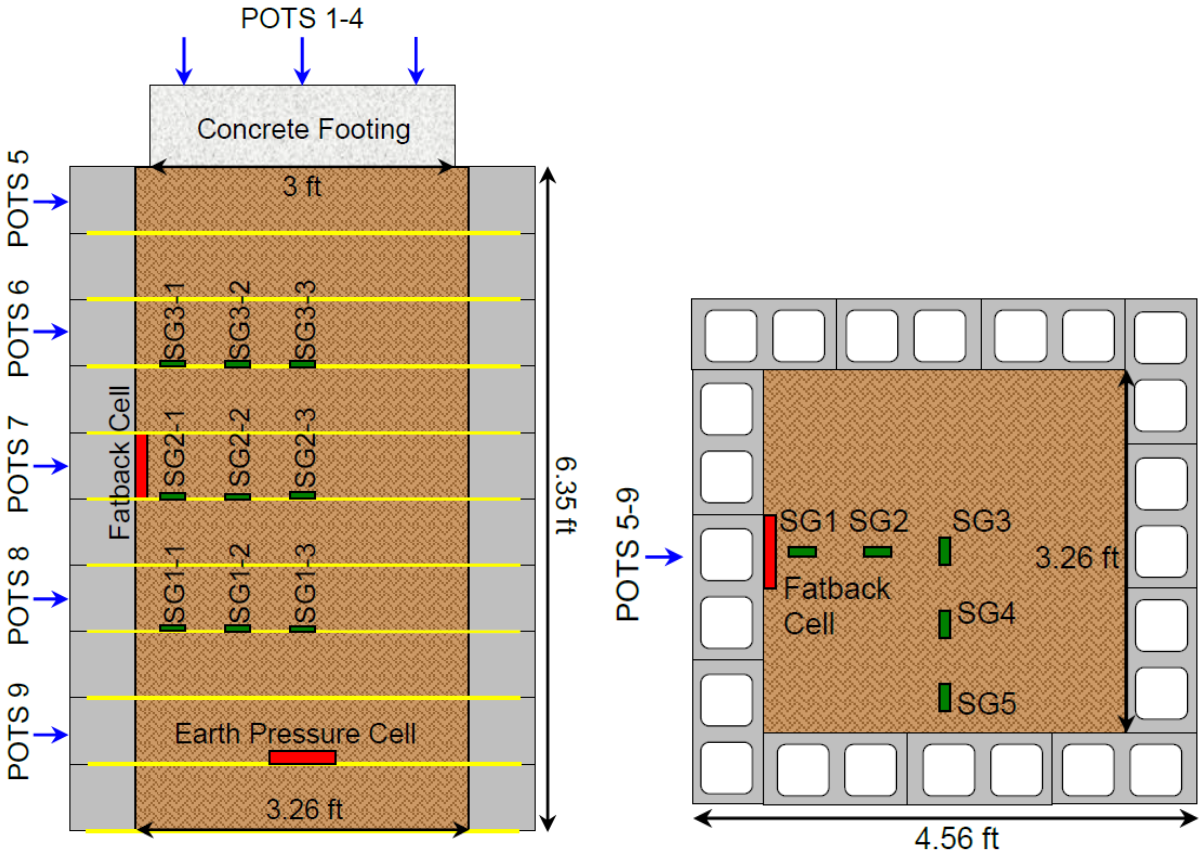

Figure 5-31. Plan and profile schematic of TF-6.
(Lwamoto, 2014).

Table 5-1. Comparison of materials properties for the FDOT and FHWA tests.

| Parameter | FDOT | FHWA ((Nicks et al, 2013)) |
|---|---|---|
| Height (in) | 72 | 76.25 |
| Inside width (in) | 36 | 39.25 |
| $S_v$ (in) | 8 | 8 |
| $T_F$ (lb/ft) | 4,800 | 4,800 |
| Facing block type | SGR | CMU |
| Block size | 8 x 12 x 18 | 7.625 x 7.625 x 15.625 |
| Block weight (lb) | 86 | 42 |
| Backfill: Well graded | | |
| Friction angle (deg) | 58.41[b] | 48[b]; 54[a] |
| Cohesion (psf) | 413.3[b] | 576.4[b]; 115[a] |
| Max dry unit weight (pcf) | 115.9 | 148.9 |
| Backfill: Open-graded (No 57) | | |
| Friction angle (deg) | 44.08[b]; 54.4[a] | 52[a] |
| Cohesion (psf) | 0 | 0 |
| Max dry unit weight (pcf) | 96.17 | 108.69 |
| Backfill: Open-graded (FGA) | | |
| Friction angle (deg) | 54.0 [a] | NA |
| Cohesion (psf) | 184 [a] | NA |
| Max dry unit weight (pcf) | 16.75 | NA |

Notes: [a]: based on 12 x12 large direct shear test; [b]: based on 6-inch diameter triaxial tests.

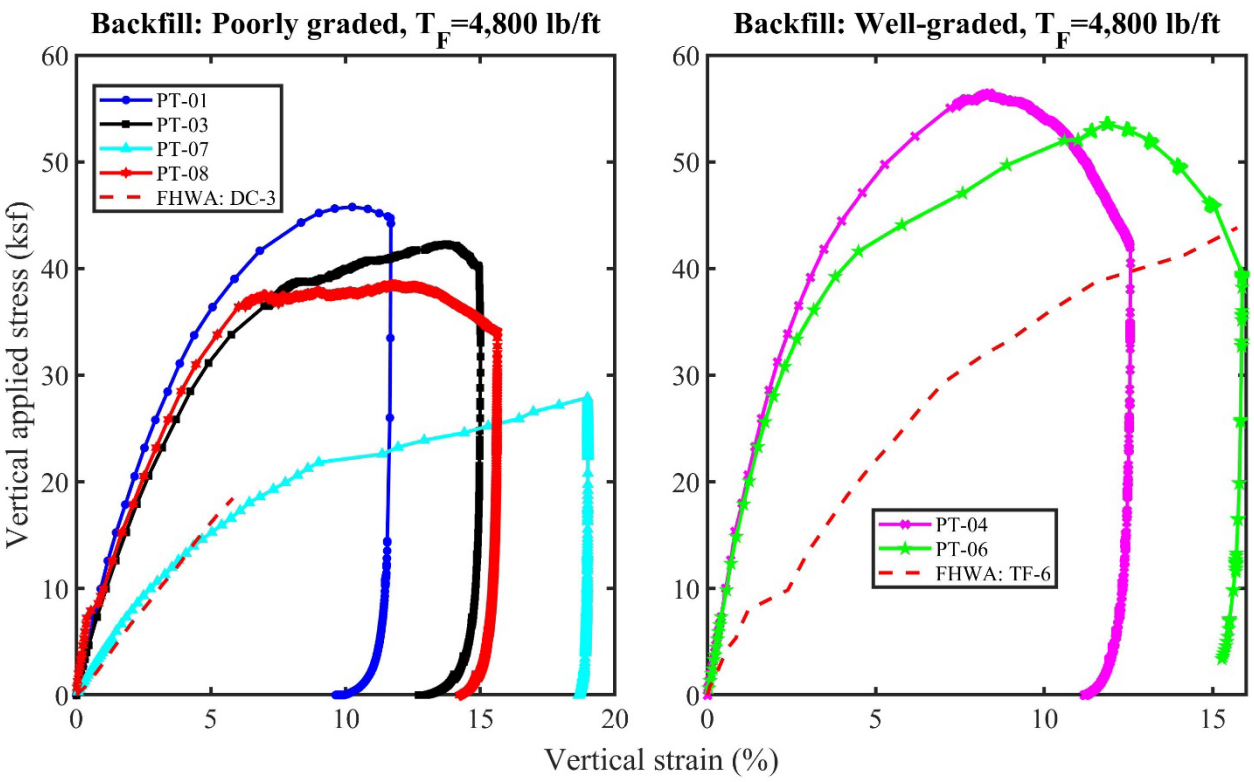


Figure 5-32. Comparison of applied vertical stress versus average vertical strain.

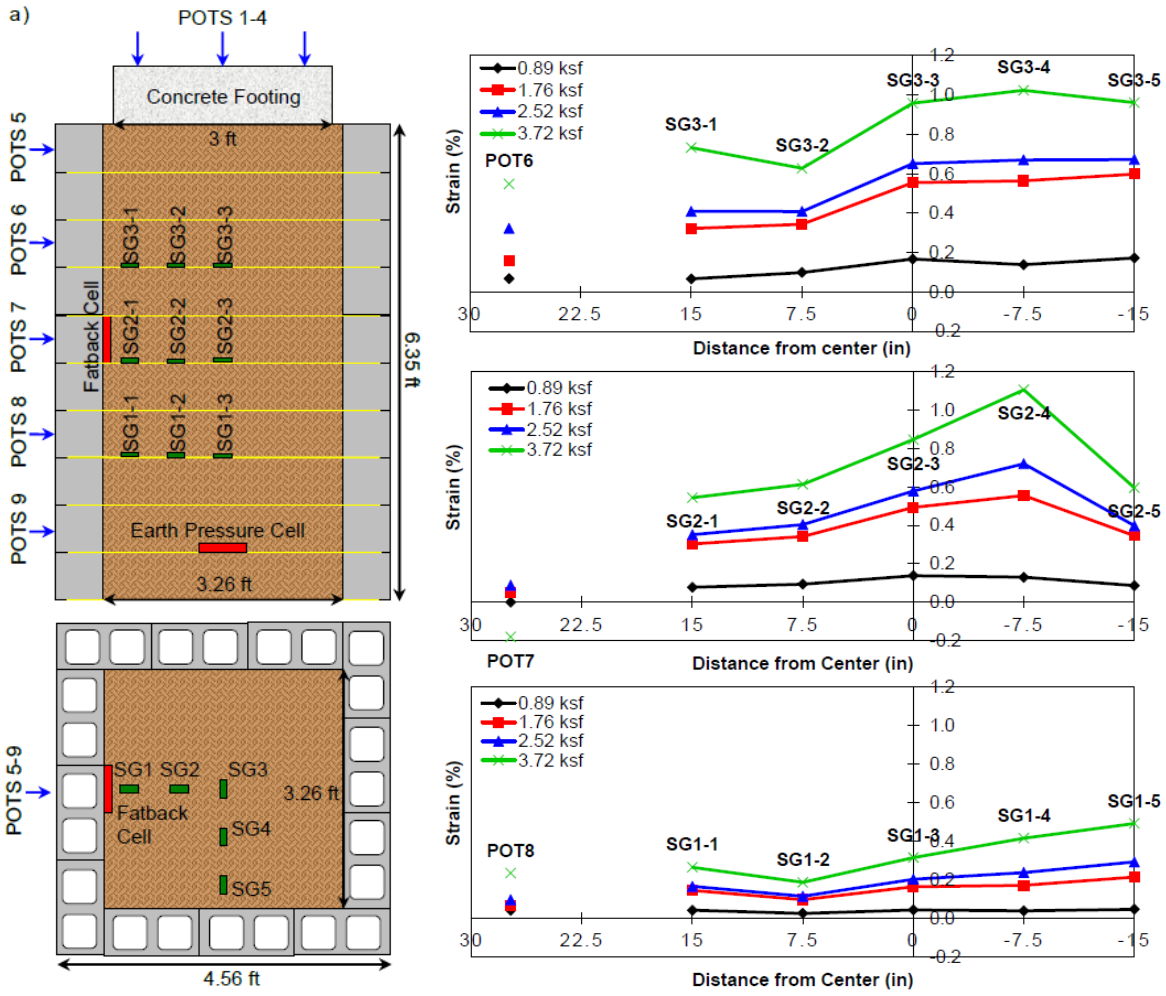


Figure 5-33. Plan and profile schematic of TF-6 and their corresponding Reinforcement strain from strain gauges at different applied vertical stresses.
(Lwamoto, 2014).

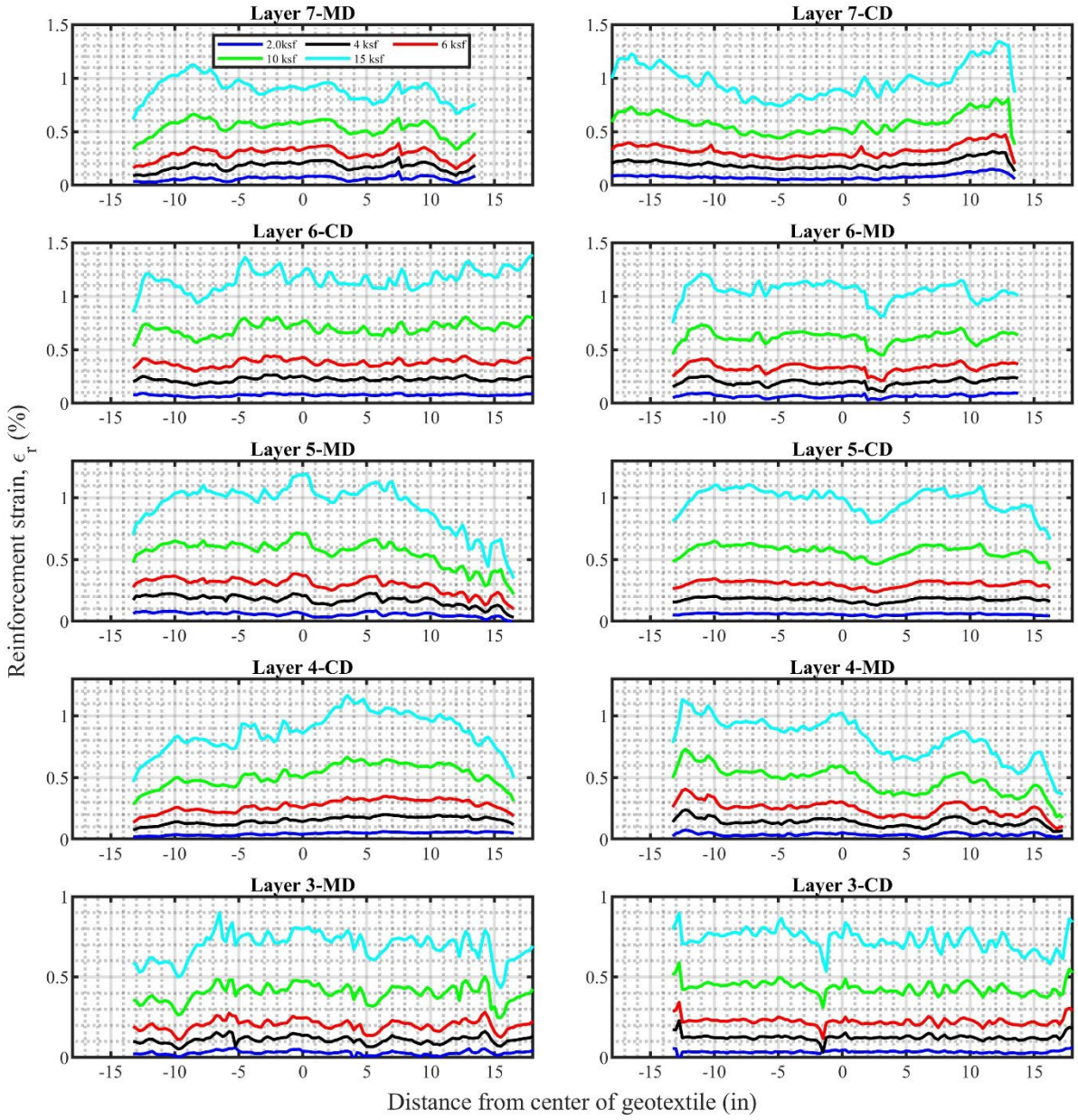


Figure 5-34. Reinforcement strain distribution in geotextile at different applied vertical stress for PT-04.

### 5.7.2 Oklahoma GRS Abutment Model

Doger (2020), Doger and Hatami (2020) and Hatami and Doger (2021) conducted a series of large-scale tests on GRS bridge abutments to explore the impact of facing type and reinforcement spacing on load-bearing performance. The study also examined the influence of compaction effort when utilizing open-graded aggregates. Structural backfill consisted of open-graded aggregate (3/8" #2 cover) and well-graded aggregates, while facing walls were constructed using either CMU or larger solid concrete blocks. Polypropylene woven geotextile was employed for reinforcement, placed at vertical spacings of 7.9 inches and 12 inches. Each test was equipped with multiple sensors to monitor vertical settlement of the footing, facing displacements, and reinforcement strains. Results indicated that using larger solid concrete blocks led to superior load-bearing performance compared to CMU, suggesting their potential suitability for GRS-IBS. Additionally, the GRS abutments met FHWA service limits and performed satisfactorily.

For comparative purposes, only GRS abutment tests with CMU facing blocks were compared with the FDOT pier tests. Table 5-2 shows the comparison of material properties, and Figure 5-35 illustrates the test setup. The segmental retaining blocks (SGR) utilized in this study were heavier than the CMU blocks in the Oklahoma GRS abutment models. Also, the backfills used in this study have higher peak friction angles compared to those in the Oklahoma GRS abutment models. Compaction of backfill in the Oklahoma GRS abutment models was achieved using jumping jack equipment, resulting in average unit weights of 101.59 pcf and 105.037 pcf for one and three passes, respectively, for compacted open-graded aggregates. For well-graded aggregates, it was 127.445 pcf for three passes of jumping jack equipment.

Figure 5-36 shows a comparison of stress-strain relationships for GRS piers and GRS abutments. In the case of poorly graded aggregates and one pass for the GRS abutment, the initial stiffness of the stress-strain curve is nearly identical for both GRS piers and abutments. However, as applied pressure increases, the stiffness of GRS abutments consistently surpasses that of the piers. When the number of passes is increased to three, GRS abutments exhibit a stiffer response than GRS piers, regardless of whether open or well-graded aggregates are used as backfill. Several factors contribute to the observed stiffness differences. GRS abutment backfills were compacted to higher densities than their respective GRS piers, improving backfill stiffness and global response. Boundary conditions also vary, with GRS piers being free to deform on all sides while

GRS abutments are constrained on three sides, reducing lateral displacements and increasing stiffness. Furthermore, the larger plan area of abutments compared to piers may result in increased geotextile confinement within the GRS abutment's inner core, further enhancing stiffness and load-carrying capacity.

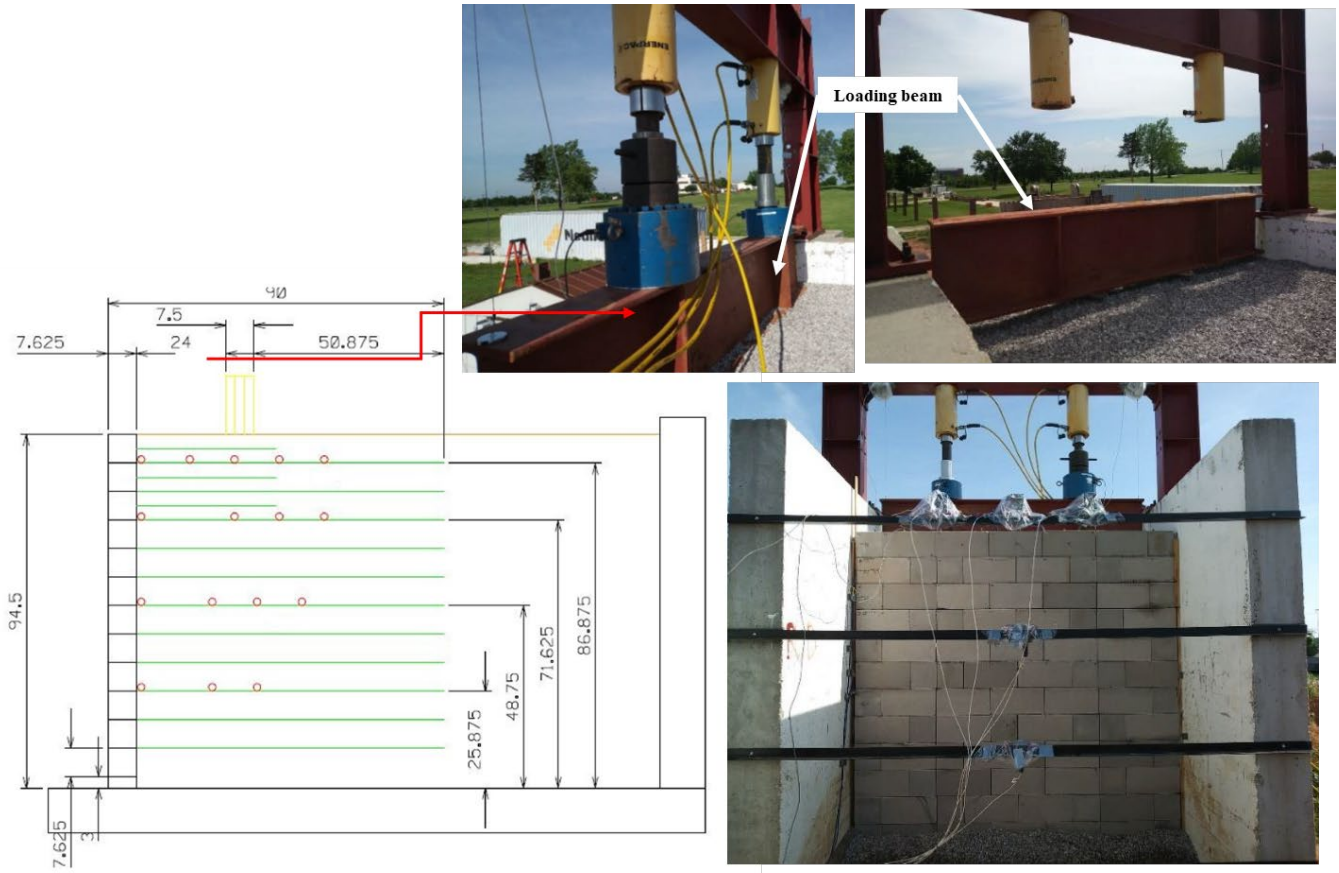


Figure 5-35. GRS Abutment model
(Doger, 2020)

Table 5-2. Comparison of materials properties for the FDOT and Oklahoma tests

| Parameter | FDOT | Oklahoma (Doger, 2020) |
|---|---|---|
| Height (in) | 72 | 94 |
| Inside width (in) | 36 | 39.25 |
| $S_v$ (in) | 8 | 7.625 |
| $T_F$ (lb/ft) | 4,800 | 4,800 |
| Facing block type | SGR | CMU |
| Block size | 8 x 12 x 18 | 8 x 8 x 16 |
| Block weight (lb) | 86 | 36 |
| Backfill: Well graded | | |
| Friction angle (deg) | 58.41[b] | 45[a] |
| Cohesion (psf) | 413.3[b] | |
| Max dry unit weight (pcf) | 115.9 | 135.27 |
| Backfill: Open-graded | | |
| Friction angle (deg) | 44.08[b]; 54.4[a] | 48[a] |
| Cohesion (psf) | 0 | 0 |
| Max dry unit weight (pcf) | 96.17 | 105.98 |

Notes
[a]: based on 12 x12 large direct shear test.
[b]: based on 4-inch diameter triaxial tests.

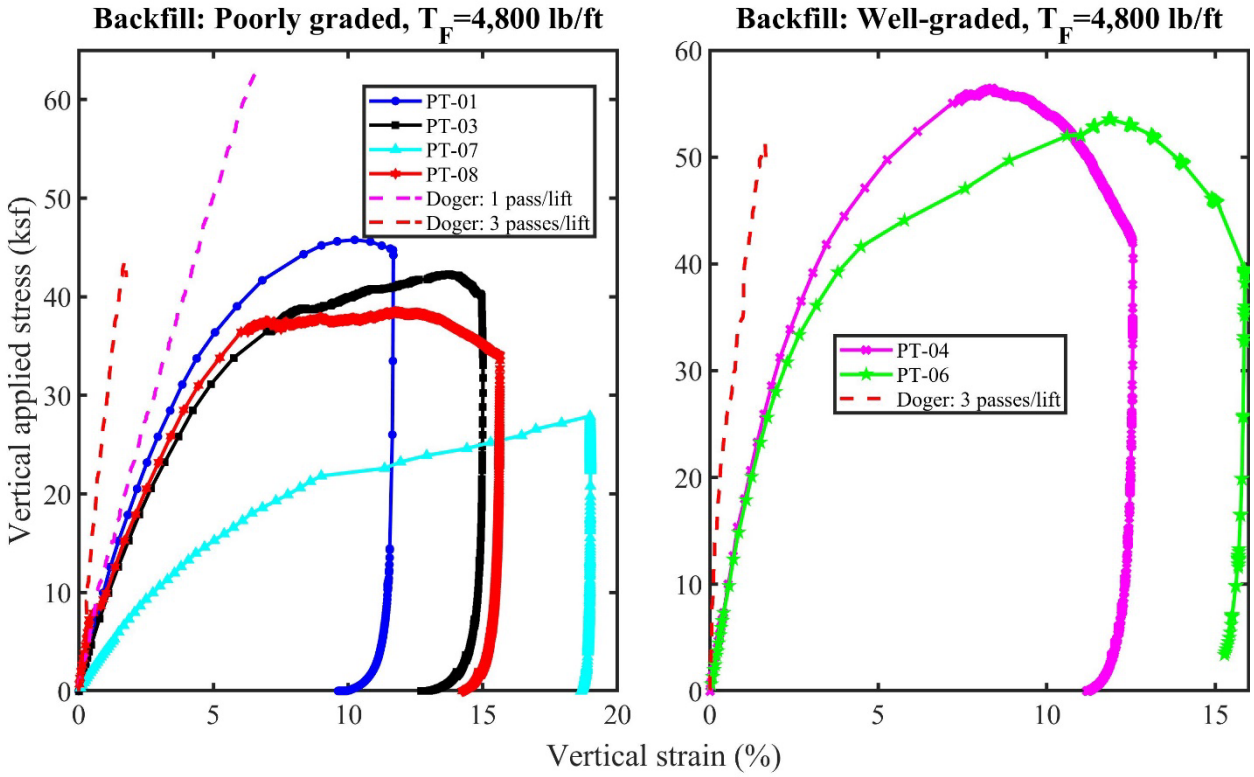


Figure 5-36. Comparison of applied vertical stress versus average vertical strain.

## 5.8 Conclusion

This report presented the results of triaxial tests and comparisons of the GRS pier test results with the design methods commonly used in the design of GRS-IBS structures. Each method was described and discussed. Based on the findings, the following conclusions are drawn:

i. RCA-GAB has a higher friction angle than No 57 aggregate.
ii. Large diameter triaxial shear tests are the most appropriate for aggregates approved for use in GRS-IBS.
iii. The residual stresses in RCA-GAB occur at axial strains 5-10%, similar to the axial strain near failure of the RCA-GAB piers, suggesting the associated friction angles should be used to predict the GRS capacity.
iv. All tested piers performed well under FHWA service limits.
v. The FHWA ultimate capacity equation was found to underpredict the measured vertical capacity if the friction angles that are associated with the axial strain at failure are used.
vi. The FHWA ultimate capacity equation consistently underestimated the measured vertical capacity of piers constructed with No. 57 compared to those built with RCA-GAB, regardless of the friction angle used in the calculation.
vii. The FHWA equation for lateral displacement accurately predicted the lateral displacement of the facing walls during loading.
viii. The assumption of zero volume change was found to hold below the service limit applied pressure of 4 ksf.
ix. The integration of strain measurements can be useful in estimating total lateral displacements.
x. The friction angle of aggregate is significant in the prediction of reinforcement loads. FHWA GRS-IBS method based on the Westergaard solution is better at predicting the reinforcement load for the GRS piers when using ultimate and residual friction angles, while the AASHTO method based on the Boussinesq method is better when the secant friction angle is used.
xi. The Westergaard method performs better in the prediction of lateral and vertical earth pressure during loading of GRS piers.

# 6 CONCLUSION AND RECOMMENDATIONS

The empirical approach, which relies on performance testing, is currently recommended by the FHWA as one of the design methods for GRS-IBS. It involves using stress-strain curves derived from performance tests. FHWA has developed a database of performance test results that can be used in the design. However, the existing FHWA database has limitations in terms of the tested materials, necessitating the need for additional tests to expand its applicability. This research aimed to investigate the behavior of GRS composites constructed with materials approved for use in Florida through a series of full-scale load tests on instrumented GRS piers. The availability of accurate stress-strain data from these experiments will contribute to the design of GRS-IBS structures, which are becoming increasingly popular in the United States. Comparisons between the experimental data existing design methods show their suitability for use by the FDOT, and incorporate the experimental results into the FHWA's performance test database. The experiments involved three types of backfill and geosynthetic materials, including the investigation of a new lightweight material for potential use in GRS-IBS. A new approach utilizing fiber optic strain sensors was proposed for measuring reinforcement strain in geotextiles. The findings of this study provide valuable insights into the performance of GRS structures constructed with the investigated materials, and the experimental results can be employed in the design of GRS-IBS. The subsequent subsections present a summary of the study's findings.

## 6.1 Summary of Findings

- Large triaxial tests are appropriate for testing well graded materials. The analysis of triaxial results showed the influence of triaxial specimen on shear strength properties of well-graded RCA-GAB. Conducting triaxial tests on 6 inch diameter specimens led to an increase in the friction angle by 11.38 degrees and 8.47 degrees for peak and residual states, respectively, compared to 4-inch specimens.
- Scalping of materials during the triaxial test did not influence the shear strength properties of No. 57 aggregates.
- The surface texture of geotextiles affect their shear interface properties with aggregates. HP570 geotextile showed a higher interface friction angle with No 57 and RCA-GAB backfill compared to HPG57 geotextile, which had the same MD and CD weaves.

- The experimental results showed that the type of backfill, and geotextile strength has a significant impact on the behavior of GRS piers. Piers constructed with HP 770 geotextile (7,200 lb/ft in MD and 5,760 lb/ft in CD) exhibited higher loading capacities compared to HP 570 and HPG 57 (4,800 lb/ft in MD and CD). The same effect was observed for backfill materials, with well graded RCA-GAB backfill resulting in stiffer and higher capacity GRS composites compared to open graded-No 57 and FGA backfill.
- Maximum lateral displacement occurred within the top one-third of wall height. Below the FHWA recommended service limit bearing pressure, the lateral displacements are greatest at the top of the wall.
- The common construction practice of incorporating concrete in the top three to five courses of blocks affected the lateral deformation and stiffness of the piers under small applied vertical stress conditions, typically below 7.25 ksf in this study. The use of concrete fill reduces the lateral displacement while increasing the axial stiffness. Lateral displacement was also influenced by the type of backfill used, with piers constructed with well graded RCA-GAB backfill exhibiting less lateral displacement.
- Bonding fiber optic strain sensors to the geotextile reinforcement provides a more effective method of measuring strains developed under different loading conditions as compared to traditional strain gauges. This method offers more measurement points, is easier to install, and produces more reliable results.
- The type of backfill materials used does not affect the strain distribution in the geotextile reinforcement, but rather the magnitude of the strain is influenced by the properties of the backfill materials. GRS constructed with backfill materials of well graded RCA-GAB backfill exhibited lower reinforcement strains than those constructed with open graded-No 57 and FGA backfill materials.
- Reinforcement strain measurements showed that highest strain magnitudes occur closest to the connection points of upper layers, while they are located near the middle for lower layers of geotextile reinforcement. Also, maximum reinforcement strain was found to occur within the upper half of the wall heights.

- The integration of reinforcement strain measurements can be useful in estimating lateral displacements. A comparison between the estimated and actual measured lateral displacements showed good agreement.
- Experimental results showed internal lateral earth pressure is influenced by the reinforcement conditions. Piers constructed with the same geotextiles exhibited nearly identical relationships between lateral earth pressure and vertical applied stress.
- All GRS piers tested met the FHWA service limit criteria for GRS-IBS satisfactorily. At an applied vertical pressure of 4 ksf, the vertical strain for all GRS piers was below 1%, with lateral strain below 0.51%. The applied vertical pressure needed to achieve 1% vertical strain ranged from 4.1 ksf to 19 ksf for all piers, while the pressure required to reach 2% lateral strain varied from 11 ksf to 32 ksf.
- Comparison of experimental data with FHWA design methods for GRS-IBS showed that the FHWA ultimate capacity equation consistently underestimated (measured/predicted > 1) the measured vertical capacity of piers constructed with open graded-No 57 backfill compared to those built with well graded RCA-GAB backfill, regardless of the friction angle used in the calculation. The use of the residual friction angle for the RCA-GAB resulted in predicted ultimate capacity less than the measured (measured/predicted = 1.16), whereas using the peak friction angle the predicted values were consistently greater (measured/predicted < 1). The agreement when using residual friction angles is based on the corresponding vertical strains in the large diameter (6 inch) triaxial tests, which are similar in the GRS pier tests using RCA-GAB. This and the observations between the 4 inch and 6 inch diameter triaxial tests, indicate that large diameter triaxial tests should be performed on aggregates for identification of their strength and volumetric behaviors.
- The FHWA equation for lateral displacement accurately predicted the lateral displacement of the facing walls during loading. The assumption of zero volume change was found to hold below the service limit applied pressure of 4 ksf.
- The friction angle of aggregate plays a big role in the prediction of reinforcement loads. FHWA GRS-IBS method based on the Westergaard solution is better at predicting the reinforcement load for the GRS piers when using ultimate and residual friction angles,

while the AASHTO method based on the Boussinesq method is better when the secant friction angle is used.

- The Westergaard method performs better in the prediction of lateral earth pressure, vertical earth pressure and reinforcement loads during loading of GRS pier.
- Based on the LRFD factored applied vertical pressure ($\gamma_{DCMAX}q_b + \gamma_{LL}q_{LL}$ = 1.25(2.6) + 1.75(1.4) = 5.7 ksf, where the load factors are form Table 6.1), the vertical strains of all the GRS piers tested are less the 0.85%, except for the LWA GRS pier which exhibited 1.3%. The horizontal strains of all the GRS piers tested were less than 0.62% at 5.7 ksf.
- The performance test data developed in this work is a contribution to the existing dataset of GRS structure performance as presented by Nicks et al. (2013). The capacity data herein provides 7 additional FHWA bearing capacity bias (measured/predicted) values for a total of N = 42 with a mean bias = 0.98 and CV (stdv/mean) = 0.30. The cumulative frequency distribution of the FHWA bearing capacity bias is shown in Figure 6.1 with normal and lognormal models fit to the data. Figure 6.1a shows the dataset N = 42 values where an outlier is present near the tail of the distribution. This was a for a minipier test by Adams et al. (2007) and an error associated with the pier itself could not be identified based on the

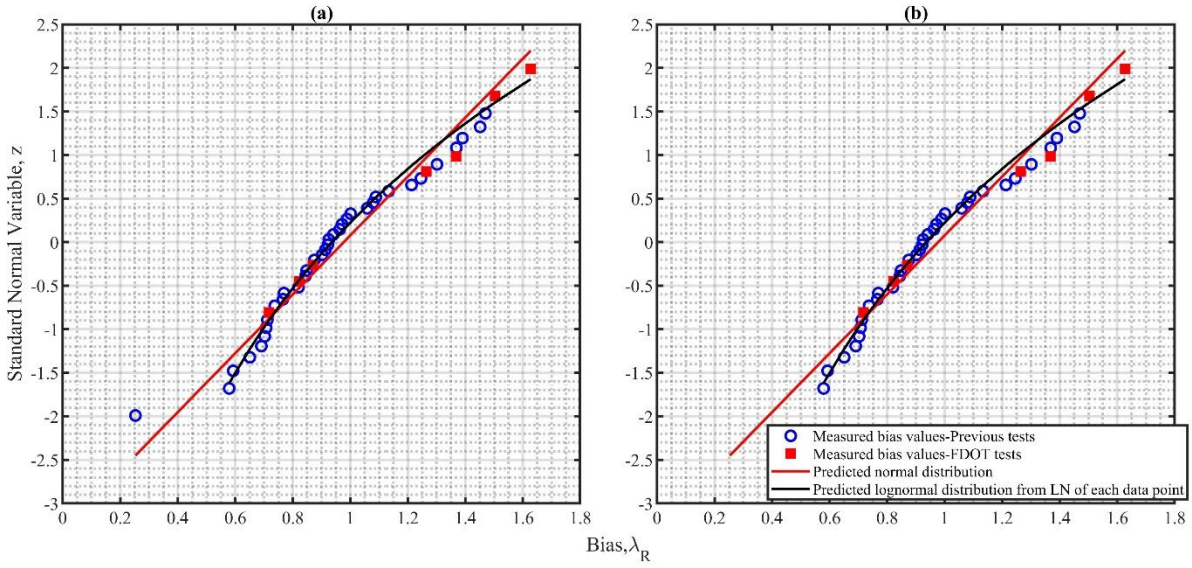


Figure 6-1. Cumulative frequency distribution of the FHWA bearing capacity bias (a) N = 42 and (b) N = 41 outlier removed.

available data. Figure 6.1b is the dataset with the outlier removed to obtain N = 41, mean bias = 0.97 and CV = 0.32.

- Following the procedure for calculating the LRFD resistance factor by Nicks et al. (2013) for the FHWA bearing capacity of GRS structures, the factors and statistics for the load and resistance based on AASHTO strength I load combination in Table 6-1 was used with the First Order Second Moment (FOSM) method in Eq. 6-1 to calculate the resistance factors.
- FHWA limits the GRS-IBS to span length of 140 ft which corresponds to approximately $\frac{Q_D}{Q_D+Q_L}$ of 0.37 which corresponds to a resistance factor of 0.53, 0.44, and 0.37 for reliability indices of 2.5, 3.0 and 3.5 (Figure 6-2), respectively, using maximum measured capacity. Nicks et al. (2013) suggested that the GRS composite to be considered as redundant foundation system due to non-catastrophic failure observed in their GRS pier tests which is also similar to what was observed in the current study. Pailkowsky (2004) recommends a target reliability index of 2.33 for redundant foundation system while Bathurst et al. (2008b) recommends a reliability index of 2.33 for internal stability of reinforced walls. Therefore, using data from literature (Nicks et al., 2013) and current study, a reliability index of 2.33 and $\frac{Q_D}{Q_D+Q_L}$ of 0.37, the resistance factor is calculated to be 0.57.
- Nicks et al. (2013) reported a resistance factor of 0.45 for a reliability of 2.5 and $\frac{Q_D}{Q_D+Q_L}$ of 0.32.

$$\Phi = \frac{\lambda_r\left(\gamma_D\left[\frac{\frac{Q_D}{Q_D+Q_L}}{1-\frac{Q_D}{Q_D+Q_L}}\right]+\gamma_L\right)}{\left(\lambda_D\left[\frac{\frac{Q_D}{Q_D+Q_L}}{1-\frac{Q_D}{Q_D+Q_L}}\right]+\lambda_L\right)\sqrt{\frac{1+{V_R}^2}{1+{V_Q}^2}}e^{\left(\beta_T\sqrt{\ln[(1+{V_R}^2)(1+{V_Q}^2)]}\right)_i}} \quad (8\text{-}1)$$

Where $Q_D$ is deal load and $Q_L$ is live load.

Table 6-1. Load factors and statistics for AASHTO strength I load combination and resistance statistics

| Item | Value | Reference |
|---|---|---|
| Load factor for dead load, $\gamma_D$ | 1.25 | AASHTO |
| Load factor for live load, $\gamma_L$ | 1.75 | |
| Load Statistics | | |
| Bias factor for dead load, $\lambda_D$ | 1.05 | |
| Bias factor for live load, $\lambda_L$ | 1.14 | Kulicki et al. (2007) |
| COV for dead load, $V_D$ | 10% | |
| COV for live load, $V_L$ | 12% | |
| COV for load, $V_Q = \sqrt{{V_D}^2 + {V_L}^2}$ | 15.62% | |
| Resistance Statistics ($q_{ult} = f(d_{max}, T_f, S_v, K_p)$ | | |
| COV for $d_{max}$, $V_{d_{max}}$ | 5 % | Nicks et al. (2013) |
| COV for $T_f$, $V_{T_f}$ | 4 % | (Benjamim et al., 2008); Nicks et al. (2013) |
| COV for $S_v$, $V_{S_v}$ | | Not random |
| COV for $K_p$, $V_{K_p}$ | 15% | Kulicki et al. (2007) |
| COV for FHWA equation, $V_m$ | 0.29 | Experimental data (literature and current study) |
| Bias factor for resistance, $\lambda_r$ | 0.98 | |
| COV for resistance, $V_{R=\sqrt{{V_{d_{max}}}^2+{V_{T_f}}^2+{V_{Kp}}^2+{V_m}^2}}$ | 0.30 | |

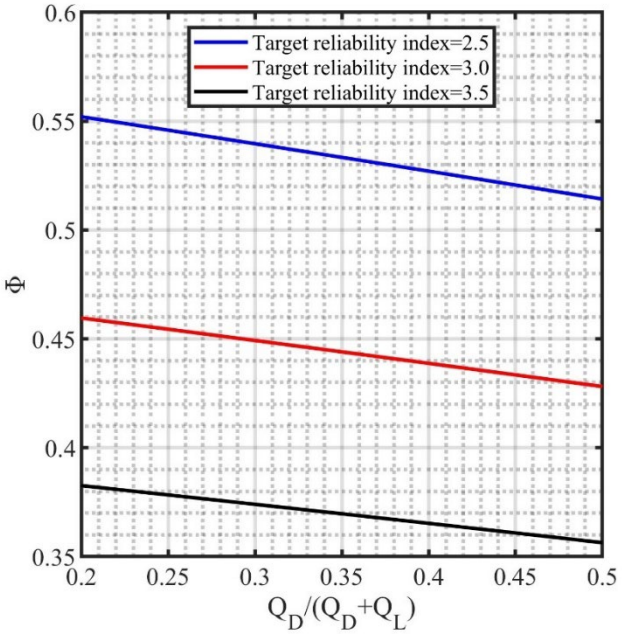


Figure 6-2. resistance factors versus dead to dead plus live load ratios for different reliability indices using all data from literature (Nicks et al., 2013) and current study.

## 6.2 Future Research Recommendations

The results of triaxial tests have showed notable differences in friction angles between tests conducted with 4-inch and 6-inch specimens, particularly for well-graded RCA-GAB backfill. As a result, it is recommended to conduct large-scale triaxial tests for these materials during the design phase of GRS. Tensile testing of HPG 57 showed lower stiffness compared to what was specified by the manufacturer. Using only manufacturer specifications for geotextile may be inappropriate and therefore properties of geotextile should be tested during the design properties of GRS.

The results of the performance tests indicate that the tested GRS piers are performing well under both the service and strength limits. The performance tests have shown that GRS piers constructed with RCA-GAB backfill exhibit a stronger response to applied load compared to those constructed with No. 57 and FGA backfill. This suggests that the use of RCA-GAB may be a better option for GRS-IBS structures in Florida. However, it is important to also consider other factors such as cost, availability, and ease of construction when choosing the type of backfill. For example, the RCA-GAB has a unit cost three times that of the No 57 and is only available in the area of Tampa, while No 57 limestone is widely available throughout the state. Additionally, RCA-GAB

must be compacted with moisture to achieve design unit weight and No 57 can be vibrated dry in place to achieve design unit weight.

A potential topic of study is the performance of GRS piers built with geogrid reinforcement in No 57. The open cell of the geogrid will leave particle to particle contact, but with provide the tensile reinforcement over the layer. Further research at the FDOT Structures lab would be necessary to investigate the use of geogrid as effective in reducing the vertical and horizontal strains of the GRS structure.

As the demand on natural resources increases costs and reduces availability, the consideration of the use of recycled materials like RCA or light weight aggregates (LWA) is becoming common in geotechnical engineering projects. GRS-IBS is one area where recycled materials can potentially be employed. Performance test 7 (PT-07) has demonstrated that FGA (a LWA) can perform well when used in GRS structures, while meeting the service limits criteria established by the FHWA for GRS-IBS. However, this was one performance test with a single type of geotextile, block, and reinforcement spacing. Performance tests should be conducted to study different geosynthetic spacing, perhaps geogrid, and composite backfill like 40% LWA and 60% mined or recycled aggregate.

In this study, all GRS piers that were tested had an identical reinforcement configuration, with a primary reinforcement spacing of 8 inches and a secondary reinforcement spacing of 4 inches. All piers also had facing blocks. For verification of performance of the GRS composite with HP770, for example, at spacing greater than 8 inches, or new aggregates, additional tests should be carried out. Furthermore, the influence of the facing blocks through comparison of pier tests without them to those with them was not performed. If future design will be for the composite GRS system, these tests should be performed where the initial confining pressure can be varied.

# 7 REFERENCES


AASHTO T 180, 2009. Standard method of test for moisture–density relations of soils using a 4.54-kg (10-lb) rammer and a 457-mm (18-in.) drop AASHTO.

Abu-Hejleh, N., Zornberg, J.G., Wang, T., Watcharamonthein, J., 2002. Monitored displacements of unique geosynthetic-reinforced soil bridge abutments. Geosynthetics International 9, 71-95.

Adams, M., 1997. Performance of a prestrained geosynthetic reinforced soil bridge pier, Mechanically Stabilized Backfill. Wu (ed.), Denver, CO, A.A. Balkema, Rotterdam, Netherlands, pp. 35-53.

Adams, M., Lillis, C., Wu, J., Ketchart, K., 2002. Vegas mini pier experiment and postulate of zero volume change, Proceedings, seventh international conference on geosynthetics, pp. 389-394.

Adams, M., Nicks, J., 2018. Design and Construction Guidelines for Geosynthetic Reinforced Soil Abutments and Integrated Bridge Systems, Report No. FHWA-HRT-17-080. Federal Highway Administration, Washington, DC.

Adams, M., Nicks, J., Stabile, T., Schlatter, W., Hartmann, J., 2012a. Geosynthetic Reinforced Soil Integrated Bridge System Interim Implementation Guide, Report No. FHWA-HRT-11-026. Federal Highway Administration, Washington, DC.

Adams, M., Nicks, J., Stabile, T., Schlatter, W., Hartmann, J., 2012b. Geosynthetic reinforced soil integrated bridge system, interim implementation guide. Federal Highway Administration.

Adams, M., Nicks, J., Stabile, T., Wu, J.T., Schlatter, W., Hartmann, J., 2011. Geosynthetic Reinforced Soil Integrated Bridge System, Synthesis Report, Report No. FHWA-HRT-11-027. Federal Highway Administration, Washington, DC.

Adams, M.T., Ketchart, K., Wu, J.T., 2007. Mini pier experiments: Geosynthetic reinforcement spacing and strength as related to performance, Geosynthetics in reinforcement and hydraulic applications, pp. 1-9.

Allen, T.M., Bathurst, R.J., 2003. Prediction of reinforcement loads in reinforced soil walls. Washington State Transportation Center (TRAC).

ASTM D3080, 2012. D3080/D3080M—11 Direct Shear Test of Soils Under Consolidated Drained Conditions, ASTM International: West Conshohocken, PA, USA, pp. 1-9.

ASTM D4253, 2006. Standard Test Methods for Maximum Index Density and Unit Weight of Soils Using a Vibratory Table (ASTMD4253),“, Annual Book of ASTM Standards, pp. 556-570.

ASTM D4254, 2006. Standard Test Method for Minimum Index Density and Unit Weight of Soils and Calculation of Relative Density, Annual Book of ASTM Standards, ASTM International, West Conshohocken, PA.

ASTM D 7181, 2020. Methods for consolidated drained triaxial compression test for soils ASTM International, West Conshohocken PA, USA.

Bathurst, R., Allen, T., Walters, D., 2002. Short-term strain and deformation behavior of geosynthetic walls at working stress conditions. Geosynthetics International 9, 451-482.

Bathurst, R., Miyata, Y., Nernheim, A., Allen, A., 2008. Refinement of K-stiffness method for geosynthetic-reinforced soil walls. Geosynthetics International 15, 269-295.

Bhattarai, T., 2018. Using Force Sensing Resistor to Evaluate Lateral Earth Pressure Distribution Between Closely Spaced Geosynthetic Reinforcements.

Boyle, S., 1995. Unit cell tests on reinforced cohesionless soils. Proceedings of Geosynthetics' 95, 1221-1234.

Broms, B.B., 1977. Triaxial tests with fabric-reinforced soil. CR Coll. Int. Soils Textiles, 129-133.

Christopher, B.R., Gill, S., Giroud, J.-P., Juran, I., Mitchell, J.K., Schlosser, F., Dunnicliff, J., 1990. Reinforced soil structures. Volume I, Design and construction guidelines, Report No. FHWA-RD-89-043. Federal Highway Administration, Washington, DC.

Daniyarov, A., Zelenko, B., Derian, A., 2017. Deployment of the Geosynthetic Reinforced Soil Integrated Bridge System from 2011 to 2017, Report No. FHWA-HIF-17-043. Federal Highway Administration, Washington, DC.

Das, B.M., 2019. Advanced soil mechanics. CRC press.

Dave, T., Dasaka, S., 2011. A review on pressure measurement using earth pressure cell. International Journal of Earth Sciences and Engineering 4, 1031-1034.

Doger, R., 2020. Influence of Facing on the Construction and Structural Performance of GRS Bridge Abutments. The University of Oklahoma.

Doger, R., Hatami, K., 2020. Influence of facing on the performance of GRS bridge abutments. International Journal of Geosynthetics and Ground Engineering 6, 1-14.

Duncan, J.M., 2007. Densities and friction angles of granular materials with standard gradations 21b and# 57. Center for Geotechnical Practice and Research, The Charles E. Via, Jr ….

Elton, D.J., Patawaran, M.A.B., 2005. Mechanically stabilized earth (MSE) reinforcement tensile strength from tests of geotextile reinforced soil. Alabama Highway Research Center, Auburn University.

FDOT, 2020. Standard specifications for road and bridge construction. Florida DOT Tallahassee, FL.

FDOT, S., 2018. FDOT Structures Design Guidelines. FDOT Structures Manual.

FHWA, 2017. Every Day Counts: Creating Efficiency Through Technology and Collaboration-EDC-3 Final Report, Every Day Counts. Federal Highway Administration, US Department of Transportation Federal Highway Administration.

Gebremariam, F., Tanyu, B., Christopher, B., Leshchinsky, D., Han, J., Zornberg, J., 2019. Evaluation of vertical stress distribution in field monitored GRS-IBS structure. Geosynthetics International, 1-57.

Giroud, J., 1989. Geotextile engineering workshop-design examples. Rep. No. FHWA-HI-89 2.

Gotteland, P., Gourc, J., Villard, P., 1997. Geosynthetics reinforced structures as bridge abutments: full scale experimentation and comparison with modelisations, International Symposium on Mechanically Stabilized Backfill, Denver, Colorado, pp. 6-8.

Gray, D.H., Al-Refeai, T., 1986. Behavior of fabric-versus fiber-reinforced sand. Journal of Geotechnical Engineering 112, 804-820.

Hatami, K., Doger, R., 2021. Load-bearing performance of model GRS bridge abutments with different facing and reinforcement spacing configurations. Geotextiles and Geomembranes 49, 1139-1148.

Hoffman, P., 2015. Plasticity and the mechanics of reinforced soil. Preservation Engineering LLC.

Hoffman, P., Wu, J.T., 2017. Geosynthetic wall performance: Facing pressure and deformation.

Iwamoto, M., Ooi, P., Adams, M., Nicks, J., 2015. Composite properties from instrumented load tests on mini-piers reinforced with geotextiles. Geotechnical Testing Journal 38, 397-408.

Jewell, R., Milligan, G., 1989. Deformation calculations for reinforced soil walls, International congress of soil mechanics and foundation works, pp. 1257-1262.

Ketchart, K., 1997. Performance of geosynthetic-reinforced soil bridge pier and abutment, Denver, Colorado, USA. Mechanically stabilized backfill, 101-116.

Ketchart, K., Wu, J.T., 1997. Loading test of GRS bridge pier and abutment in Denver, Colorado. Colorado Department of Transportation.

Ketchart, K., Wu, J.T., 2001. Performance test for geosynthetic-reinforced soil including effects of preloading, Report No. FHWA-RD-01-018. Federal Highway Administration, Turner-Fairbank Highway Research Center, McLean,VA.

Ketchart, K., Wu, J.T., 2002. A modified soil-geosynthetic interactive performance test for evaluating deformation behavior of GRS structures. Geotechnical Testing Journal 25, 405-413.

Khosrojerdi, M., Qiu, T., Xiao, M., Nicks, J., 2020. Effects of Backfill Constitutive Behavior and Soil–Geotextile Interface Properties on Deformations of Geosynthetic-Reinforced Soil Piers under Static Axial Loading. Journal of Geotechnical and Geoenvironmental Engineering 146, 04020072.

Khosrojerdi, M., Xiao, M., Qiu, T., Nicks, J., 2017. Evaluation of prediction methods for lateral deformation of GRS walls and abutments. Journal of Geotechnical and Geoenvironmental Engineering 143, 06016022.

Knierim, C.D., 2014. Geotechnical characterization and drained shear strength of a limestone aggregate. Oregon State University, Oregon State University, p. 74.

Koerner, R.M., Koerner, G.R., 2013. A data base, statistics and recommendations regarding 171 failed geosynthetic reinforced mechanically stabilized earth (MSE) walls. Geotextiles and Geomembranes 40, 20-27.

Lwamoto, M.K., 2014. Observations from load tests on geosynthetic reinforced soil. University of Hawaii at Manoa.

Mitchell, J., 2002. Behavior of Geosynthetically Reinforced Soil Bridge Piers. MS Report, University of Massachusetts at Amherst.

MOGHADAS, T.S., Asakereh, A., 2007. Strength evaluation of wet reinforced silty sand by triaxial test.

Newmark, N.M., 1935. Simplified computation of vertical pressures in elastic foundations. Engineering Experiment Station. Circular; no. 024.

Nicks, J., Adams, M., Stabile, T., Li, J., 2020. Instrumentation and 5-Year Performance Monitoring of a GRS IBS in St. Lawrence County, NY, Report No. FHWA-HRT-20-040. Office

of Infrastructure Research and Development, Turner-Fairbank Highway Research Center, McLean, VA.

Nicks, J., Gebrenegus, T., Adams, M., 2015. Strength characterization of open-graded aggregates for structural backfills. United States. Federal Highway Administration. Office of Infrastructure ….

Nicks, J.E., Adams, M., Ooi, P., Stabile, T., 2013. Geosynthetic reinforced soil performance testing—Axial load deformation relationships, Report No. FHWA-HRT-13-066. Federal Highway Adminstration- Research, Development and Technology, McLean, VA.

Nicks, J.E., Esmaili, D., Adams, M.T., 2016. Deformations of geosynthetic reinforced soil under bridge service loads. Geotextiles and Geomembranes 44, 641-653.

Ooi, P.S., Adams, M.T., Lawrence, J.B., 2019. Long-Term Behavior of a Geosynthetic Reinforced Soil Integrated Bridge System in Hawaii. Transportation Research Record 2673, 571-582.

Pham, T.Q., 2009. Investigating composite behavior of geosynthetic-reinforced soil (GRS) mass. University of Colorado Denver.

Saghebfar, M., Abu-Farsakh, M., Ardah, A., Chen, Q., Fernandez, B.A., 2017. Performance monitoring of geosynthetic reinforced soil integrated bridge system (GRS-IBS) in Louisiana. Geotextiles and Geomembranes 45, 34-47.

Schlosser, F., Long, N.-T., 1974. Recent results in French research on reinforced earth. Journal of the construction Division 100.

Talebi, M., 2016. Analysis of the field behavior of a geosynthetic reinforced soil integrated bridge system during construction and operation. University of Delaware.

Westergaard, H., 1938. A problem of elasticity suggested by a problem in soil mechanics: soft material reinforced by numerous strong horizontal sheets. Contributions to the mechanics of solids, Stephen Timoshenko 60th anniversary volume, Macmillan, New York 260, 277.

Whittle, A., Germaine, J., Larson, D., Abramento, M., 1992. Measurement and interpretation of reinforcement stresses in the APSR cell, International symposium on earth reinforcement practice, pp. 179-184.

Wu, J., 1994. Design and construction of low cost retaining walls: the next generation in technology, Publication No. CTI-UCD-1–94, Colorado Transportation Institute, Denver, Colorado, USA.

Wu, J., Lee, K., Helwany, S., Ketchart, K., 2006. Design and Construction Guidelines for Geosynthetic Reinforced Soil Bridge Abutments with a Flexible Facing, NCHRP REPORT 556. Transportation Research Board Washington, DC.

Wu, J., Pham, T., 2010. An analytical model for calculating lateral movement of a geosynthetic-reinforced soil (GRS) wall with modular block facing. International Journal of Geotechnical Engineering 4, 527-535.

Wu, J.T., 2001. Revising the AASHTO guidelines for design and construction of GRS walls. United States. Federal Highway Administration.

Wu, J.T., 2019a. Characteristics of geosynthetic reinforced soil (GRS) walls: an overview of field-scale experiments and analytical studies. Transportation Infrastructure Geotechnology 6, 138-163.

Wu, J.T., 2019b. Geosynthetic reinforced soil (GRS) walls. John Wiley & Sons.

Wu, J.T., Ketchart, K., Adams, M., 2001. GRS bridge piers and abutments. Turner-Fairbank Highway Research Center.

Wu, J.T., Pham, T.Q., 2013. Load-carrying capacity and required reinforcement strength of closely spaced soil-geosynthetic composites. Journal of Geotechnical and Geoenvironmental Engineering 139, 1468-1476.

Wu, J.T., Pham, T.Q., Adams, M., 2013. Composite Behaviour of Geosynthetic Reinforced Soil Mass, Report No. FHWA-HRT-10-077. Federal Highway Administration, Washington, DC.

Yang, Z., 1972. Strength and deformation characteristics of reinforced sand. University of California, Los Angeles.

Yazdandoust, M., Taimouri, A.B.B., 2023. Lateral Pressure Distribution and Shear Band Development in Two-Tiered MSE Walls under Footing Loading. International Journal of Geomechanics 23, 04023038.

ZEN, Y., YANG, Z., SINGH, A., 1974. Strength and deformation characteristics of reinforced sand.

Zheng, Y., 2017. Numerical simulations and shaking table tests of geosynthetic reinforced soil bridge abutments. University of California, San Diego.

Zheng, Y., Fox, P.J., Shing, P.B., McCartney, J.S., 2019a. Physical model tests of half-scale geosynthetic reinforced soil bridge abutments. I: Static loading. Journal of Geotechnical and Geoenvironmental Engineering 145, 04019094.

Zheng, Y., McCartney, J.S., Shing, P.B., Fox, P.J., 2019b. Physical model tests of half-scale geosynthetic reinforced soil bridge abutments. II: Dynamic loading. Journal of Geotechnical and Geoenvironmental Engineering 145, 04019095.

Zornberg, J., Christopher, B., Leshchinsky, D., Han, J., Tanyu, B., Morsy, A., Shen, P., Gebremariam, F., Jiang, Y., Mofarraj, B., 2018a. Defining the Boundary Conditions for Composite Behavior of Geosynthetic-Reinforced Soil Structures, Project No. 24-41 National Cooperative Highway Research Program (NCHRP) Transportation Research Board, National Academies of Sciences, Engineering, and Medicine.

Zornberg, J., Morsy, A., Kouchaki, B., Christopher, B., Leshchinsky, D., Han, J., Tanyu, B., Gebremariam, F., Shen, P., Jiang, Y., 2018b. Defining the boundary conditions for composite behavior of geosynthetic reinforced soil (GRS) structures. Project NCHRP, 24-41.

# APPENDIX A. LATERAL DISPLACEMENT

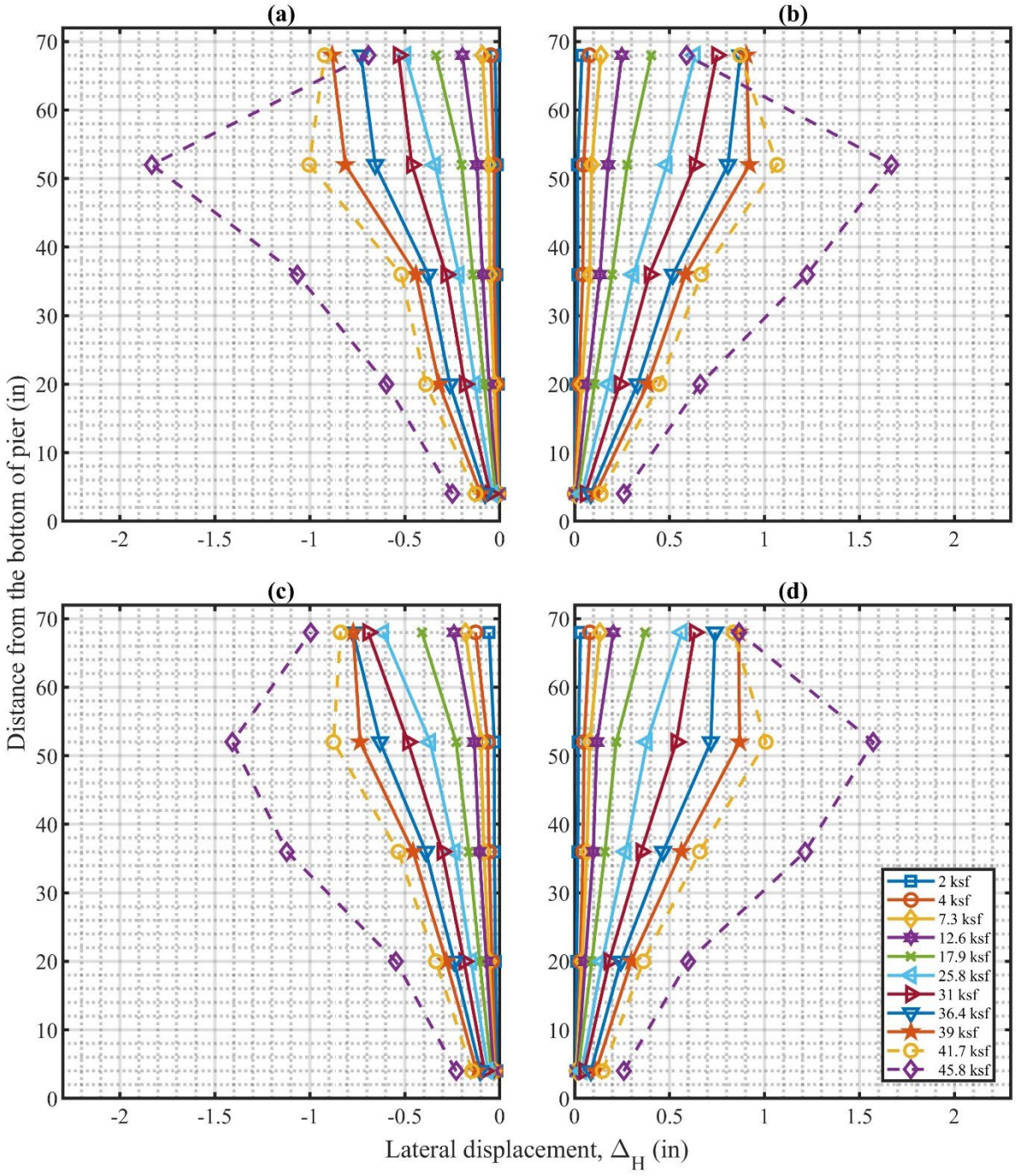


Figure A-1. Measured lateral displacements along the facing walls for PT-01.
(a) South wall; (b) North wall; (e) West wall; (f) East wall.

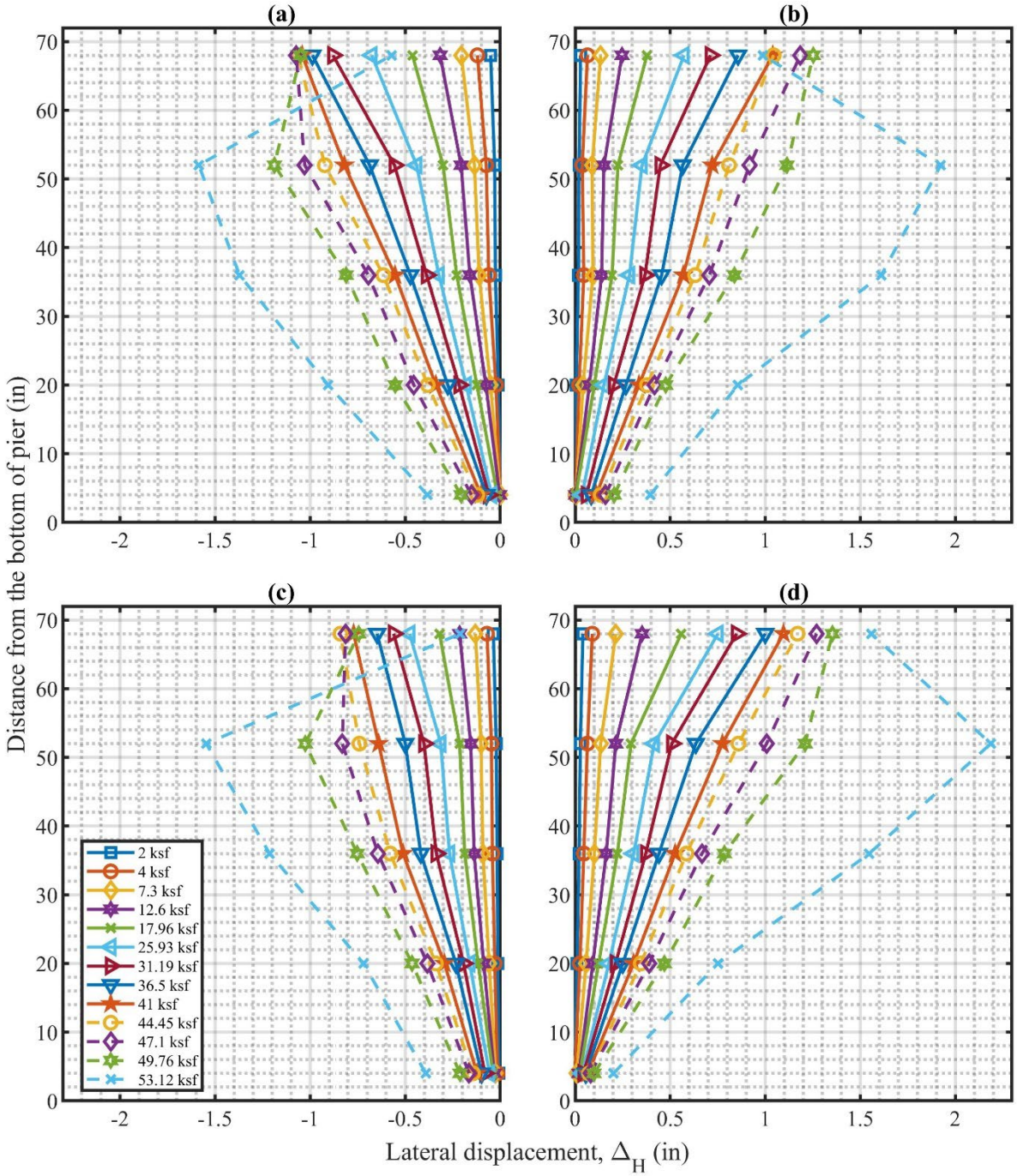


Figure A-2. Measured lateral displacements along the facing walls for PT-02.
(a) South wall; (b) North wall; (e) West wall; (f) East wall.

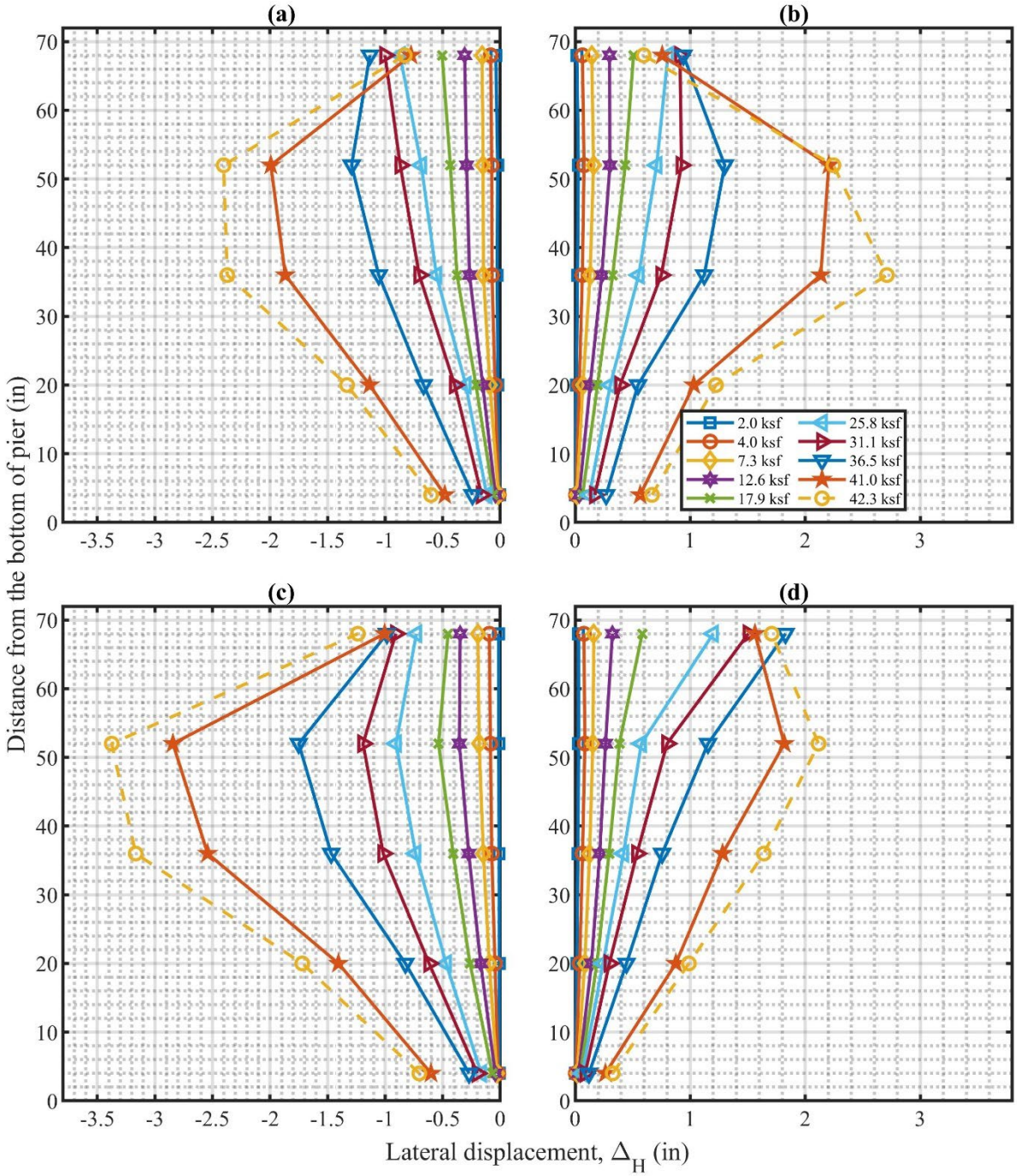


Figure A-3. Measured lateral displacements along the facing walls for PT-03.
(a) South wall; (b) North wall; (e) West wall; (f) East wall.

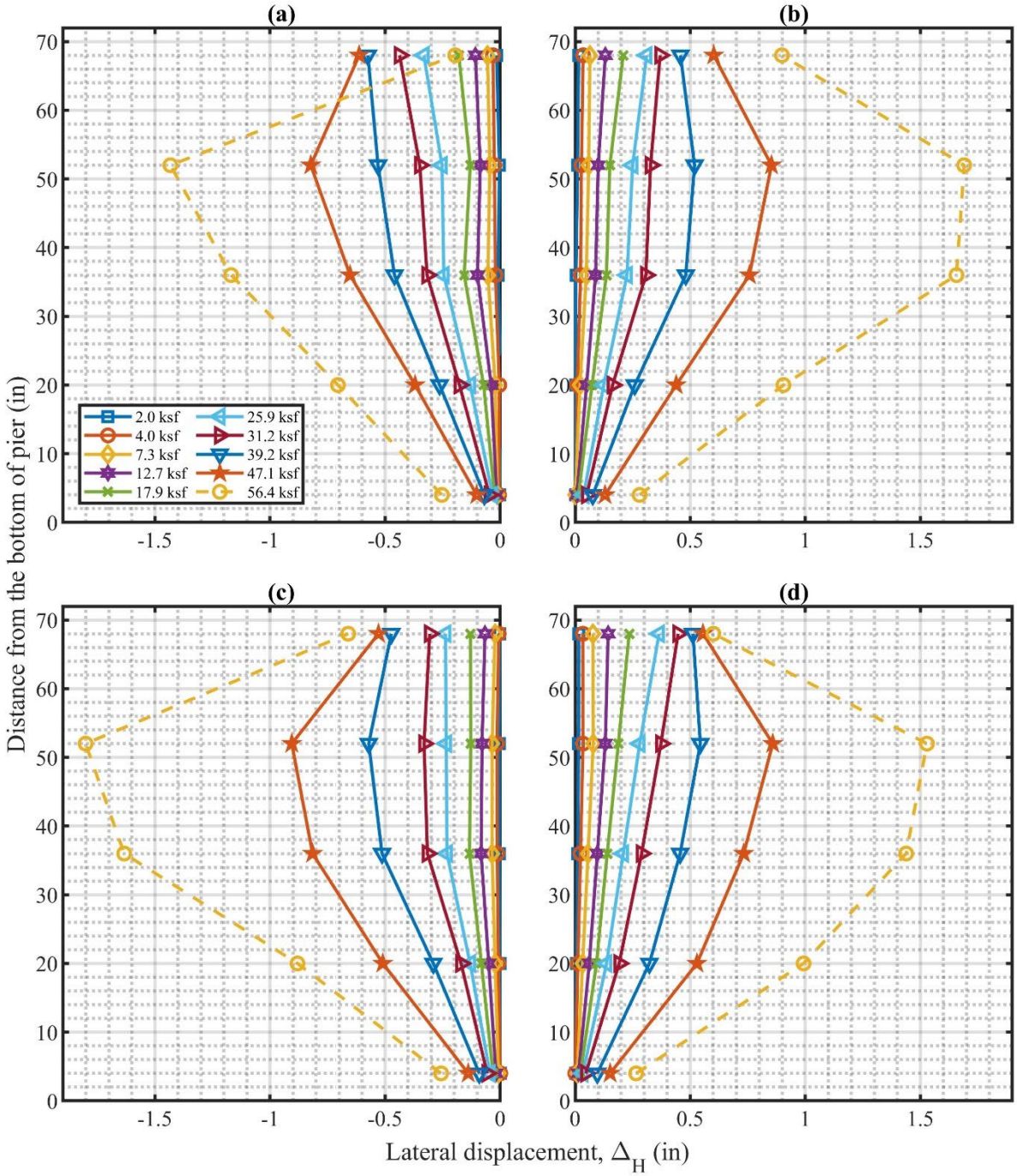


Figure A-4. Measured lateral displacements along the facing walls for PT-04.
(a) South wall; (b) North wall; (e) West wall; (f) East wall.

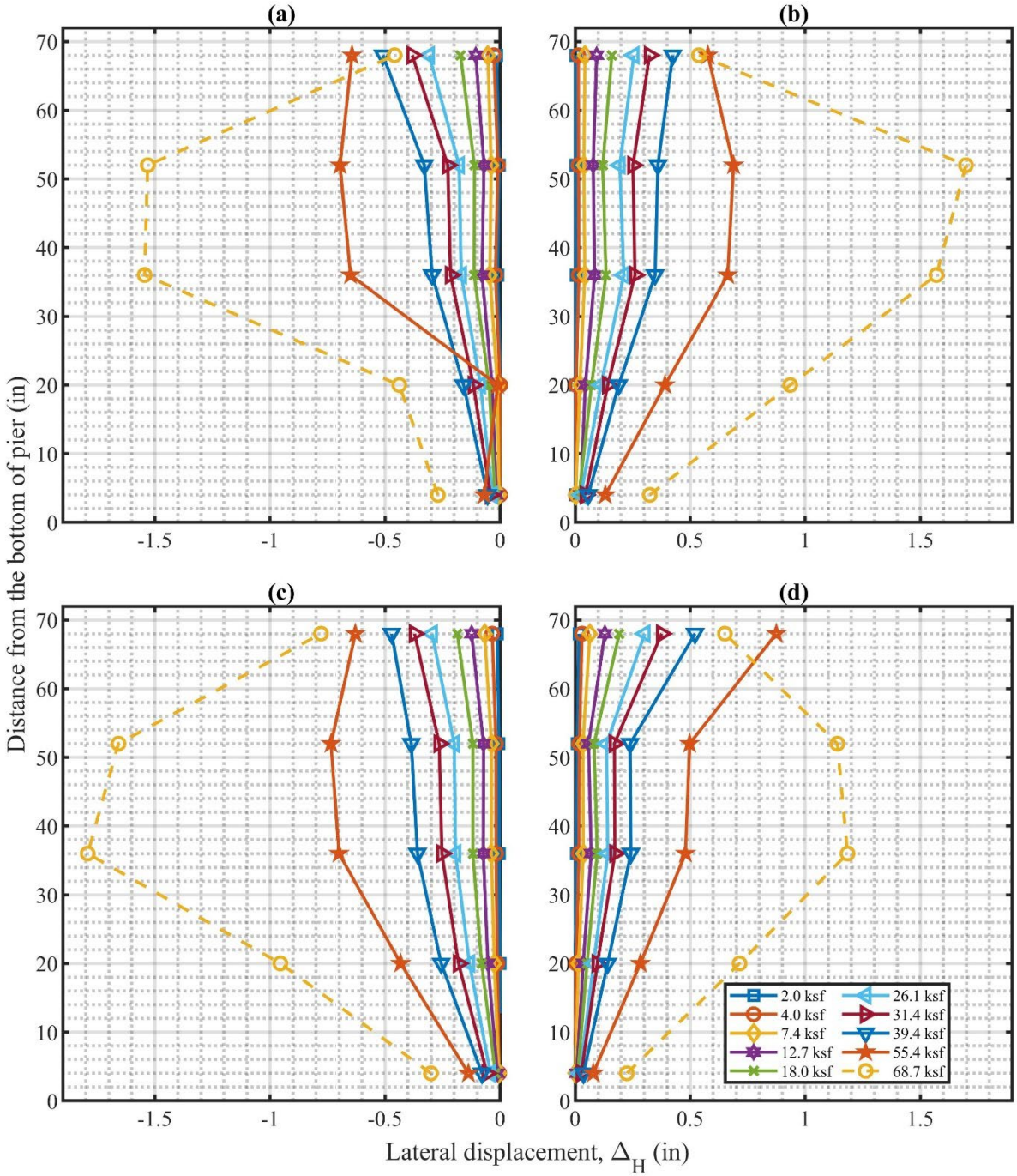


Figure A-5. Measured lateral displacements along the facing walls for PT-05.
(a) South wall; (b) North wall; (e) West wall; (f) East wall.

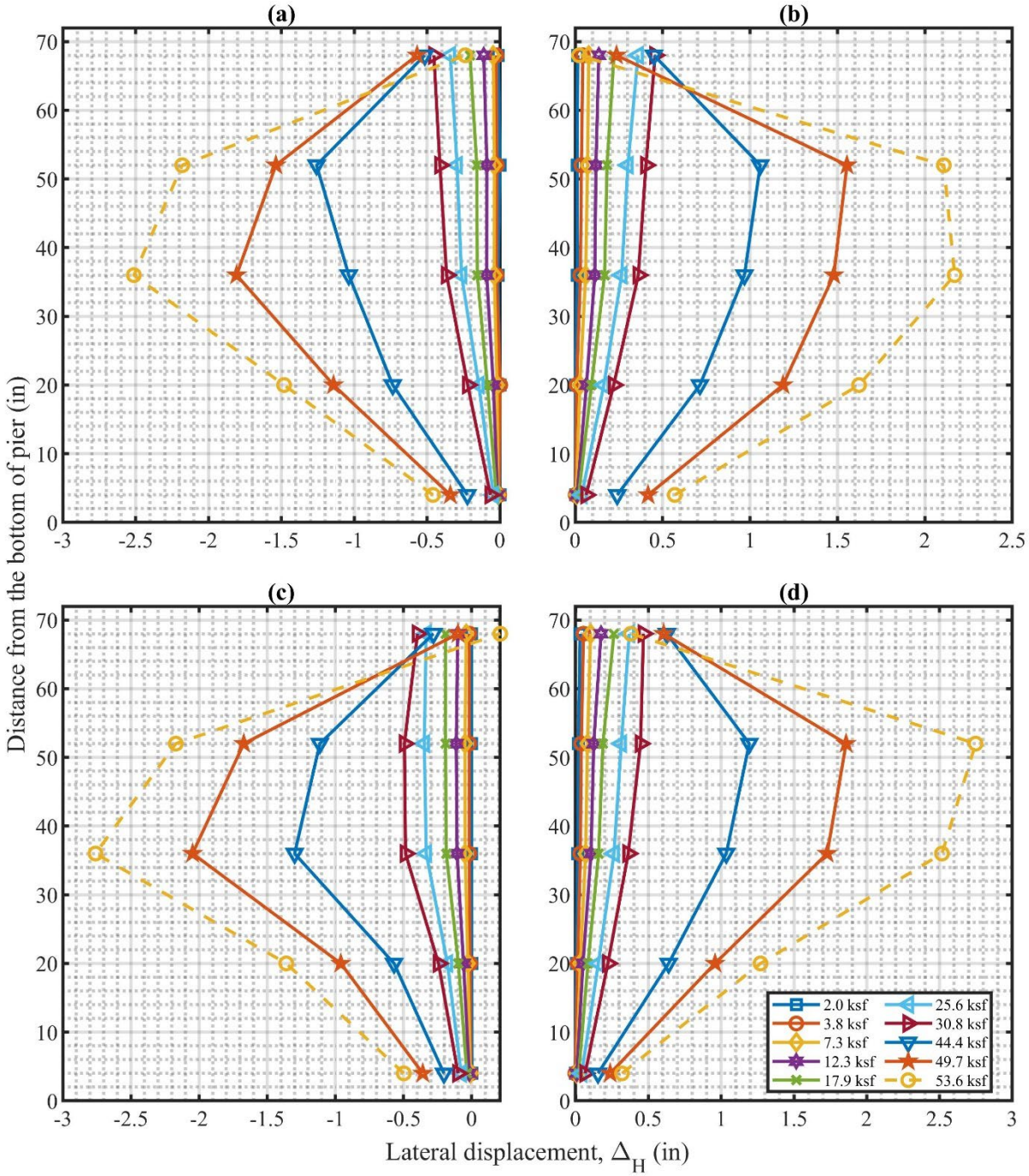


Figure A-6. Measured lateral displacements along the facing walls for PT-06.
(a) South wall; (b) North wall; (e) West wall; (f) East wall.

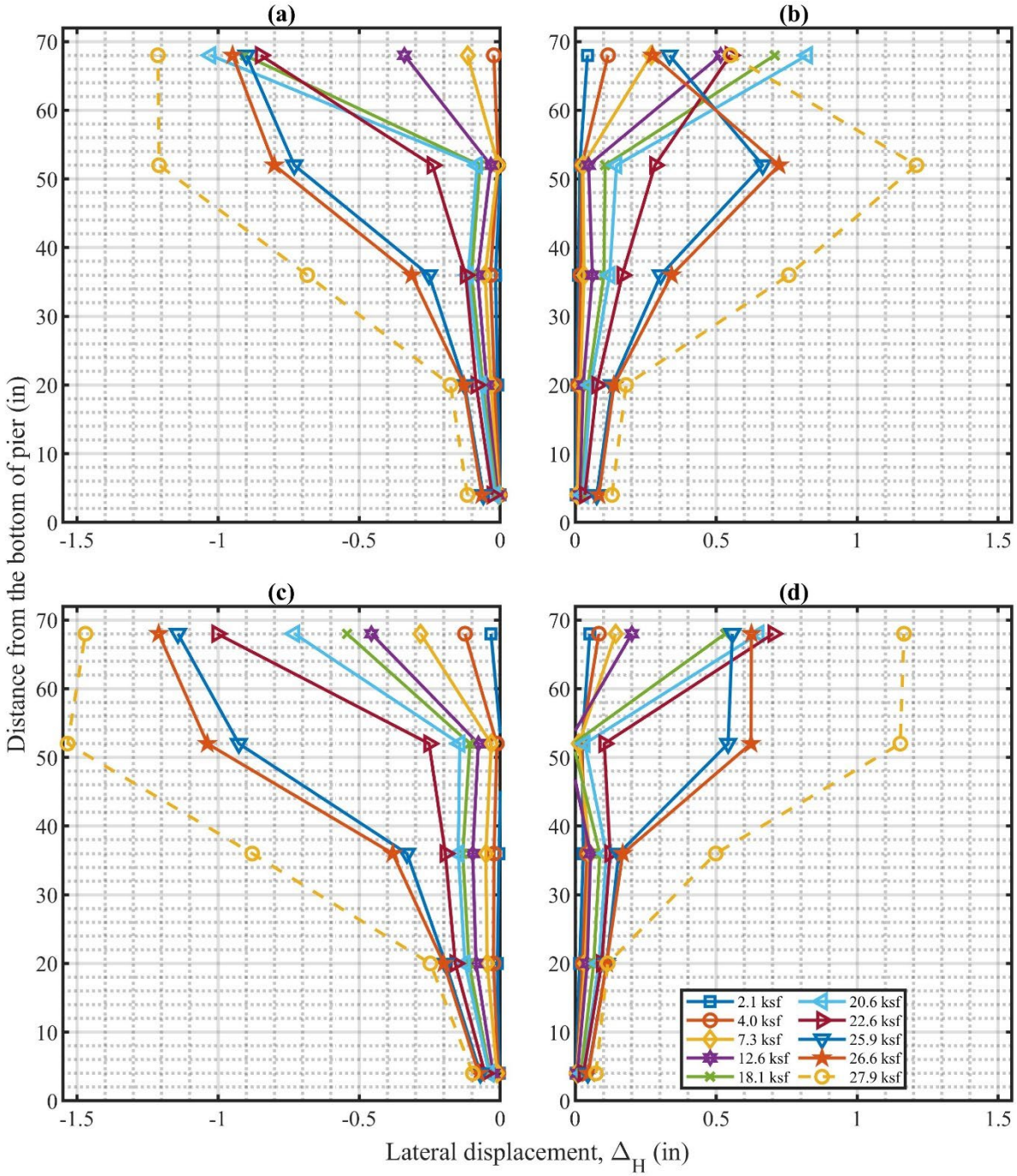


Figure A-7. Measured lateral displacements along the facing walls for PT-07.
(a) South wall; (b) North wall; (e) West wall; (f) East wall.

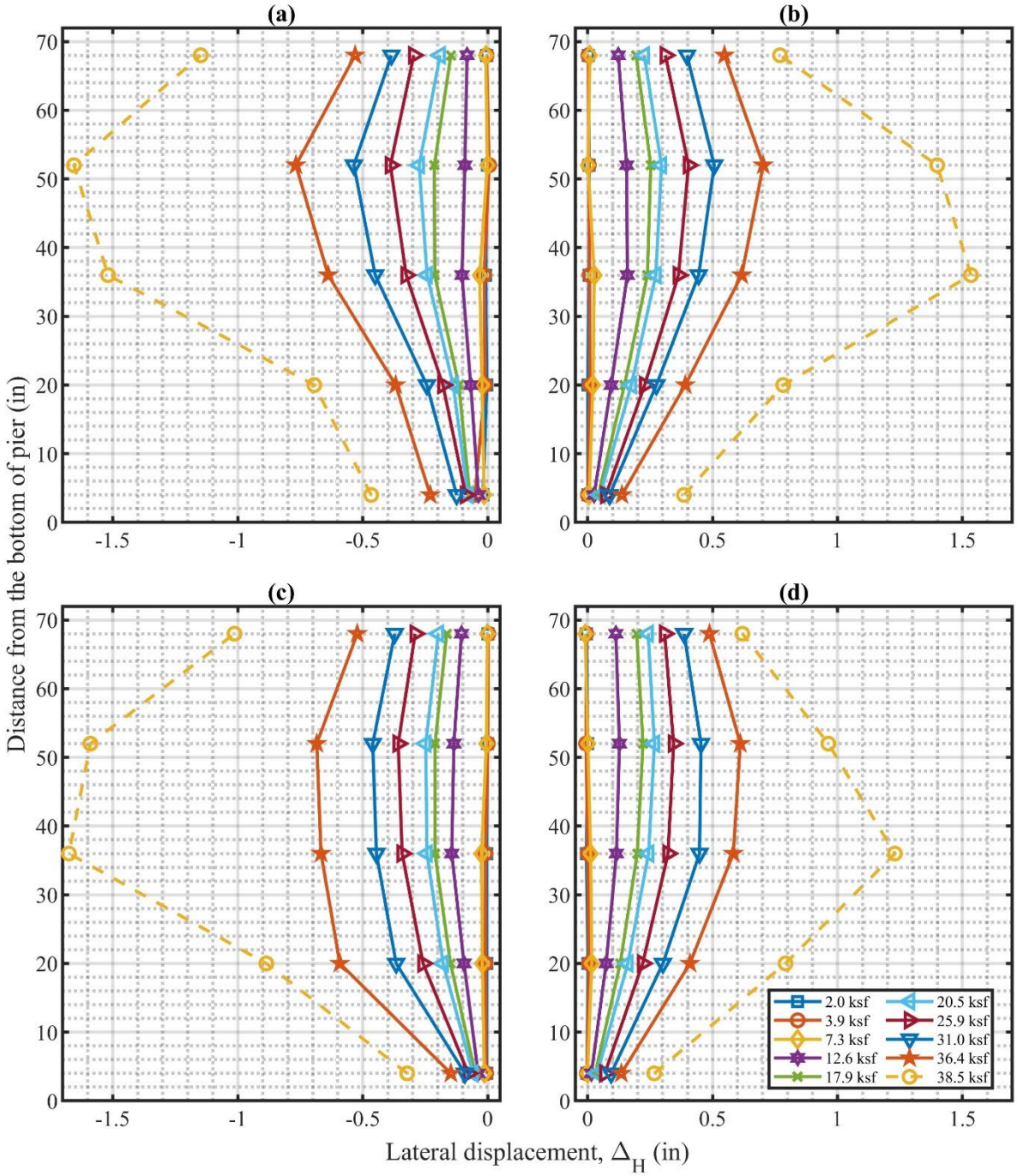


Figure A-8. Measured lateral displacements along the facing walls for PT-08.
(a) South wall; (b) North wall; (e) West wall; (f) East wall.

# APPENDIX B. REINFORCEMENT STRAIN

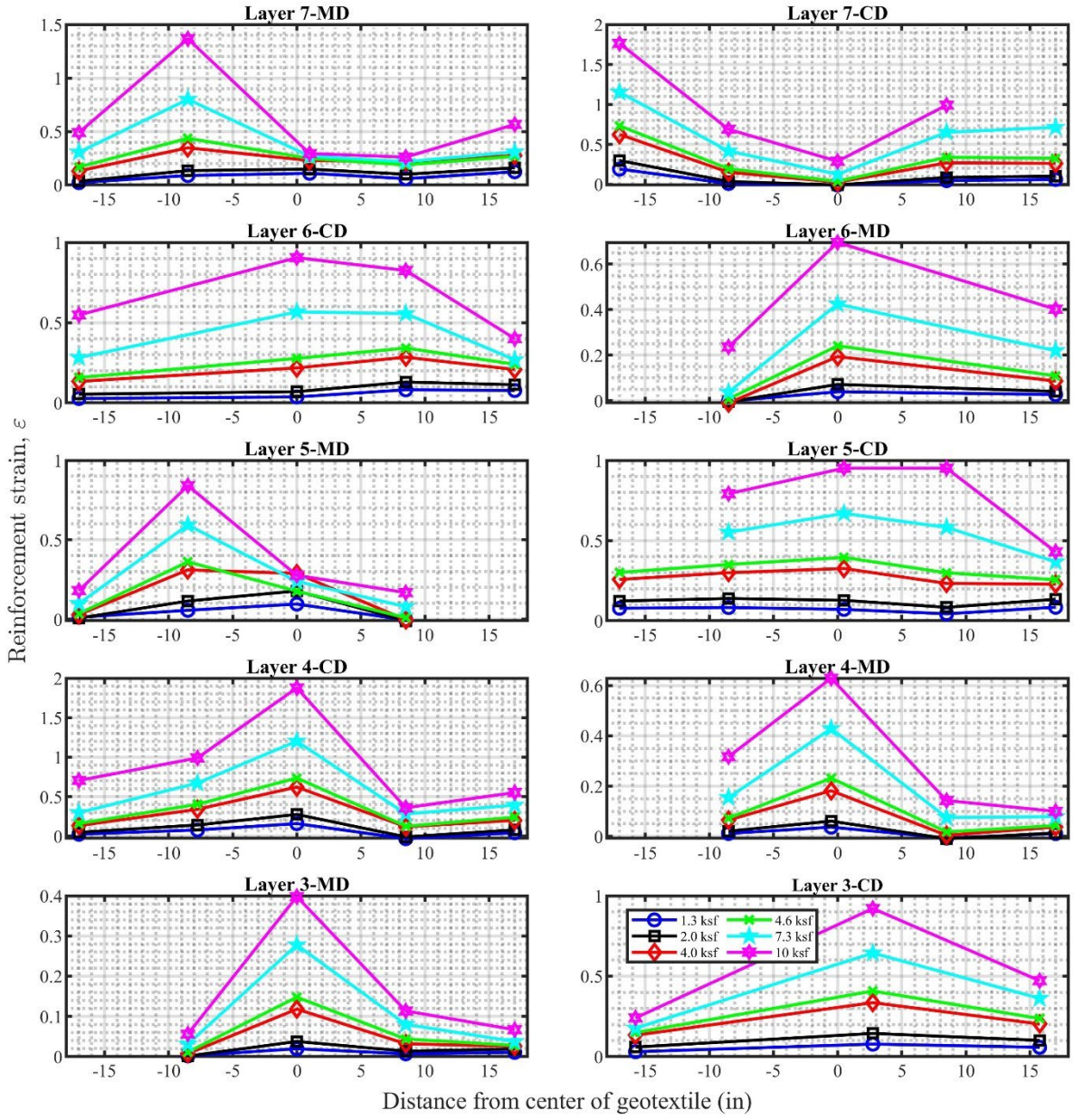


Figure B-1. Reinforcement strain distribution in geotextile at different applied vertical stress for PT-01.

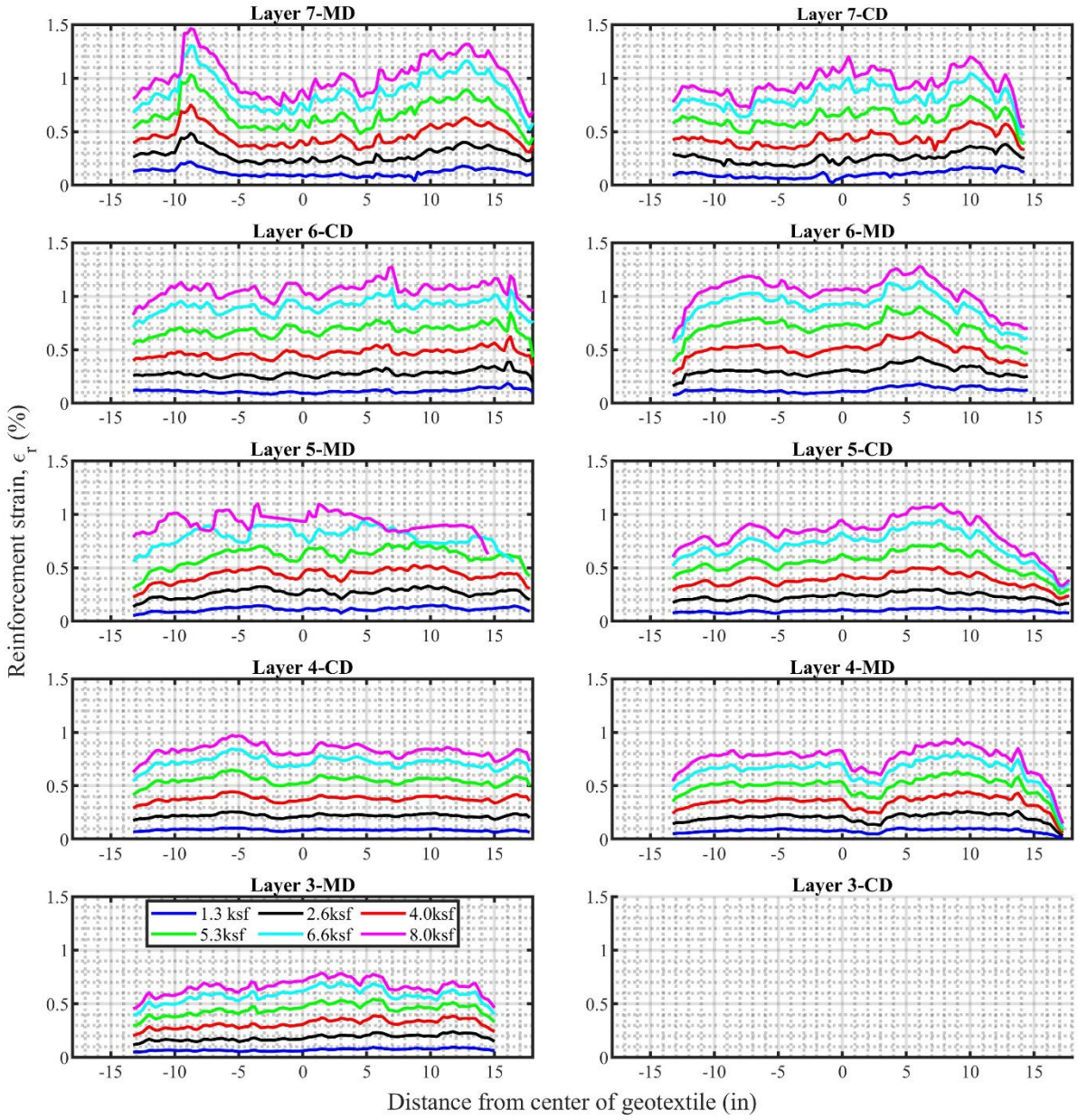


Figure B-2. Reinforcement strain distribution in geotextile at different applied vertical stress for PT-02.

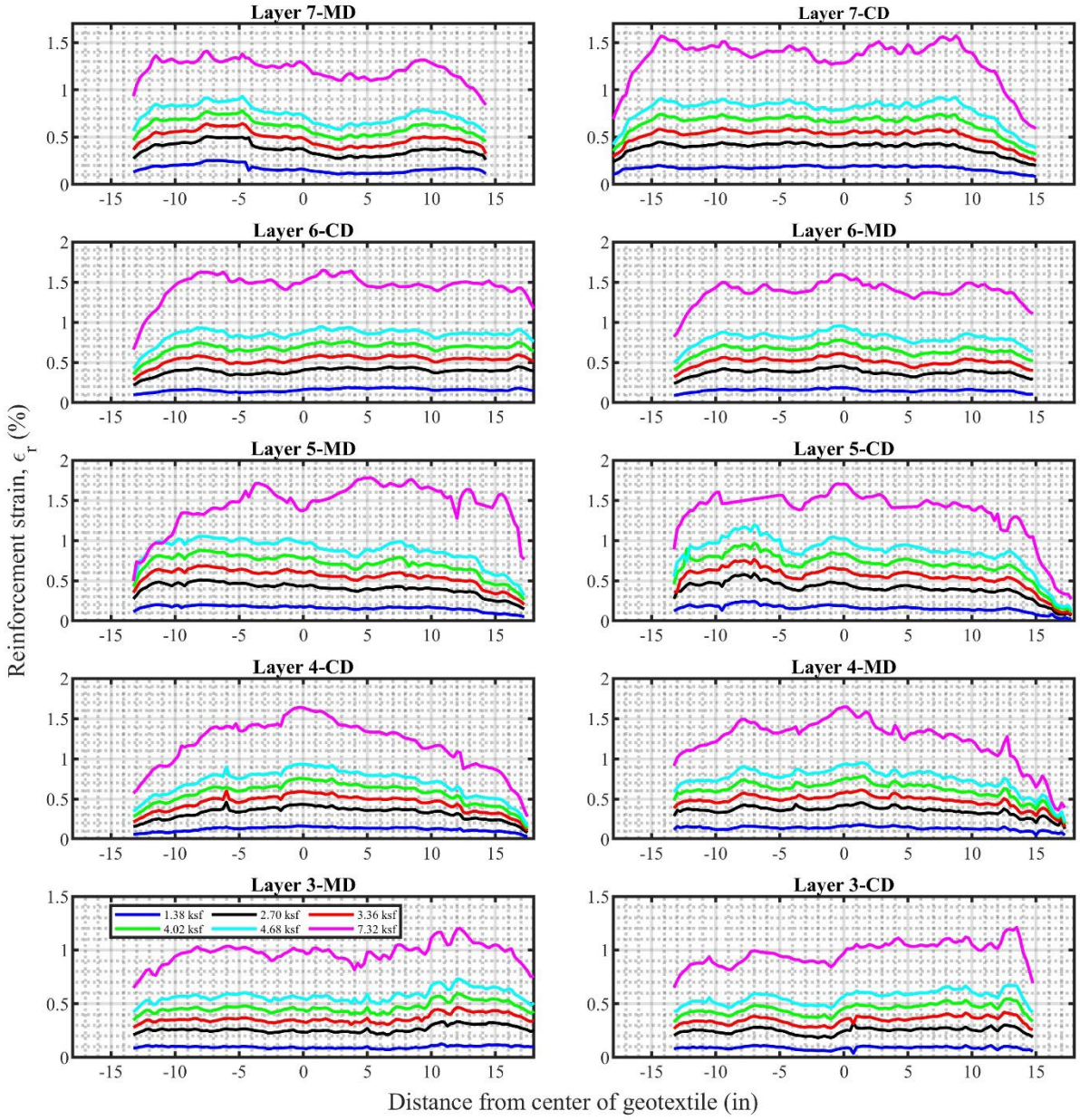


Figure B-3. Reinforcement strain distribution in geotextile at different applied vertical stress for PT-03.

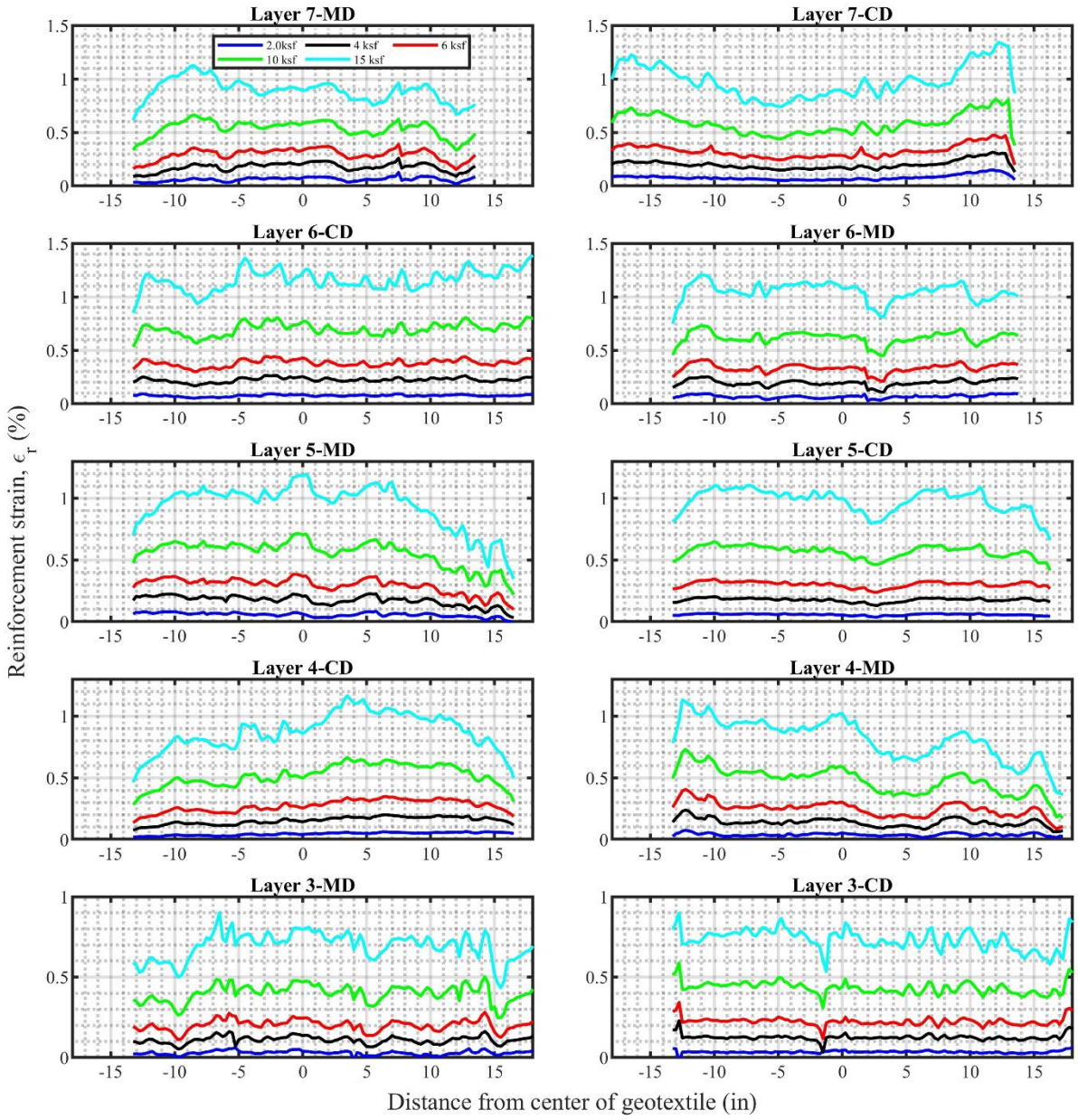


Figure B-4. Reinforcement strain distribution in geotextile at different applied vertical stress for PT-04.

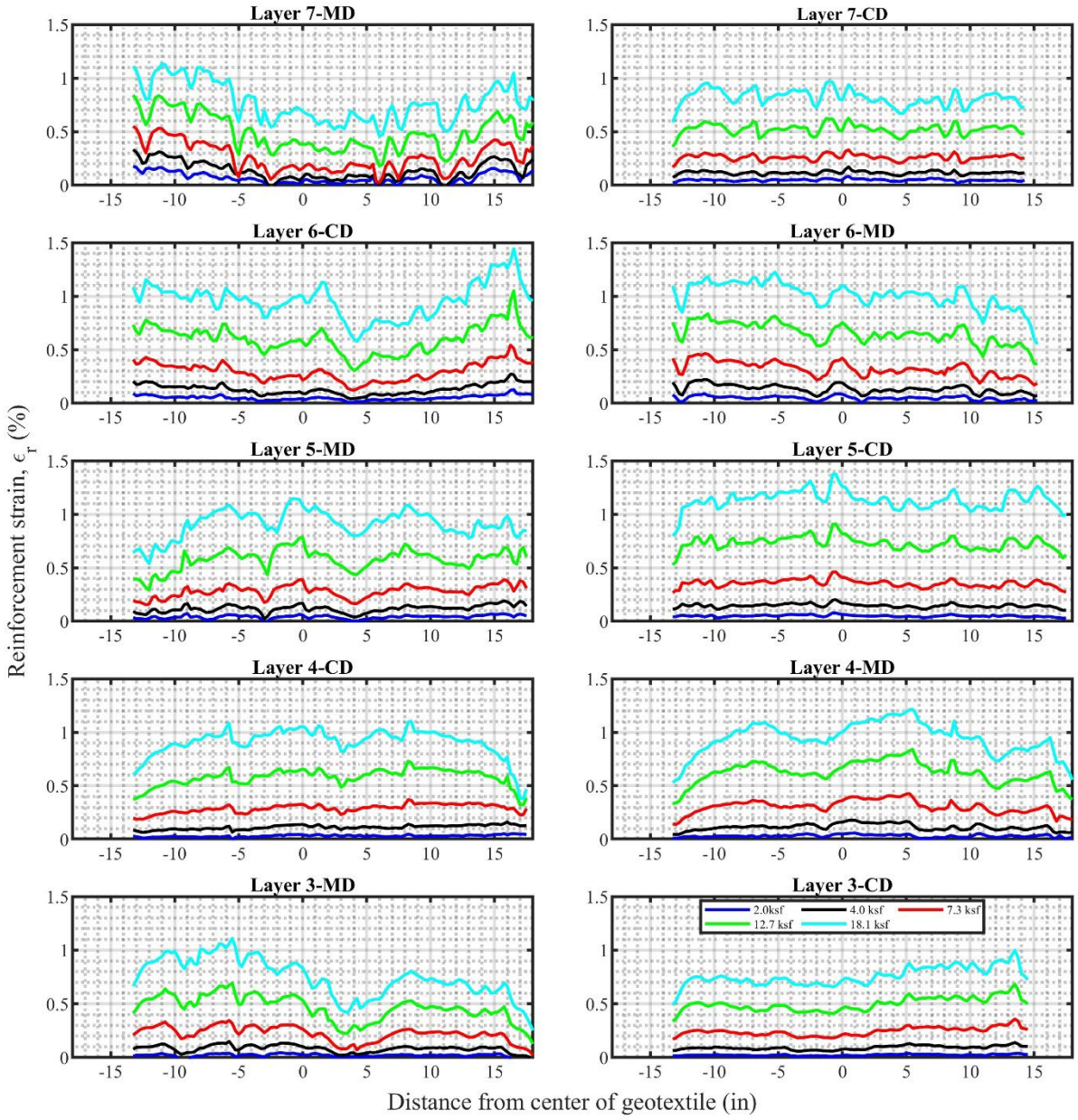


Figure B-5. Reinforcement strain distribution in geotextile at different applied vertical stress for PT-05.

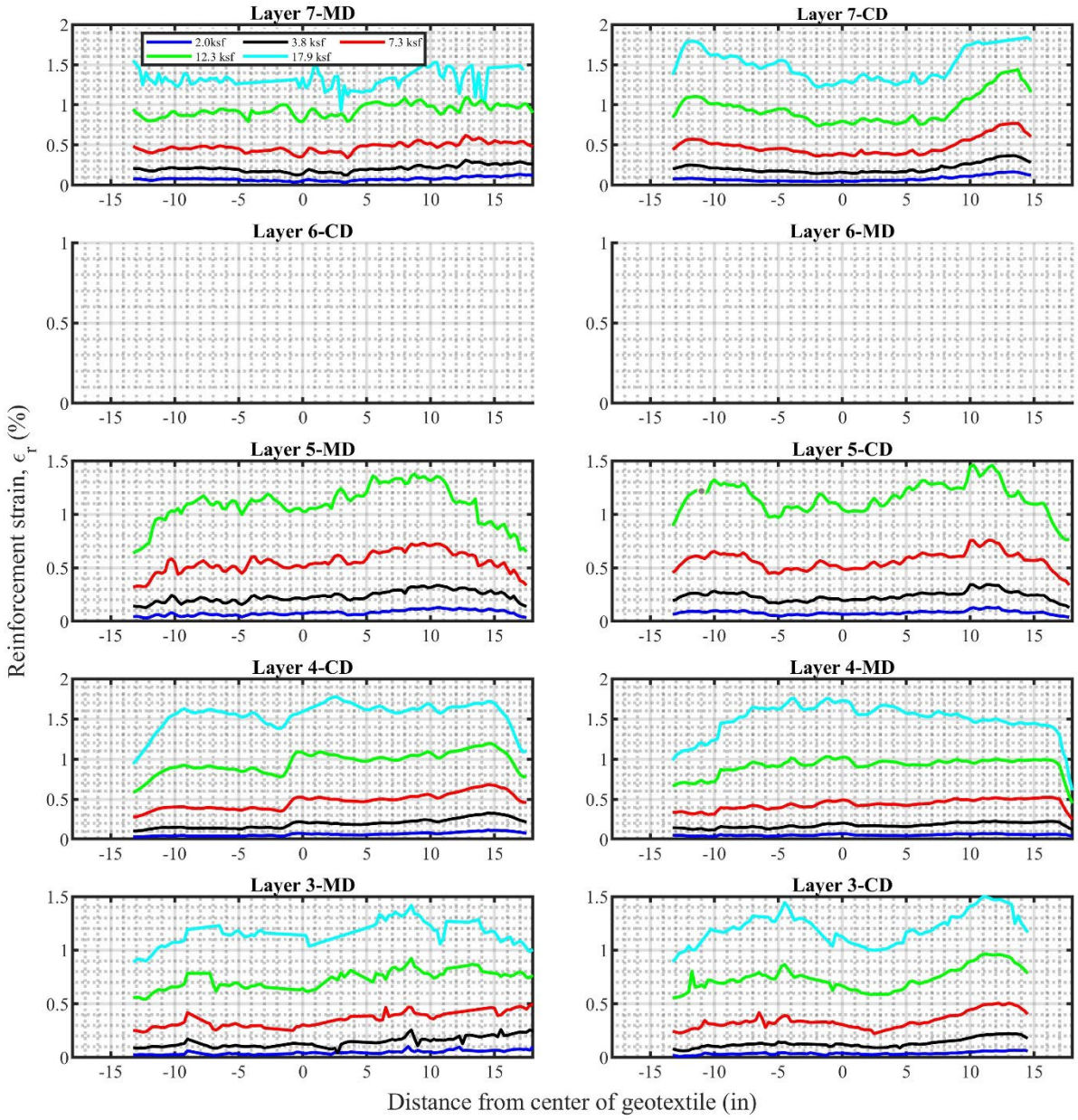


Figure B-6. Reinforcement strain distribution in geotextile at different applied vertical stress for PT-06.

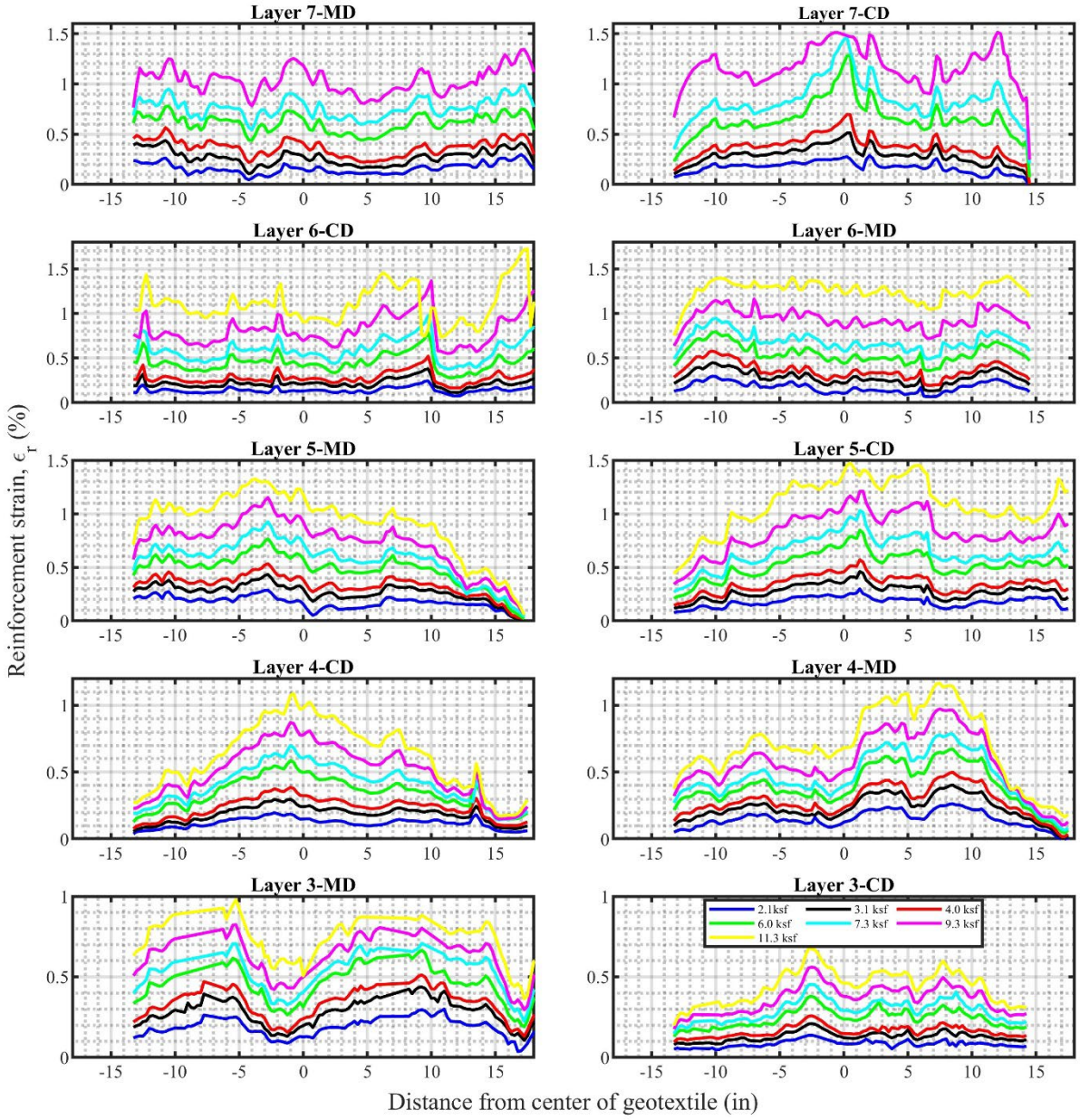


Figure B-7. Reinforcement strain distribution in geotextile at different applied vertical stress for PT-07.

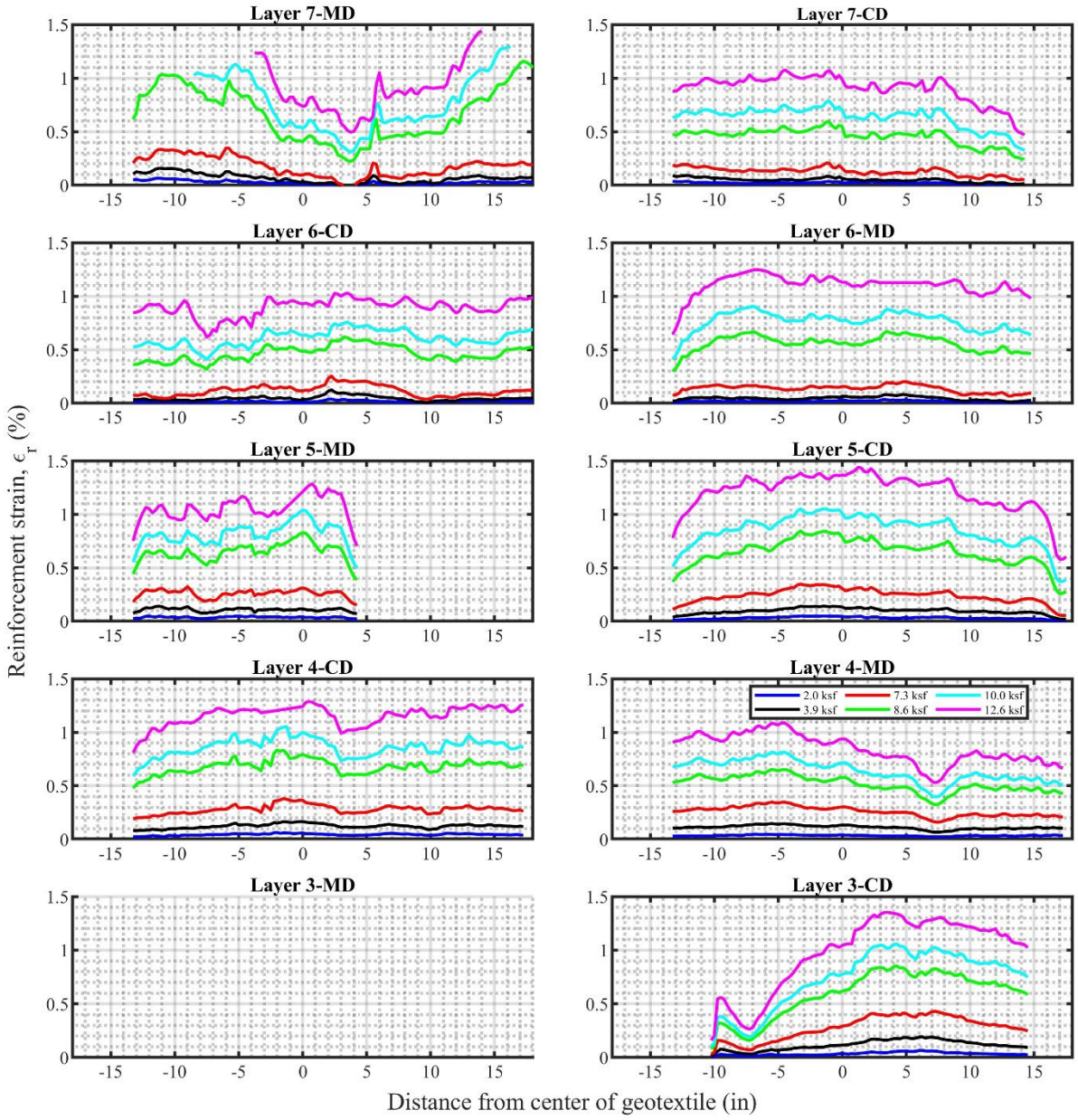


Figure B-8. Reinforcement strain distribution in geotextile at different applied vertical stress for PT-08.

## APPENDIX C. DENSITY DURING CONSTRUCTION

Table C-1. Density during construction of PT-01 determined based on weight and volume.

| Dry unit weight (pcf) | Moisture Content (%) | Distance of top of layer from bottom (in) |
|---|---|---|
| 97.15 | N/A | 8 |
| 97.80 | N/A | 16 |
| 95.90 | N/A | 24 |
| 95.67 | N/A | 32 |
| 97.06 | N/A | 40 |
| 96.69 | N/A | 48 |
| 96.61 | N/A | 56 |
| 97.36 | N/A | 64 |
| 97.65 | N/A | 72 |

Table C-2. Density during construction of PT-02 determined based on weight and volume.

| Dry unit weight (pcf) | Moisture Content (%) | Distance of top of layer from bottom (in) |
|---|---|---|
| 99.41 | N/A | 8 |
| 97.87 | N/A | 16 |
| 97.82 | N/A | 24 |
| 97.70 | N/A | 32 |
| 96.95 | N/A | 40 |
| 97.28 | N/A | 48 |
| 96.95 | N/A | 56 |
| 96.73 | N/A | 64 |
| 97.22 | N/A | 72 |

Table C-3. Density during construction of PT-03 determined based on weight and volume.

| Dry unit weight (pcf) | Moisture Content (%) | Distance of top of layer from bottom (in) |
|---|---|---|
| 95.46 | N/A | 8 |
| 96.42 | N/A | 16 |
| 96.71 | N/A | 24 |
| 96.95 | N/A | 32 |
| 96.96 | N/A | 40 |
| 96.60 | N/A | 48 |
| 96.48 | N/A | 56 |
| 96.41 | N/A | 64 |
| 96.97 | N/A | 72 |

Table C-4. Density during construction of PT-04 measured by nuclear density gauge.

| Dry unit weight (pcf) | Moisture content (%) | Distance of top of layer from bottom (in) |
|---|---|---|
| 106.74 | 11.46 | 8 |
| 116.26 | 12.33 | 16 |
| 118.03 | 12.24 | 24 |
| 109.80 | 11.37 | 32 |
| 110.03 | 12.05 | 40 |
| 113.03 | 12.18 | 48 |
| 112.88 | 12.02 | 56 |
| 110.90 | 10.57 | 64 |
| 115.37 | 12.74 | 72 |

Table C-5. Density during construction of PT-05 measured by nuclear density gauge.

| Dry unit weight (pcf) | Moisture Content (%) | Distance of top of layer from bottom (in) |
|---|---|---|
| 113.20 | 10.40 | 8 |
| 117.83 | 11.88 | 16 |
| 116.72 | 11.46 | 24 |
| 111.87 | 12.57 | 32 |
| 112.95 | 11.73 | 40 |
| 115.17 | 12.83 | 48 |
| 111.77 | 13.17 | 56 |
| 111.72 | 12.90 | 64 |
| 112.09 | 13.71 | 72 |

Table C-6. Density during construction of PT-06 measured by nuclear density gauge.

| Dry unit weight (pcf) | Moisture Content (%) | Distance of top of layer from bottom (in) |
|---|---|---|
| 113.23 | 13.67 | 8 |
| 114.73 | 15.10 | 16 |
| 116.60 | 14.73 | 24 |
| 111.60 | 13.33 | 32 |
| 115.60 | 13.67 | 40 |
| 112.40 | 13.10 | 48 |
| 115.63 | 13.97 | 56 |
| 113.33 | 14.47 | 64 |
| 112.29 | 14.09 | 72 |

Table C-7. Density during construction of PT-07 determined based on weight and volume.

| Dry unit weight (pcf) | Moisture Content (%) | Distance of top of layer from bottom (in) |
|---|---|---|
| 18.97 | N/A | 8 |
| 17.88 | N/A | 16 |
| 17.69 | N/A | 24 |
| 17.93 | N/A | 32 |
| 17.93 | N/A | 40 |
| 17.88 | N/A | 48 |
| 17.88 | N/A | 56 |
| 19.12 | N/A | 64 |
| 18.68 | N/A | 72 |

Table C-8. Density during construction of PT-08 determined based on weight and volume.

| Dry unit weight (pcf) | Moisture Content (%) | Distance of top of layer from bottom (in) |
|---|---|---|
| 97.84 | N/A | 8 |
| 96.99 | N/A | 16 |
| 96.88 | N/A | 24 |
| 96.81 | N/A | 32 |
| 96.82 | N/A | 40 |
| 96.89 | N/A | 48 |
| 96.90 | N/A | 56 |
| 97.02 | N/A | 64 |
| 96.85 | N/A | 72 |

## APPENDIX D. INTERNAL LATERAL EARTH PRESSURE

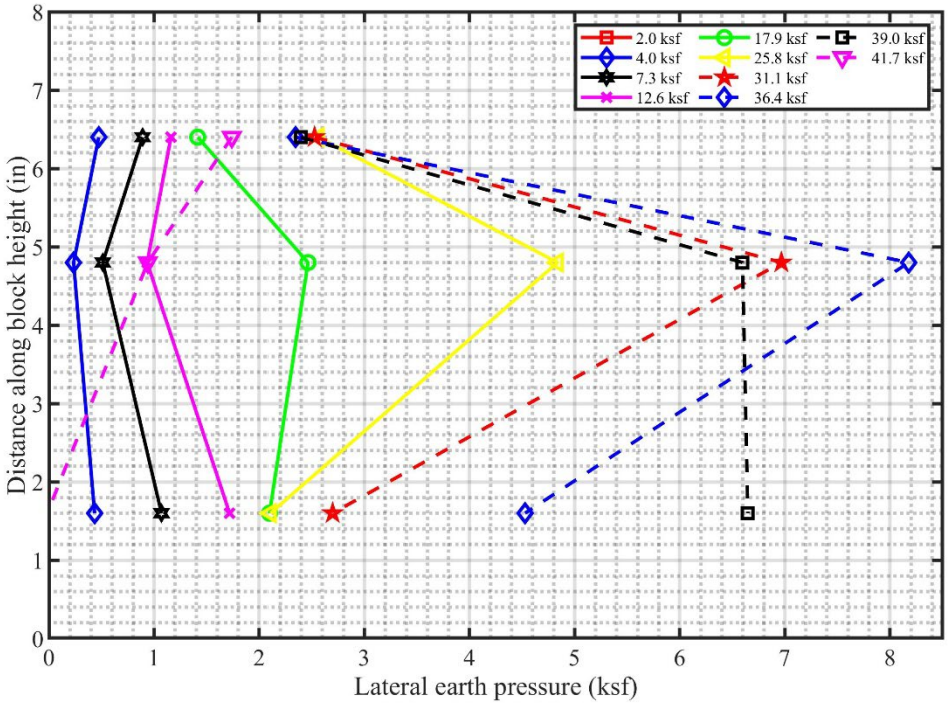


Figure D-1. Lateral earth pressure for PT-01 during axial loading of the pier.

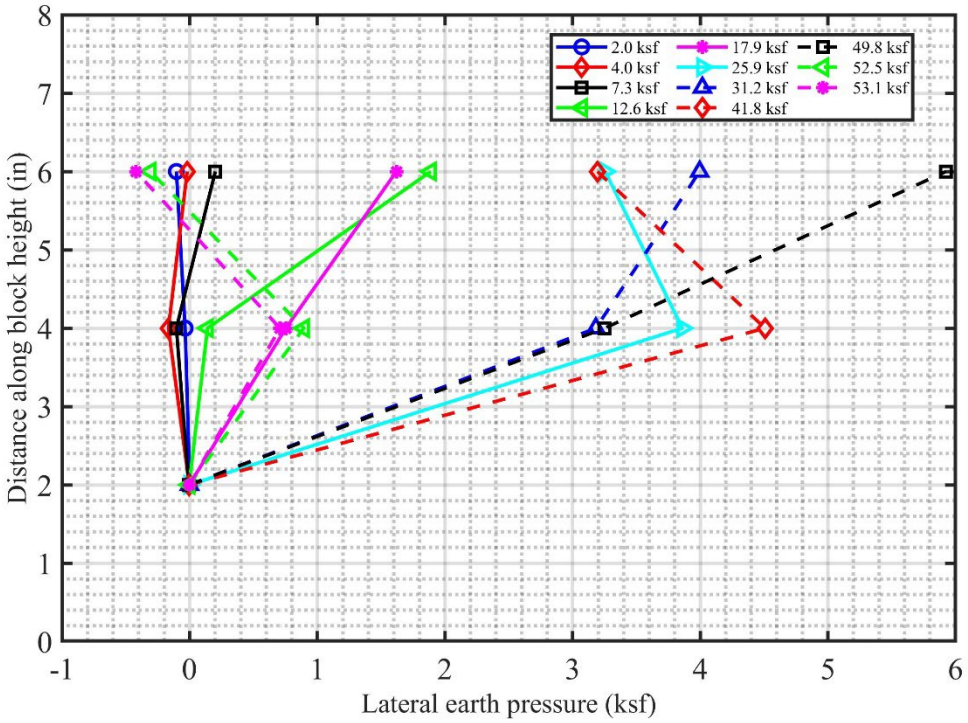


Figure D-2. Lateral earth pressure for PT-02 during axial loading of the pier.

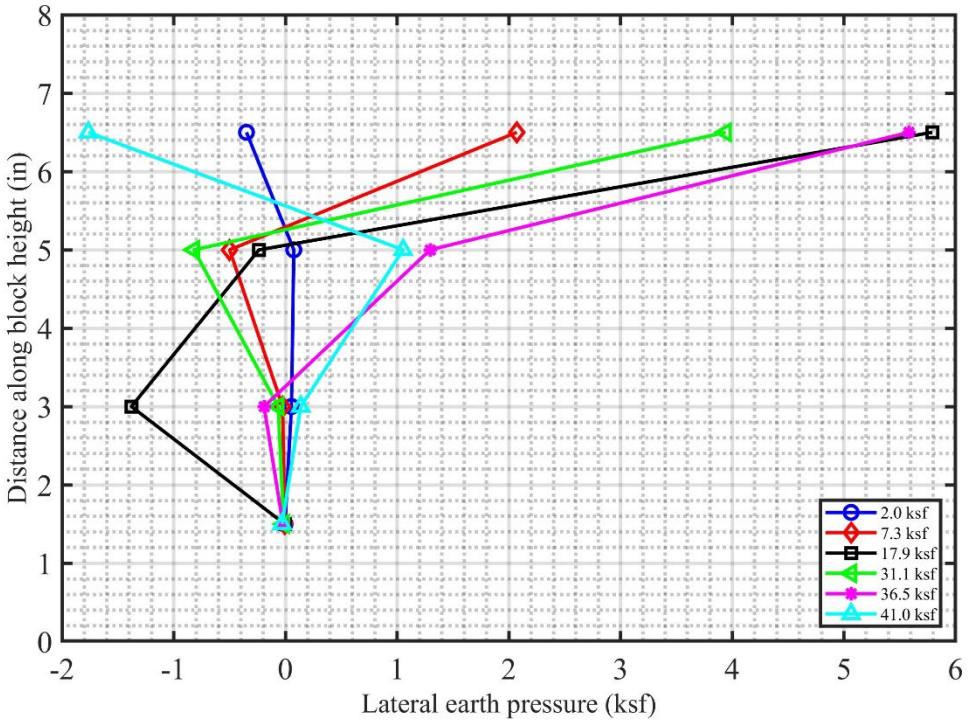


Figure D-3. Lateral earth pressure for PT-03 during axial loading of the pier.

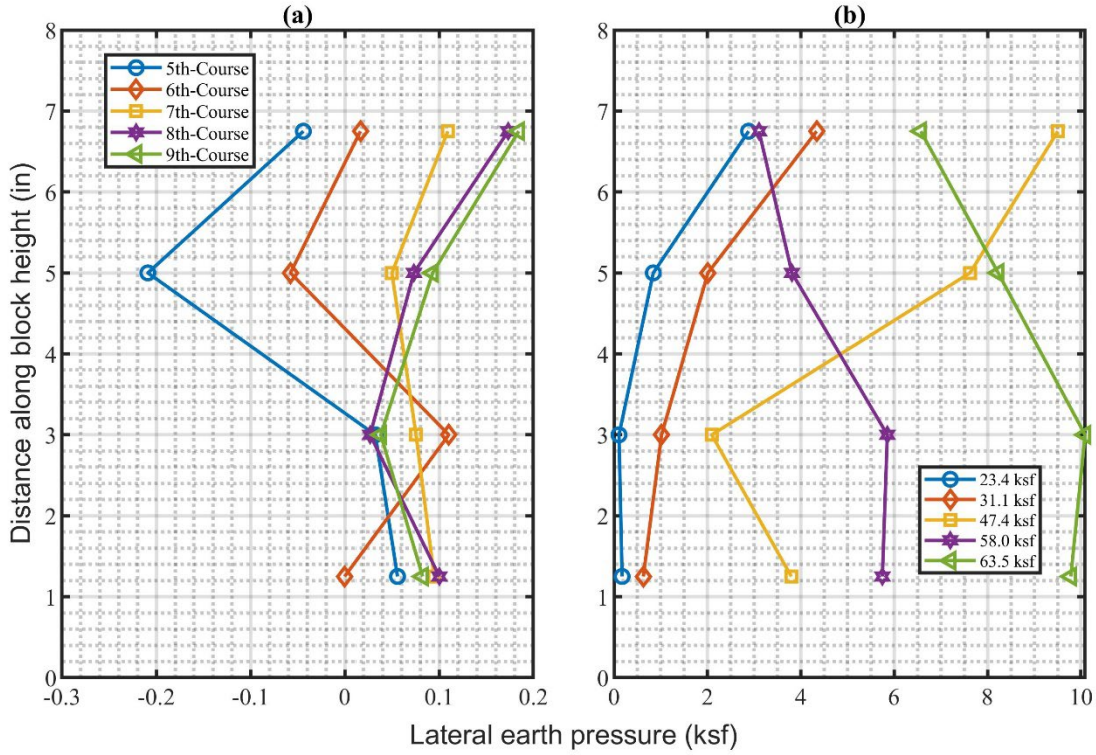


Figure D-4. Lateral earth pressure for PT-05.
(a) during construction; (b) during axial loading of the pier.

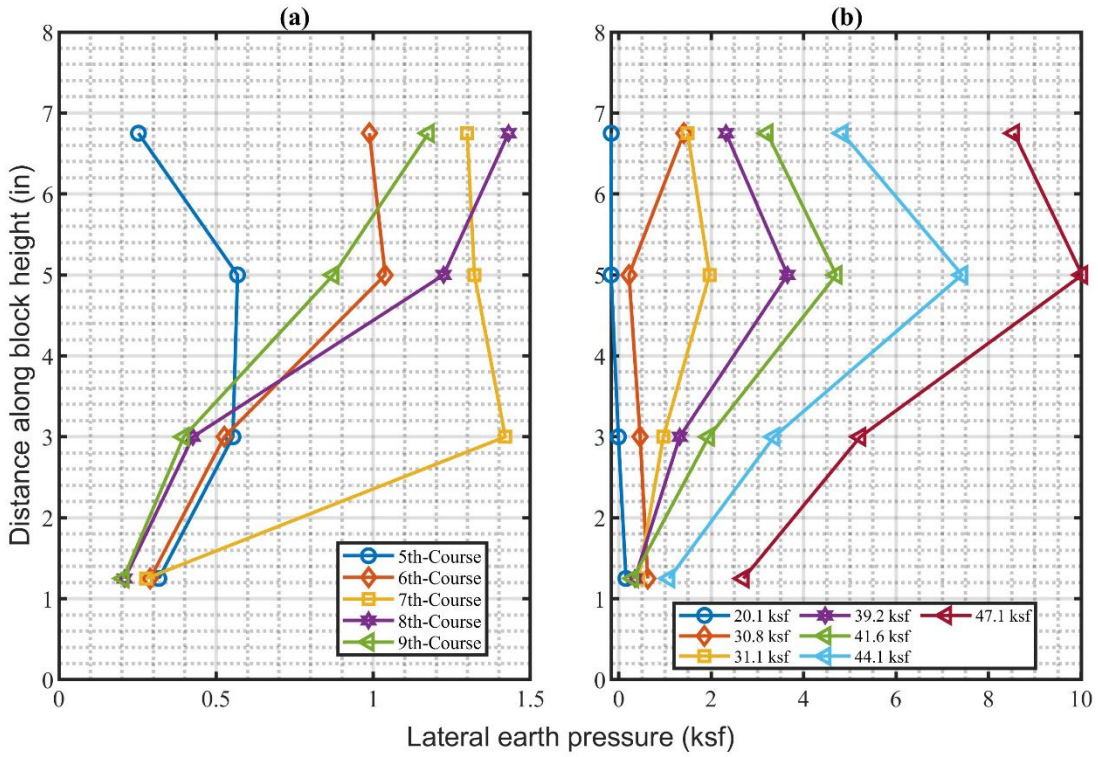


Figure D-5. Lateral earth pressure for PT-06.
(a) during construction; (b) during axial loading of the pier.

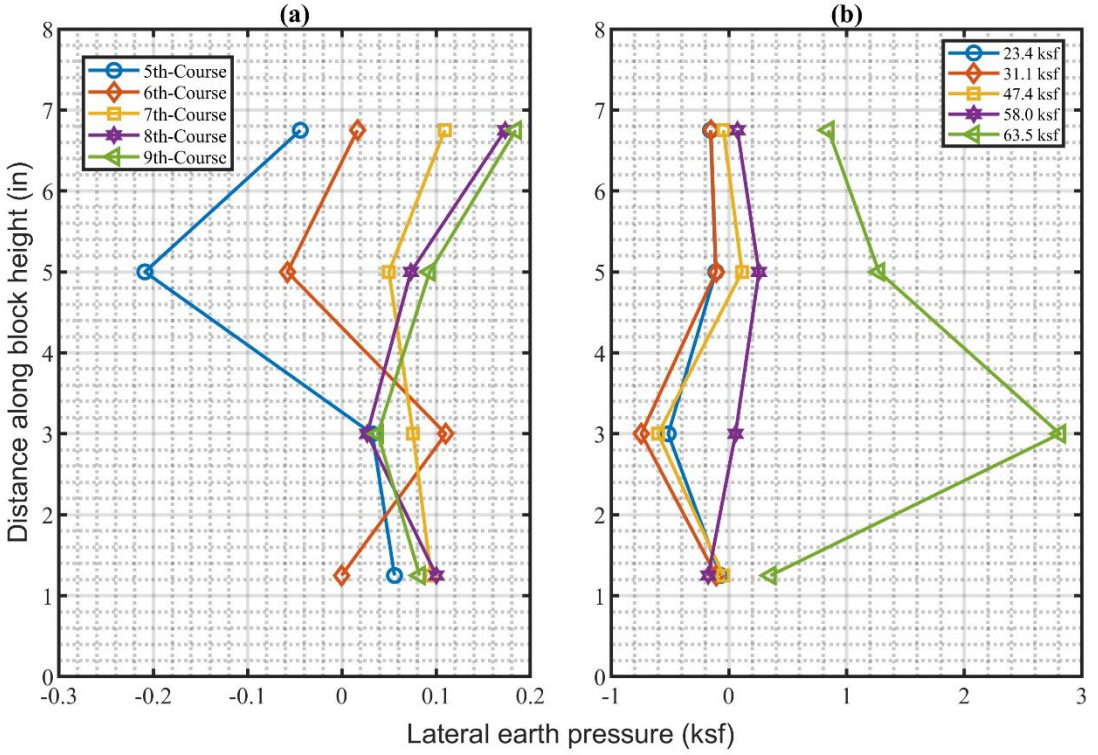


Figure D-6. Lateral earth pressure for PT-07.
(a) during construction; (b) during axial loading of the pier.

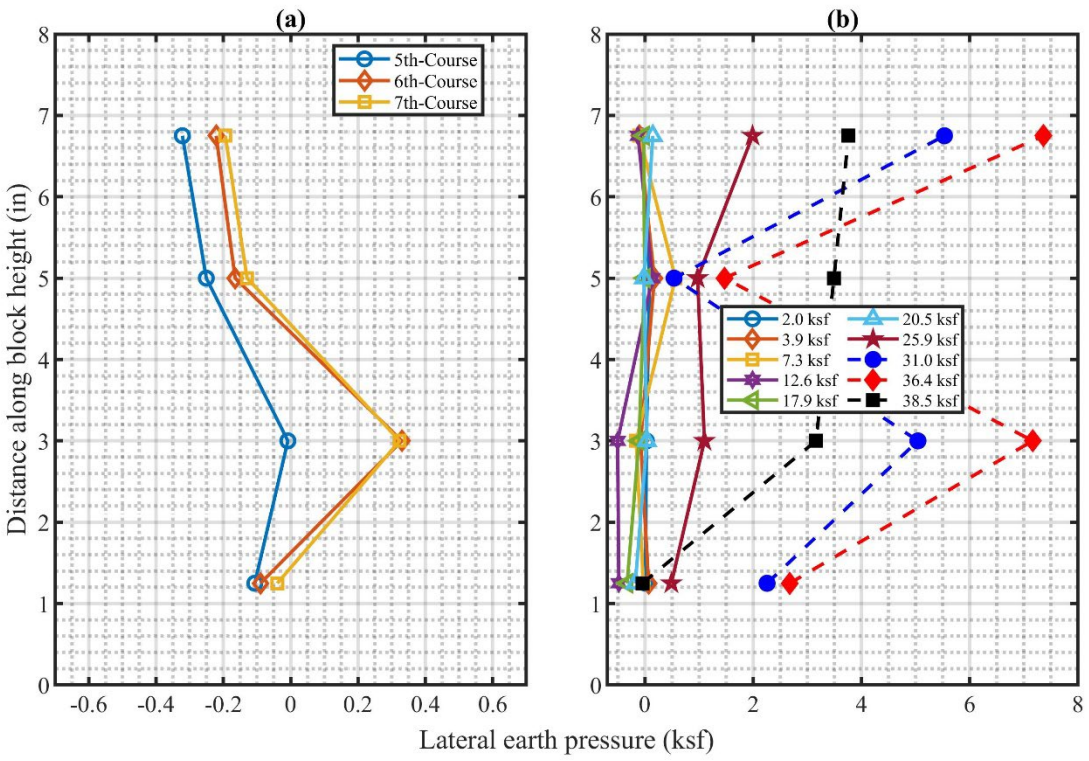


Figure D-7. Lateral earth pressure for PT-08.
(a) during construction; (b) during axial loading of the pier